

AD-A155 586

ARJ 18159.3-MS

2

DEVELOPMENT OF IMPROVED DYNAMIC FAILURE MODELS

Final Technical Report
(A Comprehensive Supplement)

15 February 1965

D. A. Shockey, D. R. Curran, and L. Seaman
With Contributions From R. D. Caligiuri,
D. C. Erlich, J. H. Giovanola, and T. Kobayashi

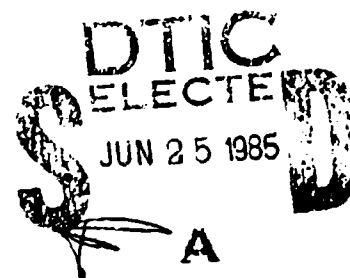
Prepared for:

U.S. ARMY RESEARCH OFFICE
P.O. Box 12211
Research Triangle Park, NC 27709

Contract No. DAAG-29-81-K-0123

Approved for public release;
Distribution unlimited

SRI International
333 Ravenswood Avenue
Menlo Park, California 94025
(415) 326-6200
TWX: 910-373-2046
Telex: 334 486



DTIC FILE COPY

42-000 142

The views, opinions, and/or findings contained in this report are those of the authors and should not be construed as an official Department of the Army position, policy, or decision, unless so designated by other documentation.

PAGES _____
ARE
MISSING
IN
ORIGINAL
DOCUMENT

UNCLASSIFIED

SECURITY CLASSIFICATION OF THIS PAGE

REPORT DOCUMENTATION PAGE

1a. REPORT SECURITY CLASSIFICATION		1d. RESTRICTIVE MARKINGS	
2a. SECURITY CLASSIFICATION AUTHORITY		3. DISTRIBUTION/AVAILABILITY OF REPORT Approved for public release; Distribution Unlimited	
2b. DECLASSIFICATION/DOWNGRADING SCHEDULE			
4. PERFORMING ORGANIZATION REPORT NUMBER(S) SRI Project 3722		5. MONITORING ORGANIZATION REPORT NUMBER(S) Contract DAAG-29-81-K-0123	
6a. NAME OF PERFORMING ORGANIZATION SRI International	6b. OFFICE SYMBOL (If applicable)	7a. NAME OF MONITORING ORGANIZATION U.S. Army Research Office	
6c. ADDRESS (City, State and ZIP Code) 333 Ravenswood Avenue Menlo Park, CA 94025		7b. ADDRESS (City, State and ZIP Code) Box 12211 Research Triangle Park, NC 27709	
8a. NAME OF FUNDING/SPONSORING ORGANIZATION U.S. Army Research Office	8b. OFFICE SYMBOL (If applicable)	9. PROCUREMENT INSTRUMENT IDENTIFICATION NUMBER	
8c. ADDRESS (City, State and ZIP Code) Box 12211 Research Triangle Park, NC 27709		10. SOURCE OF FUNDING NOS.	
		PROGRAM ELEMENT NO.	PROJECT NO.
		TASK NO.	WORK UNIT NO.
11. TITLE (Include Security Classification) Development of Improved Dynamic Failure Models			
12. PERSONAL AUTHOR(S) Shockey, Donald A., Curran, Donald R., and Seaman, Lynn			
13a. TYPE OF REPORT Final Technical	13b. TIME COVERED FROM 10-1-81 to 9-30-84	14. DATE OF REPORT (Yr. Mo. Day) 15 February 1985	15. PAGE COUNT 356
16. SUPPLEMENTARY NOTATION The views, opinions, and/or findings contained in this report are those of the author(s) and should not be construed as an official Department of the Army position, policy or decision, unless so designated by other documentation.			
17. COSATI CODES		18. SUBJECT TERMS (Continue on reverse if necessary and identify by block number)	
FIELD	GROUP	SUB. GR.	
		Shear band model, ductile fracture model, Split Hopkinson torsion bar, Taylor test, fracture surface topography	
19. ABSTRACT (Continue on reverse if necessary and identify by block number) Improved computational models were developed for dynamic material failure by shear banding and ductile fracture. The research effort involved theory, experiments and numerical analyses. A high performance split Hopkinson torsion bar was constructed and used to measure flow stress, failure strain, and shear band instability strains in VAR 4340 steel at strain rates ranging between 800 and 6000 s ⁻¹ . Taylor-type rod impact tests were performed to measure the dynamic flow curve as a function of temperature (to 947°C) and initial hardness. The fracture surface topography of tensile bars was quantitatively analyzed to ascertain details of the ductile fracture process and seek their dependence on microstructure. Observations and data from the experiments guided the modifications to the failure models.			
20. DISTRIBUTION/AVAILABILITY OF ABSTRACT UNCLASSIFIED/UNLIMITED <input type="checkbox"/> SAME AS RPT. <input checked="" type="checkbox"/> DTIC USERS <input type="checkbox"/>		21. ABSTRACT SECURITY CLASSIFICATION	
22a. NAME OF RESPONSIBLE INDIVIDUAL		22b. TELEPHONE NUMBER (Include Area Code)	22c. OFFICE SYMBOL

UNCLASSIFIED

SECURITY CLASSIFICATION OF THIS PAGE

— Viability of the models was verified and their usefulness in ordnance design was demonstrated by incorporating the models into the C-HEMP finite difference code and simulating various armor penetration scenarios. *Continued*

UNCLASSIFIED

SECURITY CLASSIFICATION OF THIS PAGE

CONTENTS

LIST OF ILLUSTRATIONS.....	vii
LIST OF TABLES.....	xv
STATEMENT OF PROBLEM.....	xvii
EXECUTIVE SUMMARY.....	S-1
I INTRODUCTION.....	I-1
II SPECIMEN MATERIAL (VAR 4340 STEEL)--HISTORY AND CHARACTERIZATION.....	II-1
A. Procurement, Chemistry and Thermal- Mechanical History.....	II-1
B. Microstructure and Inclusion Size Distribution.....	II-4
C. Standardized Heat Treatment.....	II-9
D. Mechanical Properties.....	II-10
E. Tensile Tests at Elevated Temperature and Strain Rate.....	II-11
III DYNAMIC SHEAR EXPERIMENTS.....	III-1
A. SRI High Performance Split Hopkinson Torsion Bar (SHTB).....	III-1
B. Dynamic Stress-Strain Curves for VAR 4340 Steel.....	III-5
C. Metallographic Observations.....	III-9
D. Optical Dynamic Strain Measurements.....	III-16
E. Measurements of Temperature Near Shear Bands.....	III-25
F. References.....	III-32
IV ROD IMPACT (TAYLOR) TESTS.....	IV-1
A. Historical Perspective and Technique Development.....	IV-3
B. Experimental Technique.....	IV-6
C. Analytical Technique.....	IV-9
D. Experimental and Analytical Results of the Rod Impact Tests.....	IV-17
E. References.....	IV-21

V	DERIVATION OF THE ADIABATIC SHEAR BAND NUCLEATION AND GROWTH RATE FUNCTIONS USED IN SHEAR4.....	V-1
A.	Introduction.....	V-1
B.	Nucleation Rate.....	V-2
C.	Growth Rate.....	V-8
D.	Size of Jog, B.....	V-9
E.	Discussion and Recommendations.....	V-10
F.	References.....	V-10
VI	THE SHEAR BAND MODEL (SHEAR4).....	VI-1
A.	Introduction.....	VI-1
B.	Orientations and Size Distributions.....	VI-5
C.	Microprocesses for the Shear Bands.....	VI-8
D.	Stress-Strain Relations for SHEAR4.....	VI-19
E.	Fitting the Shear Band Model to Data.....	VI-28
F.	Sample Results with the Shear Band Model.....	VI-34
G.	Concluding Remarks.....	VI-37
H.	References.....	VI-38
VII	MECHANISM OF DUCTILE TENSILE FRACTURE IN VAR 4340 STEEL.....	VII-1
A.	Introduction.....	VII-1
B.	Previous Work	VII-2
C.	Topographic Analysis of Fracture Surfaces: The Concept.....	VII-3
D.	Experimental Procedures.....	VII-4
E.	Reconstruction of the Fracture Process.....	VII-5
F.	Influence of Microstructure on Microfailure Processes.....	VIII-8
G.	Discussion.....	VIII-10
H.	References.....	VIII-11

VIII	A MICROSTATISTICAL MODEL (DFRACT2) FOR DUCTILE FRACTURE UNDER LOADINGS RANGING FROM QUASI-STATIC TO IMPACTS.....	VIII-1
A.	Introduction.....	VIII-1
B.	Previous Work.....	VIII-1
C.	Features of the Model.....	VIII-10
D.	Tests of the Model.....	VIII-24
E.	Explorations with the DFRACT2 Model.....	VIII-26
F.	Summary.....	VIII-28
G.	References.....	VIII-29
IX	RECOMMENDATIONS FOR FUTURE WORK.....	IX-1
X	PARTICIPATING SCIENTIFIC PERSONNEL.....	X-1
XI	PUBLICATIONS.....	XI-1

Accession For	
NTIS GRA&I	<input checked="checked" type="checkbox"/>
DTIC TAB	<input type="checkbox"/>
Unannounced	<input type="checkbox"/>
Justification	
By _____	
Distribution/	
Availability	
Dist	
A1	



ILLUSTRATIONS

II.1	Microstructure of 2-1/2-inch-diameter VAR 4340 Steel Bar Stock Transverse to Rolling Direction.....	II-13
II.2	Microstructure of 2-1/2-inch-diameter VAR 4340 Steel Bar Stock Parallel to Rolling Direction.....	II-14
II.3	Microstructure of 1-inch-diameter VAR 4340 Steel Bar Stock Transverse to Rolling Direction.....	II-15
II.4	Microstructure of 1-inch-diameter VAR 4340 Steel Bar Stock Parallel to Rolling Direction.....	II-16
II.5	Decarburized Surface Layers in the VAR 4340 Steel Bar Stock Produced by Republic Steel.....	II-17
II.6	Microstructure of 2-1/2-inch-diameter Air Melt 4340 Steel Bar Transverse to Rolling Direction.....	II-18
II.7	Microstructure of 2-1/2-inch-diameter Air Melt 4340 Steel Bar Parallel to Rolling Direction.....	II-19
II.8	Microstructure of 2-inch-diameter Tube of Aircraft Quality 4340 Steel Transverse to Rolling Direction.....	II-20
II.9	Microstructure of 2-inch-diameter Tube of Aircraft Quality 4340 Steel Parallel to Rolling Direction.....	II-21
II.10	Inclusion Size Distribution for 4340 Steel Processed by Different Melt Practices.....	II-22
II.11	Microstructure of 2-1/2-inch-diameter VAR 4340 Steel Bar Stock After Standardized Heat Treatment.....	II-23
II.12	True Stress-True Strain Curves (With Bridgman Correction) for HRC 40 1-inch-diameter VAR 4340 Steel Bar at Room Temperature Under Quasi-Static Loading.....	II-24
II.13	Effect of Temperature on True Stress-True Strain Curves (Without Bridgman Correction) for HRC 40 1-inch-diameter VAR 4340 Steel Bar at Elevated Strain Rate.....	II-25
III.1	Schematic of Split Hopkinson Torsion Bar.....	III-34
III.2	View of SHTB Looking Along the Input Bar Toward the Release Clamp and the Static Loading Mechanism.....	III-35
III.3	Release Clamp.....	III-36
III.4	Incident Shear Stress Wave Measured in the Input Bar...	III-37

III.5	Hexagonal Coupling Between Specimen and Bar.....	III-28
III.6	Specimen for SHTB Experiments.....	III-39
III.7	Coupling for High Temperature Insert Bars.....	III-40
III.8	Stress-Strain Curve for 4340 VAR R _C 40 for Four Strain Rates.....	III-41
III.9	Circumferential Displacement Profile Across the R _C 40 Specimen Width for Tests at Three Strain Rates.....	III-43
III.10	Stress-Strain Curve for 4340 VAR R _C 33 at Two Strain Rates.....	III-44
III.11	Circumferential Displacement Profile Across the R _C 33 Specimen Width for Tests at Three Strain Rates.....	III-45
III.12	Procedure for Metallographic Observation of Shear Specimens.....	III-46
III.13	Map of Crack Path in Specimen NT9.....	III-47
III.14	Photograph of Circumferential Edge of Fracture Surface in Specimen NT9.....	III-48
III.15	Optical Micrographs of Matching Segments of the Two Fracture Surfaces of Specimen ST16.....	III-49
III.16	Electron Micrograph of Matching Segments of the Two Fracture Surfaces of Specimen ST16.....	III-50
III.17	Electron Micrograph of Shear Fracture Surface in Specimen ST16, Showing Smeared Area and Dimple Area.....	III-51
III.18	Electron Micrograph of Shear Fracture Surface Showing Smeared Area and Changes in the Local Flow Direction.....	III-51
III.19	High Magnification Electron Micrograph of Elongated Dimple Area; Arrows Point to Carbide Particles.....	III-52
III.20	Polished and Etched Cross Sections of Specimen ST16 Showing Fine Microstructure and White-Etching Microstructure.....	III-53
III.21	Optical Micrograph of Matching Segments of the Two Fracture Surfaces of Specimen NT9.....	III-55
III.22	Electron Micrograph of Shear Fracture Surface of Specimen NT9.....	III-57
III.23	Electron Micrograph of Shear Fracture Surface of Specimen NT9 Showing Partially Smeared Dimple Area.....	III-58

III.24	Electron Micrograph of Matching Details of the Shear Fracture Surfaces of Specimen NT9.....	III-59
III.25	Schematic of Cross Section Along Dashed Line in Figure III.24b.....	III-60
III.26	Sequence of Failure of Unbroken Ligaments With Increasing Relative Displacement of Two Specimen Halves--Specimen NT9.....	III-61
III.27	Schematic of Experimental Arrangement for Optical Strain Measurements.....	III-62
III.28	Photograph of Experimental Arrangement for Optical Strain Measurements.....	III-63
III.29	Synchronization of Strain Gage Records and High-Speed Photography.....	III-64
III.30	Stress-Strain Curve for Test NT9.....	III-65
III.31	Time Sequence Photographs for Test NT9.....	III-66
III.32	Deformation Profiles at Different Times Obtained from High-Speed Photographs of Test NT9.....	III-67
III.33	Strain Profiles at Different Times Obtained from Deformation Profiles in Figure III.32 for Test NT9.....	III-68
III.34	Strain Rate as a Function of Time at the Shear Band Location for Test NT9.....	III-69
III.35	Stress-Strain Curve for Test NT6.....	III-70
III.36	Time Sequence Photographs for Test NT6.....	III-71
III.37	Deformation Profiles at Different Times Obtained From High-Speed Photographs of Test NT6.....	III-73
III.38	Strain Profiles at Different Times Obtained from Deformation Profiles in Figure III.37 for Test NT6.....	III-74
III.39	Strain Rate as a Function of Time at the Shear Band Location for Test NT6.....	III-75
III.40	Indirect Shear Band Temperature Measurement.....	III-76
III.41	Specific Heat as a Function of Temperature for 1010 Steel.....	III-77
III.42	Temperature Histories at Different Thermocouple Locations x in SHTB Experiments.....	III-78

IV.1	Schematic of Two Rod Impact Configurations.....	IV-24
IV.2	Schematic of Two Rod Impact Configurations for Elevated Temperatures.....	IV-25
IV.3	Silhouettes of Two 4340 Steel Rods at 947°C Following Double Rod Impact at 335 m/s (Test No. 7).....	IV-26
IV.4	Comparison of Ambient Temperature 4340 Steel (R_C 39) Rod Deformation Profiles ~25 μ s After Impact, From ASRI Test No. 8 and SRI Test No. 6.....	IV-27
IV.5	Comparisons of Slice Through Impact Region of 4340 Steel Rods Recovered from Ambient Temperature.....	IV-28
IV.6	Symmetric Rod Impact Tests at Ambient Temperature.....	IV-29
IV.7	Silhouettes of 4340 Steel (HRB 94) Rods During Symmetric Impact at 457 m/s (Test No. 4).....	IV-30
IV.8	End View of Apparatus for Rod Impact Tests at Elevated Temperature.....	IV-31
IV.9	Cross Section of Apparatus for Asymmetric Rod Impact Tests at Elevated Temperatures.....	IV-32
IV.10	Uncertainties in Obtaining Digitized Rod Profiles.....	IV-33
IV.11	Deformation Contours from 4340 Steel (R_B 94) Symmetric Rod Impact Test No. 4 at 457 m/s.....	IV-34
IV.12	Cell Outlines at Three Times During Simulation of Symmetric Rod Impact.....	IV-35
IV.13	Vectorial Representations of Principal Stresses and Strains During an Interval of Plastic Flow with Work-Hardening.....	IV-36
IV.14	Equivalent Plastic Strain Histories at Impact Interface.....	IV-37
IV.15	Equivalent Plastic Strain Histories Along Rod Axis.....	IV-38
IV.16	Equivalent Plastic Strain Rate Histories at Impact Interface.....	IV-39
IV.17	Equivalent Plastic Strain Rate Histories Along Rod Axis.....	IV-40
IV.18	Temperature Calculated from C-HEMP SRI Simulation of Test No. 4.....	IV-41
IV.19	Deformation Contours 28 μ s After 4340 Steel Symmetric Rod Impact at 457 m/s.....	IV-42
IV.20	Static Tensile and Compressive Data for 4340 Steel, Ambient Temperature, for Three Hardnesses.....	IV-43

IV.21	Comparison of Experimental Profile 28 μ s After Symmetric Impact of 4340 Steel Rods, with Computed Profiles, Using Different Flow Curves.....	IV-44
IV.22	Calculated and Experimental Profiles at Intermediate Times After Impact at 457 m/s.....	IV-45
IV.23	Measured Hardness Values in Deformed Regions of 4340 Steel Rods Recovered from Symmetric Impact at 457 m/s.....	IV-46
IV.24	Slice Through Impact Region of 4340 Steel Rods (R_B 94) Recovered from Symmetric Impact at 457 m/s, and Enlarged Views of the Damaged Region.....	IV-47
IV.25	Silhouettes of 4340 Steel Rod at 721°C Following Asymmetric Impact at 178 m/s (Test No. 12).....	IV-48
IV.26	Silhouettes of 4340 Steel Rod at 947°C Following Asymmetric Impact at 181 m/s (Test No. 13).....	IV-49
IV.27	Comparison of Final Experimental Rod Profile and Computational Profile 50 μ s After Simulated Impact for ASRI Test No. 9 (4340 Steel at 340°C).....	IV-50
IV.28	Comparison of Final Experimental Rod Profile and Computational Profile 50 μ s After Simulated Impact for ASRI Test No. 10 (4340 Steel at 403°C).....	IV-51
IV.29	Comparison of Final Experimental Rod Profile and Computational Profile 50 μ s After Simulated Impact for ASRI Test No. 12 (4340 Steel at 721°C).....	IV-52
IV.30	Comparison of Final Experimental Rod Profile and Computational Profile 100 μ s After Simulated Impact for ASRI Test No. 13 (4340 Steel at 947°C).....	IV-53
IV.31	Comparison of Final Experimental Rod Profile and Computational Profile 40 μ s After Simulated Impact for ASRI Test No. 8 (4340 Steel at Ambient Temperature).....	IV-54
IV.32	Input Flow Curves Used in C-HEMP Simulations of 4340 ASRI Tests.....	IV-55
V.1	Computational Simulation of Plane Strain Crack Loaded in Pure Shear.....	V-12
V.2	Static Adiabatic Yield Curves for 4340 Steel.....	V-12
VI.1	Framing Camera Photograph of Armco Iron Fragmenting Cylinder at 56 μ s After Detonation.....	VI-41

VI.2	Fragment (a) of 4340 Steel Cylinder (R_C 40) and Photomicrographs (b and c) of a Portion of Cylinder, Photographed with the Light from Different Directions to Contrast the Directions of Slip on the Bands.....	VI-42
VI.3	Relative Locations of the Coordinate Directions and Initial Orientation of the Shearing Planes.....	VI-44
VI.4	Six Shear Band Orientations Provided in the SHEAR4 Model.....	VI-45
VI.5	Shear Band Distribution for Experiment 2 in 4340 Steel, R_C 40.....	VI-46
VI.6	Shear Band Size Distribution Represented by a Series of Points and Exponential Line Segments.....	VI-47
VI.7	Shear Band Depth d Versus Displacement B Data.....	VI-48
VI.8	Comparison of Crack Opening as a Function of Stress from Several Theories.....	VI-49
VI.9	Comparison of Crack Opening as a Function of Strain from Several Theories.....	VI-50
VI.10	Stress-Strain Relations Assumed in the Theoretical Models for Crack Opening.....	VI-51
VI.11	Assumed Crack Opening Volume Changes During Loading, Unloading and Reloading.....	VI-52
VI.12	One of the Orientation Planes Showing Loading from an Initial State σ'_{k0} to a Final State σ'_k by a Combination of Elastic and Plastic Strains.....	VI-53
VI.13	Steps in Obtaining Cumulative Shear Band Distributions from Contained Fragmenting Cylinder Data.....	VI-54
VI.14	Computed Plastic Shear Strain in the Mode 1 Direction at Three Axial Positions in 4340 Steel Cylinder.....	VI-55
VI.15	Measured Number of Shear Bands Versus Computed Plastic Strain for Determining an Initial Estimate of the Nucleation Rate Parameter.....	VI-56
VI.16	Measured Size Parameters for Shear Band Versus Computed Plastic Strain for Determining an Initial Estimate of the Growth Rate Parameter.....	VI-57
VI.17	Plastic Strain Contours in 4340 Steel Fragmenting Cylinder in the Mode 1 Orientation at 100 μs after Detonation: SHEAR4 Simulation.....	VI-58

VI.18	Simulation of a Blunt 4340 Steel Rod Penetrating a RHA Plate at the Ballistic Limit (750 m/s).....	VI-59
VI.19	Simulation of a Blunt 4340 Steel Rod Penetrating a RHA Plate at 1550 m/s (at 28 μ s).....	VI-60
VI.20	Three Views of a Steel Cylinder After Impacting a Quartzite Target at 140 m/s.....	VI-61
VI.21	Contours of Plastic Strain in the Direction to Form a Core at the Head of the Projectile: SHEAR4 Simulation of a Taylor Test with 4340 Steel.....	VI-62
VI.22	Proposed Stress-Strain Path Showing Thermal Softening and the Nucleation Threshold for Shear Banding.....	VI-63
VI.23	Results of a SHEAR4 Simulation of a Taylor Test Using Thermal Softening: Contour Lines are for the Cone-Forming Orientation of Shear Bands.....	VI-64
VII.1	SEM Photographs of Conjugate Fracture Surfaces in HRC 40 VAR 4340 Steel Tensile Bar.....	VII-12
VII.2	Stereopair of SEM Photographs of Fracture Surface A (in Fig. VII.1) at 100x Magnification.....	VII-13
VII.3	Stereopair of SEM Photographs of Fracture Surface B (in Fig. VII.1) at 100x Magnification.....	VII-14
VII.4	Conjugate Topographic Maps for Stereopairs in Figures VII.2 and VII.3.....	VII-15
VII.5	Fractured Area Projection Plots.....	VII-16
VII.6	Cross-Sectional Views of FAP Plots.....	VII-18
VII.7	Correlation of Topographic Data with Microstructural Features on the Fracture Surface.....	VII-19
VII.8	Microstructures of VAR 4340 Steel on Planes Beneath the Fracture Surface, as Revealed by Different Etchants.....	VII-20
VIII.1	Void Expansion Under External Tension for Several Initial Relative Void Volumes.....	VIII-32
VIII.2	Relations Between the Elastically Computed Stress State, the Yielded State, and the Gurson Yield Curve for a Normality Condition.....	VIII-33
VIII.3	Nucleation of Voids in the Smooth Round Bar Tension Test.....	VIII-34
VIII.4	A Family of Gurson Yield (Threshold) Curves for Several Void Volumes.....	VIII-35

VIII.5	Stress-Strain Paths for Uniaxial Strain Simulation of Several Strain Rates (1145 Al with Yield = 0.2 GPa).....	VIII-36
VIII.6	Computed Histories of Axial Stress (σ_1), Mean Stresses (P), Mises Stress ($\bar{\sigma}$), Threshold Pressure (P_{th}), and Threshold Yield Stress (σ_{th}) for Uniaxial Strain Test at a Strain Rate of 10^6	VIII-37
VIII.7	Pressure-Shear Stress Paths Followed by Fracturing Aluminum at Two Strain Rates in Uniaxial Strain.....	VIII-38
VIII.8	Peak Axial Stress as a Function of Strain Rate for Uniaxial Strain Experiments.....	VIII-39
VIII.9	Uniaxial Stress Loading at Several Strain Rates.....	VIII-40

TABLES

II.1	Inventory of VAR and ESR 4340 Steel Shipped to AMMRC.....	II-3
II.2	Mechanical Properties of 4340 Steel Alloy.....	II-4
II.3	Chemical Composition, Wt% of 4340 Steel Alloy.....	II-4
III.1	Results of Temperature Measurements.....	III-3
IV.1	Rod Impact Experiments Performed.....	IV-2
IV.2	Equation-of-State Parameters Used in ASRI Simulations..	IV-12
V.1	Comparison of Derived and Experimentally Determined SHEAR4 Nucleation and Growth Parameters for 4340 Steel in CFC Experiments.....	V-11
VI.1	Orientation Options for Shear Band Modeling.....	VI-6
VI.2	Input Data for SHEAR4.....	VI-31
VI.3	Shear Banding and Yield Parameters for 4340 and RHA Steels.....	VI-33
VIII.1	Fracture Properties.....	VIII-26

STATEMENT OF PROBLEM

The traditional empirical approach for designing armor and weapons is usually lengthy and costly and is becoming less tractable as more complex systems are introduced. A more efficient approach that combines test firings with numerical finite element and finite difference methods is currently being developed by the DoD. The numerical methods are capable of handling complex shapes, deformations, and material behavior, but reliable models of material disintegration under high-rate loads are lacking. The objective of this program was to develop computational models for dynamic failure by shear banding and ductile tensile fracture.

EXECUTIVE SUMMARY

Background

The purpose of this three-year SRI program, funded by the Army Research Office, was to develop improved failure models to be used in numerical calculations of material failure under conditions of high strains and strain rates. Applications of interest to the Army include armor penetration by kinetic energy penetrators and fragmenting munitions.

The improved failure models were to be based on the actual failure phenomenology, and the model parameters were to be based on material properties measureable in the laboratory. In previous work performed for the Naval Surface Weapons Center,^{1*} the Army Materials and Mechanics Research Center,² and the Ballistic Research Laboratory,³ we had ascertained that the primary failure mode for armor penetration and fragmenting munitions was the nucleation, growth, and coalescence of adiabatic shear bands, and a secondary failure mode was the nucleation, growth, and coalescence of microscopic "ductile" voids. (The term "ductile" refers to the ellipsoidal nature of the voids, which grow by local plastic flow rather than by "brittle" cleavage cracking.) The goal of our program was therefore to develop and test improved failure models for the kinetics of adiabatic shear banding and ductile void behavior.

For ease of use in numerical wave propagation computer codes, the failure models were to represent the evolving shear band and void damage as internal state variables in the continuum constitutive relations for the material. The internal state variable chosen was the damage distribution function that gives at each material point the current

*References are listed at the end of this summary.

number per unit volume of shear bands or voids as a function of size and orientation. Thus the damage function serves as a link between the continuum level, where stresses and strains are calculated, and the microscopic level, where the damage processes actually occur. The above approach had been used successfully in previous work on dynamic cleavage cracking and void formation in a variety of solids loaded in simpler, one-dimensional strain geometries.⁴

Approach

At the beginning of the program, in cooperation with researchers in a parallel program at Brown University, we selected vacuum arc remelted (VAR) 4340 steel as the baseline material to be studied. One reason for selecting this material was that we had previously obtained extensive experiments on shear band behavior from controlled fragmenting cylinder (CFC) data on three hardnesses of 4340 steel.⁵ A second reason was that by varying the melting/processing procedures for this steel, we could obtain several different microstructures and hence examine microstructural effects on shear banding. The procurement and characterization of the VAR 4340 steel is described in detail in Section II.

The prior data base for shear banding in 4340 steel consisted mainly of the CFC data referred to above. We supplemented these data, for which the shear banding occurred under conditions of significant compression and shear, with data from Hopkinson torsion bar experiments and Taylor tests. The Hopkinson torsion bar experiments were performed under conditions of pure shear, and the Taylor tests were performed under complex conditions of compression, tension, and shear that are close to those existing during armor penetration.

Because existing Hopkinson bars were unable to adequately test the high strength steel, a first step in our program was to design and construct a new Hopkinson torsion bar facility that extended the range of testing to strain rates of 10^4 s^{-1} in materials with yield strengths of 2000 MPa. This facility represents an extension of previous capabilities

by nearly an order of magnitude in both material strength and strain rate. The details of the development of this facility are given in Section III.

The capabilities of our rod impact testing facility were also expanded during the program to allow for the testing of specimens at elevated temperatures. It was demonstrated that for 4340 steel, friction along the impact interface did not noticeably affect the specimen rod deformation profiles, and therefore an asymmetric rod impact test (hardened plate-into-rod) was almost as valid a method for determining the dynamic flow curve of this material as the symmetric rod-into-rod technique (which can only be used with room temperature specimens). The asymmetric rod impact technique was used on 4340 steel specimens at temperatures up to nearly 1000°C. Details of the Taylor test experiments are given in Section IV.

Previous work had resulted in several preliminary computer models for the nucleation, growth, and coalescence of shear bands. At the beginning of this program, a previous model, SHEAR3, was used in a series of parametric calculations for both fragmenting cylinder and armor penetration tests to determine the material properties that should most affect the shear banding behavior. Comparison of these calculations with metallographic examination of test specimens showed that deformation-induced anisotropy was expected to be an important factor, especially in dynamic punch tests or armor penetration. For example, planes in the material that were originally orthogonal were observed to become so skewed that they became almost parallel in the vicinity of a penetrator.

The SHEAR3 model could handle only rigid body rotations, and could therefore not adequately describe the predicted and observed strong skewing. We therefore embarked on the development of SHEAR4, a model that could account not only for such large deformations, but also for anisotropic hardening resulting from varying amounts of slip in different orientations.

The inputs required for the SHEAR4 model include not only the usual stress-strain relations for the intact material, but also the equations

that govern the nucleation, growth, and coalescence of the bands. These equations were derived from basic mechanics considerations and were confirmed by correlations with the experimental data. The details are given in Section V.

The SHEAR4 model, as completed, handles plasticity with a multislip plane algorithm similar to that described by Peirce, Asaro, and Needleman⁶ for single crystals, but also describes nucleation, growth, coalescence, and tensile opening of shear bands in the multiple material planes. The details of the SHEAR4 model are given in Section VI.

We also performed an experimental and theoretical effort on the secondary failure mode, ductile tensile fracture. Micromechanisms of ductile tensile failure and the sequencing of microfailure events in 4340 steel under uniaxial tension were ascertained by applying a quantitative analysis technique to the fracture surfaces of a round bar tensile specimen. The results were correlated with metallographic observations to identify the role of various microstructural features on microfailure processes. These observations and data are intended to guide development of the computational model for ductile fracture, DFRAC2. Details are given in Section VII.

The development effort for the ductile fracture model, DFRAC2, was partially funded by a parallel program for the National Science Foundation (Research Grant No. MEA 8108186). This model describes the nucleation and growth of ductile voids under both quasi-static and dynamic strain rates. We performed parametric calculations with DFRAC2 to study the predicted effect of various load paths on the void behavior, and especially on the "void softening" that has been postulated to aid in the nucleation of shear bands.⁷ We have also designed, but not performed, numerical calculations with DFRAC2 to attempt to reproduce the tensile bar results obtained from the topographic technique. The above work is described in more detail in Section VIII.

Summary of Experimental Shear Band Results

The Hopkinson bar and Taylor test results provided data that supplemented the previous CFC data; these new data resulted in a significant modification of our prior nucleation function, as well as, we believe, a significant improvement in our understanding of the nucleation process.

Before discussing these experimental results, we must first define what we mean by a shear band. Present understanding of shear band phenomenology has been recently reviewed by Asaro and Needleman.⁸ The term "shear banding" has been used in the literature to refer to a variety of phenomena ranging from plastic flow localization within a single crystal to formation of macroscopic regions of intense shear strain. The nucleation process is thought to be triggered in most cases by material softening mechanisms. On the microscopic level, as reviewed and discussed by Peirce, Asaro, and Needleman,⁶ "geometric softening" caused by the rotation of individual crystallographic slip planes can cause shear band nucleation. Another postulated microscopic softening mechanism is the interaction of microscopic voids.⁹ However, the shear bands observed in the fragmenting cylinder, Taylor test, Hopkinson bar experiment, and previous dynamic punch tests were macroscopic in size, many grains in extent. The softening mechanism believed to nucleate these bands is thermal softening caused by the nearly adiabatic heating operative at high plastic strain rates. That is, when the heating softens the material more rapidly than the material work hardens, the shear stress will begin to decrease with increasing plastic strain.

A variety of theoretical studies has shown that the above situation is conducive to the growth of perturbations in the plastic flow to cause localization of the strain into regions of intense strain. However, to our knowledge, all of the earlier localization analyses have considered a plane strain situation in which the localization occurs in a plane of infinite extent, a condition far removed from the observed situations, as discussed below.

The detailed experimental results of the earlier CFC and dynamic punch experiments, together with the Hopkinson bar and Taylor test experiments performed during the present program, are given in Sections III, IV, and VI. The results can be briefly summarized as follows:

- The observed shear bands are not infinite sheets, but nucleate as small penny-shaped or half-penny-shaped planar imperfections with radii on the order of 0.1 mm, and thereafter grow radially outward like macroscopic dislocations with edge and screw components. In the Hopkinson bar experiments the bands on different planes coalesced by ligament tearing and the associated formation of microscopic voids.
- The temperatures in the bands inferred from Hopkinson bar thermocouple measurements are extremely high, (100°-1200°C). The energy dissipated by a shear band is estimated to be about 0.17 MJ/m².
- There is no obvious correlation of the nucleation sites with microstructural features, but there is a correlation with macroscopic (~ 0.1 mm) flow perturbations such as surface ripples, large voids, or large strain gradients at projectile or specimen corners. A possible correlation between the nucleation sites and prior austenitic grain boundaries may exist, since void formation was found in Section VII to occur preferentially at prior austenite grain boundaries.
- The shear bands nucleate at a constant critical strain resolved on each individual material plane that experiences significant shear strain. That is, the nucleation is a function of the resolved plastic strain on each material plane, and is thus not a function of the equivalent plastic strain. The nucleation strain for 4340 steel (HRC 40) determined in Hopkinson bar tests is 0.1 to 0.15; in contained fragmenting cylinder tests this quantity was inferred to be about 0.25.
- In the Hopkinson bar experiments, the shear bands were invariably associated with microscopic voids.
- The extension rate or "growth velocity" of the shear bands appears to obey a growth law of the form:

$$\dot{R}_i / R_i \propto \dot{\epsilon}_i^p$$

where R is the band radius, ϵ^p is the resolved plastic strain, and the subscript i refers to the i 'th material plane.

- The "jog" or amount of slip accommodated by a band is proportional to the band radius.

Summary of SHEAR4 Development

The details of the SHEAR4 development are given in Sections V and VI. The main features of SHEAR4 are summarized as follows.

The plasticity in the intact material is handled in the manner proposed by Batdorf and Budiansky,¹⁰ and recently extended by Peirce, Asaro, and Needleman,⁶ in single crystals. All the plastic shear deformation is constrained to occur by slip on a discrete number of planes in the material. The slip is partitioned among the planes by a time-dependent stress relaxation model, thereby assuring a unique solution. On each material plane, shear bands are nucleated when a threshold strain on that plane is exceeded. The number, sizes, and spacing of the bands are determined by the initially present imperfections and by heat flow considerations, as discussed in Section V. After nucleation, the bands extend according to a growth law derived in Section V. Eventually they coalesce and form fragments with specific size distributions, as described in Sections V and VI. As the bands nucleate, grow, and coalesce into fragments, they are allowed to open under tension (see Section VI). The evolving shear bands relax both the continuum mean stress and deviator stress (J_1 and $\sqrt{J_2}$) as elastic strains are converted into plastic shear strains and band opening strains. In short, the evolving damage softens the material.

SHEAR4 has been debugged and tested in a variety of numerical calculations during this research program. For these calculations, the SHEAR4 subroutine served as the constitutive relations in the C-HEMP two-dimensional, Lagrangian wave propagation code. C-HEMP was developed in a parallel program funded by BRL (Contract No. DAAK11-78-C-0115). First, SHEAR4 was debugged by calculations that forced a single material cell through a variety of strain histories. Next, SHEAR4 and C-HEMP were used to computationally simulate CFC, Taylor tests, and dynamic punch tests. Full computational simulations of the Hopkinson bar tests have not yet been attempted, but a computation was completed of a planar imperfection in a specimen subjected to pure shear, a situation closely akin to the Hopkinson bar tests performed during the program.

The calculations were of two types. In the first type, SHEAR4 was used only in the multiplane plasticity mode--that is, no shear bands were allowed to nucleate. In such calculations we studied the conditions for nucleation and growth of individual bands. For example, in the computation of a planar imperfection subjected to pure shear, we observed the behavior that led to the derived nucleation rate and growth rate equations (see Section V). In the Taylor test calculations, we observed the nucleation and growth of a single shear band at the flow perturbation caused by the corner of the impacting rod, in agreement with experimental observations.

In the second type of calculation, both the multiplane plasticity model and the shear band kinetics model were allowed to operate simultaneously. These calculations gave good agreement with the large numbers of shear bands observed in the CFC experiments. In such computations, modeling each individual band would have been prohibitively expensive. Another such calculation simulated the impact of a long rod kinetic energy penetrator on armor plate (see Section VI). In this calculation SHEAR4 correctly predicted the coalescence of many bands to form a "plug" that allowed penetration. Furthermore, correlation with prior SHEAR3 calculations and experimental data showed that the correct ballistic limit (the impact velocity required to ensure penetration) could be inferred.

Summary of Ductile Tensile Fracture Experiments and DFRAC2 Model Development

Micromechanisms of ductile tensile fracture were studied by quantitative topographic analysis of the fracture surfaces of a round bar tensile specimen of the baseline VAR 4340 steel. Microfracture features were correlated with microstructural features, and the results can be used to guide the development of the computational model. Details of this work are given in Section VII. The results can be briefly summarized as follows:

- Ductile tensile fracture in the baseline VAR 4340 steel occurs by the nucleation, growth, and coalescence of voids. All voids that nucleate participate in the macrofracture process; that is, there is little collateral fracture damage.
- Microfracture initiates at numerous sites internal to the tensile bar. The number of nuclei increases with plastic strain; this relationship is quantifiable.
- Microfracture nucleation occurs predominantly on prior austenite grain boundaries, and microfracture growth tends to follow these grain boundaries. Thus initial stages of growth occur on surfaces oriented at large angles to the tensile axis.
- In general, microfractures expand symmetrically, and their rate of growth is quantifiable from the data. The large number of voids observed makes a statistical determination of the growth rate possible; however, such an evaluation has not yet been accomplished.
- Microfracture coalescence occurs in such a way as to maintain equiaxed fracture areas. Coalescence rates can be estimated using an analysis similar to that used for growth of individual microfractures.
- Unbroken ligaments are commonly observed within areas of coalesced microfractures.

The secondary failure mode--ductile void nucleation, growth, and coalescence--is modeled by the DFRAC22 subroutine referred to above. DFRAC22 was used in a series of calculations in which a single material element was subjected to various deformation histories. A key result was the observation that under uniaxial strain conditions the DFRAC22 model predicted rapid shear stress relaxation. This apparent softening is not a consequence of matrix material softening because the matrix material is still hardening in the calculation. Instead, the softening is a curious consequence of the imposed normality condition for the yield surface derived by Gurson.¹¹ This softening may play a key role in the observed formation of shear bands between voids in high strength steels.

In the present research program, we also designed calculations to model the intergranular void activity observed in our tensile bar experiments (Section VII). The planned calculations will require fine zoning to allow the specification of different DFRAC22 parameters in

grain boundary cells rather than in the grains themselves. However, these calculations have not yet been performed.

Conclusions and Recommendations

Improved failure models for shear band and void kinetics have been developed. As desired, the models reflect the actual microscopic process phenomenologies, and the input parameters are measured in laboratory tests. Furthermore, the preliminary computational simulations with both SHEAR4 and DFRAC2 have produced results that show promise for practical applications.

As discussed in Section V, the current shear band nucleation rate function in SHEAR4 is based on a series of assumptions that are reasonable and are in agreement with existing experimental data. However, those assumptions need to be tested further by performing experiments designed for that purpose. For example, a key parameter in the nucleation rate function is the number per unit volume of macroscopic (> 0.1 mm) plastic flow perturbations, that is, the concentration of nucleation sites. Experiments should be performed to introduce artificial perturbations, and to compare the observed shear bands with the SHEAR4 predictions.

In addition, the multiplane plasticity feature of SHEAR4 should be applied to single-crystal plasticity in the manner of Peirce, Asaro, and Needleman.⁶ Many existing problems in plasticity theory could be examined profitably in this way, including the role played by latent hardening and the conditions for formation of isothermal microscopic shear bands. Further, the SHEAR4 model should be amplified to treat plane stress deformation and tensile opening of shear bands.

Additional measurements of the strain profile as a function of time in the vicinity of a developing shear band would be most useful in the modeling effort, as would experiments to measure the effects of compressive stress on shear band behavior. Finally, a firmer knowledge of the dependence of shear band initiation and growth behavior on the macroscopic stress and strain should be sought. This knowledge could be

obtained by computational simulation of Hopkinson torsion bar experiments. Additional Hopkinson bar experiments should also be performed to further study the mixed void and shear band behavior observed during the program just completed.

Future advances in the understanding and modeling of ductile tensile fracture can be expected from further investigations of fracture surface topography using the methods described in Section VII. The topographic analysis data should be reduced to obtain quantitative relationships between strain and nucleation, growth, and coalescence of voids. Investigations at higher magnification should be conducted to examine the roles of inclusions and carbides. Surfaces of specimens fractured by dynamic loads should be examined, additional metallographic examinations should be performed, and the time-resolved fractographic results should be correlated with microstructural features.

As for the DFRAC2 model, it should not only be tested against the tensile bar data obtained during this program, but also be used to study the void softening effect on shear band nucleation, as mentioned above.

Finally, the evolving SHEAR4 and DFRAC2 models should be applied to practical applications such as armor fragmentation arising from kinetic energy penetration. This research program has brought these models to the point where their usefulness can be tested.

References

1. L. Seaman, D. A. Shockey, D. R. Curran, and R. E. Tokheim, "Development of a Shear Band Model for Fragmentation in Exploding Cylinders," SRI International Final Report on Contract NO0178-74-C-0450 for Naval Surface Weapons Center (August 1975).
2. L. Seaman and D. A. Shockey, "Models for Ductile and Brittle Fracture for Two-Dimensional Wave Propagation Calculations," SRI International Final Report on Contract No. DAAG46-72-C-0182 for Army Materials and Mechanics Research Center (February 1975).
3. (a) D. R. Curran, L. Seaman, D. A. Shockey, D. C. Erlich, R. D. Caligiuri, M. Cowperthwaite, and R. Burhack, "Computational Model for Armor Penetration," SRI International Annual Reports on Contract DAAK11-78-CO-0115 for Ballistic Research Laboratory (November 1979 and November 1980).

(b) J. Dein and L. Seaman, "User's Guide to C-HEMP, a Two-Dimensional Wave-Propagation Code," Volume 3, SRI International Final Report on Contract DAAK11-78-C-0115 for Ballistic Research Laboratory (April 1983).

(c) L. Seaman, "Development of a Model for Shear Banding: SHEAR3," Volume 2, SRI International Final Report on Contract DAAK11-78-C-0115 for Ballistic Research Laboratory (April 1983).

4. L. Seaman, D. R. Curran, and D. A. Shockey, "Computational Models for Ductile and Brittle Fracture," J. Appl. Phys. 47, 11 (November 1976).
5. D. C. Erlich, D. R. Curran, and L. Seaman, "Further Development of a Computational Shear Band Model," SRI International Final Report on Contract No. DAAG46-77-C-0043 for U.S. Army Materials and Mechanics Research Center (September 1978).
6. D. Peirce, R. J. Asaro, and A. Needleman, "Material Rate Dependence and Localized Deformation in Crystalline Solids," Acta Met. 31(12), 1951-1976 (1983).
7. L. Seaman and D. R. Curran, "A Microstatistical Model for Ductile Fracture Under Loadings Ranging from Quasi-Static to Impacts," in High Energy Rate Fabrication--1984, Proceedings of the 8th International Conference on High Energy Rate Fabrication, San Antonio, Texas, June 17-21, 1984, I. Berman and J. W. Schroeder, Eds. (The American Society of Mechanical Engineers, New York, 1984), p.99.
8. R. J. Asaro and A. Needleman, "Flow Localization in Strain Hardening in Crystalline Solids," Scripta Met. 18(5), 429-435 (May 1984).
9. A. Needleman and V. Tvergaard, "Necking of Biaxially Stretched Elastic-Plastic Circular Plates," J. Mech. Phys. Solids 25, 159 (1977).
10. S. B. Batdorf and B. Budiansky, "A Mathematical Theory of Plasticity Based on the Concept of Slip," National Advisory Committee for Aeronautics Technical Note No. 1871 (Washington, April 1949).
11. A. L. Gurson, "Continuum Theory of Ductile Rupture by Void Nucleation and Growth: Part I--Yield Criteria and Flow Rules for Porous Ductile Media," J. Engin. Mater. Tech. (January 1977).

I INTRODUCTION

The state of understanding of the response of metals to ultrahigh loading rates was recently reviewed¹ by a committee of the National Materials Advisory Board (NMAB) under contract with the Department of Defense and the National Aeronautics and Space Administration. Because of the current importance of conventional and near-term anti-armor weapons and their penetration of armor, the study focused on metallic materials under loading conditions typical of direct exposure to high explosives and impact.

The committee noted that the traditional empirical approach for designing armor and weapons has often been effective in gaining successive incremental improvements over the established state of the art. However, as more complex weapon and armor systems are introduced, the usually very lengthy and expensive empirical approach becomes less and less tractable. In recent years numerical finite difference and finite element methods have been developed to the point where they are capable of handling complex shapes, deformations, and material behavior and therefore promise to be useful in armor and anti-armor design.

The computational approach to ordnance design is an iterative procedure in which approximate computational simulations of an ordnance event are first performed using estimated values of material properties. Test firings are then conducted to evaluate the performance of the design, to provide data for comparison with calculated results, and to indicate the adequacy of the material property values. The test results then suggest changes in the initial ordnance design and guide the selection of material descriptions and dynamic material property tests for the next series of computational simulations. Test firings of a second generation design are then performed, and the results are compared with computational results, as before. The iterative process is repeated

until the ordnance refinements produce the desired performance. This approach, currently being developed by the DoD, reduces the overall design effort because the interaction of experiments and calculations leads more rapidly to an acceptable design.

Material responses that must be modeled in computational simulations of ordnance events include a thermodynamic equation of state, plastic flow, and material disintegration. The committee found that existing descriptions of thermodynamic equations of state are adequate for most calculations in ordnance design and that concepts of perfect plasticity are adequate for many ordnance applications, although continued research was recommended to extend our understanding in preparation for future needs.

The most serious limitation in efficient ordnance design was found to be in the modeling of material disintegration. Disintegration can occur by several mechanisms, depending on the material and the conditions of stress, temperature, and strain rate. Detailed examinations of material recovered from many and varied ordnance events have identified three main material failure modes: brittle fracture, ductile fracture, and localized shear failure. Of these three microscopic failure modes, the last two are more common in metallic armor.

Although simple failure criteria may suffice to obtain reliable computational simulations of certain ordnance events, other situations require a detailed model and hence a detailed physical understanding of nucleation, growth, and coalescence of cracks, voids, and shear bands. Whereas a significant amount of relevant research has already been done in this area, much more is required to allow adequate computations to be performed. The committee therefore recommended accelerated research on the mechanisms and modeling of material failure by cracks, voids, and shear bands.

The research program described in this report responds to the NMAB committee recommendations by striving toward a better understanding of the micromechanical details of material failure and toward the development of improved microfailure models. The research focused on the

failure modes most common in metallic armor, namely, failure by shear band and void activity. This report presents the results of this program.

The next section describes the baseline specimen material, vacuum-arc-remelted (VAR) 4340 steel tempered to a hardness of HRC 40, and gives the reasons for its selection. Section III describes the design and construction of a high performance Hopkinson torsion bar facility, and the results of experiments for measuring dynamic shear stress-shear strain characteristics, shear strain localization behavior, shear band nucleation and growth kinetics, and shear band temperatures.

A comprehensive analysis of the Taylor rod-on-plate impact test and several experimental modifications to this test are presented in Section IV, along with shear band observations and measured dynamic compressive stress-strain curves at various temperatures.

Nucleation and growth rate functions are derived from theoretical considerations and compared with the experimental data in Section V. In Section VI we describe the computational model for shear bands (SHEAR4) and demonstrate its use in several sample calculations.

Section VII describes the topographic technique for deducing the micromechanical details of the ductile failure process and deducing the sequence of microfailure events. We then present the results obtained from applying this technique to the rupture of a tensile bar of the baseline steel and discuss how failure on a microscale is influenced by microstructure. Section VIII describes the development of a ductile fracture model, DFRAC2. Section VIII further shows the capability of DFRAC2 in several examples. Recommendations for future work are given in Section IX.

Sections X and XI list the personnel who participated in this research and the publications and presentations resulting from the work.

CONTENTS

II SPECIMEN MATERIAL (VACUUM ARC REMELTED 4340 STEEL)-- HISTORY AND CHARACTERIZATION

A. Procurement, Chemistry and Thermal-Mechanical History.....	II-1
B. Microstructure and Inclusion Size Distribution....	II-4
C. Standardized Heat Treatment.....	II-9
D. Mechanical Properties.....	II-10
E. Tensile Tests at Elevated Temperature and Strain Rate.....	II-11

II SPECIMEN MATERIAL (VACUUM ARC REMELTED 4340 STEEL)-- HISTORY AND CHARACTERIZATION

A. Procurement, Chemistry and Thermal-Mechanical History

After discussion with personnel from the ARO, the Army Materials and Mechanics Research Center, and Brown University, SRI selected vacuum arc remelted (VAR) 4340 steel for the baseline specimen material. A primary reason for choosing 4340 steel was that shear band behavior is best characterized in this material and a significant data base already exists. A second reason was that microstructural effects, particularly effects of inclusion size distribution, can be studied in 4340 by performing shear band experiments on heats produced by different melting practices. Third, it was felt that 4340 steel represents, as well as any other material, the class of steels used in various Army ordnance applications. Vacuum arc remelting was specified because it produces a homogeneous, clean, high quality steel with excellent, reproducible mechanical properties.

Procuring an appropriate quantity of VAR 4340 steel to supply the needs of the Brown/SRI program within a time frame that would not inordinately delay the programs proved to be a formidable task. All suppliers we contacted were either unwilling to produce the material in the (relatively) small quantity we required, or quoted us delivery times of more than one year. After several months of searching, the problem was finally solved by an offer from workers at AMMRC.

The AMMRC had previously placed an order with Republic Steel Company for a quantity of VAR 4340 steel and, upon hearing of our needs, kindly agreed to allow ARO to purchase some of the steel for the Brown/SRI program.

The material for this program was obtained from heat number 8652106, a nominal 90-ton, electric-furnace, argon-oxygen-decarburized (AOD)

refined electrode heat. One 20,000-lb, 32-inch-diameter ingot, the eighth of nine ingots poured from this air-melted heat, was vacuum-arc remelted (VAR) by the consumable electrode vacuum melt process*, then forged into rod and plate. From this VAR ingot, Number 3841687, a 9-inch by 7-inch forging and a 14-inch square forging were produced.

From the 9-inch by 7-inch forging, Republic rolled two recog billets for rerolling. One recog billet was rolled to 5-9/16-inch square, then reheated and rerolled to a 2-1/2-inch round. The second recog was rolled to a 4-inch square recog, then reheated and rerolled to a 1-inch round. Both the 1-inch- and 2-1/2-inch-diameter bar products were annealed to produce a spheroidized structure and reduce the hardness to a level where the bars could be cut by a saw. The 14-inch-square forging was reheated and forged into three shapes: 8-inch square, 5-inch by 12-inch, and 4-inch by 18-inch. These slabs were then mill annealed.

Brown University requested one 10-foot-length of 2-1/2-inch-diameter bar and fifty 12-foot-lengths of 1-inch-diameter bar; SRI requested six 10-foot-lengths of 2-1/2-inch-diameter bar and eight 12-foot-lengths of 1-inch-bar. Both Brown and SRI also requested 40 feet of 6-inch-wide by 1/2-inch-thick hot rolled and annealed plate, but Republic was not able to produce this shape. Therefore, we requested Viking Metallurgical Corporation in Albany, CA, to forge, roll, and anneal ten 8 ft by 6 inch by 1/2-inch pieces from ten equal pieces of a standard slab (approximately 55 inches by 12 inches by 5 inches thick) furnished by Republic and to ship half the lot to Brown and half to SRI. The unused forgings from the ingot were shipped to the Army Materials and Mechanics Research Center, where they can be made available for future needs of Brown and SRI, as well as for other research programs.

A 33-inch-diameter, 20,000-lb ingot, the second in the nine-ingot pouring sequence (ingot No. 3710046), was electroslag remelted, forged

*The consumable electrode remelting process generates heat by an arc between the electrode and the ingot. The process is performed inside a vacuum chamber. Exposure of the droplets of molten metal to the reduced pressure reduces the amount of dissolved gas in the metal.

into slab and bar, and also shipped to the Army Materials and Mechanics Research Center to the attention of Albert A. Ancil. This ESR ingot was not planned for use in the Brown/SRI program; it is mentioned here and included in the table only as an aid for keeping track of the sum of material purchased by the Army from this particular heat. An inventory of the VAR and the ESR material is given in Table II.1.

Table II.1

INVENTORY OF VAR AND ESR 4340 STEEL SHIPPED TO AMMRC

Shape	Nominal Dimensions (inches)	Number of Pieces	Ingot Number	Remelt Practice	Weight (lb)
Bar	2 1/2 dia x 48	15	3841687	VAR	1
Bar	2 1/2 dia x 48	16	3710046	ESR	1206
Slab	5 x 5 x 48	5	3841687	VAR	1716
Slab	5 x 5 x 48	5	3710046	ESR	1702
Slab	8 x 8 x 48	1	3841687	VAR	900
Slab	8 x 8 x 48	1	3710046	ESR	960
Slab	5 x 12 x 48	3	3841687	VAR	2730
Slab	5 x 12 x 48	3	3710046	ESR	2660
Full ingot cross section	32 dia x 1 1/2	1	3841687	VAR	304
Full ingot cross section	33 dia x 12	1	3710046	ESR	3260
	33 dia x 8	1	3710046	ESR	4620
	33 dia x 1 1/2	1	3710046	ESR	340

The data on mechanical properties and chemical composition provided to AMMRC by Republic are given in Tables II.2 and II.3.

Table II.2

MECHANICAL PROPERTIES OF 4340 STEEL ALLOY*

Remelt Procedure	Dimensions of Forging	0.2% Offset Yield Strength (KSI)	Ultimate Tensile Strength (KSI)	Elongation (%)	Reduction in Area (%)
VAR	5 in. sq.	233	271	12	43
ESR	5 in. sq.	236	273	13	47
VAR	8 in. sq.	230	269	13	45
ESR	8 in. sq.	227	268	13	47
VAR	5 in. x 12 in.	234	271	12	44
ESR	5 in. x 12 in.	232	269	11	44
VAR	2.5 in. dia.	232	272	12	47
ESR	2.5 in. dia.	234	276	14	48

*Average of four - transverse orientation; tempering temperature was 475°F.

Table II.3

CHEMICAL COMPOSITION, WT. % OF 4340 STEEL ALLOY

Remelt Procedure	No.	C	Mn	P	S	Si	Cu	Ni	Cr	Mo	Al	N	O	H, ppm
AOD	8652106	0.42	0.66	0.007	0.001	0.24	0.19	1.73	0.94	0.22	0.032	--	--	--
ESR	3710046	0.41	0.70	0.008	0.001	0.26	0.21	1.73	0.90	0.22	0.035	0.008	0.004	1.8
VAR	3841687	0.42	0.46	0.009	0.001	0.28	0.19	1.74	0.89	0.21	0.031	0.005	0.001	1.0

B. Microstructure and Inclusion Size Distribution

The microstructure of both the 1-inch and the 2-1/2-inch bar stock was thoroughly examined by SRI. Figures II.1 and II.2 illustrate the microstructure of the 2-1/2-inch-diameter bar on polished and etched sections taken transverse and parallel to the rolling direction, respectively. Comparison of Figures II.1a and II.2a indicates a pronounced texture in the 2-1/2-inch-diameter bar parallel to the rolling

direction. The prior austenite grain boundaries indicated by the white patches in Figure II.1a, are not as obvious in Figure II.2a, suggesting that the austenite grains were flattened and strung out parallel to the bar axis during hot rolling. Also, there are dark bands running parallel to the bar axis in Figure II.2b, indicative of inhomogeneous segregation of chemical species during hot rolling. However, the degree of banding is less than would be produced by alternative melt practices. (See the band structure for the air melted material, Figure II.7a). Furthermore, the effect of the banding on mechanical behavior is minimum when specimens are tested in an orientation parallel to the working direction, and all tests in the SRI program were conducted in this mode.

Figures II.3 and II.4 show the structure of the 1-inch-diameter bar transverse and parallel to the rolling direction, respectively. The low magnification views in Figures II.3a and II.4a illustrate that the material is relatively inclusion free and generally isotropic. There is some indication that the bar may be slightly textured (banded) parallel to the bar axis, as is to be expected from a hot rolling operation, but the banding is not as pronounced as that in the 2 1/2-inch-diameter bar. Figures II.3b and II.4b indicate that the structure itself is a mixture of ferrite with spheroidized carbides (white areas) and fine pearlite colonies (dark areas). This structure is typical of 4340 steel that is air cooled from above the eutectoid temperature and subsequently annealed at 1200-1300°F for several hours. The implication of both of these observations is that the 2-1/2-inch-diameter bar received more hot working than the 1-inch-diameter bar, but why this should be the case is not clear.

There is one other significant difference between the 2-1/2-inch-diameter bar and the 1-inch-diameter bar. As illustrated in Figures II.1b and II.2b, the structure of the 2-1/2-inch-diameter bar is spheroidized cementite in ferrite with no pearlite. This indicates that unlike the 1-inch-diameter bar, the pearlite that formed when the 2-1/2-inch-diameter bar was cooled across the eutectoid temperature was completely spheroidized during the subsequent annealing at 1200-1300°F.

The implication is that the 2-1/2-inch-diameter bar was held at the annealing temperature much longer than the 1-inch-diameter-bar, but why this should be the case is again not clear.

These differences in microstructure are reflected in the relative hardnesses of the 1- and 2-1/2-inch-diameter bars. Hardness measurements taken across the bar cross section every 1/4 inch for the 2-1/2-inch-diameter bar varied from HRB 87.8 to 88.1 (UTS \approx 85 ksi); measurements taken every 1/8 inch on a cross-section diameter of the 1-inch-diameter bar varied from HRB 96.5 to 99.0 (UTS \approx 110 ksi). The higher hardness of the 1-inch-diameter bar is consistent with the fine pearlite present in the microstructure.

The above-described differences between the 1- and 2-1/2-inch-diameter bars is somewhat disconcerting, particularly since the bars came from the same heat and were processed by the same vendor. However, these differences probably had little bearing on the results of this program, because most of the differences visible in Figures II.1 through II.4 were eliminated by the standardized heat treatment given to all specimens before testing, as described later in this section.

The 0.5-inch-thick rolled plate was not tested in any of the experiments conducted by SRI; thus its microstructure was not analyzed.

The prolonged exposure to elevated temperatures ($>1400^{\circ}\text{F}$) during the hot rolling operation caused both the 1- and 2-1/2-inch-diameter bars to decarburize at the surface. As shown in Figure II.5, the decarburized layer in both bars is about 500 μm (0.02 inch) deep. This decarburized layer presented no problem, however, because it was machined away during specimen preparation.

One of the original objectives of the program was to assess the effect of inclusion number, size, and shape on the initiation and growth of shear bands in HRC40 4340 steel. As shown in Figures II.1 through II.4, the VAR material procured from Republic Steel contained (as expected) only a few, round MnS inclusions randomly distributed through the material. The fact that the inclusions are small and uniformly

dispersed imparts reproducible mechanical properties and promotes isotropy, making the VAR 4340 steel a desirable baseline material. However, the inclusion content in this material cannot be altered by heat treatment or further thermomechanical processing. Thus, it was necessary to procure other batches of 4340 steel produced by different melt practices to study effects of different inclusion size distributions. We obtained a 2-1/2-inch-diameter bar of air melted 4340 steel. This air-melted heat, also produced by Republic Steel (Heat Number 8090158), had nominally the same composition as the VAR heat but with substantially higher phosphorous (0.15 wt%) and sulfur (0.013 wt%) content. This is to be expected from a conventional electric furnace air melting practice.

As for the VAR material, the structure of the steel is spheroidized cementite in ferrite, Figures II.6b and II.7b, consistent with a long term anneal at 1200-1300°F. The increase in sulfur content clearly resulted in an increase in MnS inclusion content. Note particularly the long stringers of MnS inclusions and the heavily banded structure visible in Figure II.7a. Again, there is a noticeable difference in the microstructure between the transverse and parallel directions, indicating the material is highly anisotropic in properties.

To obtain a third condition of inclusion size distribution, we examined the microstructure of an existing length of 2-inch-diameter aircraft quality 4340 tubing that had been heat treated to HRC 50. Because "aircraft quality" usually means an air melt plus vacuum arc remelting, we expected the inclusion content of the tubing to be similar to that in the VAR bar. Figures II.8 and II.9 show the structure of the tubing transverse and parallel to the tube axis. Comparison of Figures II.8a and II.9a with Figures II.1a, II.2a, II.6a, and II.7a, show that the difference between the VAR and the aircraft quality material is not nearly as great as the differences between the VAR and the air-melted material. The structure of the tubing is fine, tempered martensite, consistent with a hardness of HRC 50.

In preparation for the contained fragmenting cylinder experiments to examine the effect of inclusions on shear banding (these experiments were

later deleted from the program), we quantified the inclusion size distributions for the three different heats of 4340 steel. On each of the specimens previously mounted and prepared for metallographic examination, several random areas were selected and photographed at 100x magnification. All of the inclusions visible in each of these photographs were counted and measured. If the aspect ratio of the inclusion was about one, the measured and tabulated dimension was the diameter. If the aspect ratio was greater than one, both the minimum and maximum dimension were measured and the average of the two was tabulated.

The resulting data are plotted in Figures II.10, II.11, and II.12. The ordinate is the cumulative number of inclusions per unit area greater than a given size; the abscissa is inclusion size in micrometers. In all cases the total area examined was around $3 \times 10^{-2} \text{ cm}^2$ and sufficient numbers of inclusions, usually about 100, were counted to make these cumulative size distributions statistically significant. Hence, we feel these plots are representative of the actual inclusion size distributions in the three materials.

Close examination of Figures II.10 and II.11 shows that, as expected, the air melt 4340 exhibits a greater total number of inclusions (intercept with the vertical axis--about 6×10^5 inclusions per square meter) than the VAR 4340 (about 10^5 inclusions per square meter). At any given size, there are more inclusions in the air-melted steel than in the VAR steel, and the largest measured inclusion in the air-melted steel is about twice the size of the largest inclusion in the VAR material.

Note also that the transverse and longitudinal size distributions converge at small inclusion sizes for both the air melt and the VAR (Figure II.10) materials. This is as it should be, since the only difference between the two directions is in the size of the inclusions and not in the total number. Note that, in the air-melted material, the parallel direction inclusion distribution is to the right of the transverse distribution, indicating that the inclusions appear bigger in the parallel direction. That is, the inclusions are ellipsoidal in shape, with the major axis of the ellipse parallel to the rolling

direction. In the VAR material, however, the situation is reversed, indicating that, in this material, the inclusions are shaped like thin disks, with the thin dimension perpendicular to the rolling direction.

Figure II.10 also shows the inclusion size distribution for the aircraft quality 4340 in the transverse direction; the longitudinal distribution was not measured. The aircraft quality 4340 has a higher total inclusion content ($>2 \times 10^5$ inclusions per square meter) than the VAR material, but the transverse distribution in the aircraft quality 4340 lies to the left of the transverse distribution in the VAR material, indicating that the inclusions in the aircraft quality material are, on the average, smaller. This may be because the aircraft quality material was taken from a heat with an exceptionally low sulfur content.

In general, then, these inclusion size distributions appear reasonable and are consistent with expected behavior. If experiments on the effect of inclusions on shear band initiation are undertaken in the future, these size distributions will be useful in designing and interpreting the experiments.

C. Standardized Heat Treatment

Workers at the ARO, the AMMRC, Brown University, and SRI agreed on a hardness level of HRC 40 for the baseline material for this research program. Thus it was necessary to heat-treat this material subsequent to machining specimens, but before performing the tests. It was also important to standardize this heat treatment among all investigators to prevent microstructural variations from interfering with the comparison and analysis of test results.

The following heat treatment was specified to achieve this hardness:

- Normalize: 1650°F (900°C) for 1 hour per inch of thickness, air cool.
- Austenitize: 1600°F (870°C) for 1 hour per inch of thickness, still oil quench.
- Temper: 850°F (450°C) for 1 hour per inch of thickness, oil quench.

The concern was raised that heat treatment of 4340 into the HRC 40 range could cause temper embrittlement of the material and influence the test results. After some consideration we became convinced that temper embrittlement effects would be small or nonexistent in this case because (1) 4340 steel exhibits only a very shallow trough in the toughness vs tempering temperature curves, (2) 850°F is outside the slight trough that does exist, and (3) the sulfur and phosphorus levels in this heat of 4340 are particularly low. Therefore, the above heat treatment was performed for all experiments in the SRI program.

Figure II.11 shows the microstructure of the 2-1/2-inch-diameter VAR 4340 bar stock after it was subjected to the above heat treatment. The structure is now tempered martensite instead of the spheroidized cementite plus ferrite characteristic of the received material (Figures II.1 and II.2). The acicular martensite laths are quite large, but are consistent with the 850°F temper. Hardness measurements taken across the diameter of the bar indicated that this heat treatment resulted in a uniform hardness in this material of HRC 40 \pm 1.

D. Mechanical Properties

Tensile bars, 0.350-inch in diameter with a 1-inch gage length, were machined from the 1-inch-diameter stock of the base line VAR 4340 steel. They were heat treated according to the standard schedule mentioned above. Then three quasi-static tensile tests were performed.

The tests were performed on a MTS servohydraulic machine at an extension rate of 0.4 mm per minute. The specimens were instrumented with an extensometer to measure elongation up to the point of necking. During this uniform deformation phase, the tests were stopped several times to check for the development of a neck. After the onset of necking, the extensometer was removed and specimen extension was interrupted at regular intervals to measure the neck diameter and the neck profile by means of a micrometer. This neck geometry data was used during data reduction to apply the Bridgman correction to the stress after necking.

During the extension hold periods, the specimen was observed to creep slightly until an equilibrium load was reached (after about 1 minute). The load drop during this creeping phase was as high as 5 %, but upon renewed extension of the specimen, the load increased again to the level it had reached at the beginning of the hold period. The occurrence of room temperature creep in low strength steels is well documented, but it was not expected, at least to the extent observed here, in high strength steel.

The true stress-true strain curve for the base line VAR 4340 steel at room temperature and low strain rate is shown in Figure II.12. The material has a yield stress of 175 ksi, and an ultimate tensile stress of 191 ksi and shows only limited strain hardening. The ductility was exceptionally high for a material of this strength level; we measured a reduction of area of 53% and a true strain to failure of 68%.

Fractographic observations made on the room temperature, low strain rate specimen are presented in Section VII of this report.

E. Tensile Tests at Elevated Temperature and Strain Rate

For comparison with the quasi-static tensile behavior just reported, and as an aid in the modeling effort discussed later, three additional tensile tests were performed at an elevated strain rate (4 to 6 per second) at three temperatures (20°C, 200°C, and 400°C).

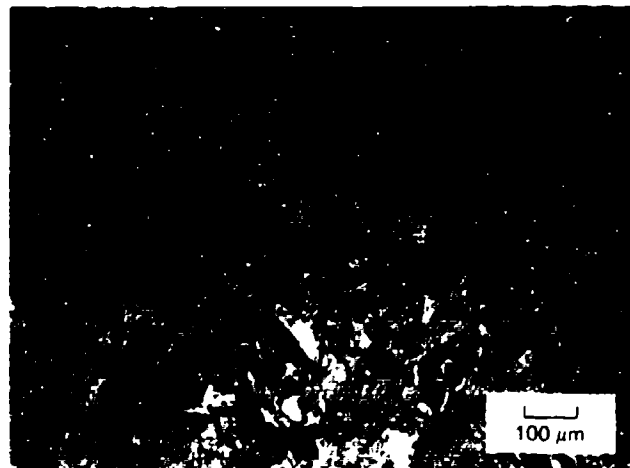
The specimens were 0.35-inch-diameter round tensile bars with a 1-inch gage length. To avoid changes in microstructural and mechanical properties from prolonged heating, we brought the specimens to temperature quickly using three 6-inch linear infrared heaters. The linear heater elements were oriented parallel to the tensile specimen axis and spaced 120 degrees apart at a distance of 9-inches from the specimen axis. Parabolic reflectors focused the infrared light on the specimen. The load was applied with an MTS loading system at its maximum cross-head rate by using a step-function command signal to a controller. Specimen deformation (elongation of the gage section and

reduction in specimen diameter) was photographed with a Hycam camera at approximately 5000 frames per second.

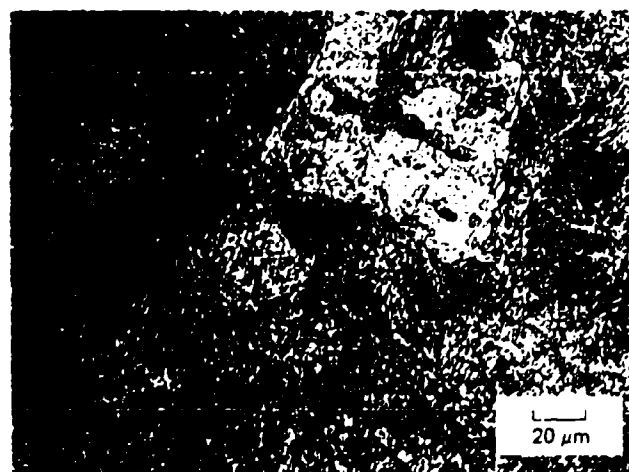
Testing was done as follows: The infrared heaters were turned on to heat the specimen, and the temperature of the specimen was monitored by an iron-constantan thermocouple spot-welded to the surface of the specimen and covered with glass fiber tape. When the temperature reached the desired level (6.5 minutes were required to reach 200°C; 15 minutes for 400°C), the heaters were switched off, and the high-speed camera drive motor was turned on. When the framing rate of the camera stabilized at the desired level, the camera generated a synchronizing pulse. This signal was used to trigger a high-intensity flash lighting system and simultaneously initiated the loading of the specimen with the MTS system. The applied load and the grip movement were recorded by a Nicolet digital oscilloscope as a function of time.

The deformation history of the specimen was determined from the high-speed photographs by measuring the gage length marked by thin strips of glass fiber tape and diameter change as a function of time. Each frame time was determined from the timing mark recorded on the film. The applied load and deformation were correlated through the time reading to establish the stress-strain relations.

The initial portion of the stress-strain relation (up to the observation of maximum load) was established by calculating the engineering stress (applied load divided by the original cross-sectional area) and engineering strain (elongation divided by the original gage length). After the maximum load was reached, the stress was computed by dividing the load by the actual cross-sectional area, and the strain by taking the logarithm of the ratio of the original cross-sectional area to the instantaneous cross-sectional area. Because we have photographs of the necked section profiles, Bridgeman's correction can be applied to account for the effect of nonuniform stresses at the necked section. However, this correction was not applied at this time. The resulting true stress-true strain curves at three temperatures are shown in Figure II.13.



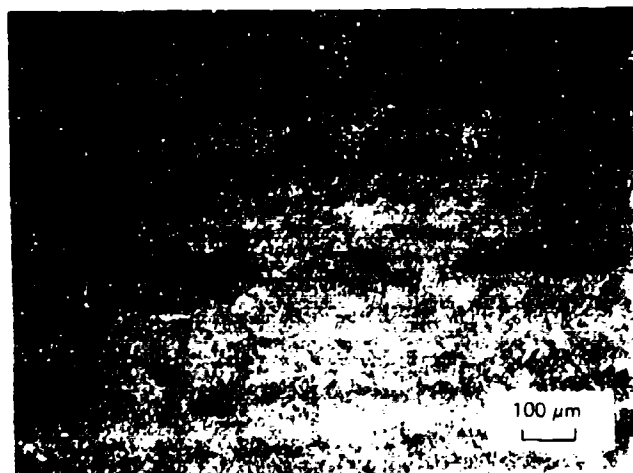
(a) Overall View Near Center of Bar Showing a Few MnS Inclusions



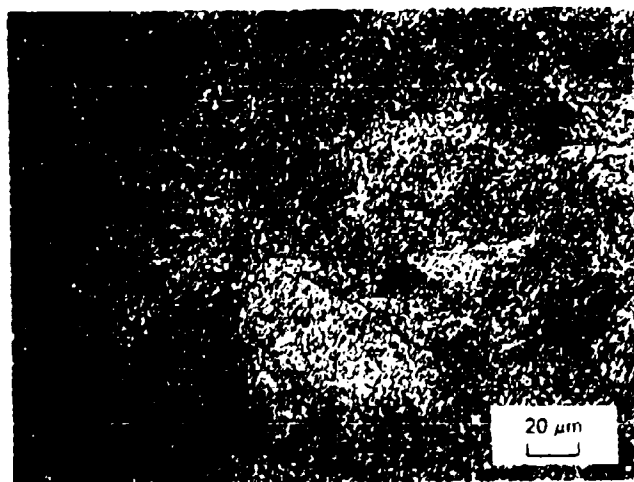
(b) Higher Magnification View: Illustrating the Spheroidized Cementite in Ferrite Structure

JP-3722-133

FIGURE II.1 MICROSTRUCTURE OF 2-1/2-INCH-DIAMETER VAR 4340 BAR STOCK TRANSVERSE TO ROLLING DIRECTION



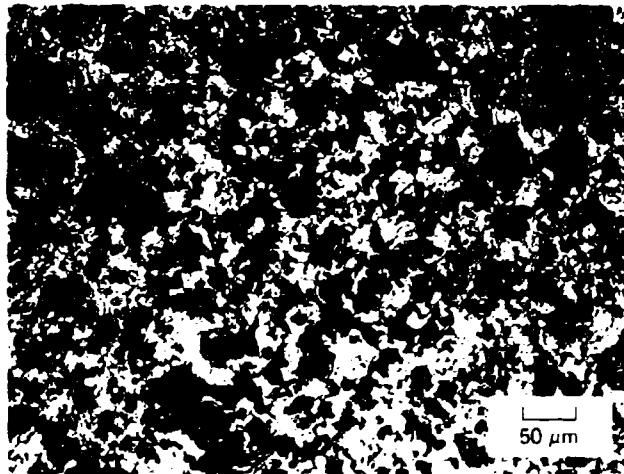
(a) Overall View Showing Substantial Banding and Some Inclusions



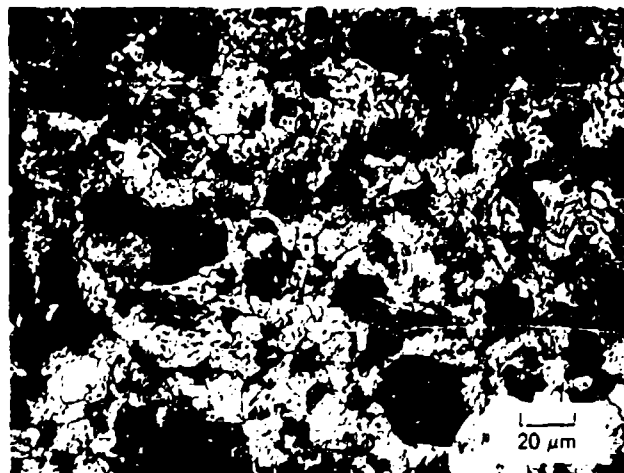
(b) Higher Magnification View Illustrating the Spheroidized Cementite and Ferrite Structure

JP-3722-134

FIGURE II.2 MICROSTRUCTURE OF 2-1/2-INCH-DIAMETER VAR 4340 BAR STOCK PARALLEL TO ROLLING DIRECTION



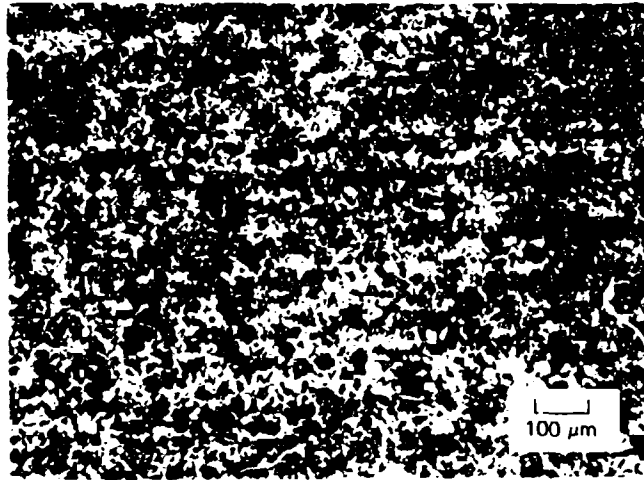
(a) Overall View Showing Lack of Inclusions



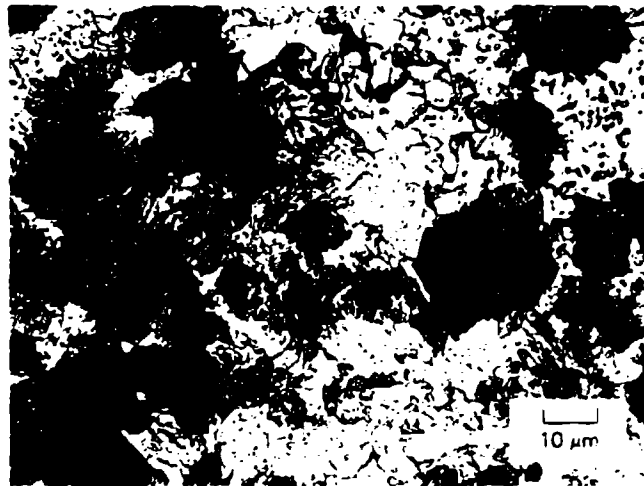
(b) Higher Magnification View Illustrating the Ferrite and Fine Pearlite Structure

JP-3722-135

FIGURE II.3 MICROSTRUCTURE OF 1-inch-DIAMETER VAR 4340 BAR STOCK TRANSVERSE TO ROLLING DIRECTION



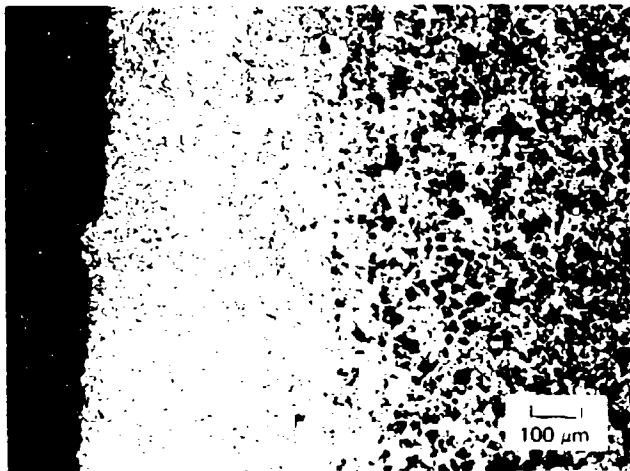
(a) Overall View Showing Slight Banding



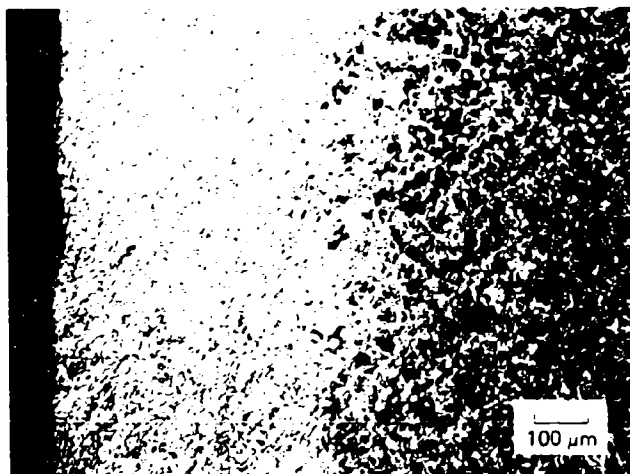
(b) Higher Magnification View Illustrating the Ferrite and Fine Pearlite Structure

JP-3722-138

FIGURE II.4 MICROSTRUCTURE OF 1-INCH-DIAMETER VAR 4340 BAR STOCK PARALLEL TO ROLLING DIRECTION



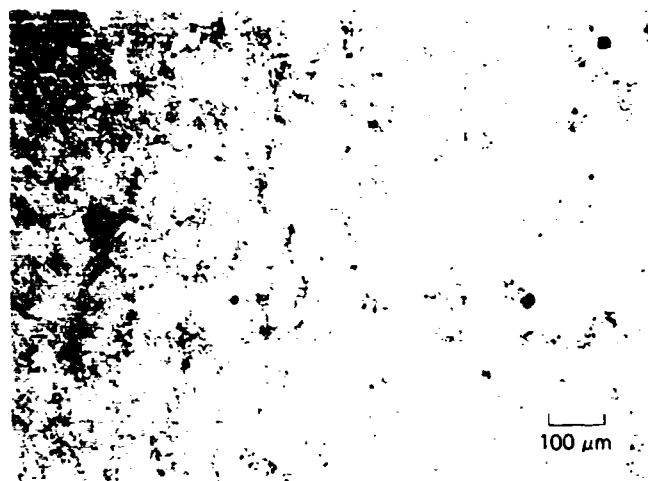
(a) 1-in.-Diameter Bar Stock



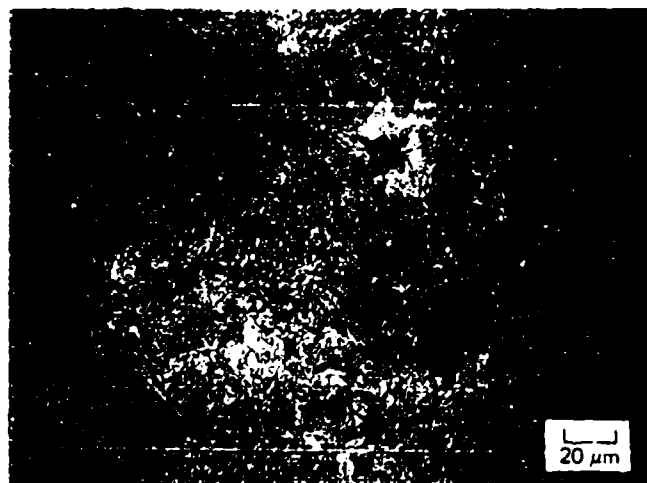
(b) 2 1/2-in.-Diameter Bar Stock

JP-3722-137

FIGURE II.5 DECARBURIZED SURFACE LAYERS
IN THE VAR 4340 BAR STOCK



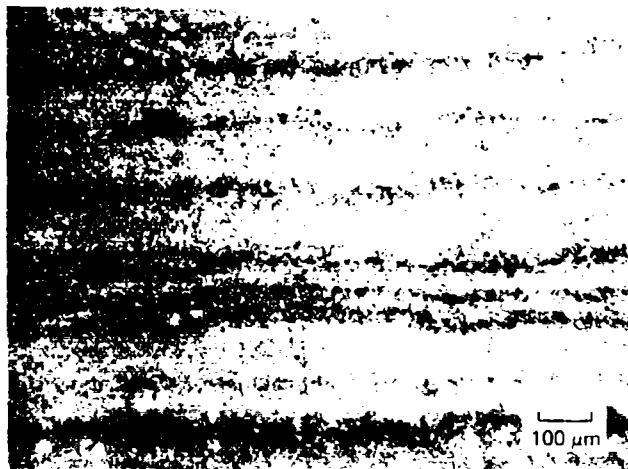
(a) Overall View Near Center Showing Distribution of MnS Inclusions



(b) Higher Magnification View Illustrating the Spheroidized Cementite Plus Ferrite Structure

JP-3722-138

FIGURE II.6 MICROSTRUCTURE OF 2-1/2-INCH-DIAMETER AIR MELT 4340 BAR TRANSVERSE TO ROLLING DIRECTION



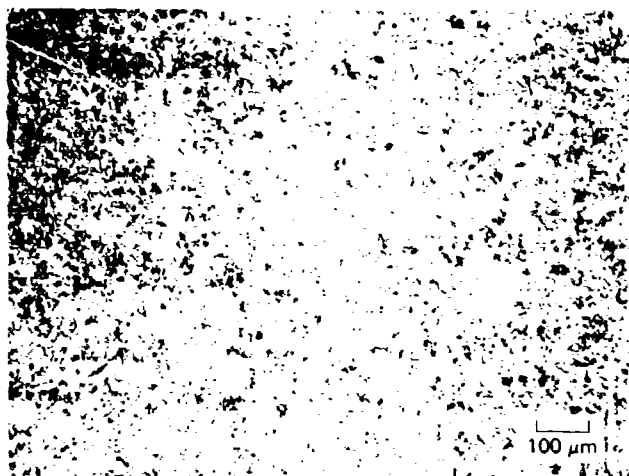
(a) Overall View Showing Extensive Banding and Strung-Out MnS Inclusions



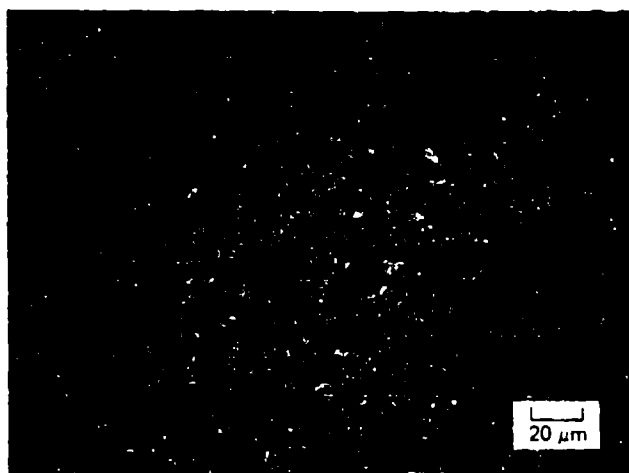
(b) Higher Magnification View Illustrating the Spheroidized Cementite Plus Ferrite Structure

JP-3722-139

FIGURE II.7 MICROSTRUCTURE OF 2-1/2-INCH-DIAMETER AIR MELT 4340 BAR PARALLEL TO ROLLING DIRECTION



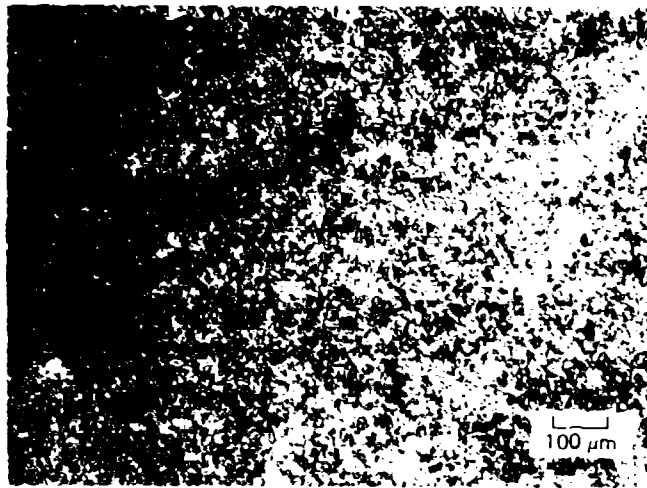
(a) Overall View Near Center Showing Distribution of MnS Inclusions



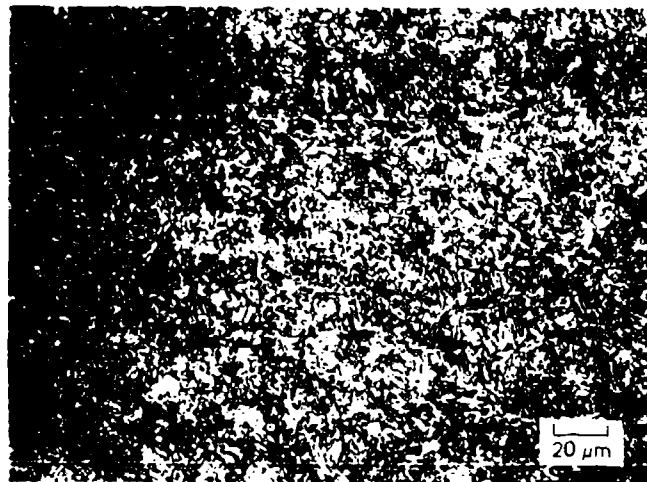
(b) Higher Magnification View Illustrating the Tempered Martensite Structure (HRC 50)

JP-3722-140

FIGURE II.8 MICROSTRUCTURE OF 2-inch-DIAMETER TUBE OF AIRCRAFT QUALITY 4340 STEEL TRANSVERSE TO ROLLING DIRECTION



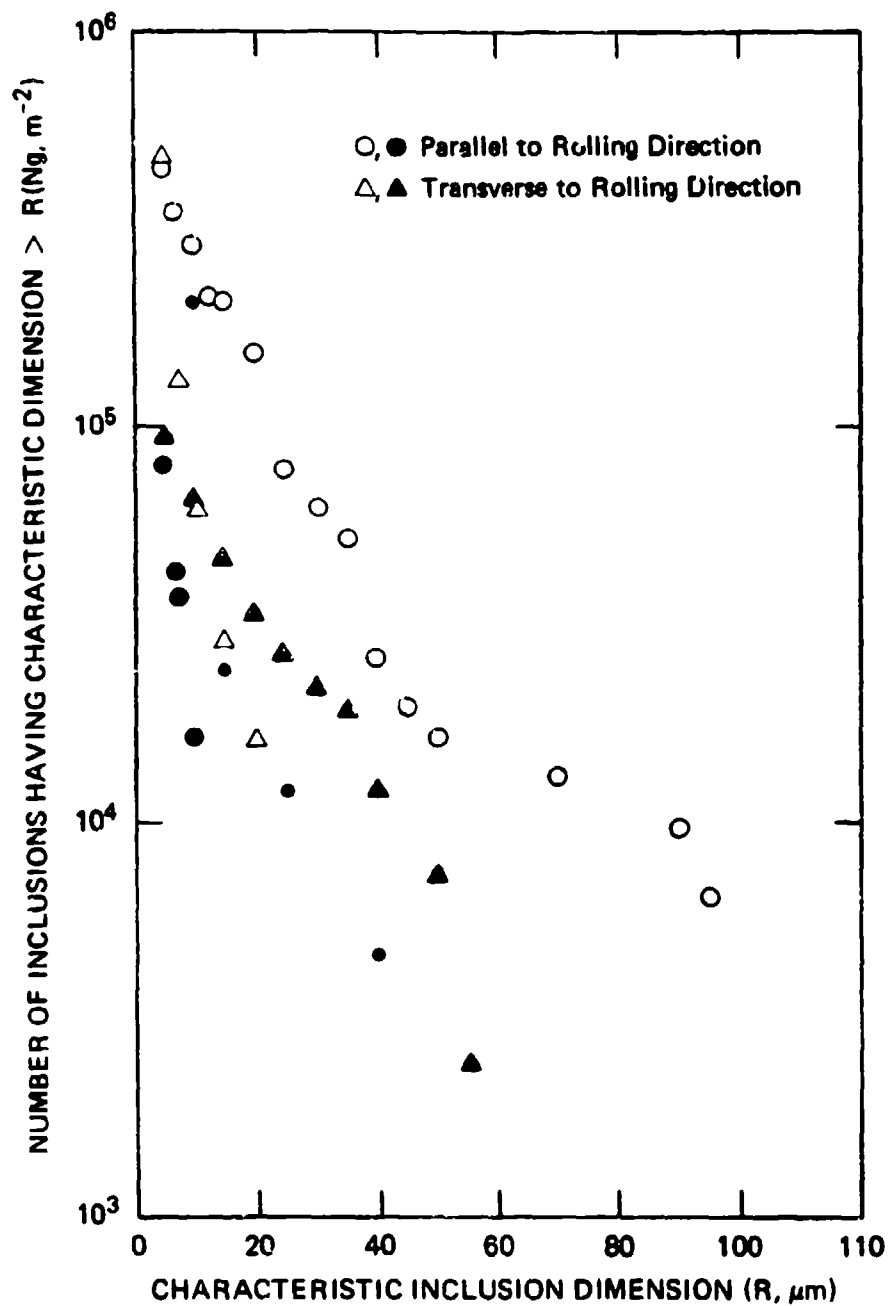
(a) Overall View Showing the Inclusion Distribution and Slight Tendency Towards Banding



(b) Higher Magnification View Illustrating the Tempered Martensite Structure (HRC 50)

JP-3722-141

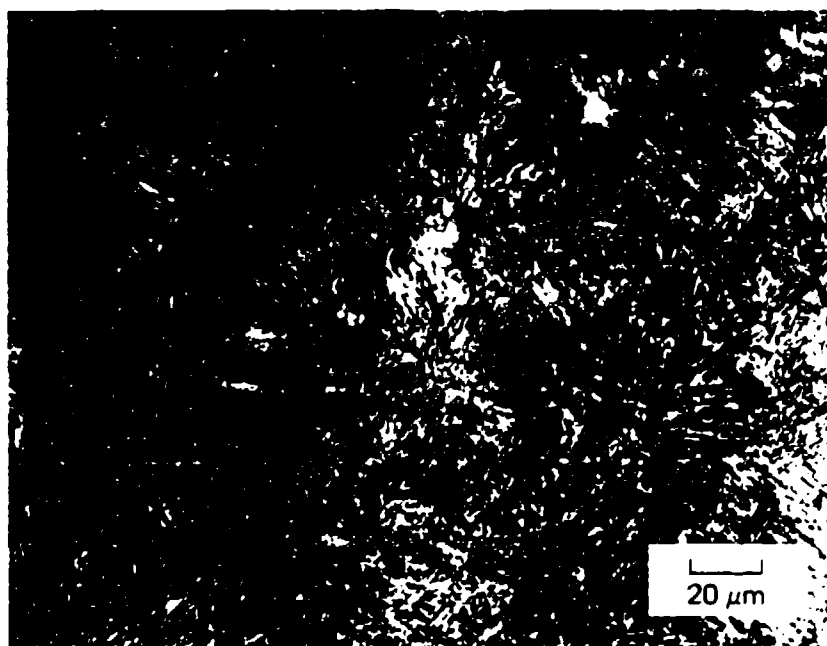
FIGURE II.9 MICROSTRUCTURE OF 2-INCH-DIAMETER TUBE OF AIRCRAFT QUALITY 4340 STEEL PARALLEL TO ROLLING DIRECTION



JA-3722-142

FIGURE II.10 INCLUSION SIZE DISTRIBUTION FOR 4340 STEEL PROCESSED BY DIFFERENT MELT PRACTICES

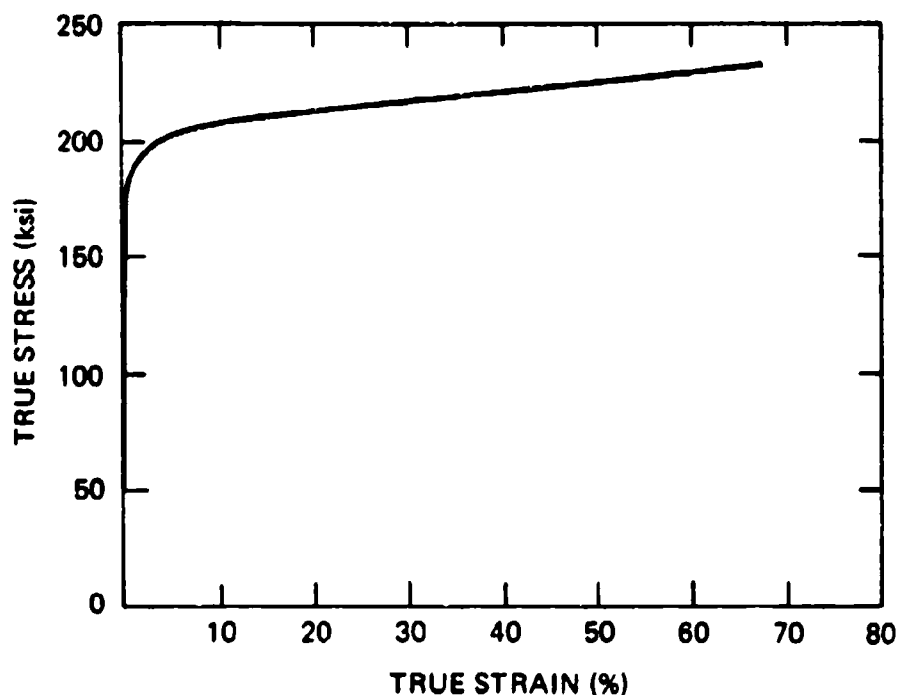
- , ▲ VAR material.
- , △ Air melt material.
- Air melt-VAR material.



JP-3722-146

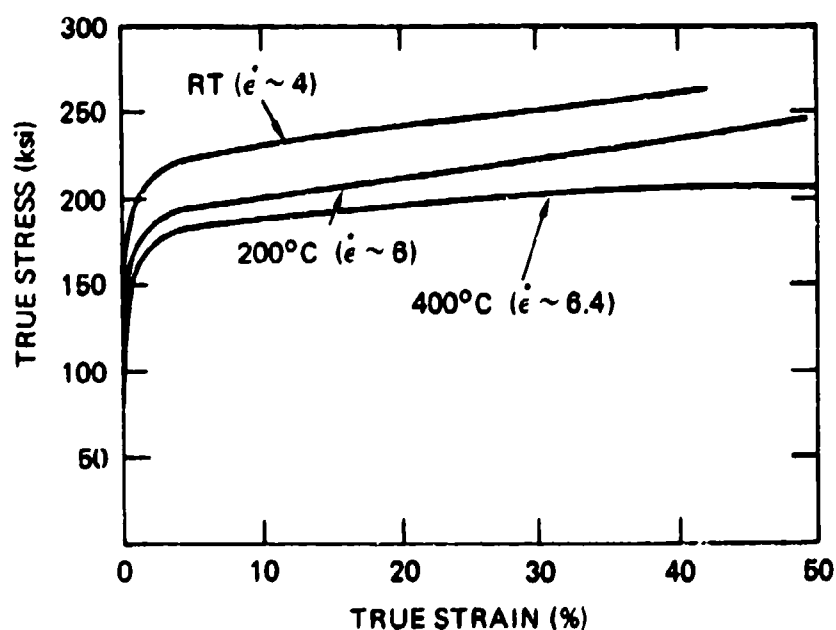
FIGURE II.11 MICROSTRUCTURE OF 2-1/2-INCH-DIAMETER VAR 4340 BAR STOCK AFTER THE STANDARDIZED HEAT TREATMENT

The structure is tempered Martensite with large, acicular Martensite laths characteristic of a 850° F temper.



JA-3722-146

FIGURE II.12 TRUE STRESS-TRUE STRAIN CURVES (WITH BRIDGMAN CORRECTION) FOR HRC 40 1-INCH-DIAMETER VAR 4340 STEEL BAR AT ROOM TEMPERATURE UNDER QUASI-STATIC LOADING



JA-3722-147

FIGURE II.13 EFFECT OF TEMPERATURE ON TRUE STRESS-TRUE STRAIN CURVES (WITHOUT BRIDGMAN CORRECTION) FOR HRC 40 1-INCH-DIAMETER VAR 4340 STEEL BAR AT ELEVATED STRAIN RATE

CONTENTS

III DYNAMIC SHEAR EXPERIMENTS

A. SRI High Performance Split Hopkinson Torsion Bar (SHTB).....	III-1
1. Characteristics.....	III-1
2. Description.....	III-2
3. Anticipated Developments of SHTB Facility.....	III-4
4. Application of SHTB.....	III-5
B. Dynamic Stress-Strain Curves for VAR Steel.....	III-5
1. Materials and Test Conditions.....	III-5
2. Experimental Results.....	III-6
3. Discussion.....	III-8
C. Metallographic Observations.....	III-9
1. Procedure.....	III-9
2. Results: Shear Failure Path.....	III-9
3. Results: Light and Scanning Electron Microscope Observations.....	III-10
4. Discussion.....	III-15
D. Optical Dynamic Strain Measurements.....	III-16
1. Experimental Technique and Specimen Preparation.....	III-17
2. Experimental Results.....	III-18
3. Discussion.....	III-23
E. Measurements of Temperature Near Shear Bands.....	III-25
1. Principle of the Indirect Temperature Measurement Technique.....	III-26
2. Experimental Procedure.....	III-28
3. Experimental Results.....	III-29
4. Discussion.....	III-31
F. References.....	III-32

III DYNAMIC SHEAR EXPERIMENTS

This section describes the development of the SRI high performance Split Hopkinson Torsion Bar (SHTB) facility and the shear experiments performed with this facility. We present and discuss the dynamic shear stress-shear strain curve for VAR 4340 steel, optical dynamic strain measurements in the vicinity of a shear band, temperature measurements near shear bands, and results of metallographic/failure surface examination.

A. SRI High Performance Split Hopkinson Torsion Bar (SHTB)

Most experiments performed to study the kinetics of shear banding involve either complex states of stress (for example, the contained exploding cylinder test), or a geometrical stress concentration (for example, the punch test). To investigate the fundamental mechanism of adiabatic shear banding and to obtain experimental data with which to compare the results of analytical investigations, it was desirable to produce adiabatic shear bands under conditions of simple shear loading.

After considering several test configurations, we selected the Split Hopkinson Torsion Bar (SHTB) to produce high strain rate shear deformation in the base line material in VAR 4340 steel subjected to the standard HRC 40 heat treatment. The SHTB configuration has the advantage of mechanical simplicity; in principle it allows easy measurement of stress and strain during the test and provides free access to the specimen for in situ measurements or for heating or cooling of the test section.

1. Characteristics

The new SHTB, developed and built at SRI International under the present contract, provides an order of magnitude improvement over

conventional SHTB, both in achievable strain rate and in the strength of specimens that can be tested. It can test high strength materials with yield strengths in excess of 1500 MPa at maximum strain rates (engineering shear strain rate) in the range of 1000 s^{-1} to $10,000 \text{ s}^{-1}$. This latter feature is particularly interesting, because there have been few investigations in this strain rate range, even though this might be the domain in which significant changes in the dynamic material behavior start to occur.

Another important new characteristic of the bar is that it can be used to perform dynamic experiments at elevated temperatures, in excess of 600°C . (Some of the accessories providing high temperature capability to the new SHTB have been developed under DARPA Contract DAAH01-84-C-0155.)

The bar is long enough to apply shear strains of up to 600%, depending on the strain rate.

Finally, the position of the release clamp and of the bearings supporting the bar can be varied arbitrarily, giving great flexibility in setting up experiments.

2. Description

A diagram of the new SHTB is shown in Figure III.1 and the actual bar is shown in Figure III.2. The new bar operates on the same principles as conventional Hopkinson bars. It consists of an input bar and an output bar between which a thin-walled tube specimen is attached. A frictional device (release clamp) clamps the input bar at a given (variable) distance from the loading end.

A static torque is applied to the bar by means of a hydraulic wrench and stored in the bar using a second clamp (fixed clamp). When the release clamp is opened, a shear wave propagates in the input bar (incident wave) and loads the specimen. Part of the incident wave is transmitted to the output bar, and part is reflected in the input bar.

The amount of strain applied to the specimen is varied by changing the length of the prestrained portion of the input bar. The stress and strain in the specimen can be determined by measuring the incident and the transmitted waves using strain gages.

The strain rate imposed on the specimen is given by:

$$\dot{\gamma} = \frac{r}{a} \frac{\tau^b}{c_t \rho l} \left[1 - 8 \left(\frac{r}{a} \right)^2 \frac{h}{a} \frac{\tau^s}{\tau^b} \right] \quad (\text{III.1})$$

where

r = radius of the specimen

a = radius of the bar

τ^b = shear stress in the prestrained portion of the bar at the outer fiber

c_t = shear wave velocity for the bar material

ρ = density of the bar material

l = width of the specimen

h = thickness of the specimen

τ^s = shear stress in the specimen.

The above equation indicates that $\dot{\gamma}$ depends primarily on τ^b and the ratio τ^s/τ^b . Thus, to achieve high strain rates with high strength materials, the stress τ^b in the input bar must be as large as possible. This poses the problem of clamping a very high static torque in the input bar and releasing it in a very short time to obtain a sharp rising shear stress wave.

This problem was solved by using a 1-inch-diameter maraging 300 steel bar in the peak hardness condition and designing the special release clamp shown in Figure III.3. The bar is clamped between two semicircular bearings by a notched three-point bend bar loaded with a hydraulic cylinder. The shear wave is released by loading the bend bar to fracture. With this release mechanism, the rise time of the incident shear wave is about 50 μ s. A plot of a typical incident wave, recorded by strain gages on the input bar, is shown in Figure III.4.

Besides being required to store high static torques, the use of a steel bar was needed for testing at high temperature.

Because of the high amplitude of the incident and transmitted stress waves when high strength materials are tested, conventional techniques for coupling the specimen to the bars, such as glueing or brazing, cannot be applied. To meet the strength requirements, we have designed the hexagonal coupling illustrated in Figure III.5. Figure III.6 shows the actual specimen. It is a thin-walled tube, 25 mm in diameter, 2 mm in width, and 0.5 mm or 1 mm in wall thickness. The specimen is notched internally to leave a smooth outer surface for in situ observations. When high temperature tests are performed, insert bars are used between the main bars and the specimen to avoid annealing of the main bars. These insert bars are then coupled to the main bars by means of the coupling shown in Figure III.7. This coupling is stronger than the hexagonal coupling and is required, because the junction between the input main bar and the input insert bar experiences significantly higher dynamic torques than the specimen-bar junction.

3. Anticipated Developments of SHTB Facility

The major development effort of the SHTB has been completed. The design requirements have been met and the bar is now being routinely used as a versatile loading device for dynamic experiments.

However, we are still working on improving some aspects of the facility. In particular, the coupling between bar and specimen is not perfect, thus causing wave reflections back into the input bar when the incident wave reaches the specimen. These reflections limit the accuracy with which dynamic strains can be measured using the measured incident and transmitted waves. At high strain rate (i.e., when the incident wave has a much higher amplitude than the transmitted wave), the reflections at the specimen-bar interfaces also significantly influence the measurement of the transmitted torque. They cause a large anomalous stress spike during the early part of deformation. As a result, the stress-strain curves presented in this report for the high strain rates

($\dot{\gamma} > 4000 \text{ s}^{-1}$) represent best estimates of the stress based on the available stress records and may be in error by 15%. This problem with the stress measurement was not anticipated and is still not fully understood, although it has also been experienced by other researchers¹. To clarify this problem and to obtain precise stress measurements at high strain rates, the shear specimens can be instrumented with miniature strain gages.

A further development anticipated for the SHTB facility is an axial loading fixture to perform combined shear-compression tests.

We are also confident that the SHTB can be used to perform mode II dynamic fracture tests. We envision using specimens with partial circumferential slots either to measure the growth of adiabatic shear bands or to measure the mode II dynamic fracture toughness.

4. Application of SHTB

In the present program, the SHTB has served to measure the dynamic stress-strain curve of VAR 4340 steel, to produce adiabatic shear bands in this material, to measure the instability strain for shear banding as a function of strain rate, to directly observe the process of shear banding, and to measure temperatures in material near to shear bands. The results of these various research tasks are presented in the following sections.

B. Dynamic Stress-Strain Curves for VAR 4340 Steel

1. Materials and Test Conditions

SP² tests were performed on VAR 4340 steel heat treated to two different hardnesses. The first heat treatment was the base line heat treatment--that is, homogenize for 1 hour at 890°C, air cool, austenitize for 1 hour at 845°C, oil quench, temper at 450°C for 1 hour, water quench--resulting in a hardness HRC 40. The second heat treatment differed from the first one only in that the tempering temperature was 600°C

instead of 450°C, resulting in a hardness HRC 33. All heat treatments were performed in vacuum to prevent surface decarburization.

Each specimen was notched after the heat treatment. A series of lines were scribed on the surface of the specimens, parallel to the specimen axis. After the test, their curvatures indicated the final strain profile across the specimen width.

The HRC 40 specimens were tested at several increasing strain rates (1000 s^{-1} to 8000 s^{-1}) to determine the dynamic stress-strain curves and the instability strain as a function of strain rate. Two HRC 33 specimens were tested at a strain rate of 2100 s^{-1} and $10,000 \text{ s}^{-1}$, respectively. The purpose of the two latter tests was also to determine the dynamic stress-strain curve and the instability for shear banding (provided shear banding occurred for material of this hardness), and to compare the results with the HRC 40 data.

2. Experimental Results

The dynamic stress-strain curves for the HRC material obtained at strain rates of 1000 s^{-1} , 4000 s^{-1} , 5500 s^{-1} , and 8000 s^{-1} are represented in Figures III.8a to III.8d, respectively. Because the strain rate increases during the test, the strain rate values quoted here are average values.

The flow curves in Figures III.8a, III.8b, and III.8c are essentially the same. They show little strain hardening and a maximum flow stress of about 850 MPa. The failure strain for all three strain rates is close to 0.15.

The flow curve obtained for the strain rate of 8000 s^{-1} (Figure III.8d) differs from the others in that the failure strain is smaller, namely 0.1.

The deformed scribe lines on the specimens tested at 1000 s^{-1} , 5500 s^{-1} , and 8000 s^{-1} are shown in Figure III.9. They were photographed after the test on an optical microscope after matching the two broken specimen halves as closely as possible. It is seen from these

photographs that the location of the failure plane along the specimen width varies from test to test, sometimes occurring close to the edge of the specimen gage. In Figure III.8d, both specimen halves have been closely matched; thus the relative displacement between the scribe line on the input half of the specimen and the scribe line on the output half is an indication of the localized shear displacement. In general, however, it is difficult to estimate the amount of localized shear displacement from posttest observations of the scribe lines, because the scribe lines are either too coarse or no longer sharply defined at the edge of the fracture surface. Estimates of the failure strain from the deformation of the scribed lines in Figure III.9 agree well with the data in Figure III.8, although there is an uncertainty regarding the contribution from the localized strain to the average strains in Figure III.8.

Figure III.10 shows the stress-strain curves for the HRC 33 material at a strain rate of 2100 s^{-1} and $10,000 \text{ s}^{-1}$. As for the R_c 40 material, the flow curves indicate little strain rate sensitivity in this strain rate range, and the two curves in Figure III.10 are very similar. The maximum flow stress is 750 MPa and thus is significantly lower than for the HRC 40 material. The HRC 33 material displays only moderate strain hardening. The failure strain is also significantly higher, being 0.35 at a strain rate of 2100 s^{-1} and 0.25 at a strain rate of $10,000 \text{ s}^{-1}$. Note, however, that whereas at the lower strain rate the specimen failed uniformly on approximately one single plane at the higher strain rate, the failure path was very irregular, proceeding on several different planes around the circumference. Therefore, although failure started at a lower strain in the high strain rate experiment, specimen unloading occurred much more gradually than in the low strain rate experiment (Figure III.10).

The deformed scribe lines for the two HRC 33 specimens are shown in Figure III.11. It can be seen that the strain is not uniform across the specimen width and that a slight amount of deformation takes place outside the specimen gage length. Although careful examination of the

strain profiles recorded by the scribe lines indicates that some degree of strain localization also took place in the softer material, it is not possible to make a more quantitative assessment.

3. Discussion

The measurement of the flow curves for VAR 4340 steel indicates that in the strain rate range 1000 s^{-1} to $10,000 \text{ s}^{-1}$, the flow stress is not strain rate sensitive (bearing in mind the uncertainty in the stress measurements at high strain rates). Raising the tempering temperature from 450°C to 600°C causes a drop in the dynamic flow stress of about 100 MPa, but the flow stress remained strain rate insensitive between 2000 s^{-1} and $10,000 \text{ s}^{-1}$.

In the HRC 40 material, strain localization occurred. The failure strain (average failure strain) was approximately 0.15 for strain rates in the range 1000 s^{-1} to 5000 s^{-1} ; for the higher strain rates, the failure strain appears to decrease to a value of 0.08 to 0.1 (see also section III.D on optical strain measurements). More data are necessary to confirm this trend.

In the HRC 33 material the failure strain is significantly higher than in the HRC 40 material, decreasing from 0.35 at 2100 s^{-1} to 0.25 at $10,000 \text{ s}^{-1}$. Limited metallographic observations suggest that strain localization also occurs in the HRC 33 material, particularly at the higher strain rate, but this conclusion awaits further confirmation.

The strain profiles recorded by the scribe lines on the specimen show that even before localization, the strain is not always uniform across the specimen width. Thus, the failure strain values obtained from the strain gage measurement of the reflected and transmitted waves may not give an accurate value of the local strain at which localization occurs. For modeling purposes, however, it is important to know precisely the local instability strain, rather than an average instability strain. To obtain these more precise instability strain measurements, we have developed an optical technique that records the

time sequence of the strain profile across the specimen width. This part of our work is presented in Section III.D.

C. Metallographic Observations

1. Procedure

To complement the stress-strain data discussed in the previous section, we have performed a detailed metallographic investigation of two HRC 40 shear specimens, namely specimens ST16 and NT9. Specimen NT9 was also used to perform optical strain measurements. Additional observations have been performed on several other specimens to ascertain that the conclusions drawn on the basis of specimens ST16 and NT9 are relevant for all the tests.

The metallographic investigation included several steps, which are illustrated in Figure III.12. First, the macroscopic shear failure path was mapped, using replica tape wrapped around the outside specimen surface.

The two broken specimen halves were then studied with a light metallograph; corresponding areas on the two fracture surfaces were matched and a light microscope map of the matched areas was produced. The same matched areas were subsequently mapped a second time, using the scanning electron microscope (SEM), and high magnification SEM micrographs of details of the failure surface were made (Figure III.12a).

In the third step, cross sections through selected regions of the matched failure areas were made, and the cross sections were polished and etched (Figure III.12b).

Finally, the etched cross sections were observed on the light metallograph to detect any microstructural changes near the fracture plane (Figure III.12c).

2. Results: Shear Failure Path

A map of the shear failure path for specimen NT9 is shown in Figure III.13. It is seen that failure occurs on a number of parallel planes

that are connected by well-defined steps. Although the height of the steps may vary (0.1 mm to 1.0 mm), this feature is encountered in all the specimens. Examples of such steps are shown in Figure III.9c (specimen NT3) and in Figure III.14 (specimen NT9). Note, in Figure III.14, the distortion of the grid line in the continuation of failure plane 3 (below failure plane 2). This suggests that at the macroscopic level (size scale 0.5 mm), the strain tries to localize on several planes simultaneously. Successful localization, or shear banding, occurs on one plane on part of the circumference, and on other planes on other parts of the circumference. Further, it appears that shear bands extend progressively around the circumference until the shear band on one plane links up with the shear band on another plane. Further evidence for this mechanism will be shown in the section on optical dynamic strain measurements.

As a result of strain localization on several planes, the shear failure process is not symmetric around the circumference. In addition, the formation of steps linking up shear-banded planes will tend to constrain the relative rotation of the two specimen halves, because they act as the teeth in a ratchet mechanism. They will also tend to force apart the two specimen halves and to displace them laterally.

3. Results: Light and Scanning Electron Microscope Observations

The metallographic observations on Specimens ST16 and NT9 are discussed separately. Specimen ST16 yielded information pertaining to the micromorphology of the shear band, whereas specimen NT9, for which optical dynamic strain measurements were performed, served to elucidate the mechanism of shear banding.

Specimen ST16 had a shallow (30 μ m) line scribed around the circumference to locate the actual specimen gage. This scribe line acted as a stress concentration from which the shear band initiated.

Figure III.15 shows a light micrograph of matching segments of the two fracture surfaces of specimen ST16. Well-defined patterns that are mirror images of each other can be identified on these micrographs. For

instance, a shiny area in the shape of a fishing hook can be seen extending from the specimen outer edge (convex side). Because the features on the two fracture surfaces can be closely matched, we consider that these fractures have been produced during the shear banding process and not during subsequent rubbing of the surfaces caused by reflected elastic waves.

Figure III.16 shows a scanning electron micrograph of the same matching areas as in Figure III.15. The fishing hook pattern of Figure III.15 can easily be identified as the darker feathery area in Figure III.16. The dark areas of Figure III.15 correspond to the light, grainy areas in Figure III.16.

Higher magnification micrographs of selected regions in Figure III.16 are presented in Figures III.17, III.18, and III.19. Figure III.17 shows a detail at the boundary between the feathery and the grainy regions. The feathery region consists of highly smeared, and seemingly layered material (therefore the light appearance in the light micrograph), whereas the grainy region is made up of small elongated cavities or dimples (therefore the dark appearance in the light micrograph).

Another view of the feathery region is given in Figure III.18. The presumed local flow direction, based on the surface striations, is indicated by the arrows. It can be seen that the flow direction may change quite significantly, even over small distances.

Figure III.19 shows the grainy area in more detail. The elongated voids are clearly seen in this picture. The arrows point to particles that have debonded from the matrix. Because the metallurgical analysis of the steel has shown a very low inclusion content, and based on the particle size (0.05 and 0.1 μm), we believe that these particles are carbides, although no chemical analysis has been performed on them. Note that the particle at the right of Figure III.19 remains stuck in the elongated void that grew around it. From the aspect ratio of the voids and assuming that the carbides were initially tightly bonded to the matrix, we can estimate the local shear strain to be approximately 5.

Both specimen halves were cross-sectioned according to the sketch of Figure III.12b and along the lines indicated in Figures III.15 and III.16. Micrographs of the four polished cross sections, etched with nital, are shown in Figure III.20. They correspond to the window shown in Figure III.12c.

As the failure plane is approached from within the material, the microstructure changes from the typical tempered martensite appearance to a very fine microstructure, difficult to resolve with the light microscope. The thickness of the fine microstructure region is about 5 to 10 μm .

Long patches of a white etching microstructure extend on the fracture surface edge of the cross sections. These patches are also 5 to 10 μm in thickness; their length agrees well with the length intercepted on the corresponding cross-sections by the feathery region in Figure III.16. Therefore, we conclude that the white-etching patches are associated with the feathery regions of smeared material in the failure plane. The presence of white-etching bands has been used as a tell-tale sign of transformed adiabatic shear bands in steels. Their formation has been attributed to the rapid heating of the material, caused by the dissipation of deformation energy, to a temperature greater than the austenite transformation temperature; the heated material is subsequently quenched to martensite by heat conduction into adjacent material. Based on the evidence of Figure III.20, we therefore conclude that transformed shear bands formed over part of the failure plane of specimen ST16. Fractures similar to those reported above for specimen ST16 have also been observed on several other specimens.

The failure surfaces of specimen NT9 were particularly well preserved, so that it was possible to match them over an extensive portion of the circumference (over one-third).

Optical micrographs of the two failure surfaces of specimen NT9 are shown in Figure III.21. These matching segments correspond to the portion of the circumference over which the optical dynamic strain measurements were performed.

The general appearance of the failure surfaces is similar to the appearance of the surfaces of specimen ST16 in Figure III.15 (i.e., a graded mixture of shiny and grainy areas). However, the surface contains several dark patches with well-defined contours and these are bordered by shiny feathery regions. These dark regions can be matched one to one on both fracture surfaces, although the relative position of one pattern with respect to another may be different in one half of the specimen than in the other. Again, we interpret the close correspondence of the dark pattern in both failure surfaces as evidence that the surfaces have not been damaged by rubbing against each other after the test was completed.

From the observations made on specimen ST16, we anticipate that the dark areas correspond to regions covered with elongated voids, whereas the shinier areas correspond to regions of smeared material. This is confirmed by the scanning electron micrographs shown in Figures III.22, III.23, and III.24.

Figure III.22 shows an expanded view of the boxed-in area in Figure III.21. It is seen that large portions of the surface are highly smeared. The degree of smearing varies from place to place, with some areas having a grainier, or more "pickled" appearance than others. The higher magnification micrograph in Figure III.23 demonstrates that the degree of graininess or pickling is due to the presence of voids that have undergone various extents of smearing. This observation explains the variation in shininess in the optical micrographs.

Figure III.24 shows matching details of the two failure surfaces, corresponding to the lower left part of Figure III.23. Comparison of the micrographs in Figures III.22, III.23, and III.24 demonstrates that the dark, well-defined patterns in the optical micrographs consist of a fine network of dimples. The contours of the dimple network in the two failure surfaces can be matched almost perfectly, as illustrated in Figure III.24b, where the contour of the network in the input half of the specimen has been superimposed on the micrograph of the output half of the specimen. Features in the smeared region--such as parabolic patterns believed to be highly sheared voids--can also be matched. In addition,

it is observed in Figure III.24 that failure occurs on several planes. This is illustrated in Figure III.25, which represents a schematic cross section along the dashed line in Figure III.24b. It therefore appears that the dimple network areas are formed when unbroken ligaments between two more or less parallel sliding planes break. Alternatively, one could conceive that such "unbroken ligaments" fail first and then act as nucleation sites for the shear band. In view of the fractographic evidence, this seems unlikely. From Figure III.21, it is seen that many such unbroken ligaments develop during the shear banding process.

Figures III.22 and III.24, also show that important variations in the flow direction can occur locally. In Figure III.24b, the dashed line represents the local flow direction, whereas the arrow represents the direction tangent to the specimen direction (i.e., the direction of the initially applied shear). Thus, radial relative displacement of the two specimen halves has taken place during shear banding.

Although no metallographic cross sections were made in specimen NT9, we infer, by comparison of the failure surface morphology with the morphology of specimen ST16, that a transformed shear band formed over large portions of the fracture surface.

Additional information about the shear banding mechanism was obtained by graphically putting back together the two failure surfaces and observing how the unbroken ligament failed as the surfaces were displaced with respect to each other.

The procedure is as follows. First, the main features (dark unbroken ligament) of one failure surface (say, of the output half of the specimen) are traced on transparent paper. This tracing is flipped over and overlaid on the map of the other fracture surface. This reveals that not all the corresponding dark areas can be matched simultaneously. Rather they can be matched sequentially, by gradually displacing the transparent overlay with respect to the micrograph.

When one realizes that the point at which the corresponding dark areas match precisely represents the point at which the unbroken ligament

failed, it follows that the shear band growth is highly nonuniform on the microscale. This is illustrated in Figure III.26, which shows the sequence of failure of the unbroken ligaments in the failure surface as a function of relative displacement between the two specimen halves. Surface matching confirms that, as was deduced from the scanning electron micrographs, the specimen halves displaced radially, as well as circumferentially. The radial displacement was estimated to be roughly 30 μm . We believe the displacement is caused by the interference of the macrosteps linking two main planes of shear band extension (see Figures III.13 and III.14). The circumferential displacement necessary to fail all the unbroken ligaments in the area of observation is about 400 μm , suggesting enormous strains within one shear band.

Figure III.26 also indicates that unbroken ligaments tend to fail first near the edges of the specimen. It is unclear whether this has any implication regarding the initiation of the shear band.

4. Discussion

This investigation has shown that on a macroscopic scale, the shear strain tries to localize on several planes. Successful localization occurs on different planes over different parts of the specimen circumference. This suggests that several discrete nucleation sources are active (nonhomogeneous nucleation) and that they might be identified by careful mapping of the fracture surfaces.

Similarly, the scanning electron micrographs have shown that at the microlevel, the shear band also propagates in several parallel planes. These planes eventually link up, either in a gradual manner, leaving little evidence of the transition, or in a rather abrupt manner by failure of previously unbroken ligaments. The presence of unbroken ligaments that gradually fail indicates that the shear plane will retain some strength even when it is already engulfed by the shear band.

The microscope observations, coupled with metallographic sectioning, have revealed that a significant portion of the material in the shear band undergoes phase transformation (white etching).

The strain in the shear band can be estimated from the elongation of dimples on the failure surface or from the displacement required to fail unbroken ligaments. These estimates yield strains of about 5 to 10 in the shear band. In Section III.D, these estimates are compared with values of the strain measured optically.

The micrographs have also revealed signs of void activity over almost the whole failure plane, either in the form of well-preserved elongated dimples, or in the form of highly sheared and smeared dimples. We think that this is a very significant result because it implies that void kinetics strongly interact with the shear banding process. In fact, it is possible that softening due to cavity growth may play an equal or even a more important role in promoting localization than thermal softening. In that case, void kinetics would become an integral part of the shear banding process.

These conclusions require further verification. In particular, it would be desirable to pursue the surface matching work, and to produce stereo-images of the fracture surfaces. The current results, however, already provide a significant body of new experimental information useful in guiding the shear band modeling effort.

D. Optical Dynamic Strain Measurements

Because of the very nature of the strain localization process, only limited information can be obtained about adiabatic shear banding from average strain measurements, such as those performed with strain gages on the SHTB. This has already been pointed out in Section II, where we mentioned that a complete time sequence of strain profiles across the specimen width would provide an invaluable new insight into shear localization. Therefore, during this program we have developed an optical technique, with high spatial and time resolution, to measure strain profiles during the SHTB tests. This technique is described below and the results of the first successful experiments are presented. In conjunction with the metallographic observations, these results reveal new details of the shear banding process.

1. Experimental Technique and Specimen Preparation

The experimental technique to obtain dynamic strain measurements during SHTB tests consists of taking high-speed photographs of deforming grid lines on the specimen. The photographs of the grid lines, which represent a time sequence of the deformation across the specimen width, are then digitized, smoothed, and differentiated to obtain a time sequence of the strain profile.

To obtain the grid pattern on the specimen, the specimen is first polished to a mirror finish. A thin film of negative photoresist is then deposited on the polished surface and a mask containing the grid pattern is wrapped around the specimen. As a mask, we use an electrochemically etched nickel foil, containing a square grid with a line spacing of 0.1 mm. The nickel grid is commercially available from Buckbee-Mears, St. Paul, Minnesota. The specimen with photoresist and mask is exposed to ultraviolet light and the resist is then developed, leaving the material between the grid lines uncoated. The specimen is finally lightly etched with a nitric acid solution. The result is a set of bright grid lines on a dark background, as illustrated in Figure III.14.

The experimental set up for the optical dynamic strain measurements is sketched in Figure III.27 and the actual arrangement is shown in Figure III.28. The specimen is illuminated during the test with a high-intensity xenon flash lamp and photographed with a high-speed framing camera capable of taking 48 frames at rates of up to 4.5 million frames per second. The light pulse duration of the flash lamp can be varied between 50 and 600 μ s.

To focus on a small 2.5 by 1.5 mm area, corresponding to the actual specimen region, we have mounted a relay lens in front of the standard camera lens. Because of the lack of space between the relay lens and the specimen, the specimen has to be lighted indirectly, by means of the concave perforated reflector shown in Figure III.28b. The light from the flash tube is concentrated by a Fresnel lens, reflected off the white reflector onto the specimen, and reflected again by the specimen surface

through the orifice in the reflector and the lenses onto the rotating prism of the camera.

The framing camera does not have a shutter; hence, the point at which the camera begins to record is controlled by the time at which the flash lamp is fired. To synchronize the firing of the flash lamp with the stress wave loading of the specimen, the signal from a strain gage on the input bar is used as a trigger source and as reference time zero (see Figure III.29). In addition, because the flash lamp has an inherent triggering delay of about 20 μ s, and reaches its full intensity only after 15 μ s, it is necessary to trigger the lamp before the stress wave reaches the specimen. It is also necessary to use a separate optical marker that will accurately indicate on the photographs the trigger time of the flash lamp, so that we can correlate the transmitted load signal, recorded in the output bar, and the optical strain measurement. This is accomplished by firing an exploding bridge wire (which has a rise time to full light intensity of a couple microseconds) at the time the flash lamp is triggered. The bridge wire is fired at one end of a fine optical fiber; the other end of the fiber is positioned in the lower left corner of the camera field of view to produce a sharp bright spot.

This arrangement has worked successfully in the two experiments performed during this program--experiments NT6 and NT9.

2. Experimental Results

In test NT9 localization occurred on several planes (see Figure III.13) but was close to the midsection over a large portion of the circumference. This was the region photographed with the high-speed camera.

The results of test NT9 are shown in Figures III.30 to III.34. The average strain rate in the test was 5900 s^{-1} . The stress-strain curve obtained from strain gage measurements is presented in Figure III.30. The average strain to failure is 0.13, in good agreement with the data reported in Section II, and consistent with the theory reported in Section V.

A series of time sequence photographs is presented in Figure III.31. The interframe time is $2.5 \mu\text{s}$. It is possible to resolve the early time deformation on the photographs and to estimate the yield point. The time scale of the photographs can be matched with the time scale of the transmitted torque signal. Thus, the events on the photographs can be related to the strain gage signal within the uncertainty due to the oscillations on the transmitted torque. In Figure III.31, time zero was chosen as the time when the specimen is first loaded.

Yield occurs at $25 \mu\text{s}$. Strain localization starts at the center of the specimen section after about $45 \mu\text{s}$ and the shear band starts to fail at $50 \mu\text{s}$. The shear band is recognized to fail at that time because the input half of the specimen appears blurred in the photograph of Figure III.31f, indicating a sudden acceleration of its rotation.

The deformation profiles photographed during test NT9 were digitized and smoothed; however, no image enhancement technique was used. The time sequence of deformation profiles obtained from the photographs in Figure III.31 is shown in Figure III.32. The corresponding strain profiles, obtained by numerical differentiation, are shown in Figure III.33. Figure III.33 indicates that the strain is not uniform across the specimen width. There is a region with strong gradients near the edges with a central region of approximately 1 mm in width where the strain is almost uniform. Just before localization, the strain in the central region varies from 0.12 to 0.15. Strain localization occurs near the center of the central region at a local strain of 0.13. It is interesting to note that this is not the highest strain in the specimen, suggesting that local perturbations (such as a microstructural inhomogeneity or a machining mark at the specimen interior surface) have played a dominant role in localizing the strain. As soon as the shear band forms, the strain rapidly builds up in the band to reach 2 within $7 \mu\text{s}$. The strain in the band was estimated assuming a band thickness of $60 \mu\text{m}$, based on the photographic observations. This band thickness is an upper bound, so that the strain values represent a lower bound. The

average strain in the specimen at the time of localization ($t = 42.5 \mu s$) can be calculated to be 0.11 from the deformation profile in Figure III.32. This is somewhat lower than the value of 0.13 obtained from the strain gage measurements at the beginning of the drop in load carrying capacity.

Late-time photographs of the specimen halves indicate that the relative displacement accumulated across the shear band before a gap opens up (due to the wedging action of the steps around the circumference) is about 300 to 400 μm . This value agrees well with the estimate obtained by matching the failure surfaces (Section C).

The strain rate history at the location of the shear band for test NT9 is plotted in Figure III.34. During uniform deformation the strain rate increases gradually from $1000 s^{-1}$. This is in agreement with the value obtained from strain gage measurements. Upon localization, the strain rate jumps by more than an order of magnitude to reach values in excess of $100,000 s^{-1}$.

In test NT6 deformation localized very close to the input edge of the specimen. Although small steps, of a height of a few tens of micrometers, were formed between parallel shear banding planes, no macroscopic shear plane transition occurred. The transmitted wave record in test NT6 was lost because of electronic noise produced during the firing of the exploding bridge wire. The stress record could therefore be obtained only from the first reflection of the transmitted wave. This prevented an accurate correlation of the photographs with the stress records. Further, parts of the image in the high speed photographs are out of focus, because of specimen curvature and a small misalignment of the camera. (The optical axis of the camera did not extend through the specimen axis.) This made difficult the processing of the pictures taken during the initial part of the deformation. As a result, there is some uncertainty about the exact point of yielding, and the deformation profiles may contain a systematic error of about 50 μm in the circumferential displacement. Therefore, the data for test NT6 are less reliable. They are nevertheless presented, because they reveal some

interesting aspects of the shear failure process not observed in test NT9.

Figure III.35 shows the dynamic stress-strain curve for test NT6 obtained from the strain gage measurements. The average strain rate for the test is 6000 s^{-1} and the average failure strain is 0.14, again in good agreement with data presented in Section II.

A time sequence of twelve photographs taken during the experiment is shown in Figure III.36. The interframe time for this test is $3 \mu\text{s}$. Note that not all the pictures taken during the test are shown in Figure III.36. The point at which appreciable distortion of the grid lines is noticable on the photographs has been chosen as time zero. It is seen from the time sequence photographs that the deformation remains uniform only up to about $18 \mu\text{s}$ after time zero. At $24 \mu\text{s}$, it appears that the deformation has been blocked at the center of the specimen, resulting in an inflection in the grid lines, and then has started to concentrate in the specimen half close to the input bar. At $30 \mu\text{s}$ the strain localizes further in the second to last grid row near the input edge of the specimen. Failure occurs at $33 \mu\text{s}$ and a failing shear band can be seen developing in Figure III.36f. Note, however, that in the grid row where the strain has localized, the strain is not uniform in the circumferential direction; it decreases from the bottom to the top of the picture. This strain gradient occurs because at the top of the grid row, the shear band changes its propagation path and a step, about $40 \mu\text{m}$ in height, is formed that constrains the shear deformation. The presence of the step is more evident in the sequence of photographs of Figures III.36g to III.36l. The photographs demonstrate, that besides constraining the shear deformation, the step resulting from the change in the shear banding plane wedges apart the two specimen halves, as was mentioned in Section III.C. Figures III.36e to III.36h also suggest that the shear band may be gradually propagating from the bottom of the photographs to link up with another shear band on a neighboring plane.

The deformation profiles photographed during test NT6 were digitized and the profiles corresponding to the photographs in Figure III.36a to

III.36f are plotted in Figure III.37. The difficulties in processing the high-speed photographs are apparent in Figure III.37, where the displacement accumulated between time zero and 6 μ s appears too large compared with subsequent displacements. The zone of frozen deformation developing near the center of the specimen can be clearly seen in Figure III.37.

The time sequence of strain profiles obtained by differentiation of the deformation profiles in Figure III.37, is plotted in Figure III.38. Shear deformation begins concentrating in the input half of the specimen (right-hand side of the figure) at a strain of about 0.1, and gradually localizes further near the specimen edge. At a strain of 0.2, an actual shear band forms at the edge. Based on a shear band width of 20 μ m determined from the high-speed photographs, the strain in the shear band at the point of failure approaches 3 for a grid line at the bottom of Figure III.36f. Note also that the frozen deformation in the center of the specimen has caused a pronounced dip in the strain profile.

The strain rate in the bottom part of the grid row where strain localization took place is plotted on a semilogarithmic scale in Figure III.39. The dots in Figure III.38 represent strain rates determined from the curves in Figure III.38. The oscillations in the strain rate are due to the uncertainty in reducing the data of the high-speed photographs of test NT6. The full line represents the fitted strain rate history for the test. As for test NT9, the strain rate increases by an order of magnitude once shear banding has taken place.

The average strain in the specimen, just before final localization into a shear band, can be calculated from the deformation profile in Figure III.37. The value of 0.14 obtained from this estimate agrees very well with the value obtained from the strain gage measurements taken when the load-carrying capacity begins to decrease.

3. Discussion

The technique developed to obtain complete strain profile histories during the SHTB experiments has proved very successful. To our knowledge these are the first real-time observations of the shear banding process.

The optical dynamic strain measurements have allowed the determination of the local strain at the onset of instability. They have shown that the strain before localization is not always uniform, that localization may be attempted at several locations on parallel planes, and that the strain at the point of localization may be lower than at other locations in the specimen. These results all emphasize the necessity and the advantages of performing detailed strain measurements.

The optical strain measurements have further allowed direct determination of the width of the shear band and of the strain and strain rate within the shear band. Strain rates in the band are in excess of $100,000 \text{ s}^{-1}$. Based on the optical strain measurements and on the metallographic observations, it appears that very large displacements can be accumulated in the band before complete material failure is achieved. As a result, strains of 5 to 20 are experienced by the band.

With the high-speed photographs, we have observed that shear banding occurs in two stages. First, the deformation concentrates in a band of 60 to 100 μm (from 42.5 to 47.5 μm in Figures III.36 and III.37 for test NT9). Then as deformation proceeds, a second localization takes place, this time in a much narrower band, estimated to be 10 to 20 μm wide. The onset of the second phase has been considered the actual failure point. The first phase of shear banding is believed to correspond to the formation of a deformation shear band; the second phase would correspond to the formation of a transformation shear band. Although large strains are concentrated in the band during the first phase (up to 100% in test NT9), the greater part of the displacement accumulated across the band is experienced during the second phase. We believe that a critical strain (or a critical energy dissipation) is also required to trigger the second phase.

Direct observation of the shear banding process suggests that an appreciable portion of the load-carrying capacity may be retained during the first phase of localization. This conclusion is based on the observation of the acceleration of the specimen input half in test NT9. This conclusion should be confirmed by a better correlation of strain profile history and transmitted torque history than could be performed here.

The shear banding processes observed in tests NT6 and NT9 differ significantly in that test NT9 showed strain localization nucleating in an essentially homogenous field, whereas test NT6 showed localization caused by a geometric strain concentration (the change in section at the specimen edge). Although the final phase of the shear failure is the same in both cases, strain localization occurs much more gradually in the case of the geometric strain concentration. This observation suggests that aside from the material constitutive behavior (strain hardening, thermal softening, strain rate sensitivity), the nature, or in other words the strength, of the perturbation at which a shear band nucleates may significantly affect the degree of localization and the onset of the second phase of shear banding. This observation agrees with the conclusion, based on simulations of Taylor experiments, that geometrical constraint greatly affects the formation of shear bands if critical strain conditions are reached (see Sections IV, V, and VI of this report).

The energy dissipated in the shear band can be estimated by assuming a linear decrease in the shear band strength with the relative displacement between specimen halves accumulated in the band. Thus, for an initial strength of 850 MPa and a displacement up to total failure of 350 μm , the dissipated energy per unit area of shear band is:

$$(850 \cdot 10^6 \times 350 \cdot 10^{-6})/2 = 0.14875 \text{ MJ m}^{-2} \quad (\text{III.2})$$

In test NT6 we observed a change in shear banding plane and a decrease in shear band strain as the transition region is approached;

this indicates that interaction between two neighboring bands is strong. It also indicates that the band does not propagate simultaneously around the circumference. Thus, the SHTB test together with optical strain measurements can be used to study shear band growth as well as initiation.

Although successful, the optical dynamic strain measurement technique needs several improvements. In the future an undeforming reference frame should be placed in the field of view to help in reducing the data. Further, a more sophisticated digitization procedure should be used, in which the light intensity of the grid lines is measured and contour lines are fitted through the light intensity peaks. A thorough assessment of the degree of image distortion due to the camera and to specimen curvature should be performed. Finally, a better timing of the photographs and of the torque records should be achieved so as to estimate the degradation of load-carrying capacity with shear band deformation.

E. Measurements of Temperature Near Shear Bands

Thermal softening caused by adiabatic heating of the material through plastic deformation is believed to be an important factor in the process of shear banding. The observation of phase transformation in part of the shear band formed in high strength steels also indicates that very high temperatures are reached in the shear band material. Knowledge of the temperature history in the shear band region would provide an essential piece of experimental evidence on which to base shear band model development. It would allow us to relate the shear band behavior to isothermal stress-strain curves determined in separate tests for the material. Moreover, the achievement of a critical temperature in a material element is an appealing criterion for controlling both the nucleation and the growth of a shear band in a constitutive model.

Because of the small width of the shear band and the short duration of the instability event, real-time measurement of the temperature in the band, although feasible, is at the limit of current experimental error

technology. Such measurements have been attempted in a parallel research program on adiabatic shear banding sponsored by ARO at Brown University. In our program we have taken a different approach to obtain estimates of the energy dissipated and of the temperature in the band, by using indirect temperature measurements. This section discusses the principle of the technique and then presents the results of several measurements performed in conjunction with SHTB experiments.

1. Principle of the Indirect Temperature Measurement Technique

To obtain estimates of the energy dissipated and of the temperature in the shear band, we have recorded with thermocouples the temperature variation immediately after the test in the specimen material a small distance away from the shear band (Figure III.40a). The temperature records are interpreted using a one-dimensional heatflow model in which the shear band is treated as an instantaneous concentrated heat source.² Based on the experimentally determined shear band width of 60 μm , which corresponds to about 3% of the specimen width, the concentrated heat source assumption appears justified in first approximation. Given the short duration of the experiment compared to the time required for heat to flow, say, over 0.5 mm, which is of the order of several milliseconds, the instantaneous heat source assumption is also justified.

The anticipated temperature history at the thermocouple location is represented in Figure III.40b. The temperature is expected to rise rapidly, because of the (presumably homogeneous) plastic deformation at the thermocouple position during the test. A second temperature rise is recorded at later times, which corresponds to the temperature elevation caused by the heat flow from the shear band plane. Only this latter temperature increase is considered when estimating the shear band temperature.

The energy dissipated in the band, Q_T , is then related to the maximum temperature elevation, ΔT_{max} , recorded with thermocouples at a distance x from the shear band through the relation:

$$Q_T = \Delta T_{\max} \rho c x \sqrt{2\pi e} \quad (\text{III.3})$$

where c is the specific heat and ρ is the density of the material tested.

The energy Q_T represents the energy per unit (circumferential) area dissipated in the shear band, from the beginning of shear localization to the point of complete loss of load-carrying capability. It can be expressed as:

$$Q_T = \rho d_{SB} \int_0^{T_{SB}} c(T) dT \quad (\text{III.4})$$

where d_{SB} is the shear band width and T is the temperature in the shear band. The ambient temperature has been taken as 0°C .

In equation III.4, c is now taken as a function of temperature to account for the large temperature changes expected to occur within the shear band. The variation of the specific heat of 1010 steel with temperature is shown in Figure III.41. The specific heat for 4340 steel has a similar behavior. To facilitate integration, a linear approximation of the function in Figure III.41 is used when reducing the experimental data, namely:

$$c(T) = 450 + 0.6875T \quad (\text{III.5})$$

where the temperature T is in degrees Celsius. This linear approximation is also shown in Figure III.41. Because the mass density varies only by about 5% between room temperature and 1400°C , an average, constant value can be used in Equation III.2. Here we have used $\rho = 7600 \text{ kg/m}^3$.

Knowing Q_T and the width of the shear band (either from metallographic observations or from high-speed photographs), we can estimate the temperature in the shear band by integrating Equation III.4, after insertion of Equation III.5, and by inverting. Thus the shear band temperature is given by:

$$T_{SB} = \frac{-450 \rho d_{SB} + \sqrt{(450 \rho d_{SB})^2 + 1.375 \rho d_{SB} Q_T}}{0.6875 \rho d_{SB}} \quad (III.6)$$

If the value Q_T obtained from Equation III.1 is used together with the total shear band width (deformed band region and transformed band region), Equation III.6 gives an estimate of the average band temperature. However, if the temperature in the transformed part of the band is sought, a correction must be made to the heat source term to account for the contribution due to plastic deformation in the deformed band region (Figure III.40a), That is:

$$Q_T = Q_{DB} + Q_{TB} \quad (III.7)$$

where Q_{DB} is the contribution from the deformed region and Q_{TB} is the contribution from the transformed region

Q_{DB} is calculated (based on experimental observations) as the deformation energy of a region 50 μm in width and subjected to a strain of 1 at a flow stress of 850 MPa. Thus Q_{DB} is given by:

$$Q_{DB} = 850 \times 10^6 \times 50 \times 10^{-6} \times 1 = 0.0425 \text{ MJ m}^{-2} \quad (III.8)$$

The temperature in the transformed shear band is finally calculated using Equation III.6, with Q_{TB} as the heat source term and taking d_{SB} as the width of the transformed shear band.

2. Experimental Procedure

The temperature measurements were performed during SHTB tests.

Temperature histories near the shear band were measured with steel-constantan thermocouples. Constantan wires, 75 μm in diameter, were spot welded directly on the specimen surface, and the specimen itself formed the second half of the couple. The thermocouple junctions produced in this way afforded the required size and time response (better than 1 ms).

Four active thermocouples were placed with even spacing across the specimen gage. They were also spread over approximately a quarter of the circumference. Four additional thermocouples were placed outside the gage region to serve as reference junctions. This arrangement allowed differential measurements to be made conveniently. The signal from the thermocouples was amplified and recorded on digital oscilloscopes.

Three circumferential lines were lightly scribed on the shear specimens used for the temperature measurements. These lines marked the edges and the center of the specimen gage and were intended to facilitate the positioning of the active thermocouples. The scribe lines acted as nucleation sites for the shear bands. Comparison of the results of tests with or without scribe lines demonstrated that the scribe lines had little effect, other than constraining the shear band on specific planes.

3. Experimental Results

Temperature measurements were performed during three experiments at strain rates between 1900 s^{-1} and 3500 s^{-1} . At higher strain rates we experienced difficulties because the thermocouples tended to break away owing to the large accelerations during the tests.

The experimental data are summarized in Table III.1. Figure III.42 shows a set of three temperature histories, measured during the same experiment, at locations on the specimen 0.35 mm to 1.69 mm away from the shear band. In the first millisecond of the record, there is a sharp increase in temperature that corresponds to the homogeneous deformation of the specimen during the actual shear experiment. Later, the temperature rises gradually, to reach a maximum after a time that increases with the distance from the shear band. The maximum temperature elevation decreases rapidly with increasing distance from the band. The maximum measured temperature elevations vary between 4°C and 60°C . These are relatively low values, but it must be remembered that they represent the temperature elevation due to heat flow from the shear band, and not the temperature in the shear band itself.

The measured temperature histories agree qualitatively well with the expected histories, based on one-dimensional heat flow considerations (compare Figures III.40b and III.42). The time response of the thermocouples is high enough to record the temperature elevation during the shear deformation. The sharp spikes occurring at the beginning and at the end of loading are believed to be caused by electromagnetic noise (reverse magnetostrictive effect in the specimen).

The values of the energy dissipation in the band, Q_T , calculated from the experimental temperature with Equation III.1 are listed in Table III.1. The values of the dissipation in the transformation band, Q_{TB} , are also listed. Values of Q_T vary between 0.075 and 0.215 MJ m⁻², with most values around 0.17 MJ m⁻². Correspondingly, values of Q_{TB} vary between 0.0325 MJ m⁻² and 0.1745 MJ m⁻², with most around 0.13 MJ m⁻².

The average temperature in the shear band T_{av} , has been calculated using a shear band width of 60 μ m. Estimates of the temperature in the transformed band have been made for three different thicknesses: 10, 20, and 30 μ m, respectively. High-speed photography and metallographic observations indicate that 20 μ m is the most likely value. Average band temperature estimates range from 300 to 700°C, with most values around 600°C. For a band width of 20 μ m, the transformed band temperature estimates vary between 370°C and 1300°C, with most values around 1100°C.

The temperature elevation due to plastic deformation at the thermocouple location decreased with distance from the shear band and varied from essentially zero up to 16°C. Using these temperature values to calculate the plastic energy density dissipated, we estimated the plastic strain at the location of the thermocouple. The strain estimates range from about 8% near the band to zero. This suggests a strain gradient in the specimen, as has indeed been observed in the high-speed photographs, although the strains estimated from the temperature records are somewhat smaller than the optically measured strains.

4. Discussion

The results of the temperature measurements indicate that the temperature in the shear band reaches several hundred degrees. With four exceptions, all the estimates of the temperature in the transformed band exceed 700°C, irrespective of the band thickness assumed. For the most likely band thickness of 20 μm , most measurements indicate a temperature of 1000°C to 1200°C. This shows that high enough temperatures are produced during localization for the austenitic transformation to occur. This is supported by the metallographic evidence (see Section III.C). In particular, for the temperature measurement numbered ST14-TC1, the two failure surfaces were observed in detail at the thermocouple location. They were matched to ascertain they had not been damaged after the failure, and then they were cross sectioned, polished, and etched. The cross-sections revealed that at the level of the thermocouple, a transformed band had formed, with a thickness of about 20 μm . The presence of the transformed band is consistent with the indirect temperature measurement of 1133°C for the thermocouple under consideration.

The values of Q_T obtained from the thermal measurements are consistent with the estimate based on the amount of deformation to failure and a linearly decreasing stress in the region where strain localized (Section III.D).

The results in Table III.1 represent a large variation in the value of the energy dissipated in the shear band, ranging from 0.075 to 0.217 MJ m^{-2} . Variations occur, even for measurements performed on the same specimen during the same test. These variations may be due to the non-uniform nature of the shear banding process, both on the macroscale and on the microscale, noted in previous sections. Thus the lower Q_T values would correspond to regions where localization is less intense, or to regions where a transformed band formed over a lesser portion of the failure surface. Because a systematic metallographic evaluation has not been undertaken for all thermocouple locations, this explanation cannot be verified beyond the evidence already presented. The highest value

measured (0.217 MJ m^{-2}) may be explained by the thermocouple being located near a failure plane transition region and thus may have registered contributions from sources other than the shear band itself (i.e., from the deformation to form the step joining the two shear planes).

The fact that transformed bands may form over only part of the specimen width and that great variations in deformation are observed even at the microscopic level suggests a nonuniformity in temperature. The temperature estimates given in Table III.1 represent averages over a small failure surface area in the vicinity of the thermocouple position. It is likely however, for the reasons discussed above, that the temperature will not be uniform in this area and that hot spots will form.

A possible source of error that has not been considered in our study is the contribution to the measured temperature elevation due to rubbing of the specimen surfaces against each other after failure is complete. In case of severe gouging, as has been observed on some occasions near a failure plane transition region, this contribution may not be negligible.

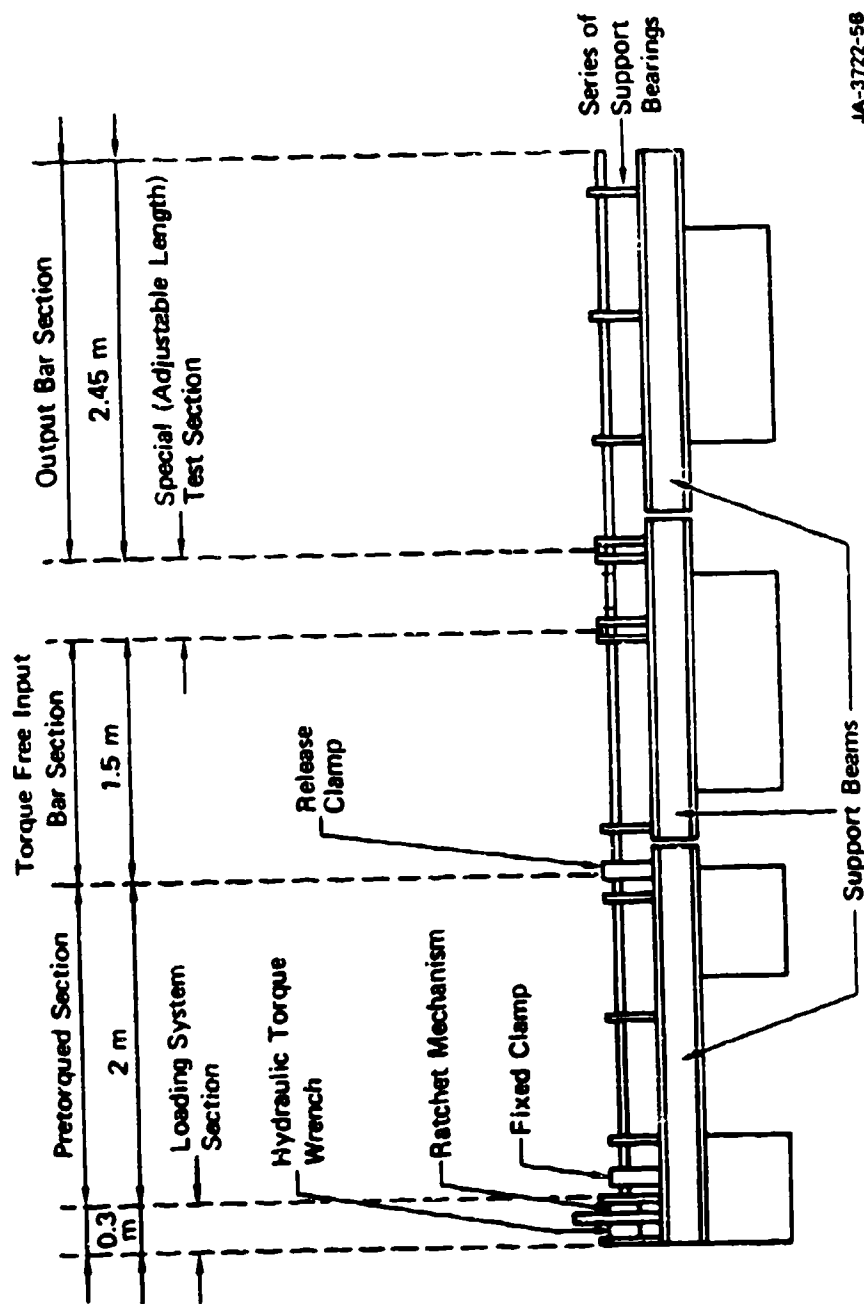
Nevertheless, in view of the consistency of several of the results, one of which has been backed by careful metallographic observations, we believe that a reliable estimate of the energy dissipated in the shear band is 0.16 to 0.17 MJ m^{-2} . From this value we estimate that the average deformed band temperature reaches 500°C to 600°C , whereas the transformed band temperature reaches 1000°C to 1200°C . These results await verification by comparison with direct temperature measurements when they become available.

F. References

1. C. Y. Chiew, private communication (1984).
2. H.S. Carslaw and J. C. Jaeger, Conduction of Heat Solids, second edition (Oxford, Clarendon Press, 1959).

Table III.1
RESULTS OF TEMPERATURE MEASUREMENTS

Specimen Number	x (mm)	ΔT_{pp} (°C)	ΔT_{max} (°C)	Q_T (MJ/m ²)	T_{av} ($d_{98} = 40 \mu m$)	Q_{98} (MJ/m ²)	T_{98} ($d_{98} = 10 \mu m$)	T_{98} ($d_{98} = 20 \mu m$)	T_{98} ($d_{98} = 30 \mu m$)
						(°C)	(°C)	(°C)	(°C)
898-PC3	0.04	6.7	6.8	0.075	290	0.0325	636	570	264
898-PC3	1.16	5.8	10.7	0.175	508	0.1325	1691	1067	601
898-PC4	1.37	2.6	10.7	0.175	581	0.1395	1666	1050	748
8914-PC3	0.35	15.8	42.1	0.217	692	0.1765	2012	1286	975
8914-PC3	0.36	7.4	22.6	0.107	610	0.1465	1706	1135	853
8914-PC4	1.00	0.0	4.7	0.110	432	0.0755	1167	716	525
897-PC3	0.43	10.5	25.3	0.161	551	0.1105	1574	900	730



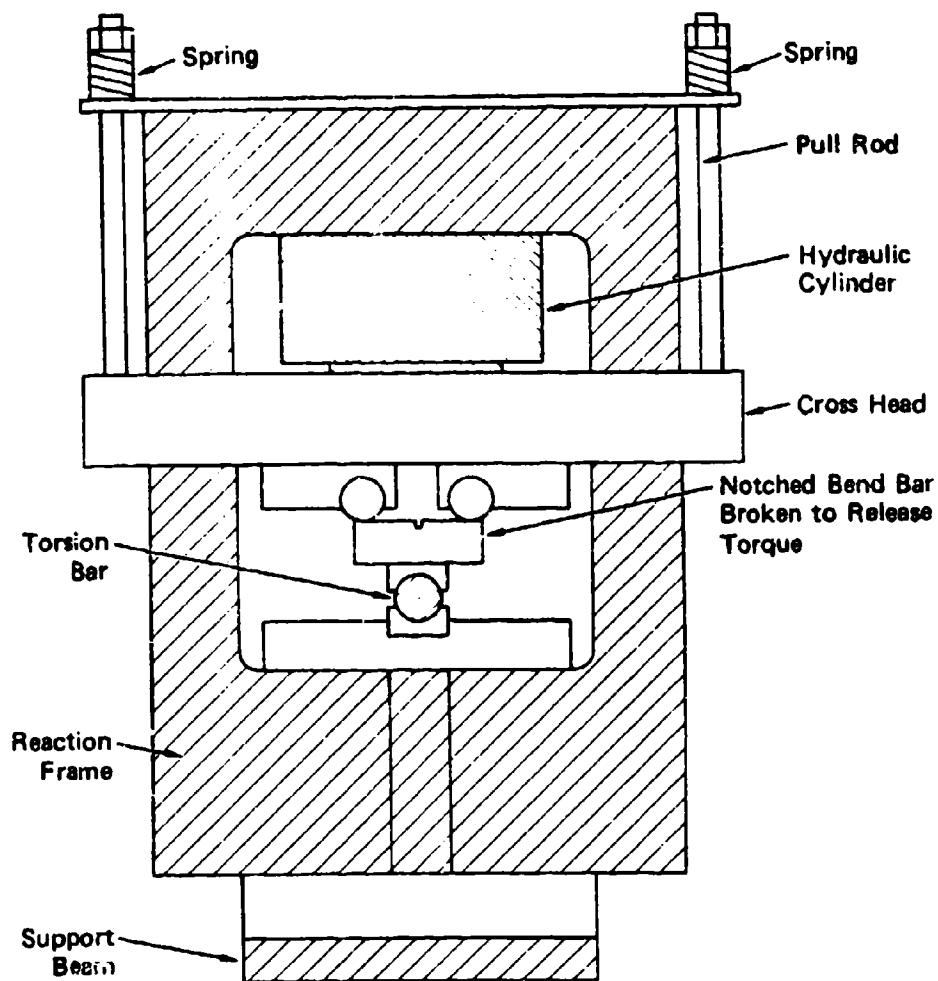
JA-3722-58

FIGURE III.1 SCHEMATIC OF SPLIT HOPKINSON TORSION BAR



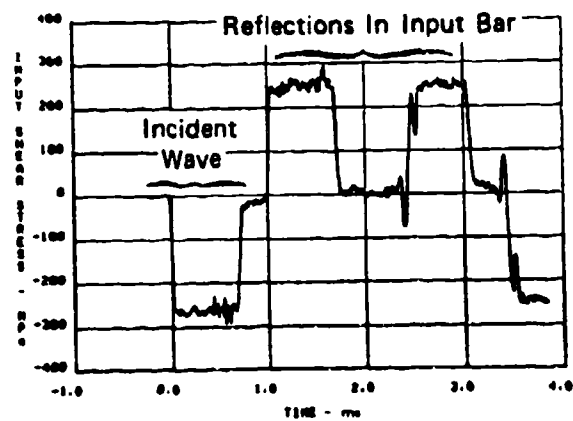
JP-3722-55

FIGURE III.2 VIEW OF SHTB LOOKING ALONG THE INPUT BAR
TOWARD THE RELEASE CLAMP AND THE STATIC
LOADING MECHANISM



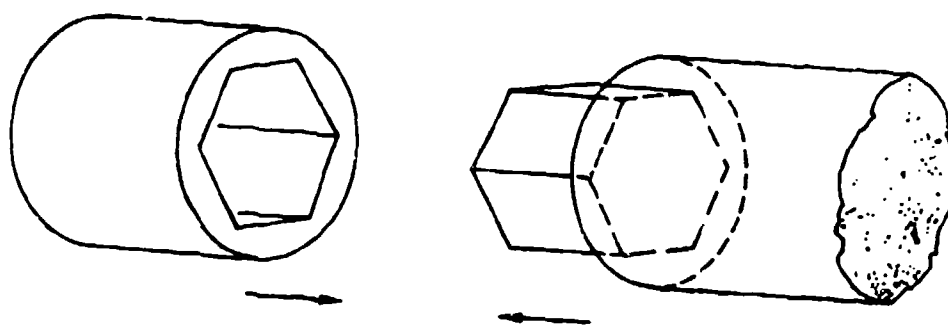
JA-3722-36

FIGURE III.3 RELEASE CLAMP



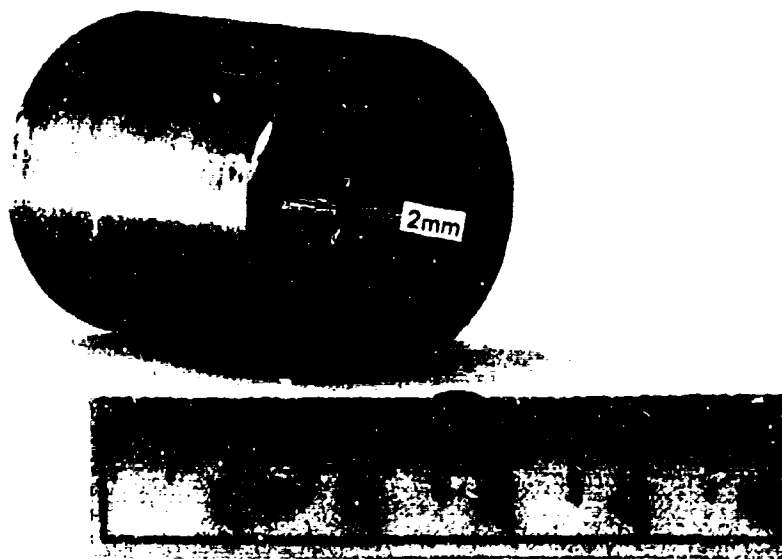
JA-3722-52

FIGURE III.4 INCIDENT SHEAR STRESS WAVE MEASURED
IN THE INPUT BAR

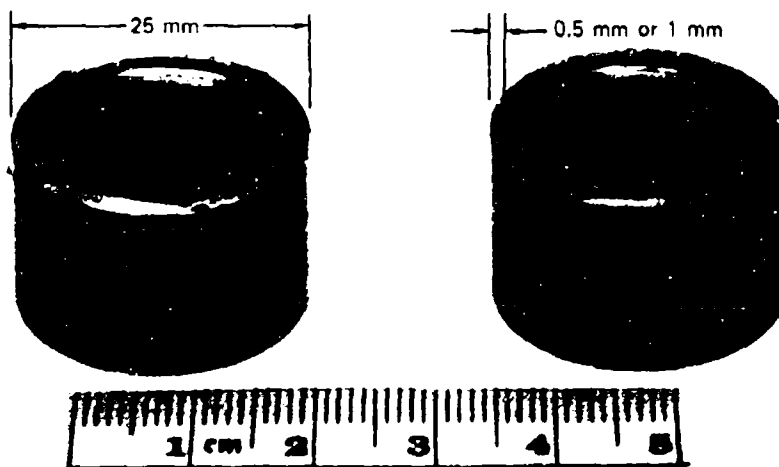


JA-3722-94

FIGURE III.5 HEXAGONAL COUPLING BETWEEN SPECIMEN AND BAR



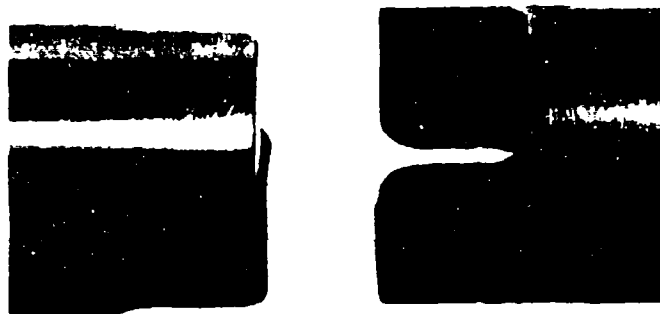
(a)



(b)

JP-3277-93

FIGURE III.6 SPECIMEN FOR SHTB EXPERIMENTS (a) BEFORE TESTING,
(b) TWO HALVES OF BROKEN SPECIMEN



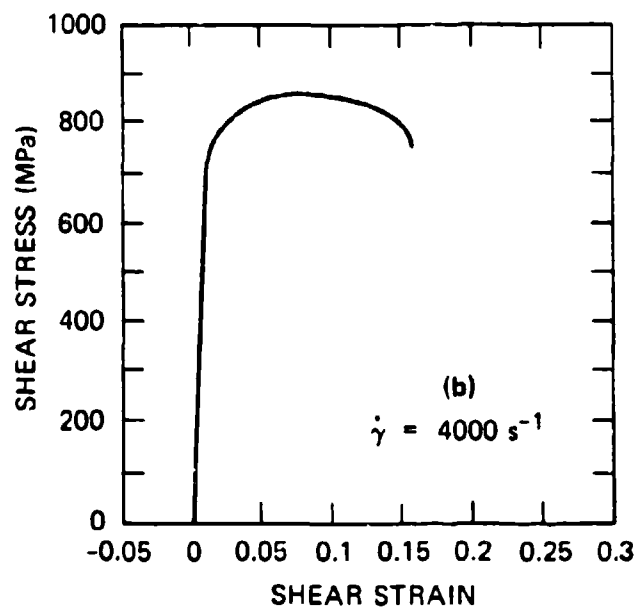
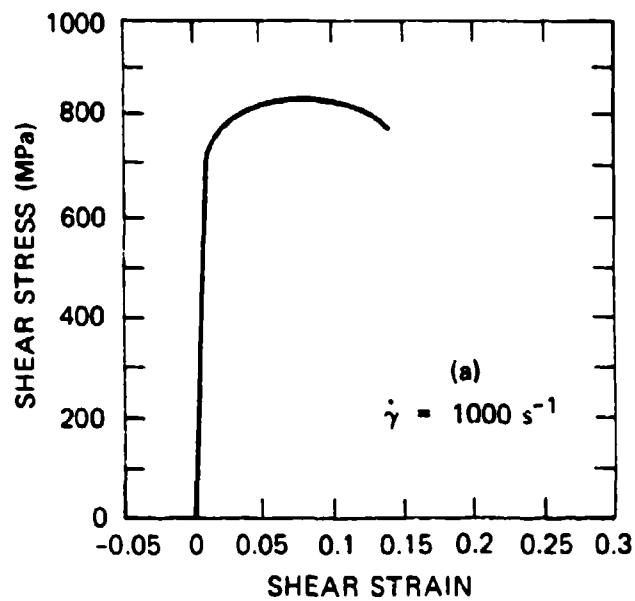
(a)



(b)

JA-3722-95

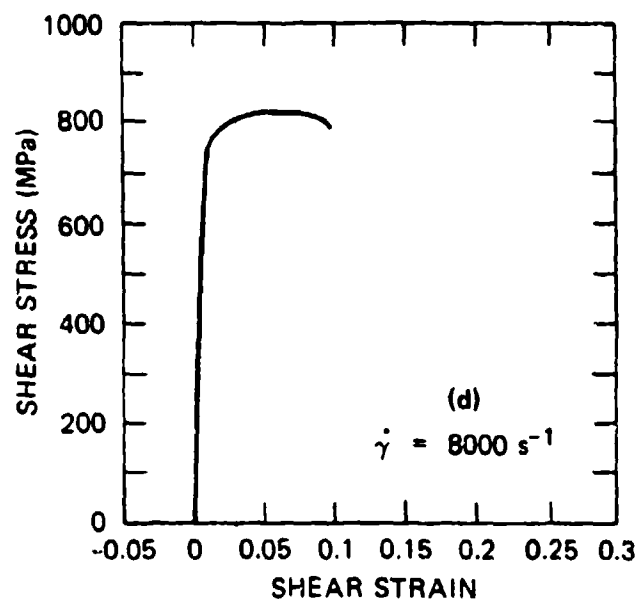
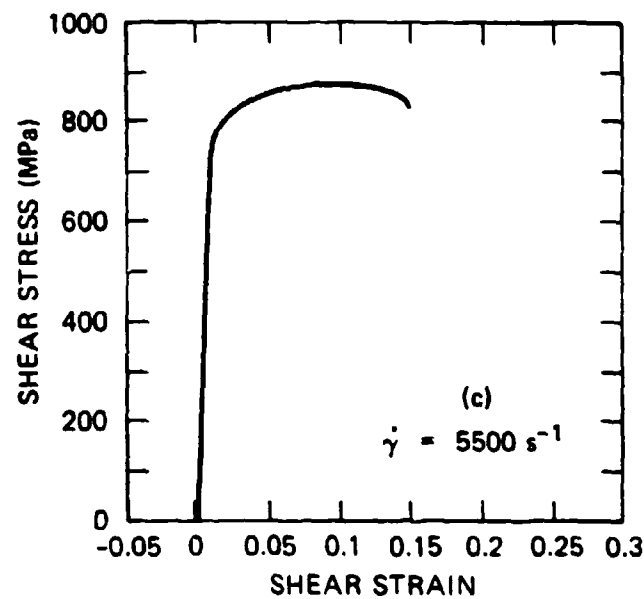
FIGURE III.7 COUPLING FOR HIGH TEMPERATURE INSERT BARS
(a) UNCOUPLED, (b) COUPLED



JA-3722-96

FIGURE III.8 STRESS-STRAIN CURVE FOR 4340 VAR R_C40
 FOR FOUR STRAIN RATES

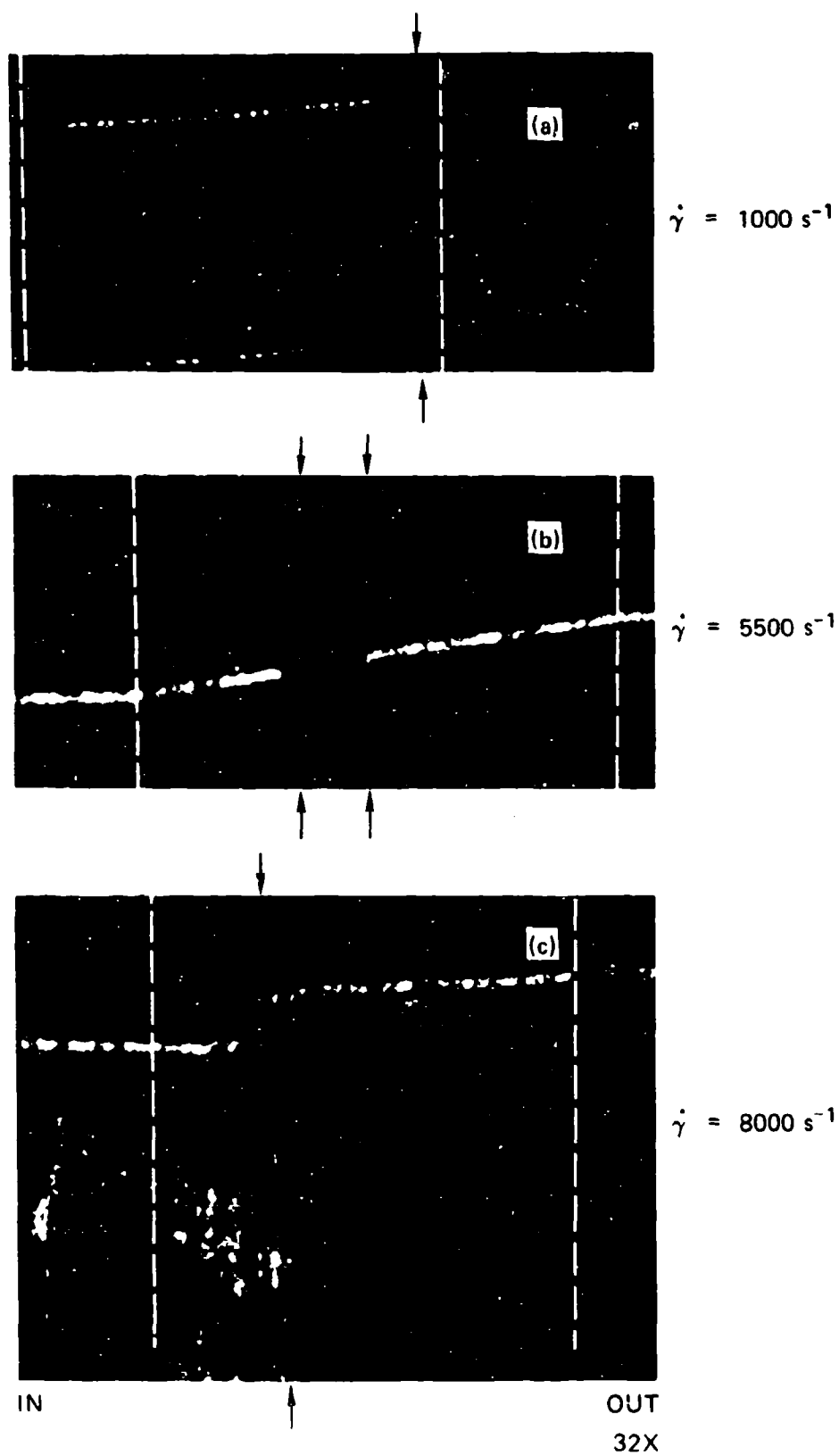
(a) $\dot{\gamma} = 1000 \text{ s}^{-1}$, (b) $\dot{\gamma} = 4000 \text{ s}^{-1}$, (c) $\dot{\gamma} = 5500 \text{ s}^{-1}$,
 (d) $\dot{\gamma} = 8000 \text{ s}^{-1}$



JA-3722-97

FIGURE III.8 STRESS-STRAIN CURVE FOR 4340 VAR R_C 40
 FOR FOUR STRAIN RATES (Concluded)

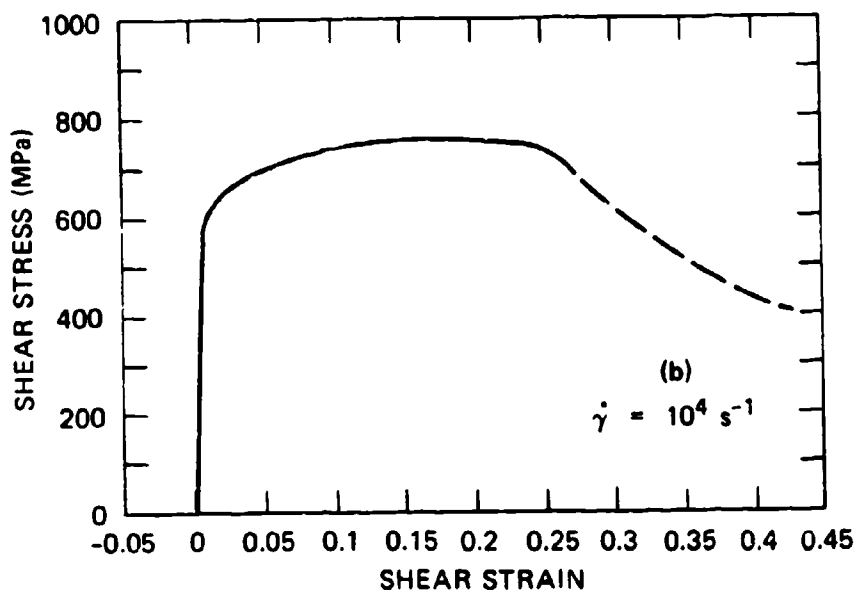
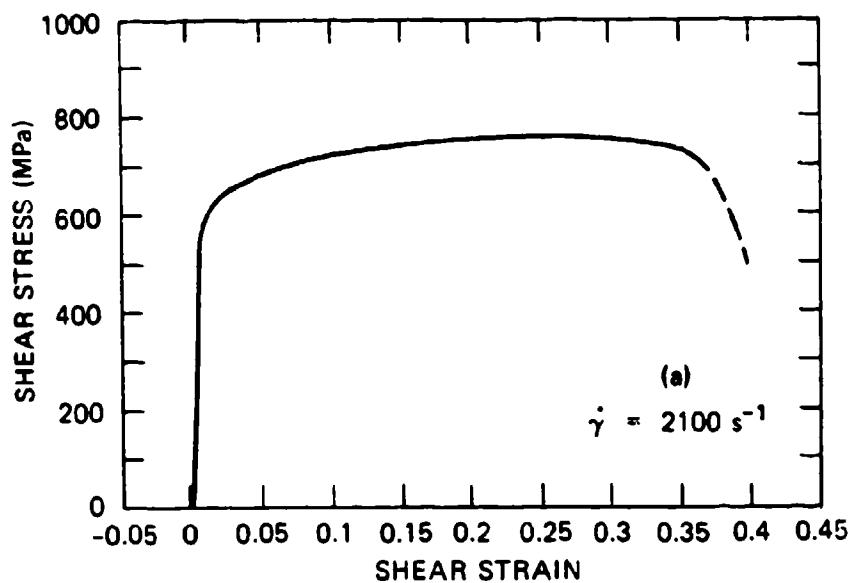
(a) $\dot{\gamma} = 1000 \text{ s}^{-1}$, (b) $\dot{\gamma} = 4000 \text{ s}^{-1}$, (c) $\dot{\gamma} = 5500 \text{ s}^{-1}$,
 (d) $\dot{\gamma} = 8000 \text{ s}^{-1}$



JP-3722-98

FIGURE III.9 CIRCUMFERENTIAL DISPLACEMENT PROFILE
ACROSS THE R_c40 SPECIMEN WIDTH FOR TESTS
AT THREE STRAIN RATES

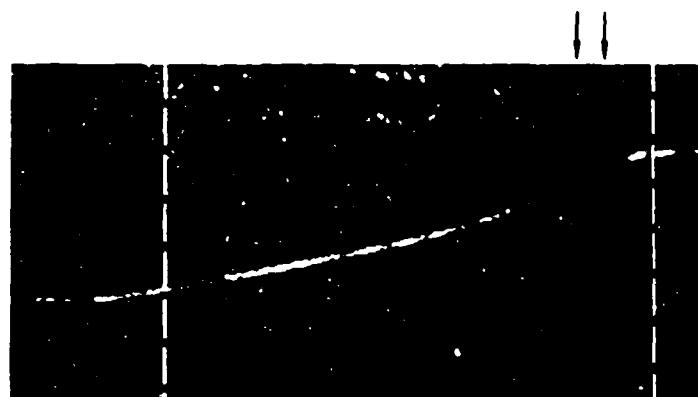
(a) $\dot{\gamma} = 1000 \text{ s}^{-1}$, (b) $\dot{\gamma} = 5500 \text{ s}^{-1}$, (c) $\dot{\gamma} = 8000 \text{ s}^{-1}$



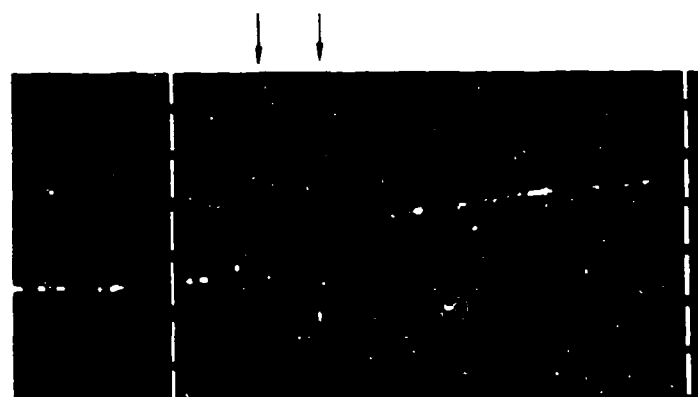
JA-3722-99

FIGURE III.10 STRESS-STRAIN CURVE FOR 4340 VAR R_C 33
AT TWO STRAIN RATES

(a) $\dot{\gamma} = 2100 \text{ s}^{-1}$, (b) $\dot{\gamma} = 10,000 \text{ s}^{-1}$



(a) $\dot{\gamma} = 2100 \text{ s}^{-1}$



IN

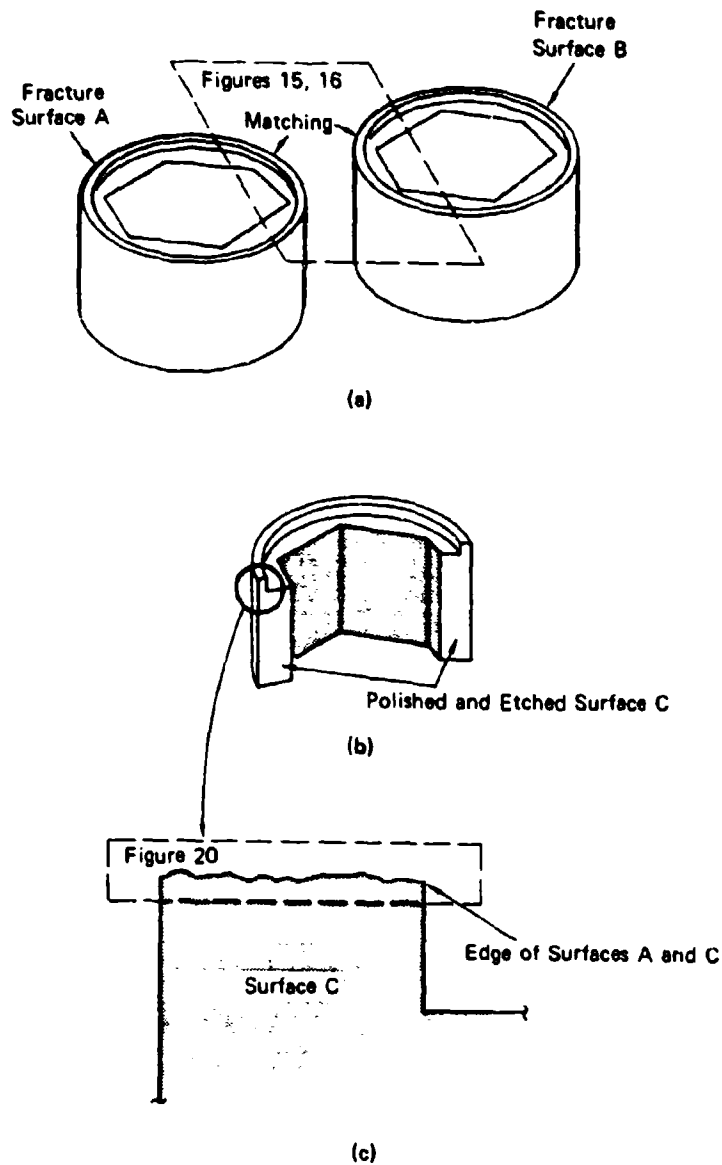
OUT
32X

(b) $\dot{\gamma} = 10,000 \text{ s}^{-1}$

JP-3722-100

FIGURE III.11 CIRCUMFERENTIAL DISPLACEMENT PROFILE
ACROSS THE R_{C33} SPECIMEN WIDTH FOR TESTS
AT TWO STRAIN RATES

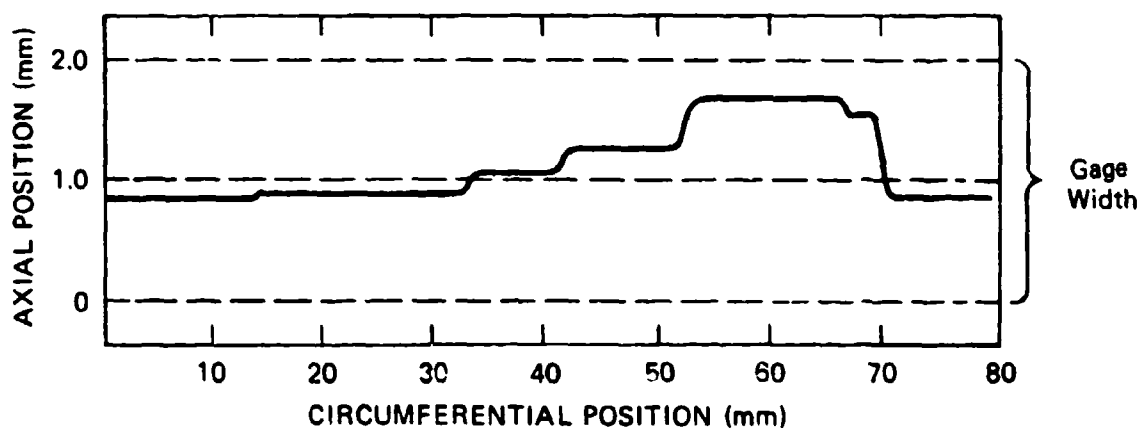
(a) $\dot{\gamma} = 2100 \text{ s}^{-1}$, (b) $\dot{\gamma} = 10,000 \text{ s}^{-1}$



JA-3722-101

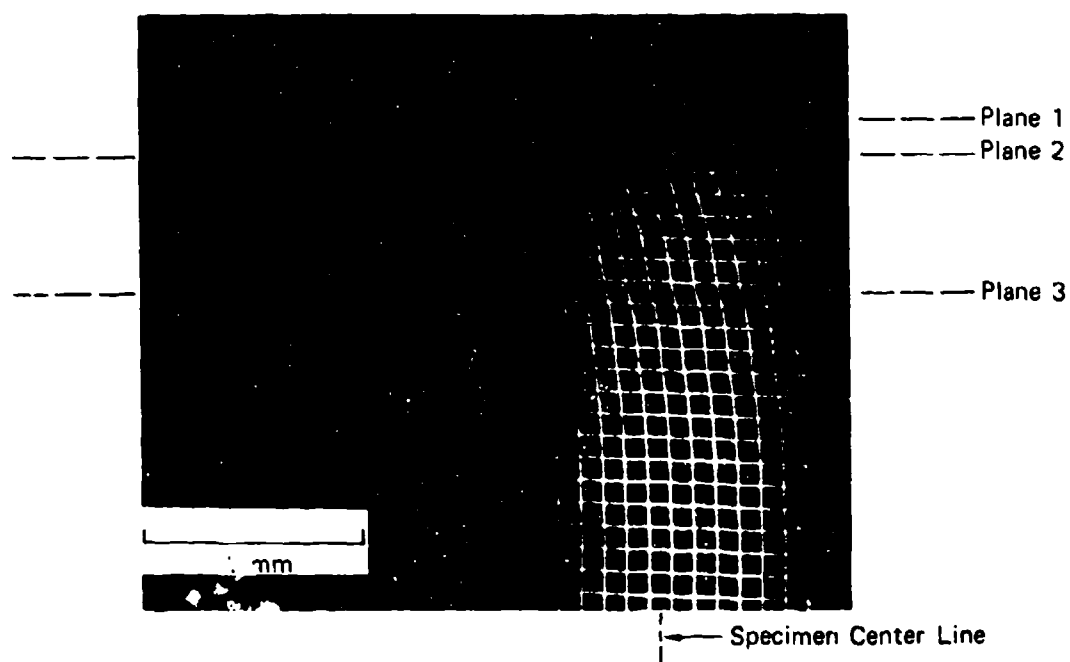
FIGURE III.12 PROCEDURE FOR METALLOGRAPHIC OBSERVATION OF SHEAR SPECIMENS

(a) Mapping of failure path, matching of two fracture surfaces, light and scanning electron microscopy, (b) sectioning, polishing, and etching, (c) observation of edge of fracture surface.



JA-3722-102

FIGURE III.13 MAP OF CRACK PATH IN SPECIMEN NT9



JA-3722-103

FIGURE III.14 PHOTOGRAPH OF CIRCUMFERENTIAL EDGE
OF FRACTURE SURFACE IN SPECIMEN NT9

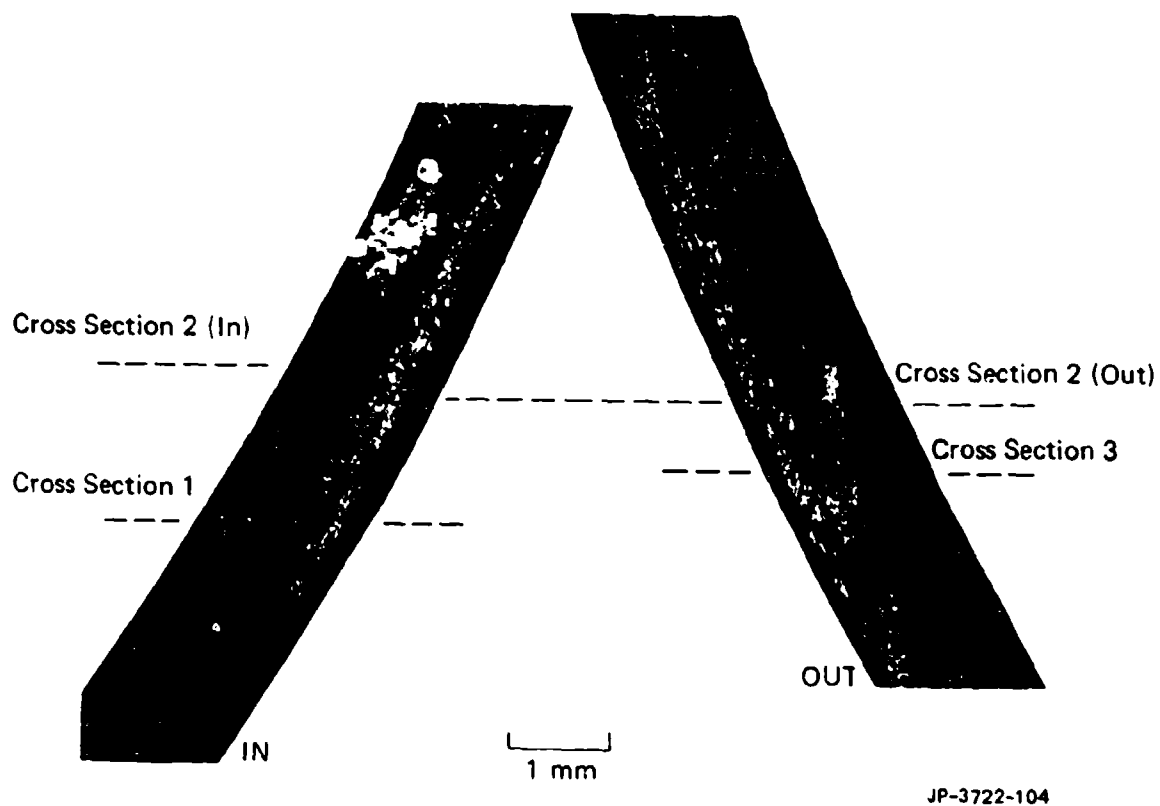
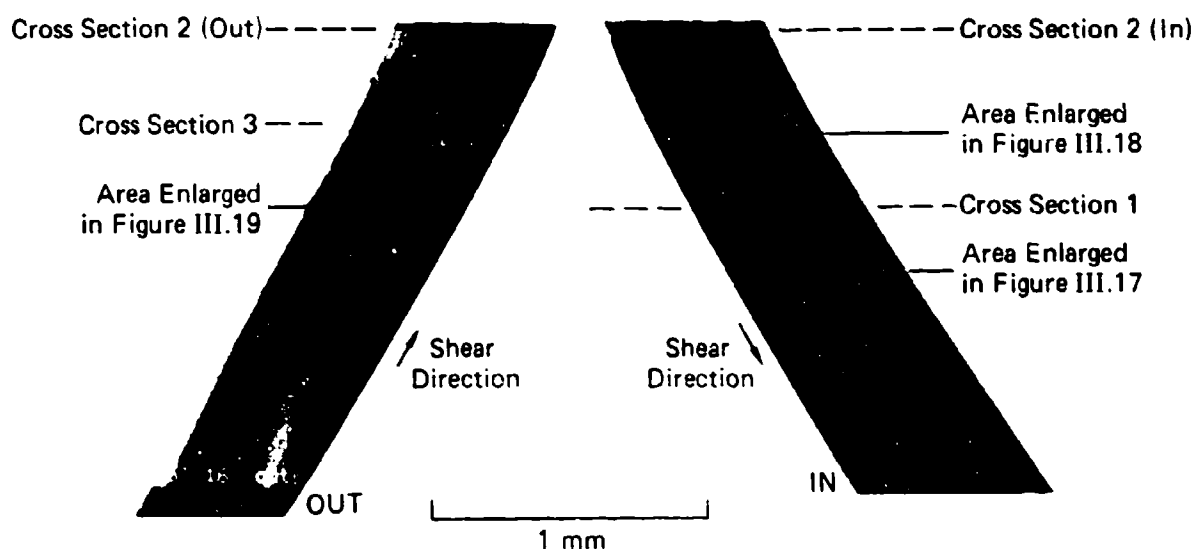
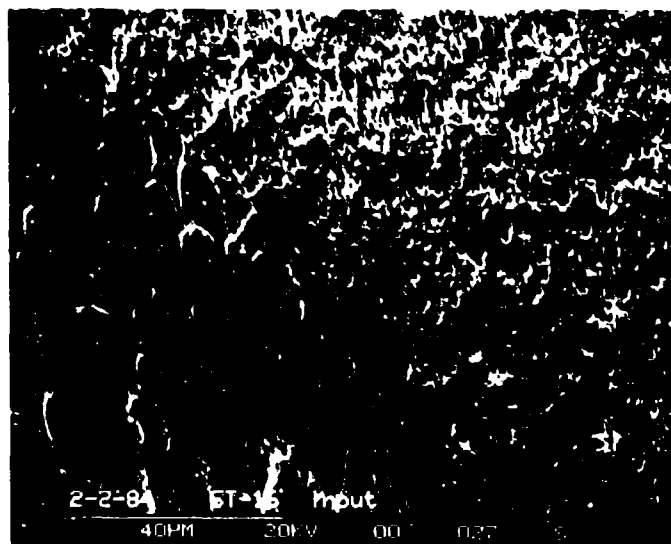


FIGURE III.15 OPTICAL MICROGRAPHS OF MATCHING SEGMENTS OF THE TWO FRACTURE SURFACES OF SPECIMEN ST16



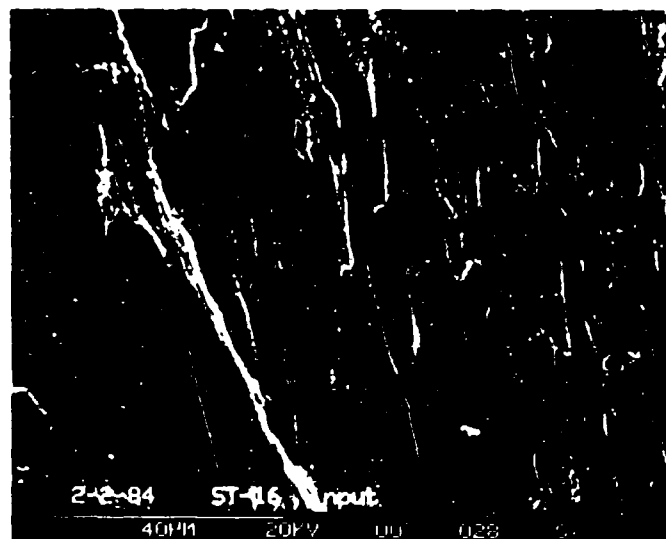
JP-3722-105

FIGURE III.16 ELECTRON MICROGRAPH OF MATCHING SEGMENTS OF THE TWO FRACTURE SURFACES OF SPECIMEN ST16 (AREA SHOWN CORRESPONDS TO AREA IN FIGURE III.15)



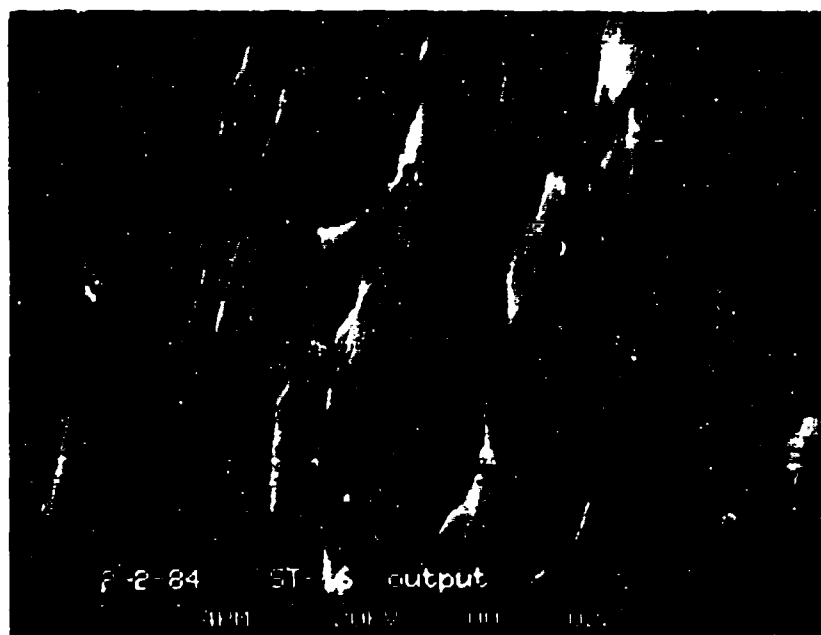
JP-3722-106

FIGURE III.17 ELECTRON MICROGRAPH OF SHEAR FRACTURE SURFACE IN SPECIMEN ST16, SHOWING SMEARED AREA AND DIMPLE AREA (SEE FIGURE III.16 FOR LOCATION)



JP-3722-107

FIGURE III.18 ELECTRON MICROGRAPH OF SHEAR FRACTURE SURFACE SHOWING SMEARED AREA AND CHANGES IN THE LOCAL FLOW DIRECTION (SEE FIGURE III.16 FOR LOCATION)



JP-3722-108

FIGURE III.19 HIGH MAGNIFICATION ELECTRON MICROGRAPH OF ELONGATED DIMPLE AREA; ARROWS POINT TO CARBIDE PARTICLES (SEE FIGURE III.16 FOR LOCATION)



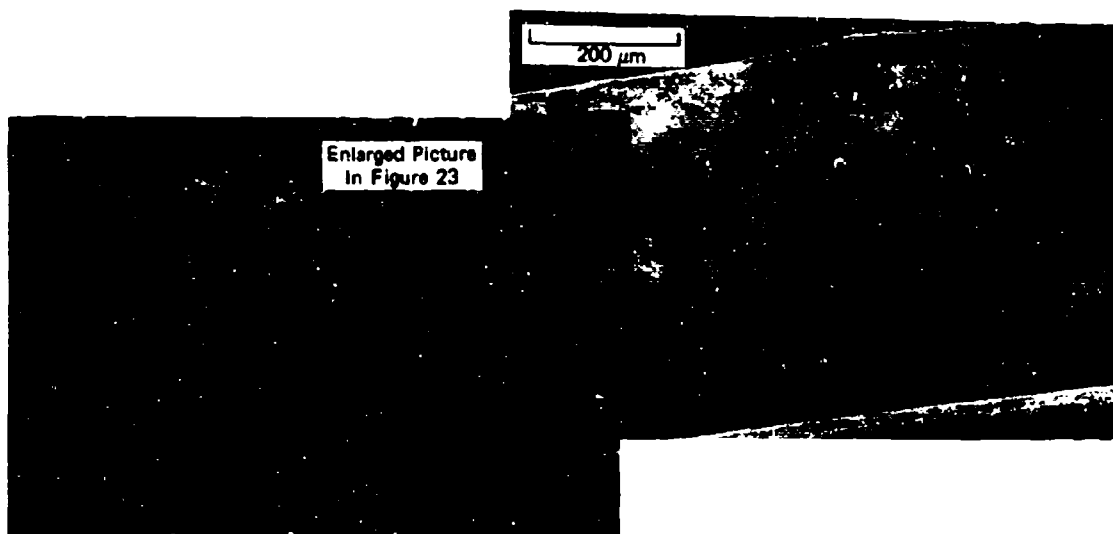
J8-3722-109

FIGURE III 20 POLISHED AND ETCHED CROSS-
SECTIONS OF SPECIMEN ST16
SHOWING FINE MICROSTRUC-
TURE AND WHITE ETCHING
MICROSTRUCTURE (SEE
FIGURE III 16 FOR LOCATION
OF CROSS-SECTION)



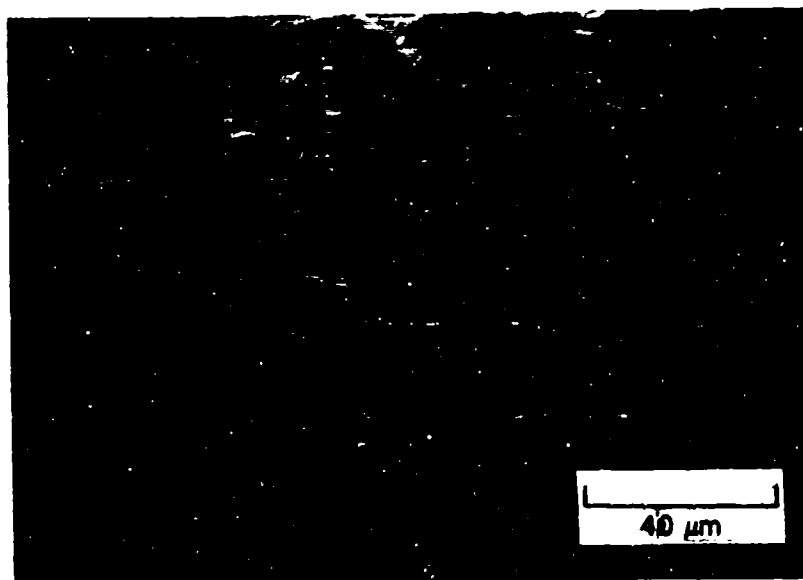
J8-3722-111

FIGURE III 21 OPTICAL MICROGRAPH OF
MATCHING SEGMENTS OF
THE TWO FRACTURE
SURFACES OF SPECIMEN
NT9



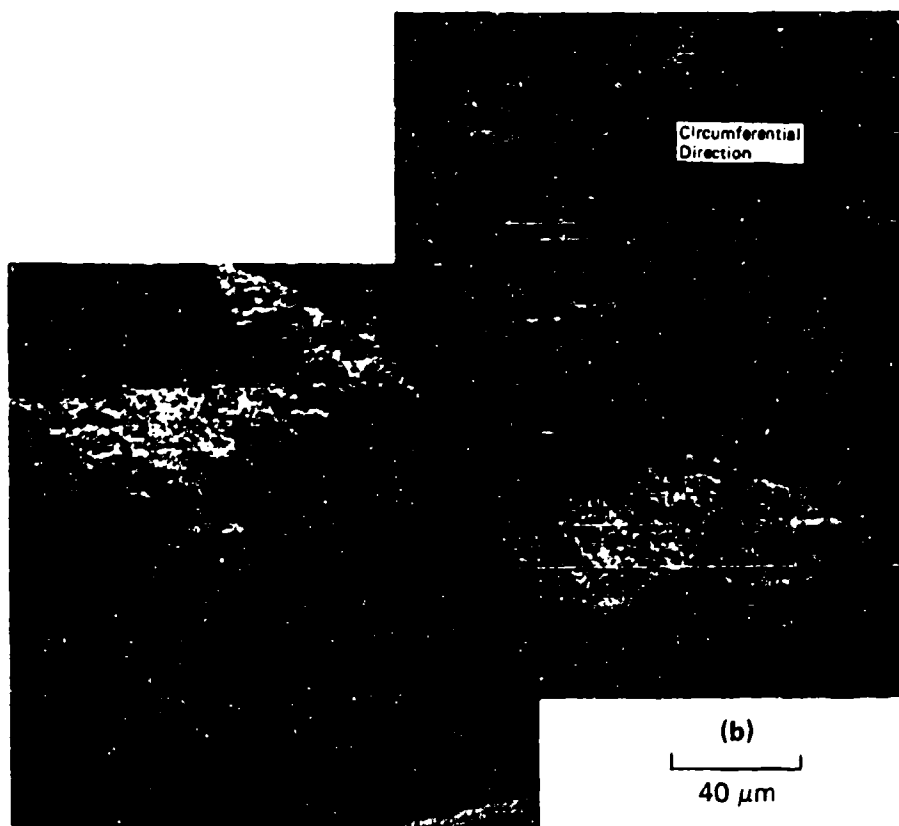
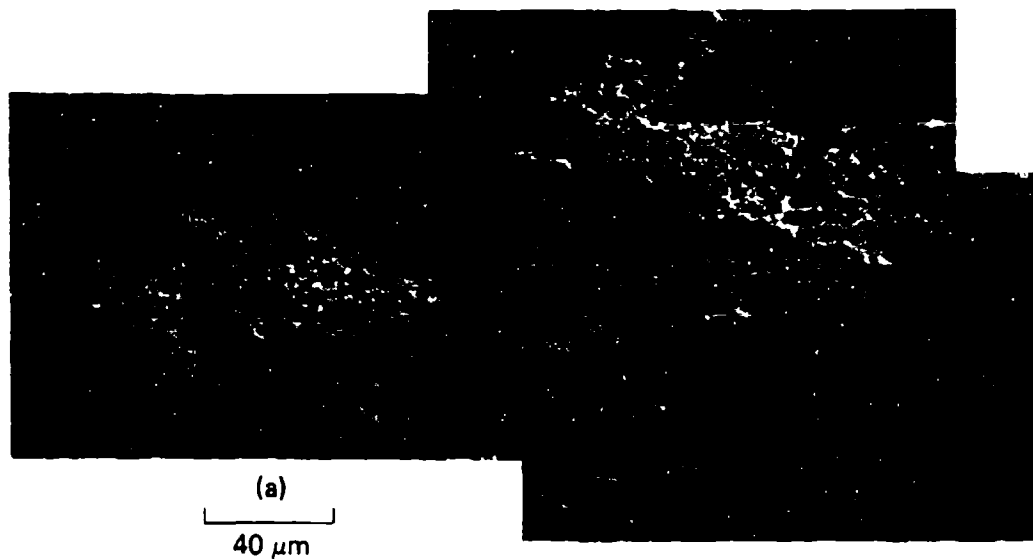
JP-3722-111

FIGURE III.22 ELECTRON MICROGRAPH OF SHEAR FRACTURE SURFACE
OF SPECIMEN NT9 (SEE FIGURE III.21 FOR LOCATION)



JP-3722-112

FIGURE III.23 ELECTRON MICROGRAPH OF SHEAR FRACTURE
SURFACE OF SPECIMEN NT9 SHOWING PARTIALLY
SMEARED DIMPLE AREA (SEE FIGURE III.22
FOR LOCATION)



JP-3722-113

FIGURE III.24 ELECTRON MICROGRAPH OF MATCHING DETAILS OF THE SHEAR FRACTURE SURFACES OF SPECIMEN NT9

(a) Input half, (b) output half with outline of dimple area in (a) superimposed.

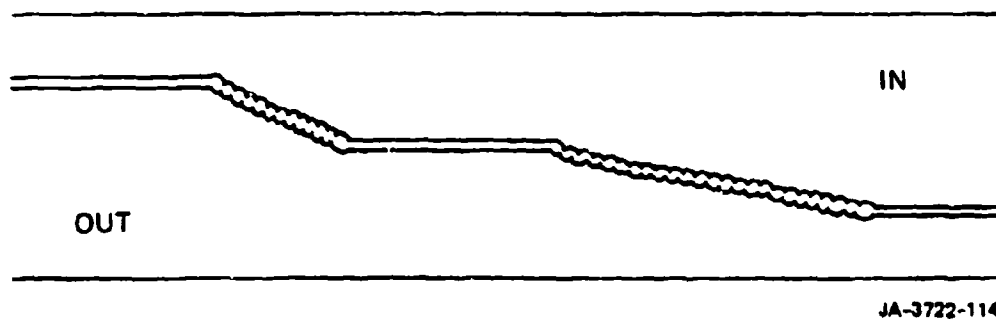
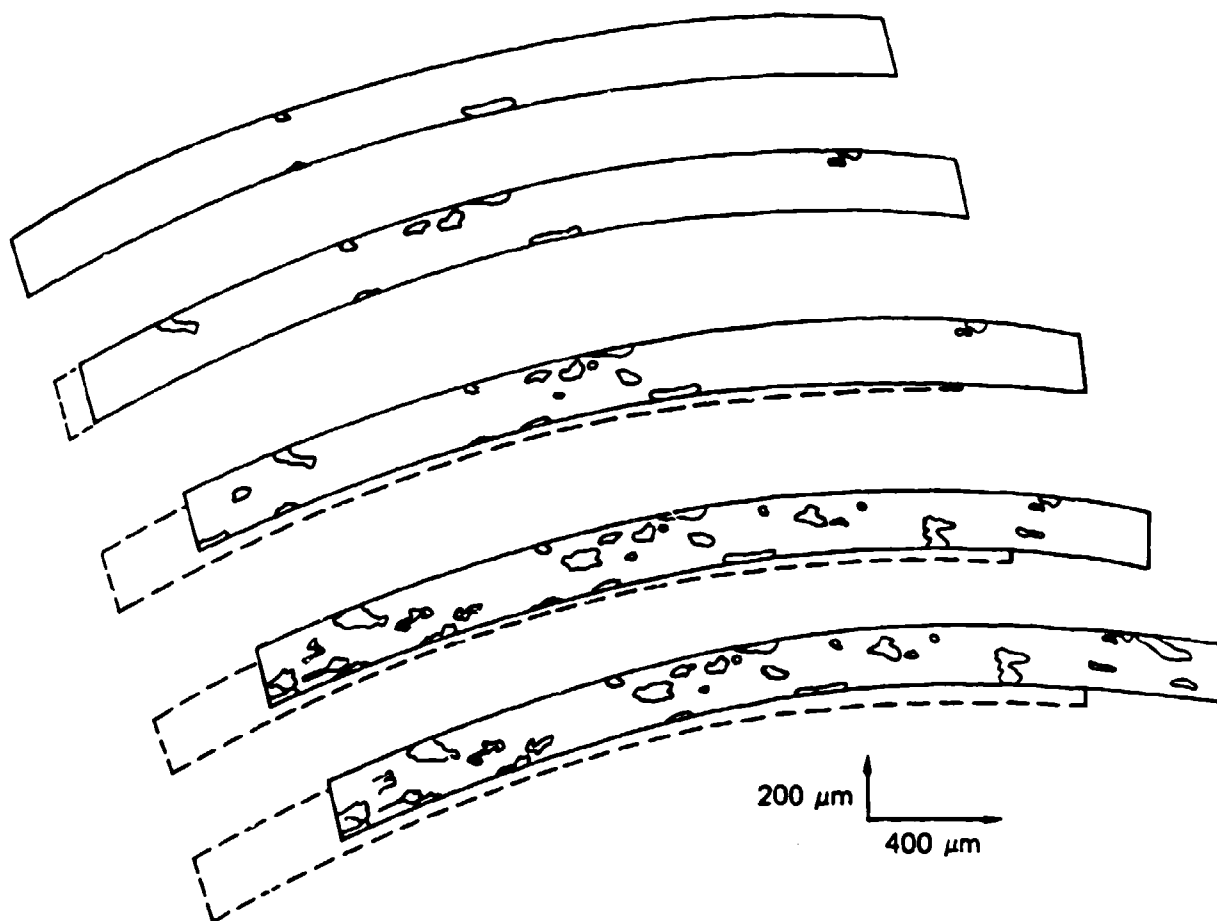
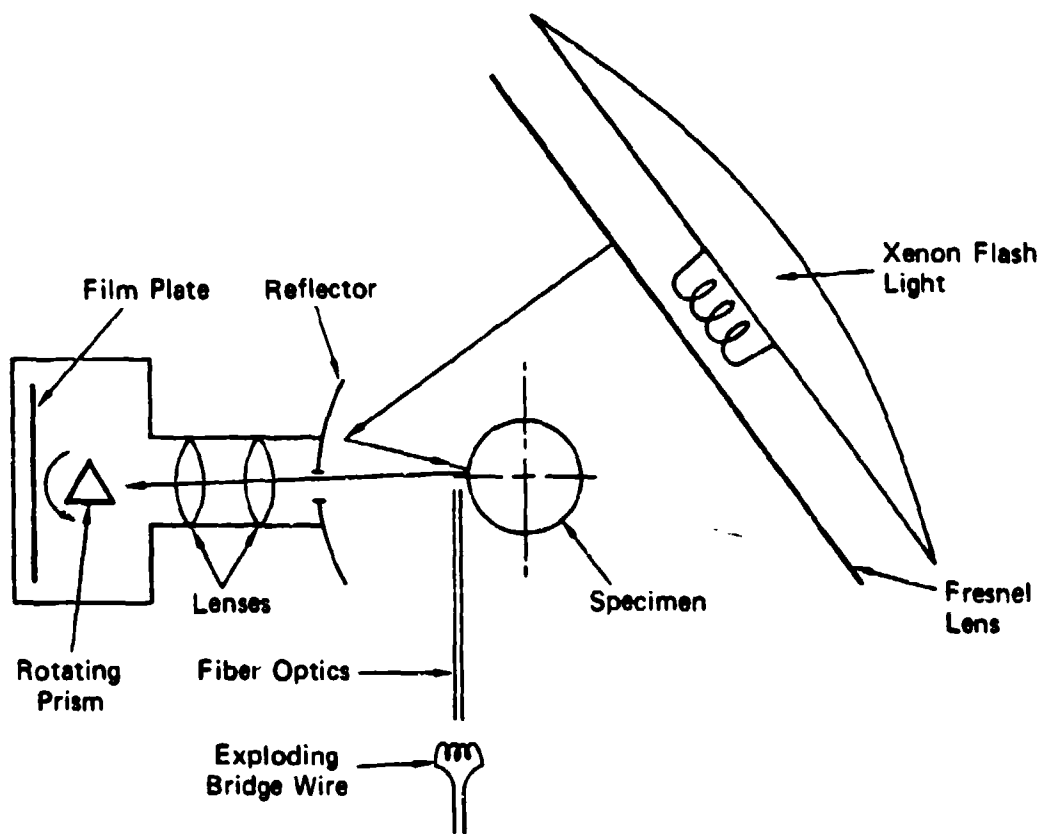


FIGURE III.25 SCHEMATIC OF CROSS SECTION ALONG DASHED LINE
IN FIGURE III.24b



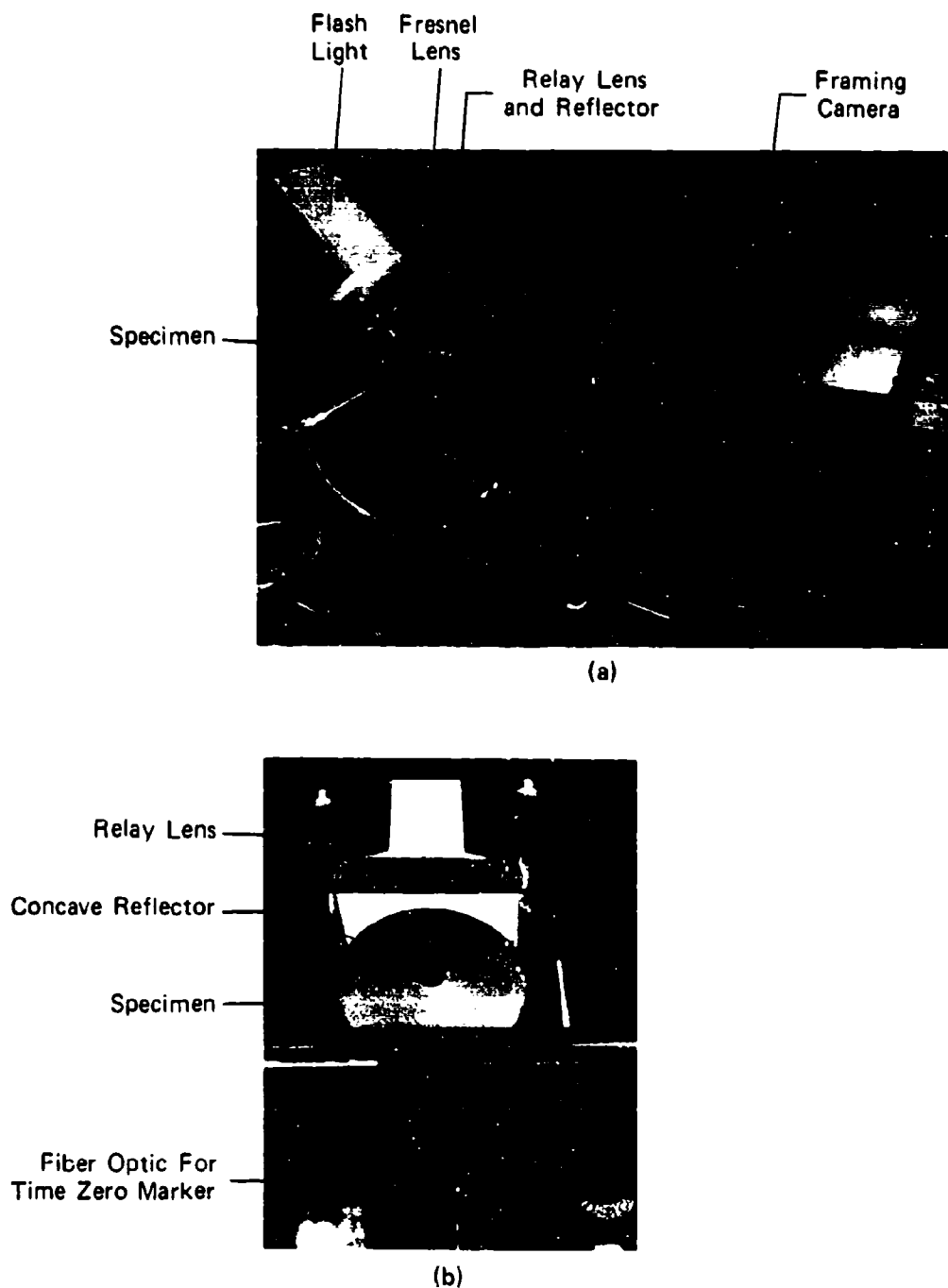
JA-3722-115

**FIGURE III.26 SEQUENCE OF FAILURE OF UNBROKEN LIGAMENTS WITH INCREASING
RELATIVE DISPLACEMENT OF TWO SPECIMEN HALVES (DISPLACEMENTS
DRAWN TO A DIFFERENT SCALE THAN FRACTURE SURFACE) SPECIMEN
NT9**



JA-3722-116

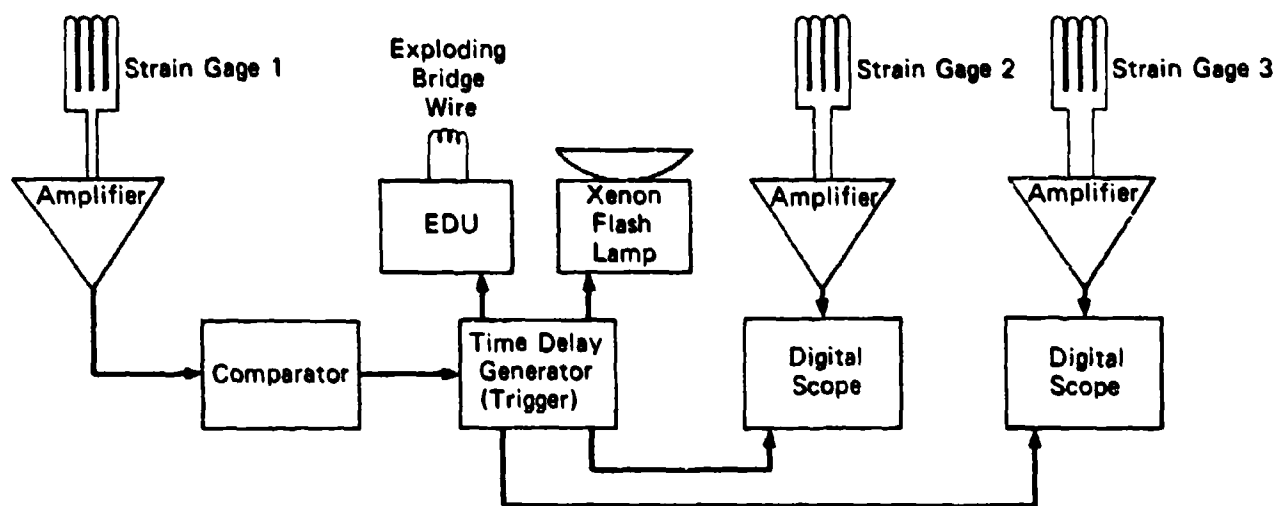
FIGURE III.27 SCHEMATIC OF EXPERIMENTAL ARRANGEMENT FOR OPTICAL STRAIN MEASUREMENTS



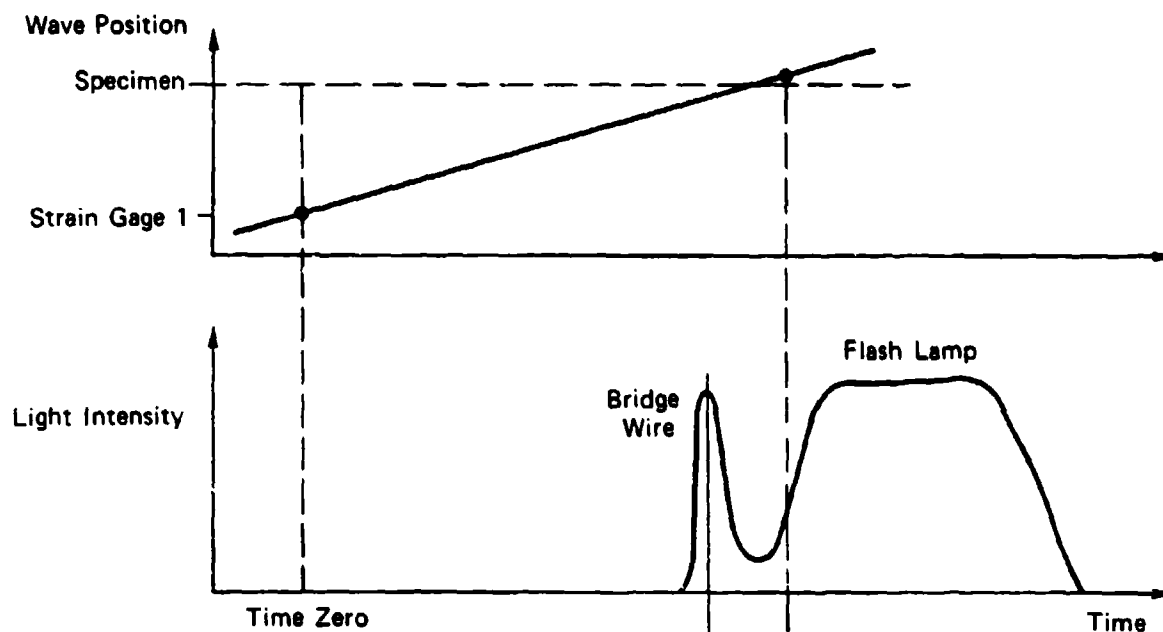
JP-3722-117

FIGURE III.28 PHOTOGRAPH OF EXPERIMENTAL ARRANGEMENT FOR OPTICAL STRAIN MEASUREMENTS

(a) Overall view, (b) detail view showing specimen and reflector.



(a)

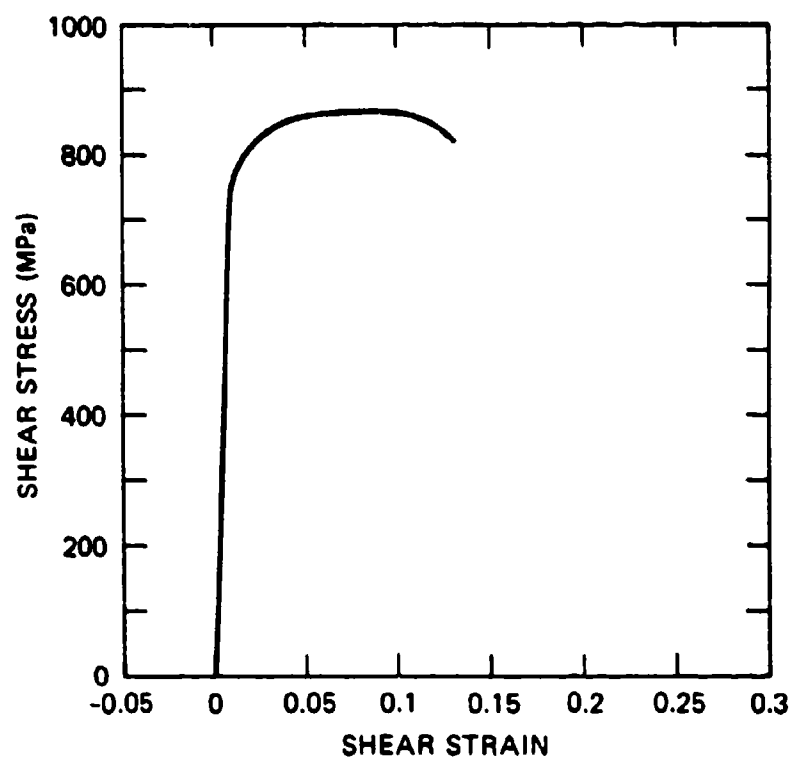


(b)

JA-3722-118

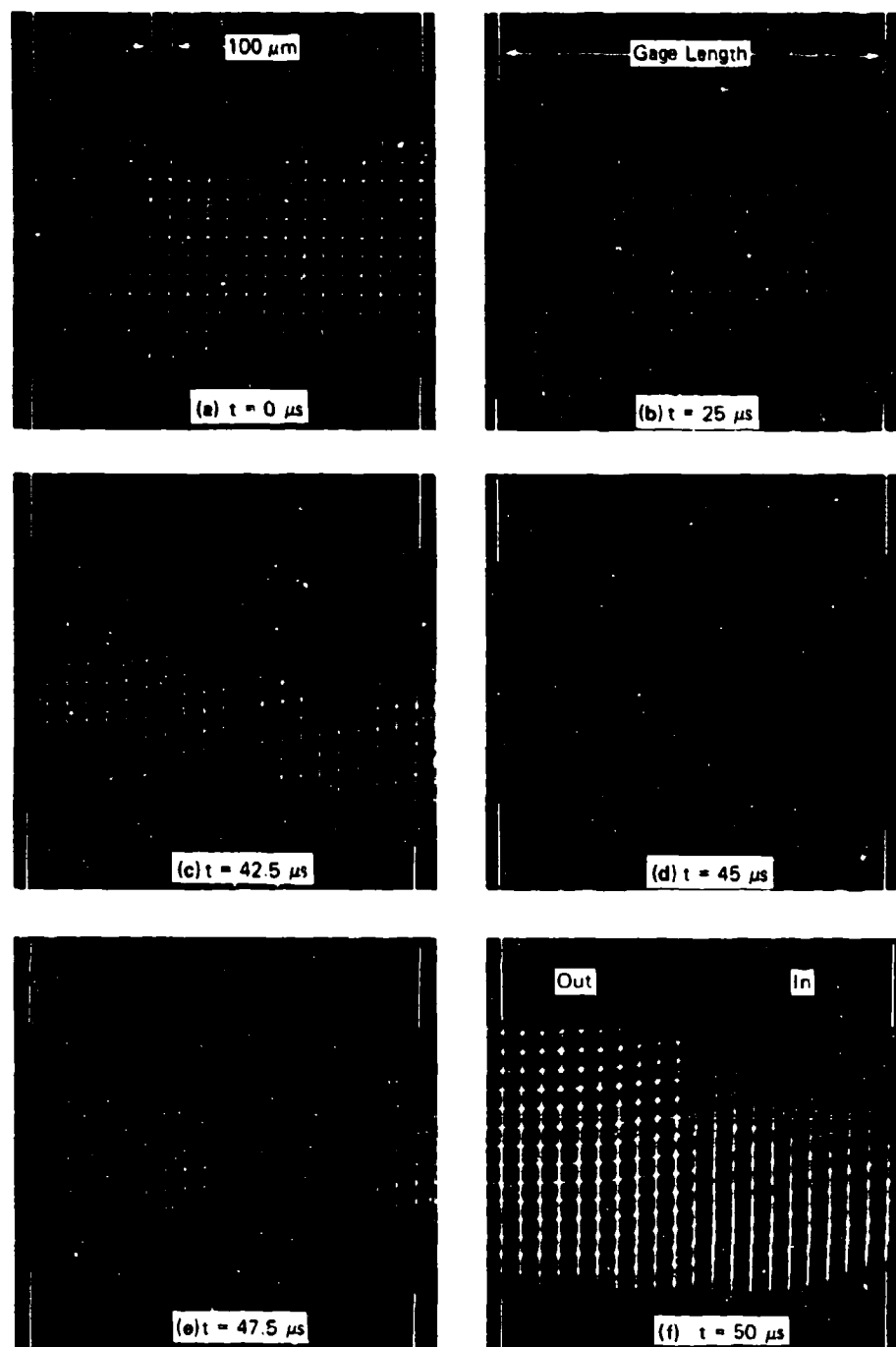
FIGURE III.29 SYNCHRONIZATION OF STRAIN GAGE RECORDS AND HIGH-SPEED PHOTOGRAPHY

(a) trigger circuit, (b) time sequence of events.



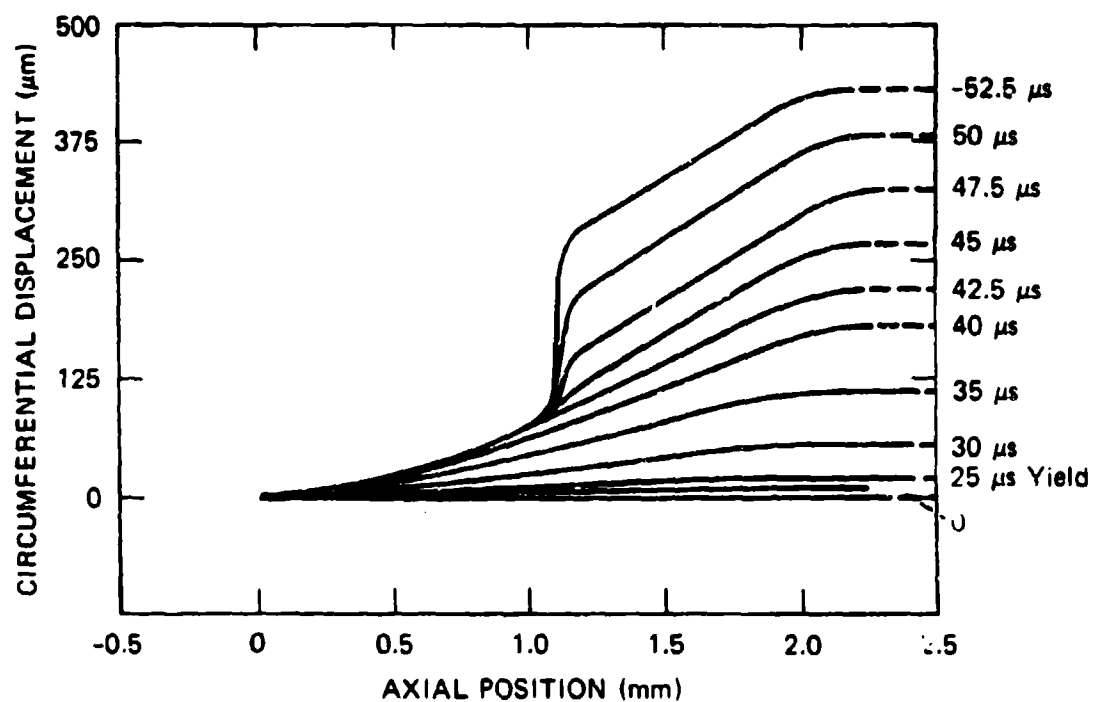
JA-3722-119

FIGURE III.30 STRESS-STRAIN CURVE FOR TEST NT9



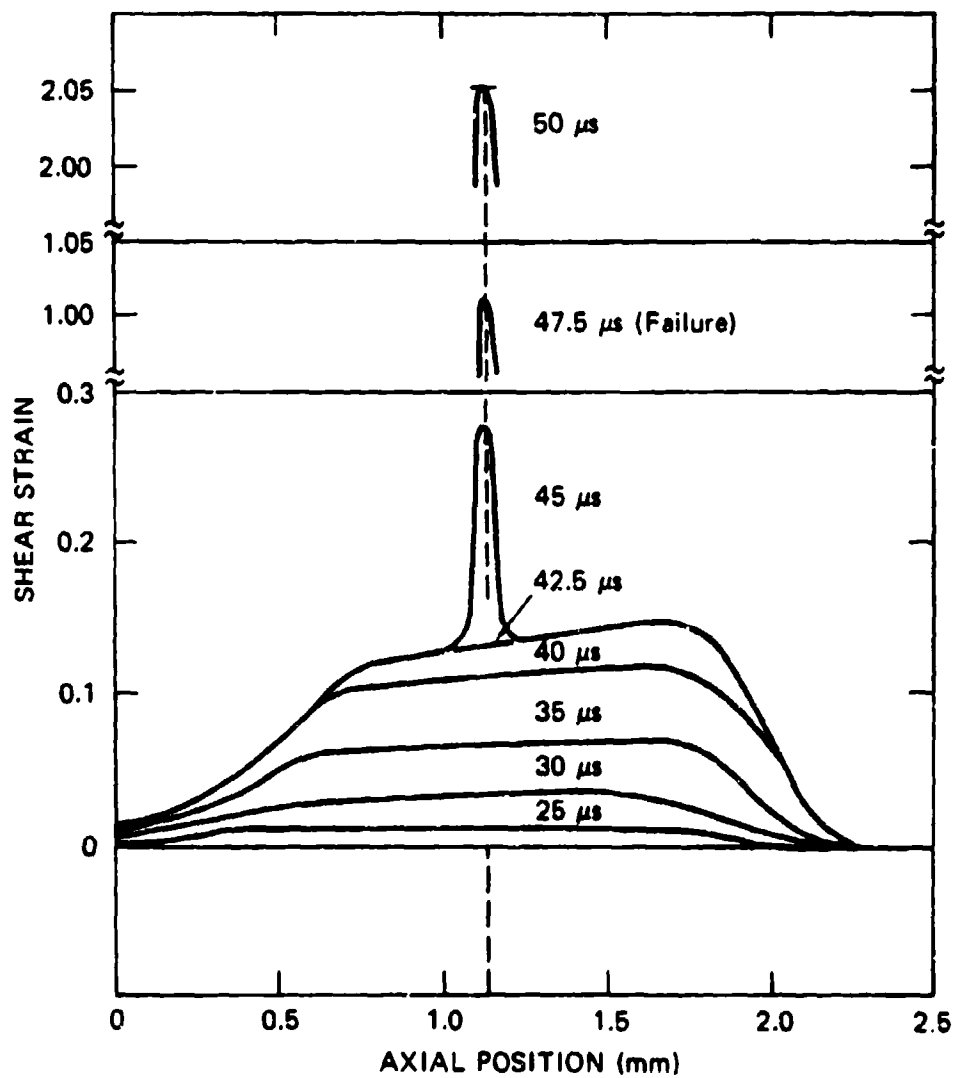
JP-2777-29

FIGURE III.31 TIME SEQUENCE PHOTOGRAPHS FOR TEST NT9



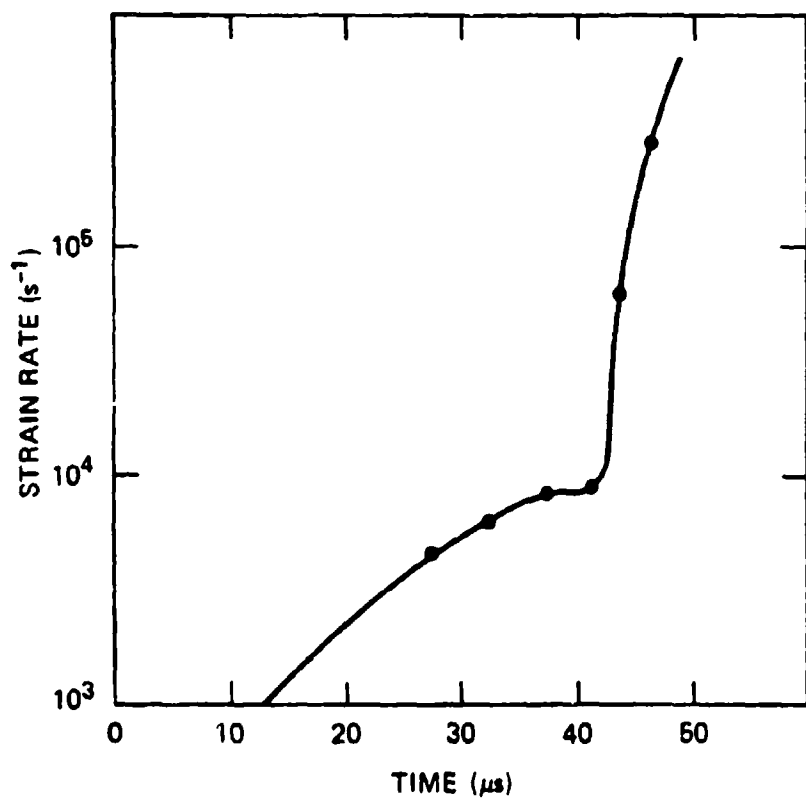
JA-3722-121

FIGURE III.32 DEFORMATION PROFILES AT DIFFERENT TIMES OBTAINED FROM HIGH-SPEED PHOTOGRAPHS OF TEST NT9



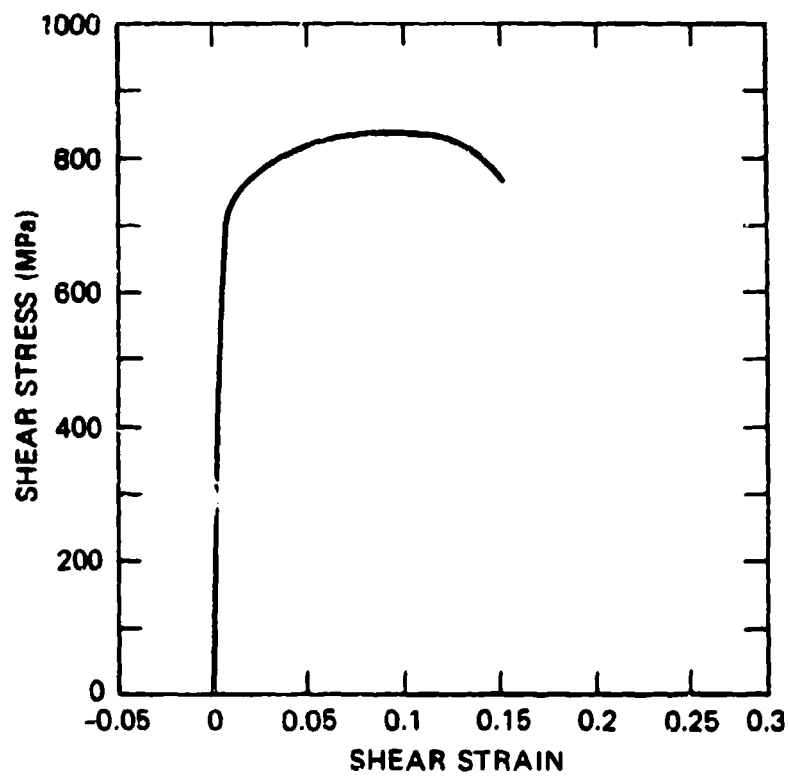
JA-3722-122

FIGURE III.33 STRAIN PROFILES AT DIFFERENT TIMES OBTAINED FROM DEFORMATION PROFILES IN FIGURE III.32 FOR TEST NT9



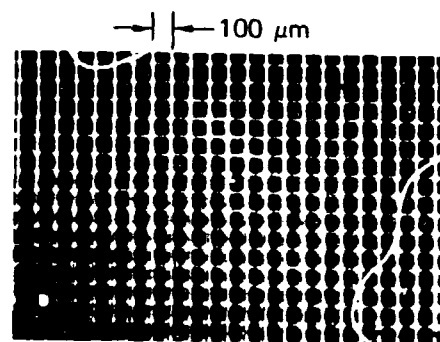
JA-3722-123

FIGURE III.34 STRAIN RATE AS A FUNCTION OF TIME
AT THE SHEAR BAND LOCATION FOR
TEST NT9

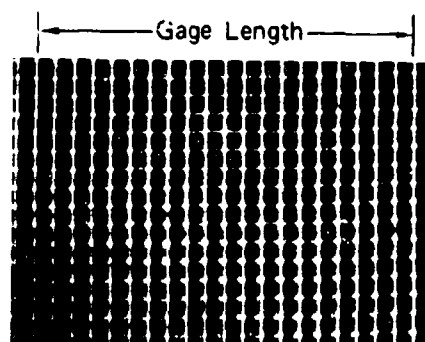


JA-3722-124

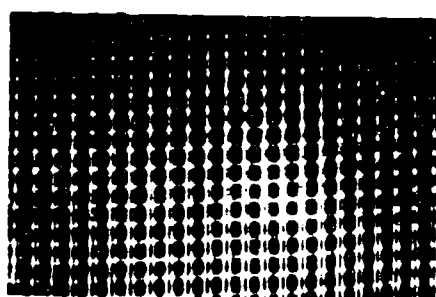
FIGURE III.35 STRESS-STRAIN CURVE FOR TEST NT6



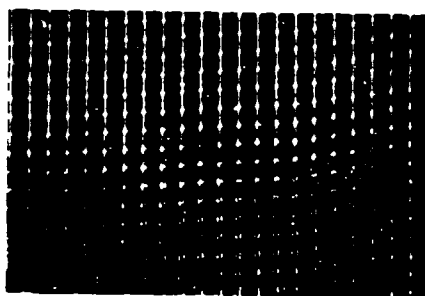
(a) $t = 0$ (Yield)



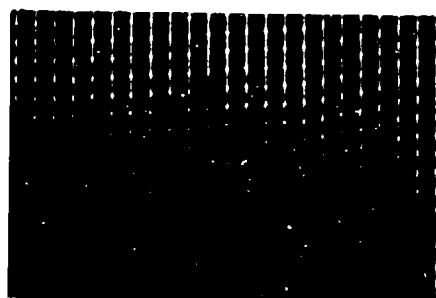
(b) $t = 12 \mu s$



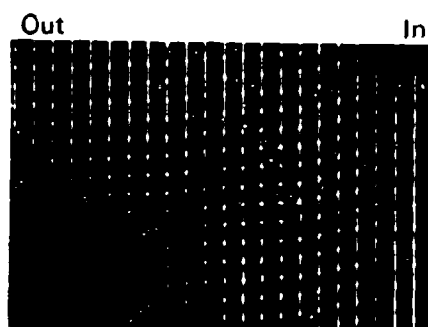
(c) $t = 18 \mu s$



(d) $t = 24 \mu s$



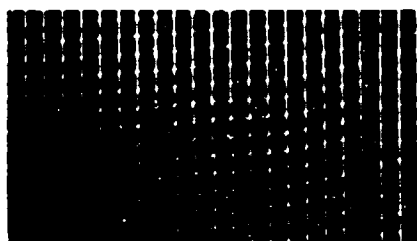
(e) $t = 30 \mu s$



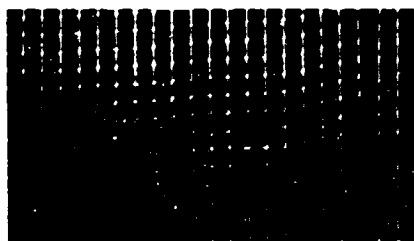
(f) $t = 33 \mu s$ (Failure)

JP-3722-125

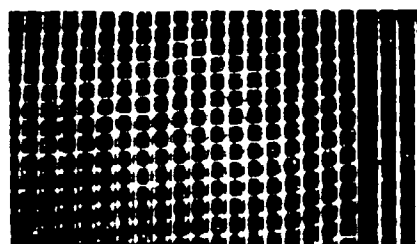
FIGURE III.36 TIME SEQUENCE PHOTOGRAPHS FOR TEST NT6



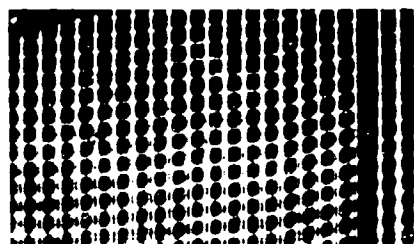
(g) $t = 36 \mu s$



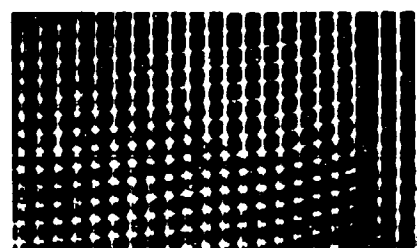
(h) $t = 42 \mu s$



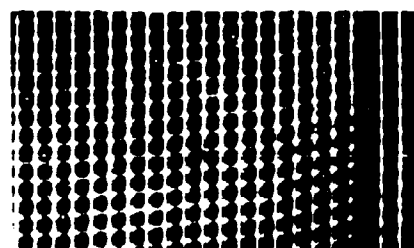
(i) $t = 54 \mu s$



(j) $t = 60 \mu s$



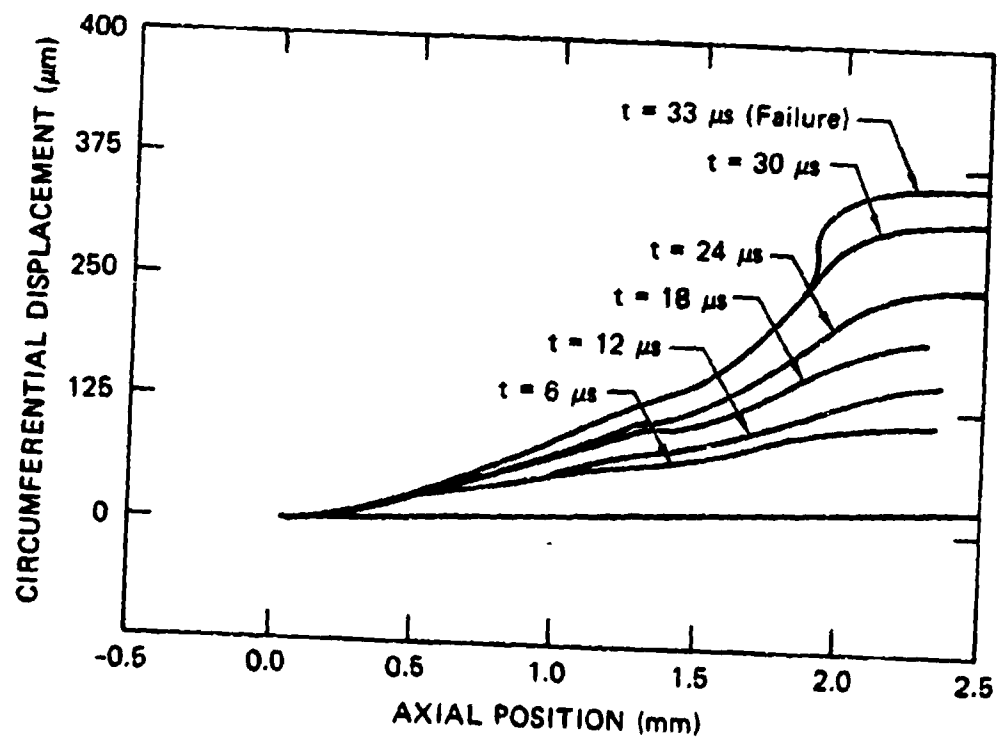
(k) $t = 63 \mu s$



(l) $t = 66 \mu s$

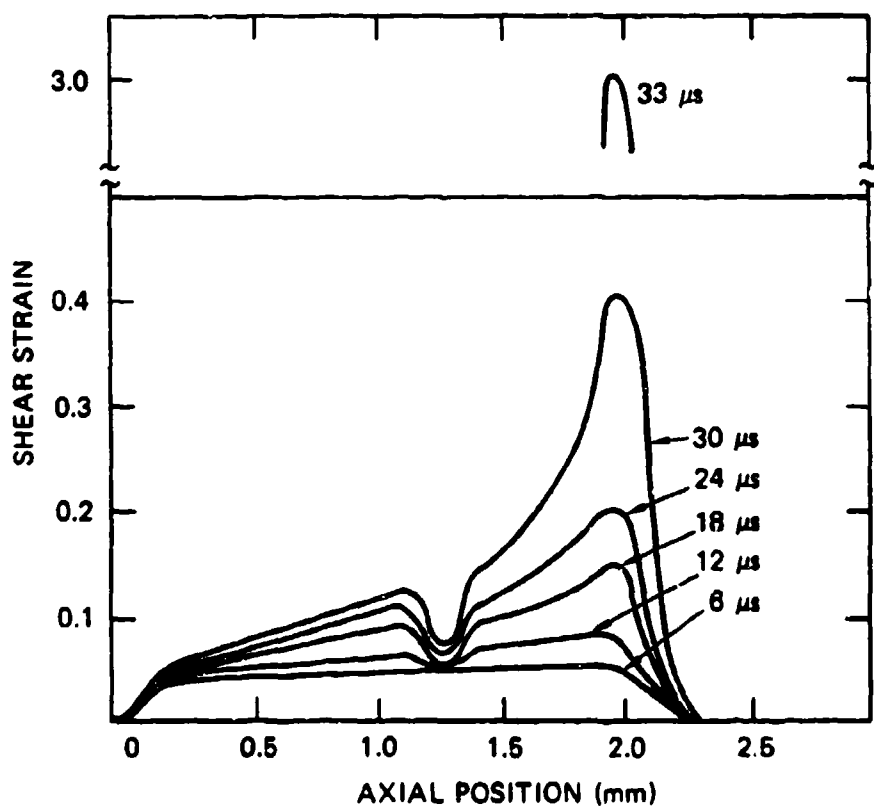
JP-3722-128

FIGURE III.36 TIME SEQUENCE PHOTOGRAPHS FOR TEST NT6 (Concluded)



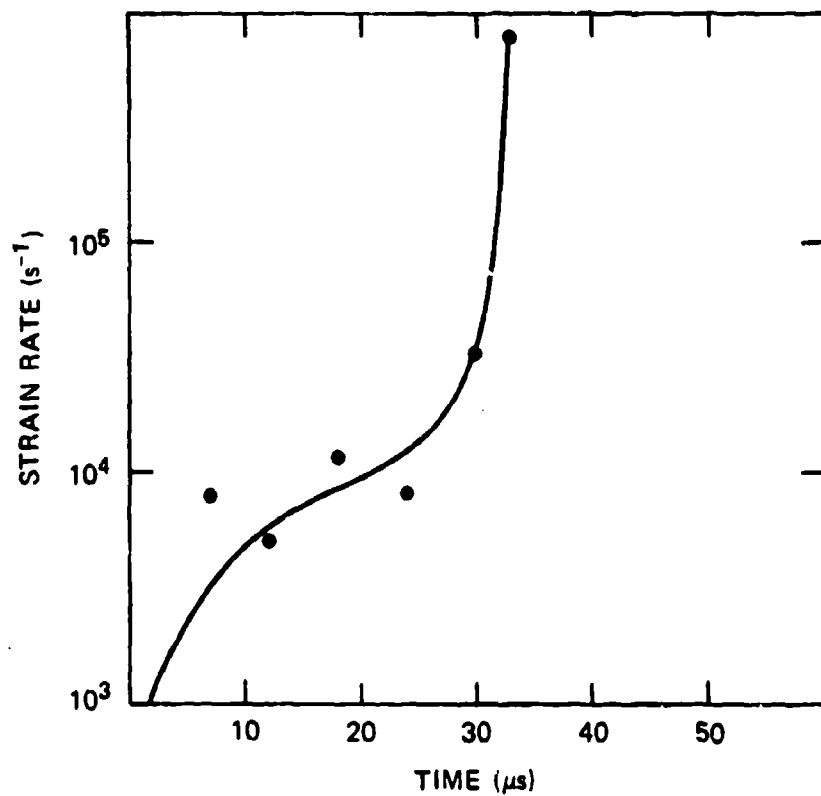
JA-3722-127

FIGURE III.37 DEFORMATION PROFILES AT DIFFERENT TIMES OBTAINED FROM HIGH-SPEED PHOTOGRAPHS OF TEST NT6



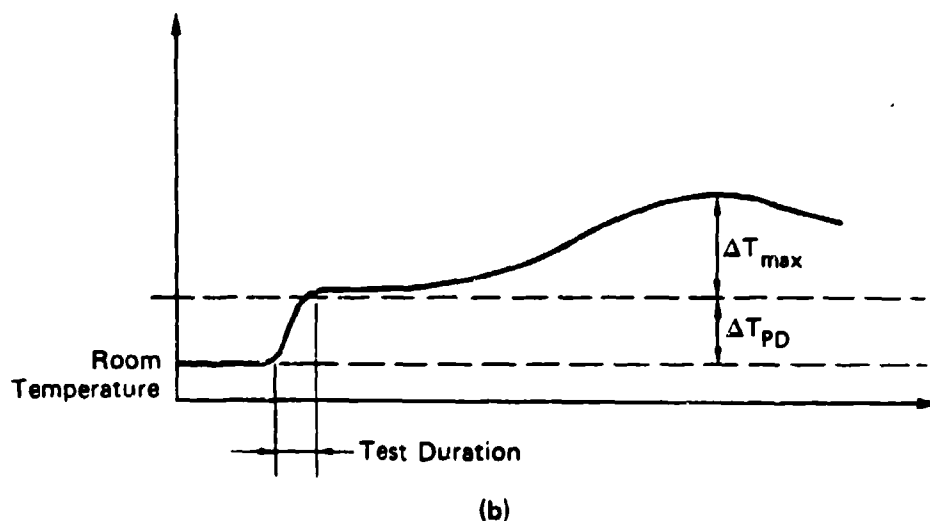
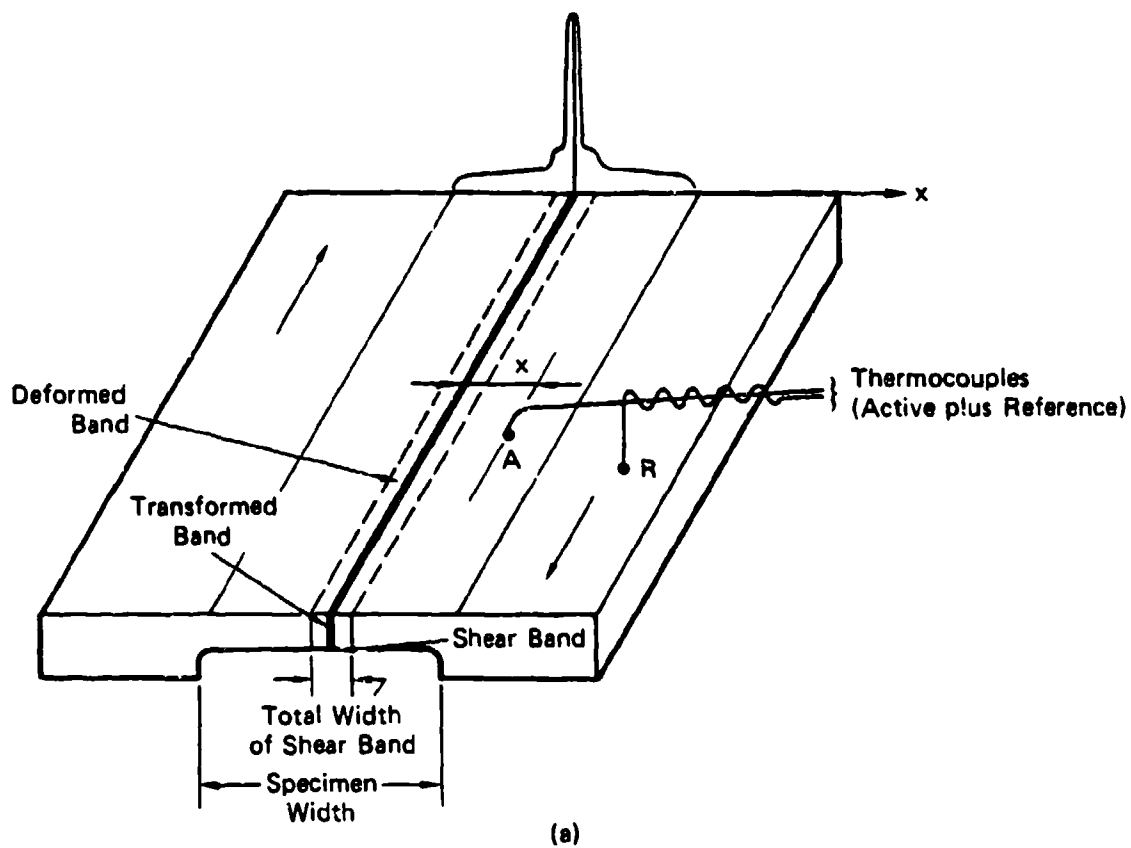
JA-3722-128

FIGURE III.38 STRAIN PROFILES AT DIFFERENT TIMES OBTAINED FROM DEFORMATION PROFILES IN FIGURE III.37 FOR TEST NT8



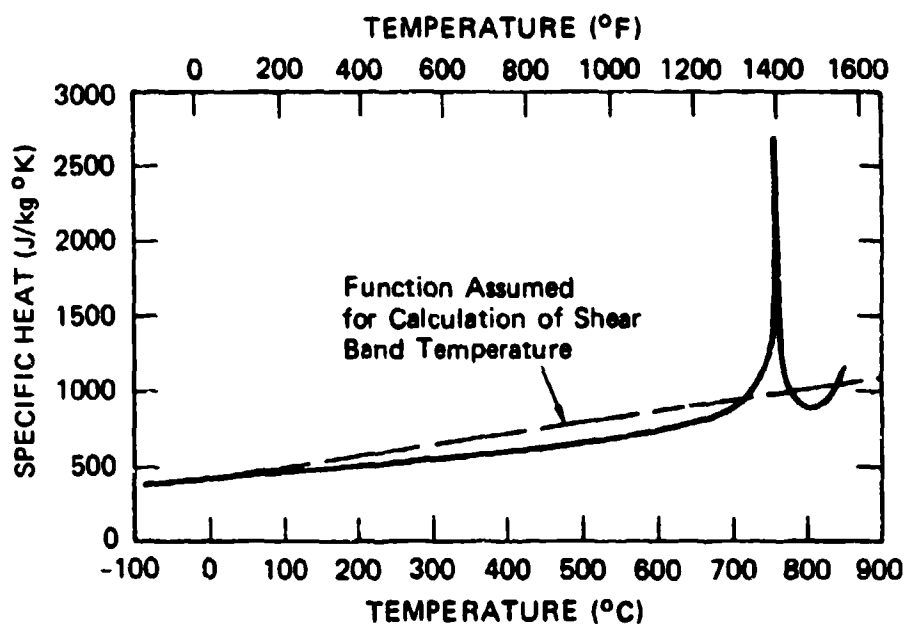
JA-3722-129

FIGURE III.39 STRAIN RATE AS A FUNCTION OF TIME
AT THE SHEAR BAND LOCATION
FOR TEST NT8



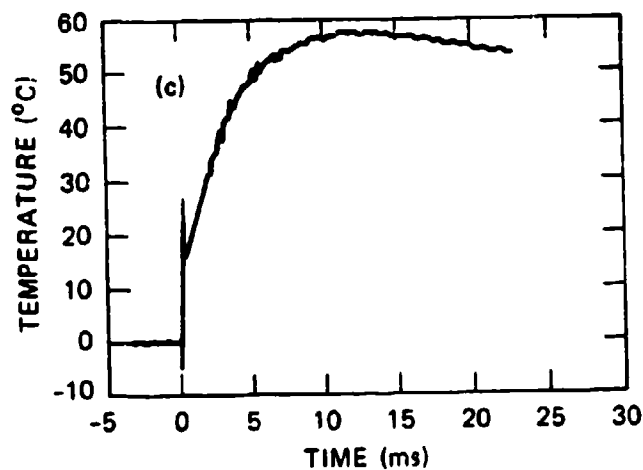
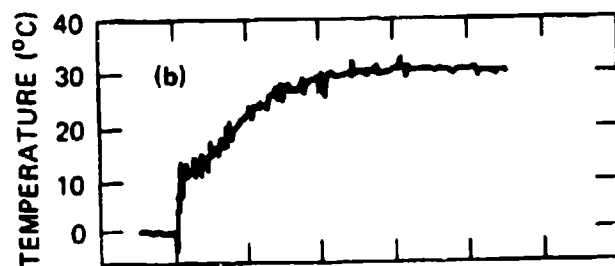
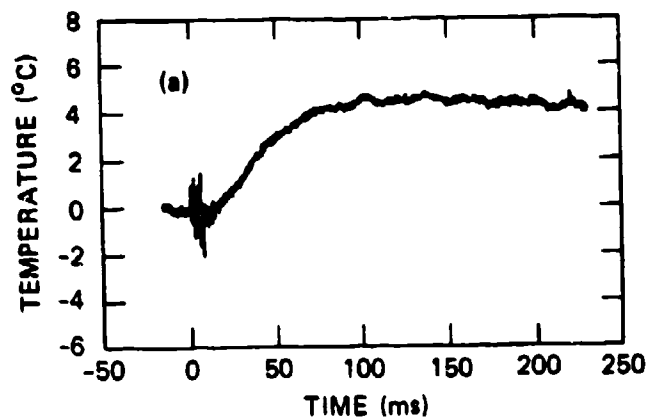
JA-3722-130

FIGURE III.40 INDIRECT SHEAR BAND TEMPERATURE MEASUREMENT
(a) principle of the technique, (b) expected temperature variation with time.



SOURCE: From ASM Metal Handbook Ninth Edition Volume 1. JA-3722-131

FIGURE III.41 SPECIFIC HEAT AS A FUNCTION OF TEMPERATURE FOR 1010 STEEL



JA-3722-132

FIGURE III.42 TEMPERATURE HISTORIES AT DIFFERENT THERMOCOUPLE LOCATIONS x IN SHTB EXPERIMENT

(a) $x = 1.69$ mm, (b) $x = 0.56$ mm, (c) $x = 0.35$ mm.

CONTENTS

IV ROD IMPACT EXPERIMENTS ON 4340 STEEL

A. Historical Perspective and Technique Development.....	IV-3
1. Classic Taylor Test.....	IV-3
2. Symmetric Rod Impact Test.....	IV-3
3. Recent Rod Impact Testing at Elevated Temperatures.....	IV-4
4. Development of Asymmetric Rod Impact Technique Under ARO Program.....	IV-5
B. Experimental Technique.....	IV-6
1. SRI Test at Ambient Temperature.....	IV-6
2. ASRI Test at Elevated Temperature.....	IV-8
3. Test Procedure.....	IV-8
C. Analytical Techniques.....	IV-9
1. Measurements of Rod Deformation Profiles.....	IV-9
2. Computer Simulation of Rod Impact Tests.....	IV-10
3. Constitutive Model Used in the Computer Simulations.....	IV-11
4. Considerations of Strain Rate and Temperature.....	IV-15
D. Experimental and Analytical Results of Rod Impact Tests.....	IV-17
1. Flow Curve Determination from SRI Tests at Ambient Temperatures.....	IV-17
2. Metallographic Studies of Recovered SRI Specimens.....	IV-19
3. Flow Curve Determinations from ASRI Tests.....	IV-20
E. Summary.....	IV-21
F. References.....	IV-22

IV ROD IMPACT EXPERIMENTS ON 4340 STEEL

The study and characterization of the shear banding behavior of a material requires a knowledge of the homogeneous behavior of that material before and during the shear banding process. This knowledge would help determine the deformation conditions for the onset of shear banding and the partitioning of subsequent deformation between homogeneous flow and shear band growth.

The primary goal of this phase of the ARO program was, therefore, to study the homogeneous deformation behavior of 4340 steel loaded in compression at high strain rates, large plastic strains, and over a wide range in temperature--just the conditions for which shear banding has been observed. A secondary goal was to determine the absence or presence of shear banding under loading conditions quite different from other tests (contained fragmenting cylinder tests) used in previous quantitative shear banding studies.

Determination of high strain-rate constitutive behavior of materials is by no means a routine process. The availability of experimental techniques that allow such determinations at strain rates of around 10^4 or 10^5 s^{-1} and large plastic strains of 50-150% has been extremely limited, if not nonexistent. Recently a technique called the symmetric rod impact (SRI) test, based upon the Taylor test for measuring the dynamic yield strength,¹ was developed and improved to the point where it could determine the entire stress-strain flow curve for a material loaded in compression at ambient temperature.

Our approach for this phase of the ARO program was to devise and implement a method for modifying the rod impact test capabilities to include specimens at elevated temperatures, and then to use the SRI test and the newly modified rod impact test to determine the dynamic

constitutive behavior of 4340 steel over as wide a range in temperature as possible.

In the remainder of this section, we briefly review the historical development of rod impact testing prior to the beginning of this program, describe the improvements and modifications made during this program, and then give detailed descriptions of both the experimental and analytical aspects of the technique. Finally we present the experimental data and analytical results obtained from the series of rod impact tests performed during this program. Some of these tests are referred to by a number that corresponds to the test matrix given in Table IV.1.

Table IV.1 ROD IMPACT EXPERIMENTS PERFORMED

Test No.	Specimen Material ^c	Specimen Temp. (°C)	Impact Geometry ^b	Impact Velocity (m/s)	Purpose of Test
1	HRC 38	Ambient	Sym.	287	Preliminary tests to locate impact velocity range for subsequent tests
2	HRC 38	Ambient	Sym.	343	
3	HRB 94	Ambient	Sym.	342	
4	HRB 94	Ambient	Sym.	457	Determination of dynamic flow curves for various hardnesses at ambient temperature
5	HRC 31	Ambient	Sym.	456	
6	HRC 39	Ambient	Sym.	457	
7	HRC 39	401	DRI.	335	Development of test method for elevated temperatures
8	HRC 39	Ambient	Asym.	238	
9	HRC 39	340	Asym.	224	Determination of dynamic flow curves for elevated temperatures
10	HRC 39	403	Asym.	235	
11	HRC 39	612	Asym.	236	
12	HRC 39	721	Asym.	178	
13	HRC 39	947	Asym.	180	

^aHRC 39 is the baseline material (VAR 4340 steel) for this project; other hardnesses are commercially obtained 4340 steels.

^bSym. denotes rod-into-rod (symmetric), Asym. denotes plate-into-rod (asymmetric), and DRI. denotes plate-into-rod-into-rod (double) impacts.

A. Historical Perspective and Technique Development

1. Classic Taylor Test

In 1947, Taylor and Whiffin^{1,2} accelerated cylindrical specimen rods into a "rigid" plate (see Figure IV.1a). The plastic deformation at the impact end shortens the rod, and the fractional change in rod length can, by one-dimensional rigid-plastic analysis, be simply related to the dynamic yield strength. The authors showed this relationship to be independent of both the rod aspect ratio and the impact velocity for a wide variety of materials, including copper, lead, paraffin wax, and various steels.

Though appealing in its simplicity, the Taylor test had only a moderate follow-up. In 1954, Lee and Tupper,³ using a one-dimensional characteristics code with an elastic-plastic model, attempted a theoretical determination of the strain distribution in a Taylor test specimen rod. In 1968, Hawkyard, Eaton, and Johnson,⁴ performed Taylor tests with copper and steel specimens at temperatures from 20 to 700°C. They investigated several one-dimensional analyses, but found that none could successfully predict the final rod deformation.

It was not until 25 years after the original Taylor tests that use of two-dimensional wave propagation codes allowed better understanding of and renewed interest in this technique. In 1972, Wilkins and Guinan,⁵ using the HEMP code and an elastic-plastic model with work-hardening, were able to correctly simulate the final shapes, as well as the final lengths, of Taylor test specimens of several metallic alloys at ambient temperatures. Their results showed a good correlation between the dynamic yield strength and the fractional change in rod length for a wide range of impact velocities and rod aspect ratios, thus confirming many of the Taylor/Whiffin conclusions.

2. Symmetric Rod Impact Test

In the early 1980s, Erlich, Shockey, and Seaman⁶ implemented two major modifications to the classic Taylor technique, as a method for

obtaining the entire stress-strain flow curve for materials undergoing high strain-rate compressive and shear loading to large plastic strains. The first was to use ultrahigh-speed photography to monitor the deformation history of the specimen rod. This allows intermediate, as well as final deformation states to be compared with two-dimensional computer simulations, thus improving the reliability of the flow curve determination.

The second modification was to replace the "rigid" plate with another rod of the same geometry and material as the impacting rod (see Figure IV.1b). This arrangement, referred to as the "symmetric rod impact" (SRI) technique, allows the impacting ends of the two specimen rods to deform together symmetrically, thus eliminating boundary condition uncertainties in the analysis that arise from the unknown friction conditions at the rod-plate interface and from the deformation of the "rigid" plate adjacent to that interface. By use of the SRI technique, dynamic flow curves at ambient temperature were obtained for 6061-T6 aluminum⁶ and a titanium alloy.

3. Recent Rod Impact Testing at Elevated Temperatures

In the early 1980s, Gust⁷ used a reverse ballistics variation of the classic Taylor test to measure fractional changes in the length of various metallic rods at initial temperatures up to about 1000°C. In this variation, the "rigid" plate is launched into a stationary specimen rod preheated to the desired temperature.

Concurrently, researchers at SRI International were stymied in their attempts to use the symmetric rod impact technique to determine dynamic flow curves at elevated temperatures (because of the infeasibility of heating the moving specimen rod). An attempt to impact a stationary heated rod with an identical but unheated rod was unsatisfactory because the gross difference in deformability of the two rods created large uncertainties in the boundary conditions at the impact interface.

4. Development of Asymmetric Rod Impact Technique under ARO Program

To solve the problems of rod impact testing at elevated temperatures, we investigated several alternatives. One possibility was to combine the reverse ballistics impact of a heated rod with high-speed photographic measurements of the resulting deformation, to form the "asymmetric rod impact" or ASRI technique (Figure IV.2a). However, the boundary condition uncertainties inherent in the ASRI technique needed to be examined. Computer simulations of the proposed ASRI test showed that the presence or absence of friction had a profound effect upon the rod deformation, while the use of ideal rigid or realistic material properties for the impactor plate had a noticeable but minor effect.

Another possibility was to position co-axially (but with a gap between them) two identical specimen rods preheated to the same desired temperature and impact one with a plate, thereby accelerating the undeformed end of the first rod into the as-yet-undeformed second rod (Figure IV.2b). In this proposed "double rod impact" (DRI) test, the first impact (between the plate and the rod) was the same as in the ASRI technique, with its yet-to-be-determined boundary condition uncertainties. However, the second impact (between the two specimen rods) is identical to a symmetric rod impact for most of its deformation history (until information about the asymmetry of the distal ends of the rods travels back to the deforming proximal ends), and might therefore be subjected to analysis with the existing SRI techniques.

One DRI test was performed on 4340 steel at 401°C (Test 7), and the photographic results are shown in Figure IV.3. It was expected that the deformation produced by the second impact would be approximately half that of the first if the impact velocities were identical. However, the much smaller than expected second impact deformation indicated that the undeformed end of the first rod had not been allowed to accelerate to the desired velocity before impacting the second rod. In fact, the gap between the two rods could not be set correctly for a known-velocity impact of two stress-free rods without foreknowledge of the deformation behavior of the first rod. Hence, we concluded that the DRI technique,

although possibly useful in the future as a proof test, holds no advantage over the simpler ASRI technique, and we could no longer avoid determining experimentally the effect upon the rod deformation of friction at the impact interface.

Identical 4340 specimen rods at room temperature were therefore impacted in two experiments--one an SRI test (No. 6) and the other an ASRI test (No. 8) at approximately half the impact velocity. (The stresses and resulting deformations from a symmetric impact are attained by impact with an impactor plate at about half the impact velocity.) The resulting specimen rod deformations in the two cases differ very slightly (Figure IV.4), and metallographic examination of the recovered ASRI specimen showed some frictional effects in a very narrow region at the center of the impact end (Figure IV.5). However, computer simulations (details of which will be presented in a later section) of both tests yielded identical flow curves, to well within the experimental uncertainties, provided that we assigned realistic material properties to the impactor plate (an ultrahigh strength maraging steel) and used a frictionless rod-plate interface condition.

Thus it was concluded that frictional effects, though existent, were insufficient to significantly influence the rod deformation profiles or the resultant dynamic flow curves, at least for this particular combination of specimen and impactor materials. Further studies should be performed to validate this conclusion for a wider range of materials. Once this is done, the ASRI technique can be used with confidence to determine dynamic flow curves for any materials at ambient or elevated temperatures.

B. Experimental Technique

1. SRI Test at Ambient Temperature

A schematic diagram of the experimental arrangement for the SRI test at ambient temperature is shown in Figure IV.6. The specimen rods are identical right circular cylinders, 44.4 mm long by 9.5 mm in diameter (these dimensions are arbitrary), whose ends are machined flat and

parallel to within about 0.01 mm. The impacting rod is mounted on the front end of a projectile, which is accelerated by expanding helium in a 6.35-cm-diameter gas gun. The stationary rod is held in place by six ceramic fingers attached to a target mounting fixture, which in turn is affixed to an alignment plate at the muzzle of the gun. The position of the latter rod can be adjusted by rotating the threaded bars into which the ceramic fingers are inserted. Alignment of the two rods is critical to ensure that the impacting ends are parallel and coaxial. Misalignment by as little as 0.1 mm can have a noticeable effect upon the deformation profiles.

The specimen rods are back lighted by a fast rise-and-fall-time, high-intensity light source triggered just before impact. A series of exploding bridge wires were used for the first eight tests, and a custom-built xenon flash tube was used for the remaining tests. The silhouettes of the deforming rods are recorded by a high-speed framing camera at framing rates between one-half and one million frames per second. Selected frames from SRI Test No. 4 are shown in Figure IV.7.

After the deformation is complete (about 30 to 40 μm after impact), the specimen rods fly into a recovery pipe filled with rags or other energy-absorbing materials that minimize additional deformation. The pipe is sufficiently narrow to prevent the projectile from entering and reimpacting the specimen. The recovered rods are then sectioned along the axis and examined metallographically to ascertain the extent of internal damage. The impact velocity must be low enough to suppress the formation of tensile voids (which may occur at early times by the focusing of the radial release waves on the rod axis) or shear bands (which may occur at later times as a result of large plastic deformation near the impact end). Although a small amount of incipient damage can be tolerated, any significant amount of damage will affect the shape of the deforming rod profiles. Of course any significant amount of damage may cause the rod to fail and come apart during the deformation process; such was the case with Test 11.

2. ASRI Test at Elevated Temperature

The ASRI technique for specimens at elevated temperatures differs from the SRI technique in only a couple of ways. First the impactor is a 5-cm-wide, 1-cm-thick disk of ultrahigh strength maraging steel backed by a thicker aluminum projectile head. The stationary specimen rod needs to be aligned parallel to the direction of impact, but the co-axiality condition critical to the SRI test is not necessary here, since the rod can impact anywhere near the middle of the disk.

Second, preheating of the specimen is performed by three infrared line heaters arranged, as shown in Figures IV.8 and IV.9, so that radiation from the linear filament is focused by an elliptical reflector onto the stationary rod approximately 15 cm distant. A double layer of quartz windows (only one layer is shown) protects the heaters from the blast wave and fragment debris.

The temperature of the specimen rod is monitored by a chromel-alumel thermocouple attached to the nonimpacted end. By use of a variable 280-volt, 100-amp power supply, a temperature of 1000°C can be attained in about 150 s. Thermal uniformity of the rod is quite good, because of the relatively short thermal equilibrium times (a couple of seconds) for metallic rods of this diameter.

3. Test Procedure

The following description of the experimental procedure is applicable to both the SRI and ASRI tests.

The heater assembly (for elevated tests) and the specimen recovery pipe are placed in position near the muzzle of the gas gun (see Figure IV.9). The target alignment plate is adjusted so that it is concentric with that of the gun barrel and on it is mounted the target assembly containing the specimen rod, positioned to be concentric with the front target support plate. The projectile is inserted at the breech of the gun, the target chamber is closed and evacuated to about 10^{-5}

Then, the gas gun breech is pressurized, and the specimen is preheated to the desired temperature. Then the firing sequence begins.

The room is darkened, the framing camera shutter is opened, and the rotating mirror in the camera is activated. When the mirror's rotational velocity, as measured by a frequency counter, falls within the desired range, the fire button on the gas gun control panel is pushed, launching the projectile down the barrel. As the projectile nears the end of the barrel, it contacts a series of pins, which record its velocity and activate a delay generator. After a preset delay, at a few microseconds before impact, a signal is sent that turns on the light source and records the rotational velocity of the mirror (from which the framing rate at impact can be determined).

Impact occurs, and for the next 40 to 70 μ s, the camera takes pictures of the deforming silhouettes. Then the light intensity drops rapidly to avoid double exposure. The deformed specimen rods travel into the recovery pipe where they are gradually decelerated and recovered for subsequent metallographic analysis. Specimens recovered from ASRI tests are usually in excellent condition, with negligible recovery damage, and with the impact interface very nearly perpendicular to the rod axis. Such is not often the case with specimens recovered from SRI tests. The two rods decelerating together can reimpact, causing additional surface damage, and slight misalignments in coaxiality can cause the impact interface to be skewed with respect to the rod axis.

C. Analytical Techniques

1. Measurement of Rod Deformation Profiles

The first step in the analysis procedure is to digitize and plot the rod profiles for subsequent comparison with computer simulations at various times during the deformation. For the SRI tests, the profiles are obtained exclusively from the framing camera records. For the ASRI test, however, in addition to the photographic records, we can measure the recovered specimens to obtain the final deformation profile.

There is an uncertainty in the measurements of the rod profiles. For the photographic records, errors may be caused by photographic nonlinearities and aberrations, target misalignments (SRI tests only), parallax errors, but mostly by the fuzziness of the magnified image. If we make the assumption that the error band has a constant width, $\pm \Delta y$, independent of axial position, as shown in Figure IV.10, we can make estimates of the magnitude of the uncertainty in radial expansion $\Delta y/\Delta R$, both for the photographic measurements, as well as the considerably more accurate recovered rod profile measurements (ASRI tests only).

The results, depicted in the table in Figure IV.10, show that the error in radial expansion for a particular axial position, can vary from 2% for the sharpest photographs of large deformations (100% $\Delta R/R^0$), to 25% for the poorest quality photographs of smaller deformations (20% $\Delta R/R^0$). For the same two deformations, measurements of the recovered rod profiles would yield radial expansion errors of 0.3 and 1.5%, respectively. The digitized profiles (averaged top-to-bottom) from SRI Test 4 (shown in Figure IV.7), are plotted at 5- μ s intervals in Figure IV.11.

2. Computer Simulations of Rod Impact Tests

Determination of the dynamic flow curve of a material from a rod impact test is made by computationally simulating the experiment, varying the input flow curve until the computed profiles agree with those determined experimentally at various times during the deformation history. The computer code we have used for these simulations is the recently-developed C-HEMP.⁸ This is a two-dimensional finite-difference code for treating stress wave propagation, in either planar or axisymmetric flow, caused by impacts or explosive detonations.

The specimen rods (and the impactor, for ASRI test simulations) are divided into a series of rectangular zones, or computational cells; each of these, in the axisymmetric geometry appropriate to the rod impact test, represents an annulus of revolution about the rod axis. The corners, or nodes, of the cells are given an appropriate initial

velocity. Then the subsequent node velocities and the resulting deformations are determined for successive small time increments by solving the Lagrangian equations of motion for a continuous medium. Figure IV.12 shows, for a typical SRI test simulation, the original, an intermediate, and the final cell profiles.

A rate-independent elastic-plastic model with work hardening is used to describe the plastic deformations in each cell. Various flow curves are tried. (A quasi-static compressive or tensile flow curve is a good starting point, since there are few dynamic curves to be found in the literature.) The computed results are then compared with the experimental results until agreement within the experimental error is obtained.

3. Constitutive Model Used in the Computer Simulations

The stress tensor σ_{ij} is separated into a pressure deviator, $P = \frac{\sigma_{kk}}{3} \delta_{ij}$ (where δ_{ij} is the Kronecker delta), and a stress deviator, σ'_{ij} :

$$\sigma_{ij} = P + \sigma'_{ij} \quad (IV.1)$$

• Pressure: Equation of State

The pressure is related to specific volume V and specific internal energy E by an equation of state derived from the usual combination of the $P(V)$ -Hugoniot, the Mie-Grüneisen equation, and the Hugoniot equation for conservation of energy:

$$P = (C\mu + D\mu^2 + S\mu^3) \left(1 - \frac{\Gamma\mu}{2}\right) + \Gamma\rho E \quad (IV.2)$$

where

$$\mu = \frac{V_0}{V} - 1 \quad (V_0 = \text{initial specific volume})$$

$$\rho = \frac{1}{V} \quad (\text{density})$$

$\Gamma(V)$ = Grüneisen ratio

C, D, and S are 1st, 2nd, and 3rd terms in the polynomial expansion of the bulk modulus.

For 4340 steel, the initial density is 7.85 g cm^{-3} and the Grüneisen ratio is 1.69. The other equation-of-state parameters from Equation (IV.1), as well as the shear modulus, G, from equation (IV.4) below, are presented in Table IV.2 for ambient temperature and the four elevated temperatures at which we obtained ASRI data that can be analyzed.

Table IV.2 EQUATION-OF-STATE PARAMETERS USED IN ASRI SIMULATIONS*

	Temperature (°C)				
	20	340	403	721	947
C ($\times 10^{12}$ dyne cm^{-2})	1.59	1.46	1.43	1.29	1.19
D ($\times 10^{12}$ dyne cm^{-2})	5.17	4.76	4.65	4.19	4.19
S ($\times 10^{13}$ dyne cm^{-2})	5.17	4.76	4.65	4.19	4.19
G ($\times 10^{11}$ dyne cm^{-2})	8.19	7.62	7.53	6.96	6.55

*The variation of the bulk and shear moduli as a function of temperature are calculated from data presented on page 194 of Reference 9. Computer simulations have shown, however, that the calculated rod deformations are quite insensitive to variations in the elastic moduli.

When no internal energy is added by heating from outside of the body, the internal specific energy of a cell is calculated in an intermediate step: The displacements of the nodes surrounding the cell are simply multiplied by the forces acting on the nodes.

• Deviator Stress

The strain increments are divided into elastic and plastic parts

$$d\epsilon_{ij} = d\epsilon_{ij}^E + d\epsilon_{ij}^P \quad (\text{IV.3})$$

Elastic relation:

$$\sigma'_{ij} = 2G\epsilon'_{ij} \quad (IV.4)$$

$$\epsilon'_{ij} = \text{deviatoric strain} = \epsilon_{ij} - \frac{\epsilon_{kk}}{3} \delta_{ij}$$

Plastic relations:

We used the Prandtl-Reuss law or "incremental plasticity with associated flow rule," which states that the deviator stress in any direction is proportional to the plastic strain increment in that direction:

$$d\epsilon^P_{ij} = \sigma'_{ij} d\lambda \quad (IV.5)$$

where $d\lambda$ is a constant scalar that depends on the material. In other words, the Reuss flow rule states that the vector increment of plastic strain in the strain space is normal to the yield surface in the stress space. For convenience, an effective stress $\bar{\sigma}$ has been defined

$$\bar{\sigma} = \sqrt{\frac{3}{2} \sigma'_{ij} \sigma'_{ij}} \quad (IV.6)$$

where $\bar{\sigma}$ is such that the Von Mises yield criterion can be simply expressed as

$$(\bar{\sigma})_{\text{yield}} = Y \quad (IV.7)$$

where Y is the yield strength on a one-dimensional stress path. The equivalent plastic strain increment is

$$d\epsilon^P = \sqrt{\frac{2}{3} d\epsilon^P_{ij} d\epsilon^P_{ij}} \quad (IV.8)$$

Hence, equation (IV.5) can be rewritten as

$$\overline{d\epsilon^P} = \frac{2}{3} d\lambda (\bar{\sigma})_{\text{yield}} \quad (\text{IV.9})$$

or

$$d\epsilon_{ij}^P = \frac{3}{2} \sigma'_{ij} \frac{\overline{d\epsilon^P}}{(\bar{\sigma})_{\text{yield}}} \quad (\text{IV.10})$$

To obtain a solution for an increment of strain, we must know $\overline{d\epsilon^P}$. The C-HEMP code computes first a pseudo-deviator stress increment, $\Delta\sigma'_{ij}^N$ (Figure IV.13), which would occur if the strain were entirely elastic. That is,

$$\Delta\sigma'_{ij}^N = 2G(\Delta\epsilon'_{ij}) \quad (\text{IV.11})$$

If the final state of stress is outside the yield locus (point B in Figure IV.13a), it must be numerically "relaxed" back to the yield surface (note that point B corresponds to $\vec{\epsilon}$ in the strain space, Figure IV.13b). To satisfy the Reuss rule (plastic strain increment normal to the yield surface), the "relaxation" path must be a radius. This transformation results in an elastic state $(\vec{OA}, \vec{\epsilon}^E)$ on the yield surfaces and a plastic strain increment $\overline{\Delta\epsilon^P}$ (\vec{AB} , Figure IV.13b).

$$\overline{\Delta\epsilon^P} = \vec{\epsilon} - \vec{\epsilon}^E \quad (\text{IV.12})$$

$$\overline{\Delta\epsilon^P} = \vec{\epsilon} - \frac{\vec{\sigma}^E}{2G} \quad (\text{IV.13})$$

Equation (IV.13) can be transformed to a scalar equation because all the vectors are coaxial.

If we use $\overline{\Delta\epsilon^P}$ (which is deviatoric by definition) and introduce $\bar{\sigma}^N$ in analogy to the definition of $\bar{\sigma}$, equation (IV.13) can be rewritten as

$$\overline{\Delta\epsilon^P} = \frac{\bar{\sigma}^N - (\bar{\sigma})_{\text{yield}}}{3G} \quad (\text{IV.14})$$

which finally allows calculation of each component of plastic strain from equation (IV.10).

For perfect plasticity, $(\bar{\sigma})_{\text{yield}} = Y_0$

When work-hardening occurs,

$$(\bar{\sigma})_{\text{yield}} = Y(\bar{\epsilon}^P) \quad (\text{IV.15})$$

Equations (IV.14) and (IV.15) can then be combined and solved by any iterative scheme to obtain the plastic strain increments. The plastic yield curve derived from the comparison of the $\bar{\sigma}$ - $\bar{\epsilon}^P$ plots with experimental rods profiles will be expressed in the form of equation (15).

Note that in equation (IV.15), $\bar{\sigma}$ and $\bar{\epsilon}^P$ as defined by (IV.6) and (IV.8) are invariants $\bar{\sigma} = \sqrt{3 J_2'}$ and $\bar{\epsilon}^P = \sqrt{\frac{4}{3} I_2'}$, where J_2' and I_2' are the second invariants of the deviator stress and strain tensors. Then, (IV.6) and (IV.8) can be easily expressed in terms of principal strains and stresses

$$\bar{\epsilon}^P = \sqrt{2/9} \left[(\epsilon_1^P - \epsilon_2^P)^2 + (\epsilon_2^P - \epsilon_3^P)^2 + (\epsilon_3^P - \epsilon_1^P)^2 \right]^{1/2} \quad (\text{IV.16})$$

$$\bar{\sigma} = \sqrt{1/2} \left[(\sigma_1' - \sigma_2')^2 + (\sigma_2' - \sigma_3')^2 + (\sigma_3' - \sigma_1')^2 \right]^{1/2} \quad (\text{IV.17})$$

4. Considerations of Strain Rate and Temperature

Computer simulations have shown that the equivalent plastic strains (as defined in the previous section) and strain rates vary significantly as a function of time and of axial and radial position within the specimen rod. Figures IV.14 through IV.17 show equivalent plastic strain and strain rate histories for the computer simulation shown in Figure IV.11, for various computational cell locations. (Note that the large fluctuations in plastic strain rate seen for the first 3 to 4 μs are caused by radial ringing.) For positions near the impact interface, the

average strain rate along the rod axis is two to three times higher than that near the edge. For positions along the rod axis, the average strain rate near the impact interface is about four times higher than that one rod radius distant.

It is important to consider that the experimentally measured radial rod expansion at a particular axial position is not the result of a region of material undergoing deformation at a specific strain rate; rather it is the result of various regions of material deforming over a range of strain rates. Therefore, the rod impact technique should not be viewed as a method for accurately determining the strain rate sensitivity of the flow curve within the range of strain rate observed in the test, namely between about 10^4 and $5 \times 10^4/\text{s}^{-1}$, rather, it is a means of determining the average flow curve over that range.

Furthermore, if a material's flow stress exhibited a very large strain rate sensitivity within the observed strain rate range, then no matter what flow curve we would try in our rate-independent simulation, we could not match the experimental profiles throughout the deformation history; in fact, we might not be able to match the profiles well at any particular time. Conversely, if we are able, by using a particular flow curve, to match the experimental profiles well throughout the deformation history, then the material exhibits no significant strain rate sensitivity within the range noted above.

The computer simulations have also shown that large temperature increases caused by plastic work are created in the highly deformed regions of the specimen rods. This is as expected for any high-strain-rate process, where the deformation is too rapid to allow temperature equilibration throughout the specimen. Figure IV.18 plots the calculated temperature as a function of strain rate for SRI test 4, and shows the 40°C - 430°C range of temperature increase in the proximal end of the rod 20 μs after impact.

The rod impact test is thus an adiabatic, rather than an isothermal, process, and there is no way to separate the temperature effect upon the flow curve from the plastic strain (or work-hardening) effect. This

makes it difficult to compare the flow curve obtained from rod impact tests with those obtained at a specific temperature from other tests. However, we did not consider this a serious limitation, because the processes that we are characterizing are for materials undergoing similar rates of deformation, and hence similar temperature histories.

D. Experimental and Analytical Results of the Rod Impact Tests

1. Flow Curve Determination from SRI Tests at Ambient Temperatures

A complete analysis was made for ambient temperature SRI tests 4 (initial hardness of HRB 94), 5 (initial hardness of HRC 31), and 6 (baseline material; initial hardness of HRC 39), based on the framing camera records at various times throughout the deformation. Photographic records for test 4 and the resultant digitized profiles have been shown in Figures IV.7 and IV.11, respectively.

A comparison of the late-time profiles (approximately 28 μ s after impact) for all three of these tests is shown in Figure IV.19. Although the three profiles do not precisely coincide, they all lie within the band of experimental uncertainty, $\pm \Delta y$. This was somewhat surprising, since quasi-static data for the 3 hardnesses^{10,11} show quite dissimilar flow curves. (Figure IV.20).

A series of computer simulations was performed, first using the HRB 94 and HRC 39 static flow curves and then varying the input flow curves until the computed rod profiles matched the experimental data to within $\pm \Delta y$. Figure IV.21 shows the various flow curves used in these calculations and compares their resultant late-time profiles with the experimental rod profiles (an average from the three tests). The static curves did not come close to providing a good match to the data. Elastic-perfectly plastic curves at flow stresses (Y) of 13 and 14 kbar (Cases 1 and 2, respectively) provided better approximations. A flow curve that work hardens from $Y = 11$ kbar at zero strain to $Y = 13$ kbar at a strain of 0.2 (Case 3), and is perfectly plastic at further strains, provided the desired match.

One can note by comparing $\pm \Delta y$ with the difference in the profiles resulting from Cases 1 and 2, that the uncertainty in the framing camera results leads to an uncertainty in the flow stress of no greater than ± 1 kbar. Also note that we could have improved the match by slight alterations to the Case 3 input flow curve, but the experimental uncertainties did not justify such an effort.

We also compared the profiles at several intermediate times in the Case 3 flow curve calculations with the corresponding experimental profiles. The results are shown in Figure IV.22 for the three different hardnesses. Some discrepancies can be noted at the later times; there is insufficient work hardening in the HRB 94 calculation and too much in the HRC 39 calculation. Again, however, the fact that the maximum discrepancies were of the same order as the experimental uncertainty made further refinements in the flow curve unjustifiable.

How can we explain relative insensitivity of the dynamic flow curve upon the initial hardness, when static data (Figure IV.20) show as much as a factor of two difference in the initial yield point? We sliced the recovered specimens along the rod axis, polished the slice, and took hardness traverses at various axial positions. The results, shown in Figure IV.23, indicate that the material of vastly different initial hardness (from HRB 94 to HRC 39) ends up at only slightly different final hardness (from HRC 39 to HRC 43) after large deformations (e.g., 60-100%). Furthermore, material of lower initial hardness experiences a dramatic increase to nearly its final hardness at relatively small strains. Therefore, for all but the early part of their deformation history, all three materials have nearly the same constitutive behavior.

One final question could be asked about the lack of work hardening at higher strains (above about 20%), as compared to the static data, in which the work hardening appears to continue, albeit at a reduced rate, as far as the curves go (again see Figure IV.20). We believe the answer to this question lies in thermal considerations. Unlike the isothermal static tests, the adiabatic SRI test involves considerable increases in temperature for the highly deformed regions. Thermal softening of the

material at these elevated temperatures would tend to oppose the effect of work hardening, thus reducing the slope of the dynamic flow curve.

2. Metallographic Studies of Recovered SRI Specimens

The deformed region of the 4340 steel specimen rod pairs recovered from SRI tests 4, 5, and 6 were sliced axially, polished, etched, and examined metallographically to determine the presence or absence of internal damage. We were particularly interested in observing shear banding, since these rods had all experienced equivalent plastic strains of as much as 100%. Previous studies using contained fragmenting cylinder tests¹² had shown that 4340 steel at HRC 40 underwent significant shear band nucleation and growth at strains of less than 50%, whereas 4340 steel at HRC 21 experienced no shear banding at those strains.

The rods recovered from tests 5 and 6 (HRC 31 and HRC 39, respectively) showed complete absence of any internal damage (Figure IV.5a, for example), while both rods from test 4 (HRB 94) exhibited a small region of tensile voids and shear bands along the axis near the impact interface (Figure IV.24). It is important to note, first, that the amount of damage is too low to have any appreciable effect upon the deformation profile of the rods. Then it is of interest to consider the origin of the damage.

A close inspection of the metallographs for test 4 reveals some tensile voids in regions away from shear bands, but that all shear bands are in close association with the voids, either extending between small voids (inset A of Figure IV.24) or nearly slicing apart a larger void (inset B). Computer simulations have shown that the only significant tensile pressures occur at early times (1 or 2 μ s after impact) and are caused by the convergence upon the axis of the radial release waves from the initial impact. (These tensions are in fact large enough to cause the central region of the impact interface of the two rods to separate for a short duration.) Hence, the voids are formed at these early times and only in the softest of the three materials, because, apparently, only

in that material does the tension exceed the nucleation threshold for void formation.

Shear bands, on the other hand, would form later in the deformation process, when the plastic strains became large. Because specimens of all three hardnesses experienced nearly identical strain histories, and because previous studies¹² have shown that the harder material will shear band at lower plastic strains, it would seem that shear bands are most likely to nucleate, barring any inhomogeneous strain deformities, in the HRC 39 material. This did not occur, and thus the only conclusion is that the shear bands in the softest material nucleated at the previously formed tensile voids, where the local strain inhomogeneities together with the homogeneous plastic strain exceeded the threshold for shear band formation.

3. Flow Curve Determinations from ASRI Tests

Framing camera results for two of the higher temperature ASRI tests are shown in Figures IV.25 and IV.26. The deformations appear to extend further along the length of the rod (see Figure IV.26d) than in ambient temperature tests, where the deformation is largely localized to regions near the impact interface. This indicates the existence of significant work hardening at higher temperatures, or a large slope to the stress-strain flow curve. Initial large deformations near the impact interface raise the local flow stress, thus shifting subsequent deformations to regions that have undergone less deformation and therefore have a lower flow stress.

Analyses based upon the recovered rod profiles were performed for four elevated temperatures--test 9 at 340°C, test 10 at 403°C, test 12 at 721°C, and test 13 at 947°C--in addition to ASRI test 8 at ambient temperature. Computer simulations were performed, varying the input flow curves in an attempt to match the final calculated profiles with the experimental profiles. Our current best matches for the five different temperatures are shown in Figures IV.27 through IV.31, and the input flow curves used in these simulations are plotted in Figure IV.32. Noting

that the uncertainty $\pm \Delta y$ in the measurements of the final rod profile is only about 0.03 mm, not more than a few times the width of the line in the plots, one sees a reasonably good match between the experimental and computational profiles for the three lowest temperature ASRI tests.

The match for the two higher temperature tests is not nearly as good. This could mean that we have just not yet tried an adequately accurate flow curve, and so further simulations are needed. Or, particularly in the 947°C case, sufficient strain rate dependence may exist in the material (within the strain rate range of the ASRI test) to make it impossible to match the profiles using a strain rate-independent model. Preliminary comparisons of the computational and experimental profiles at earlier times in the deformation (using the framing camera records) showed larger differences than those for the late-time profiles, thus supporting the latter explanation.

One final note: a discrepancy exists for ambient temperature 4340 steel between the flow curve obtained from the recovered final rod profile for ASRI test 8 (shown in Figure IV.32), and that obtained from the framing camera records about 25 μ s after impact for SRI test 6 (shown in Figure IV.21) and supported by framing camera data for test 8 (see Figure IV.4). Data from the recovered rod specimens would tend to be more credible than the data from the framing camera records, the latter having about an order of magnitude greater experimental uncertainty in digitization of the profiles and also subject to the accuracy of such measurements as the camera framing rate. We are currently investigating the cause of this discrepancy.

E. Summary

The rod impact experiments described in this section provided previously unavailable data on the homogeneous plastic deformation of VAR 4340 steel loaded in compression at high rates, at large plastic strains, and over a range of temperatures to about 1000°C (i.e., under conditions similar to those experienced by material failing by shear bands in armor penetration applications). Hence these data and results help define the

deformation conditions for the onset of shear band formation and, after shear banding has occurred, on the partitioning of deformation between shear bands and homogeneous flow.

Furthermore, the experiments reported here produced large plastic strains in specimens of significantly different geometry and loading history than used in the torsional Hopkinson bar or contained fragmenting cylinder experiments, thus providing an opportunity to evaluate certain aspects of the shear band model during its development. The prediction of shear bands by the model was not in accord with observations on impacted rods, suggesting necessary modifications to the SHEAR4 model and parameters. These modifications are described in Section VI.F.

F. References

1. G. I. Taylor, "The Use of Flat-Ended Projectiles for Determining Dynamic Yield Strength: I. Theoretical Considerations," Proc. Roy. Soc. A 194, 289-299 (1948).
2. A. C. Whiffin, "The Use of Flat-Ended Projectiles for Determining Dynamic Yield Strength: II. Tests on Various Metallic Materials," Proc. Roy. Soc. A 194, 200-232 (1948).
3. E. H. Lee and S. J. Tupper, "Analysis of Plastic Deformation in a Steel Cylinder Striking a Rigid Target," J. Appl. Mech. 21, 63-70 (1954).
4. J. B. Hawkyard, D. Eaton, and W. Johnson, "The Mean Dynamic Yield Strength of Copper and Low Carbon Steel at Elevated Temperatures from Measurements of the 'Mushrooming' of Flat-Ended Projectiles," Intl. J. Mech. Sci. 10, 929-948 (1968).
5. M. L. Wilkins and M. W. Guinan, "Impact of Cylinders on a Rigid Boundary," J. Appl. Phys. 44, 1200-1206 (1973).
6. D. C. Erlich, D. A. Shockey, and L. Seaman, "Symmetric Rod Impact Technique For Dynamic Yield Determination," AIP Conference Proceedings No. 78, Second Topical Conference on Shock Waves in Condensed Matter (Menlo Park, CA), 402-406 (1981).
7. W. H. Gust, "High Impact Deformation of Metal Cylinders at Elevated Temperatures," J. Appl. Phys. 53(5), 3566-3575 (1982).

8. L. Seaman, T. Cooper, and D. Erlich, "Users' Manual for C-HEMP, a Two-Dimensional Wave Propagation Code," SRI International Final Report for Ballistic Research Laboratory, Aberdeen Proving Ground, MD (1984).
9. G. Simmons and H. Wang, Single Crystal Elastic Constants and Calculated Aggregate Properties: A Handbook, MIT Press, Cambridge, MA (1971).
10. Metals Handbook, American Society for Metals, 9th Edition (1978).
11. F. R. Larson and J. Nunes, ASM Trans. 53, 663-682 (1960).
12. D. C. Erlich, D. R. Curran, and L. Seaman, "Further Development of a Computational Shear Band Model," SRI International Final Report for Army Materials and Mechanics Research Center, Watertown, MA (1980).

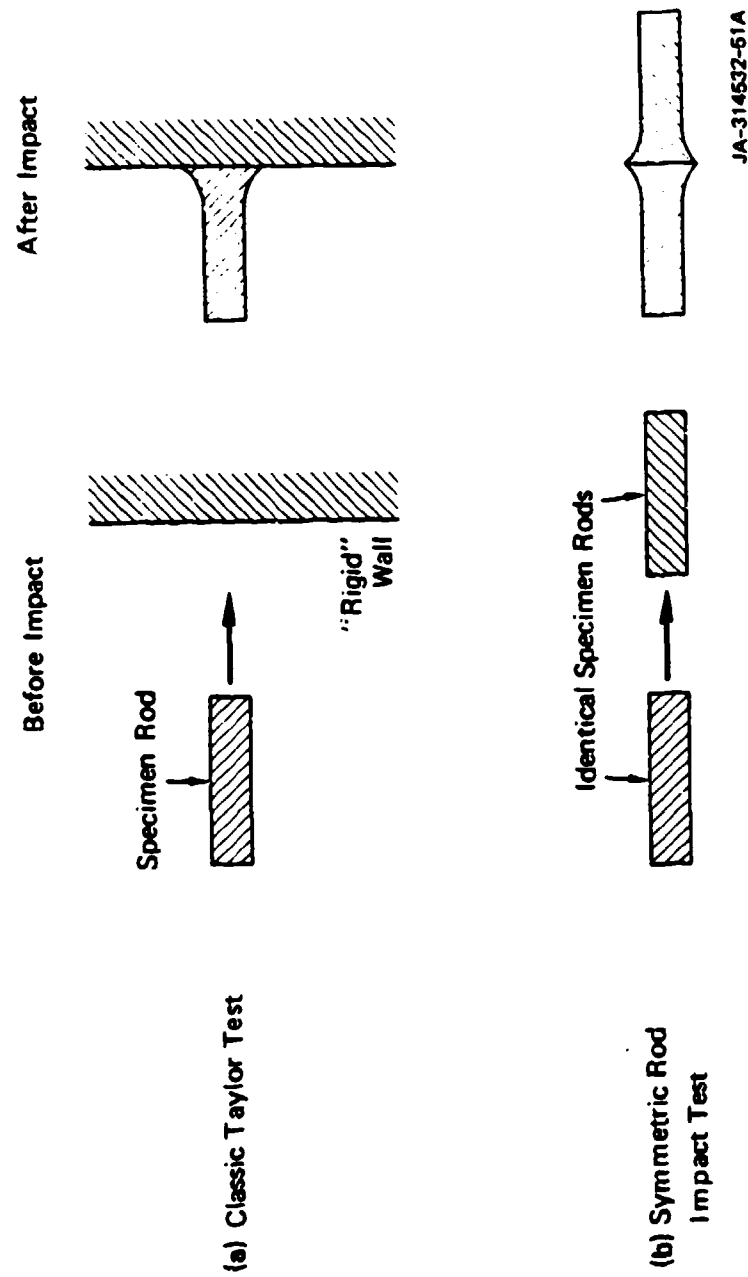
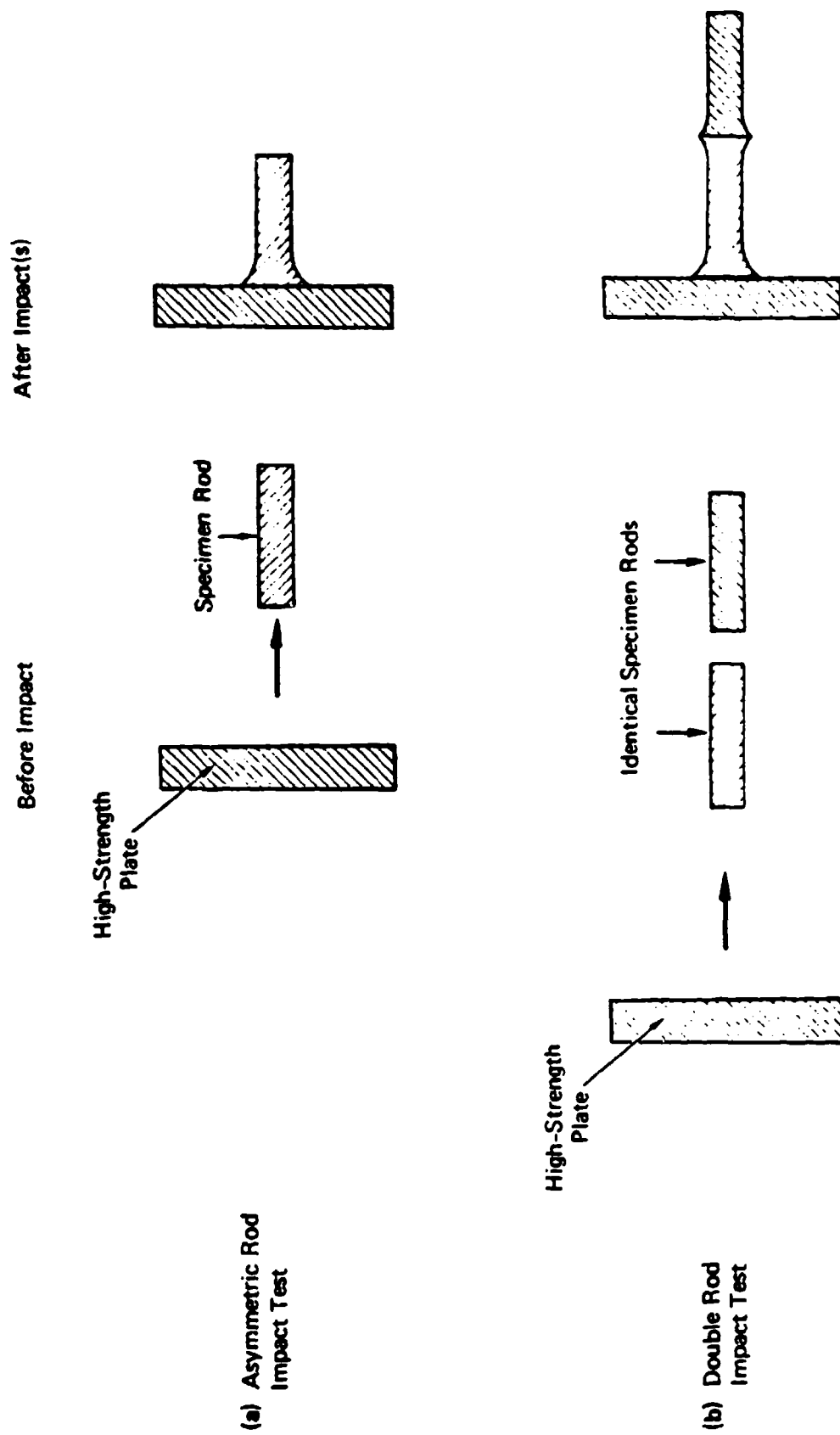


FIGURE IV.1 SCHEMATIC OF TWO ROD IMPACT CONFIGURATIONS

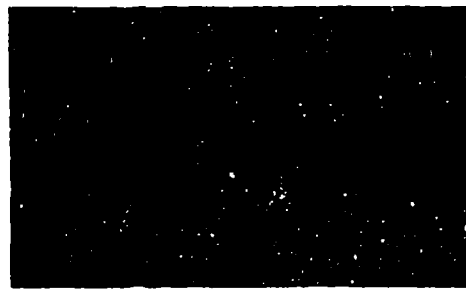


JA-314532-518

FIGURE IV.2 SCHEMATIC OF TWO ROD IMPACT CONFIGURATIONS FOR ELEVATED TEMPERATURES



(a) At \approx first impact



(d) 29.3 μ s after first impact



(b) 5.5 ms after first impact



(e) At \approx second impact
142.1 μ s after first impact)



(c) 11 μ s after first impact



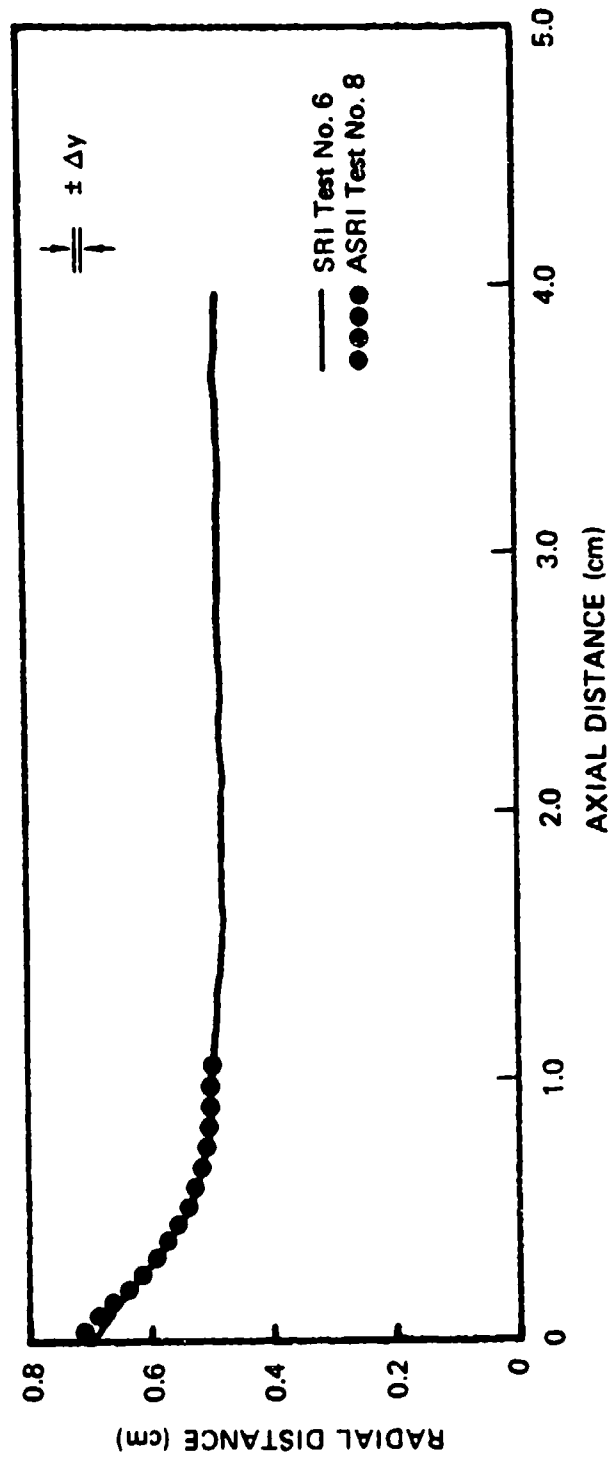
(f) 9.2 μ s after second impact
151.2 μ s after first impact)

50 mm

JP-2777-14

FIGURE IV.3 SILHOUETTES OF TWO 4340 STEEL RODS AT 947° FOLLOWING DOUBLE ROD IMPACT AT 335 m/s (TEST NO. 7)

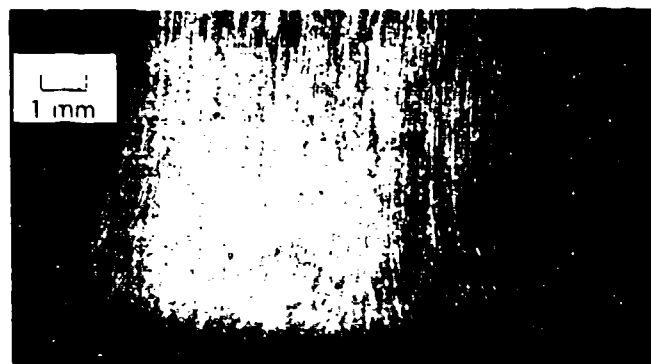
Impactor plate is at the left.



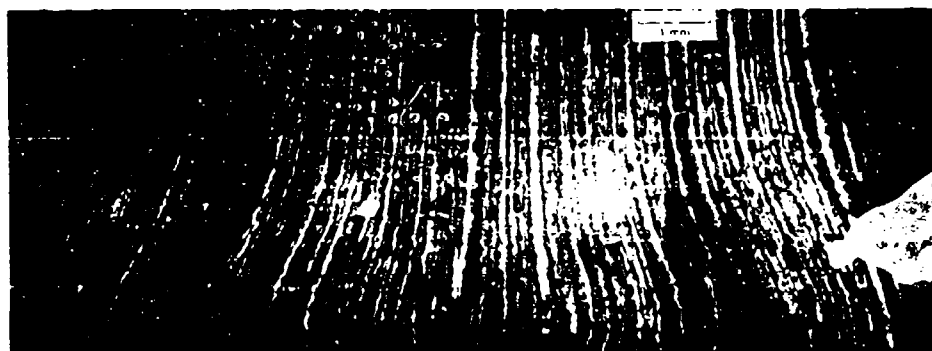
JA-3722-88

FIGURE IV.4 COMPARISON OF AMBIENT TEMPERATURE 4340 STEEL (R_c 39) ROD DEFORMATION PROFILES $\approx 25 \mu s$ AFTER IMPACT, FROM ASRI TEST NO. 8 AND SRI TEST NO. 6

Minor difference is caused by compressibility of impactor in ASRI test.



(a)

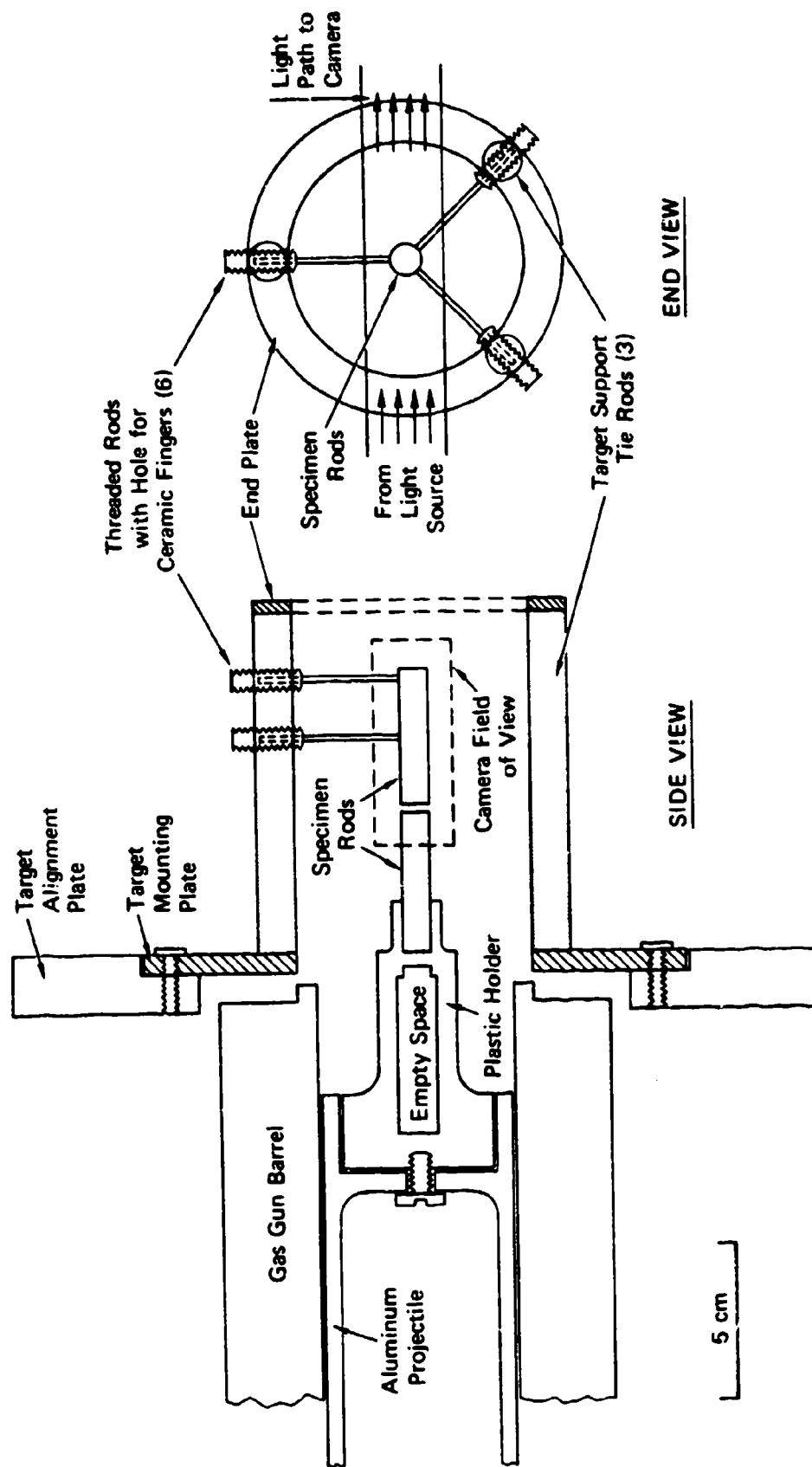


(b)

JP-3722-63

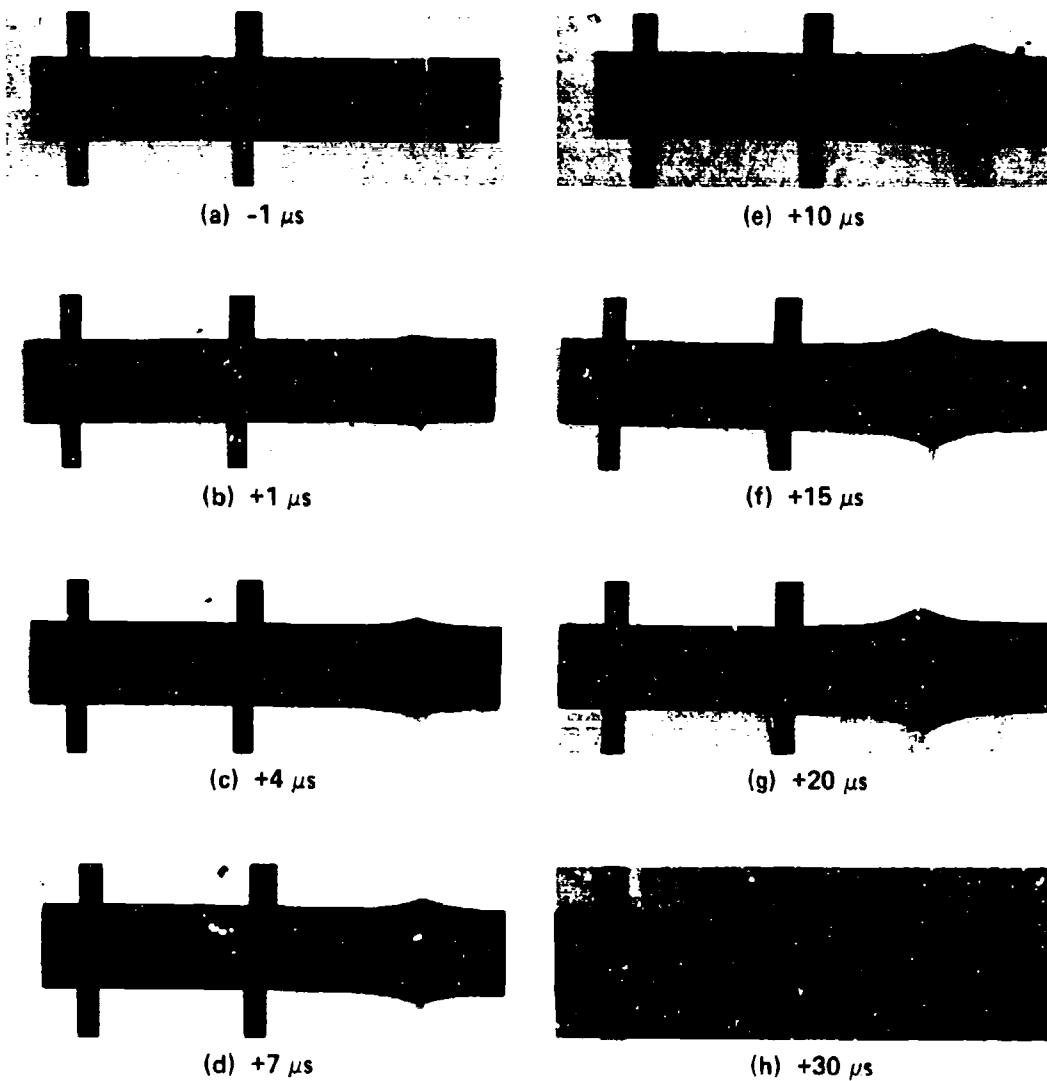
FIGURE IV.5 COMPARISONS OF SLICE THROUGH IMPACT REGION OF 4340 STEEL RODS RECOVERED FROM AMBIENT TEMPERATURE (a) SRI TEST (457 m/s IMPACT VELOCITY) AND (b) ASRI TEST (238 m/s IMPACT VELOCITY)

Note curvature of texturing lines in (b) in small region near center of impact plane.



JA-3772-20A

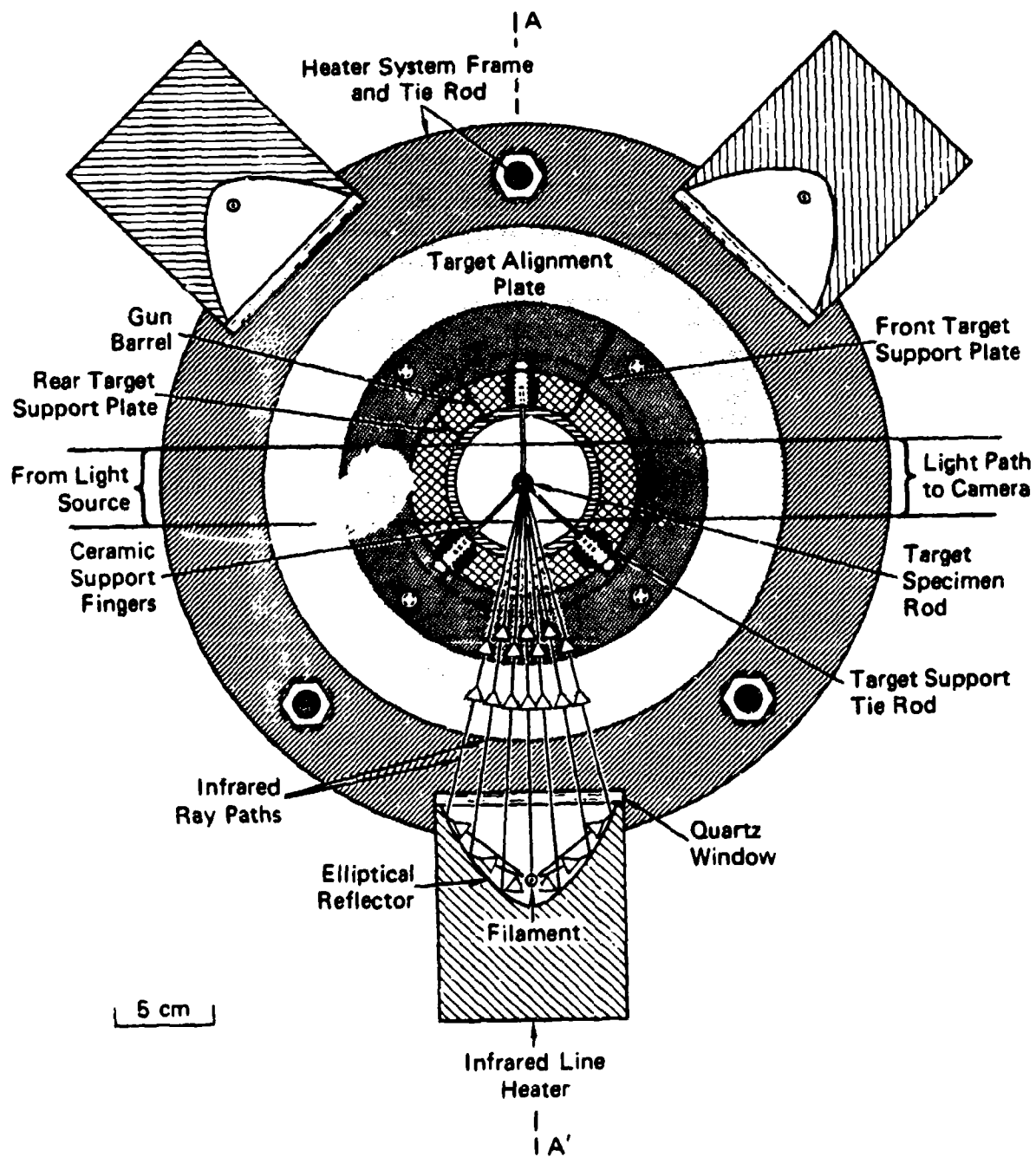
FIGURE IV.6 SYMMETRIC ROD IMPACT TESTS AT AMBIENT TEMPERATURE



JP-3722-8

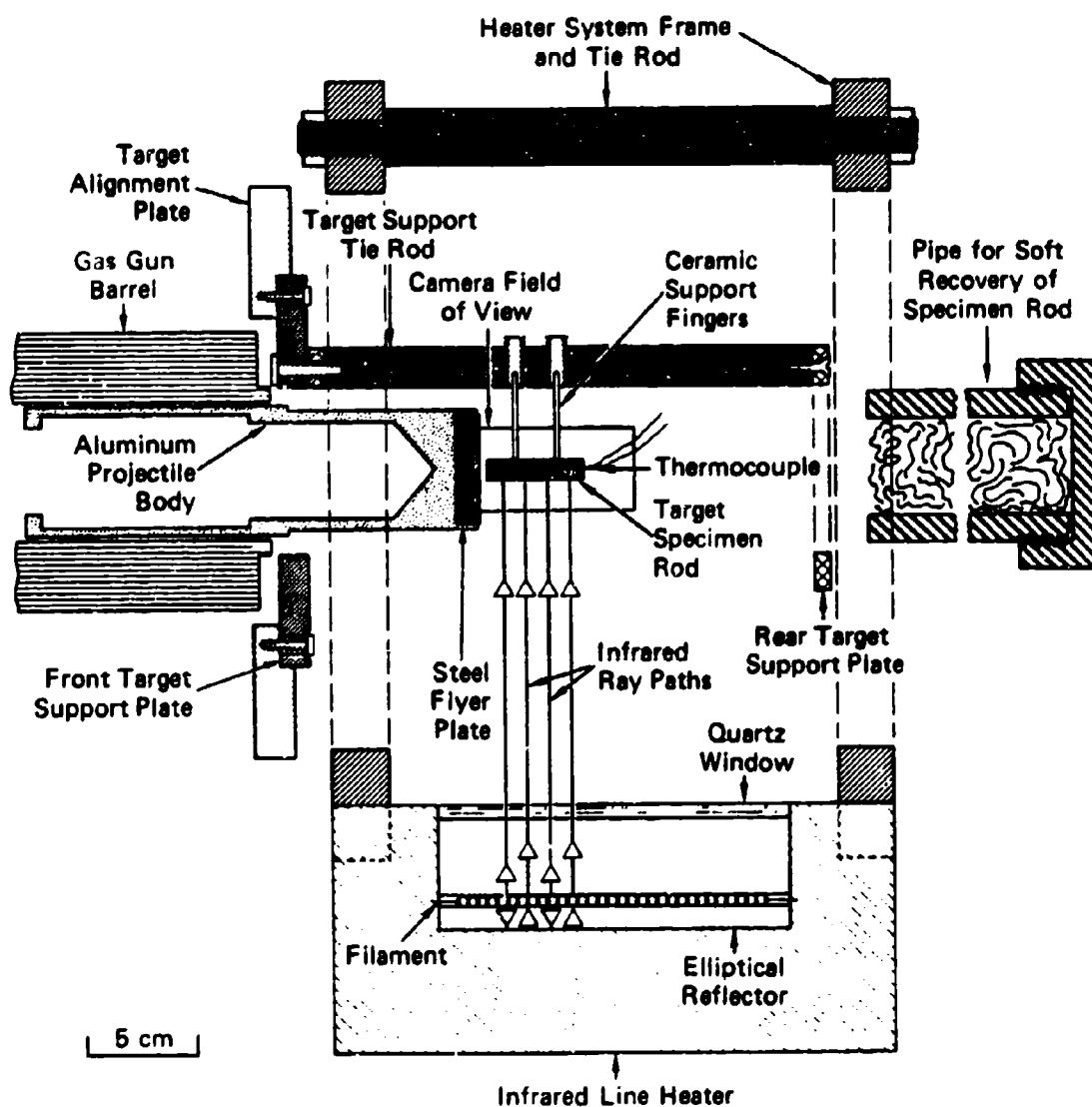
FIGURE IV.7 SILHOUETTES OF 4340 STEEL ($R_{\text{p}}94$) RODS DURING SYMMETRIC IMPACT AT 457 m/s (TEST NO. 4)

Times shown are approximate times from impact. Original rod dimensions are 9.5 x 44.5 mm.



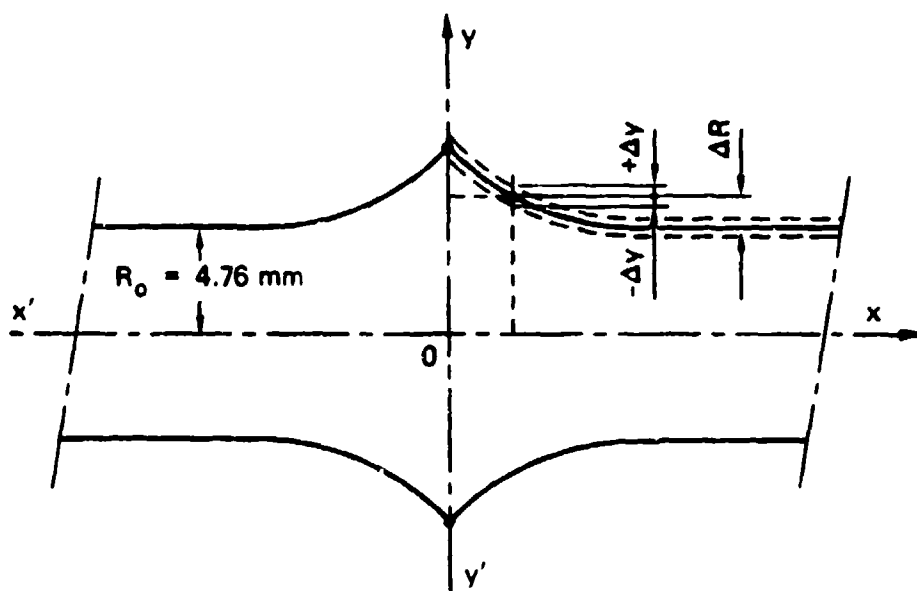
JA-2777-12A

FIGURE IV.6 END VIEW OF APPARATUS FOR ROD IMPACT TESTS AT ELEVATED TEMPERATURE



JA-2777-13A

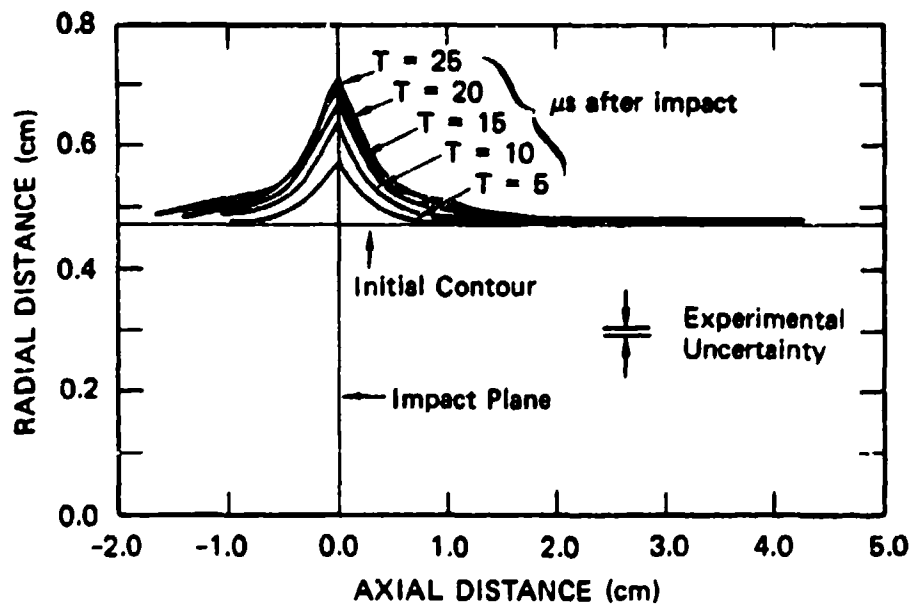
FIGURE IV.9 CROSS SECTION (THROUGH A-A' OF FIGURE IV.8 OF APPARATUS FOR ASYMMETRIC ROD IMPACT TESTS AT ELEVATED TEMPERATURES



	ΔY (mm)	$\frac{\Delta Y}{R_0}$	$\Delta Y / \Delta R$ for		
			$\frac{\Delta R}{R_0} = 20\%$	$\frac{\Delta R}{R_0} = 50\%$	$\frac{\Delta R}{R_0} = 100\%$
Framing Camera Silhouettes	0.1 - 0.25	2-5%	10-25%	4-10%	2-5%
Recovered Rod Profiles	0.015	0.3%	1.5%	0.6%	0.3%

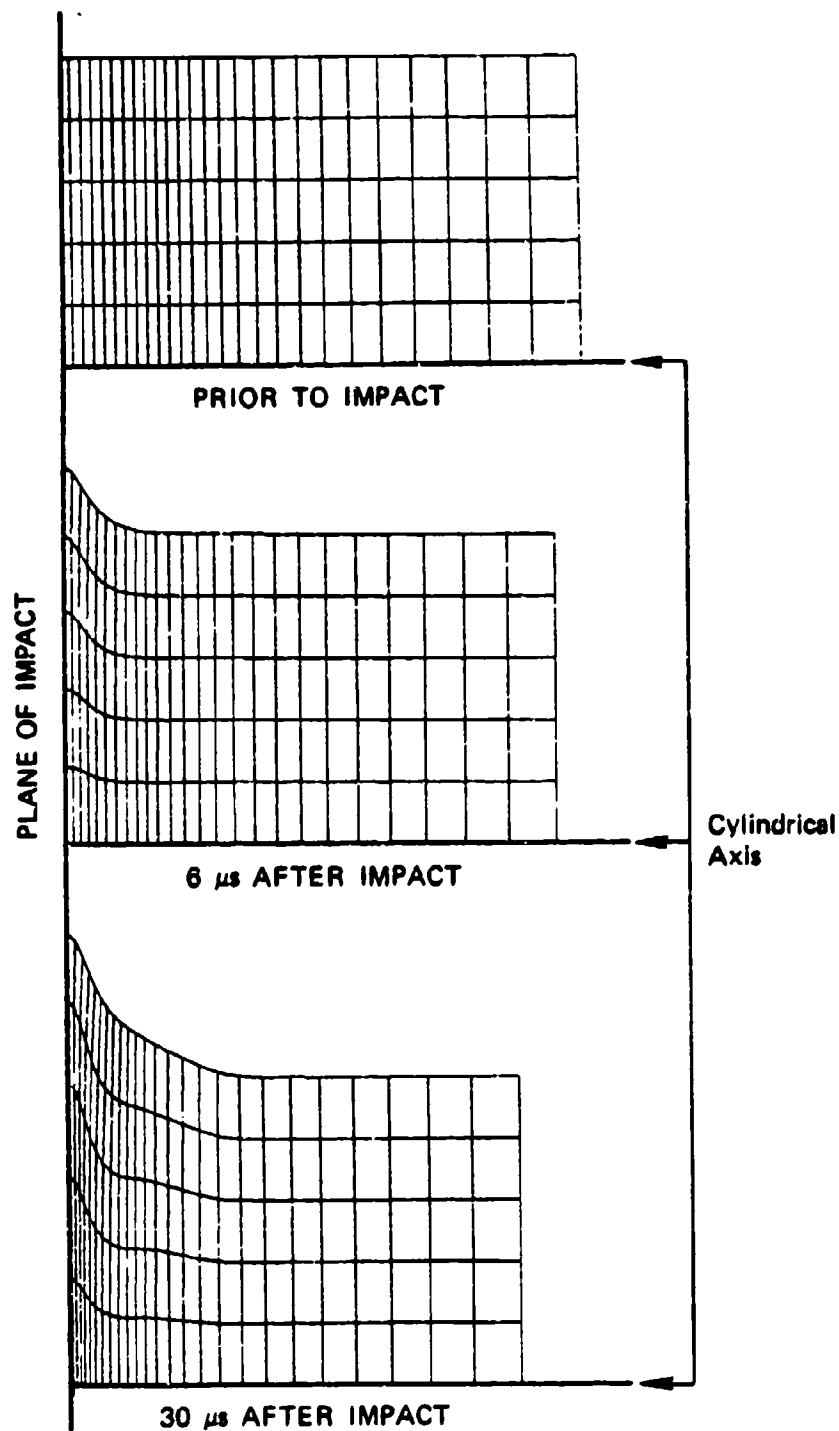
JA-314832-54A

FIGURE IV.10 UNCERTAINTIES IN OBTAINING DIGITIZED ROD PROFILES



JA-3722-21A

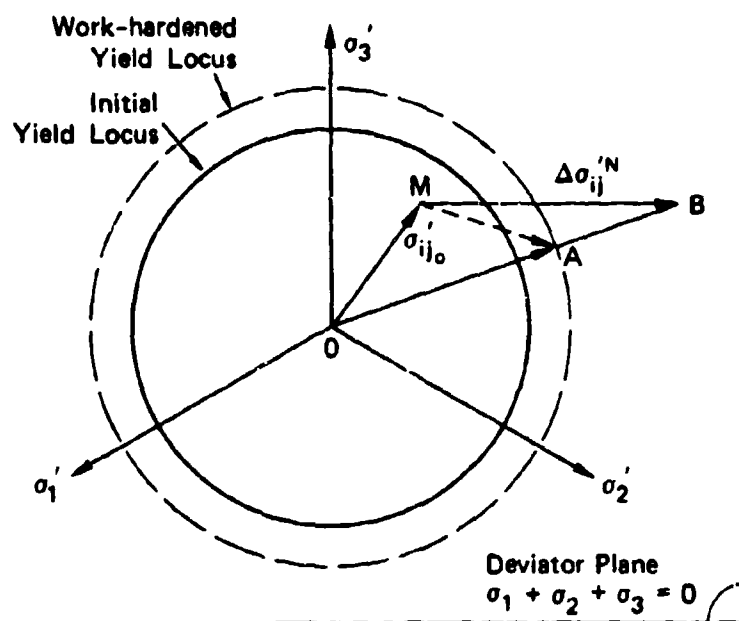
FIGURE IV.11 DEFORMATION CONTOURS FROM 4340 STEEL ($R_B 94$)
SYMMETRIC ROD IMPACT TEST NO. 4 AT 457 m/s



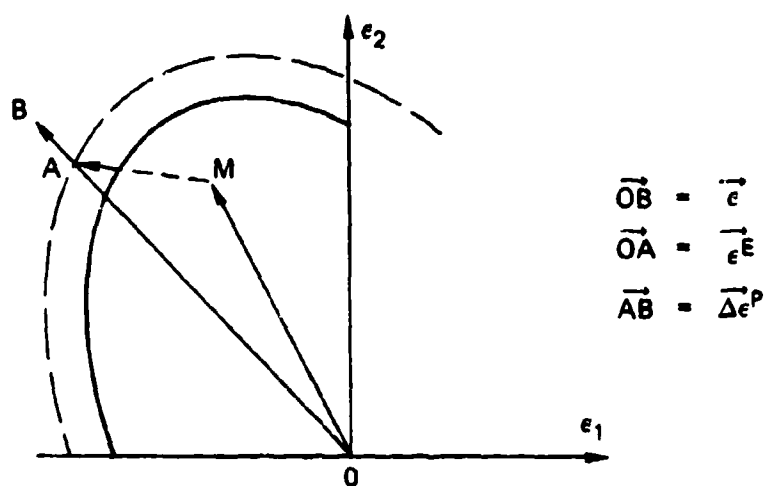
JA-3722-58

FIGURE IV.12 CELL OUTLINES AT THREE TIMES DURING SIMULATION OF SYMMETRIC ROD IMPACT

Note: Horizontal and vertical axes not to scale.
Cells near impact plane are originally square.



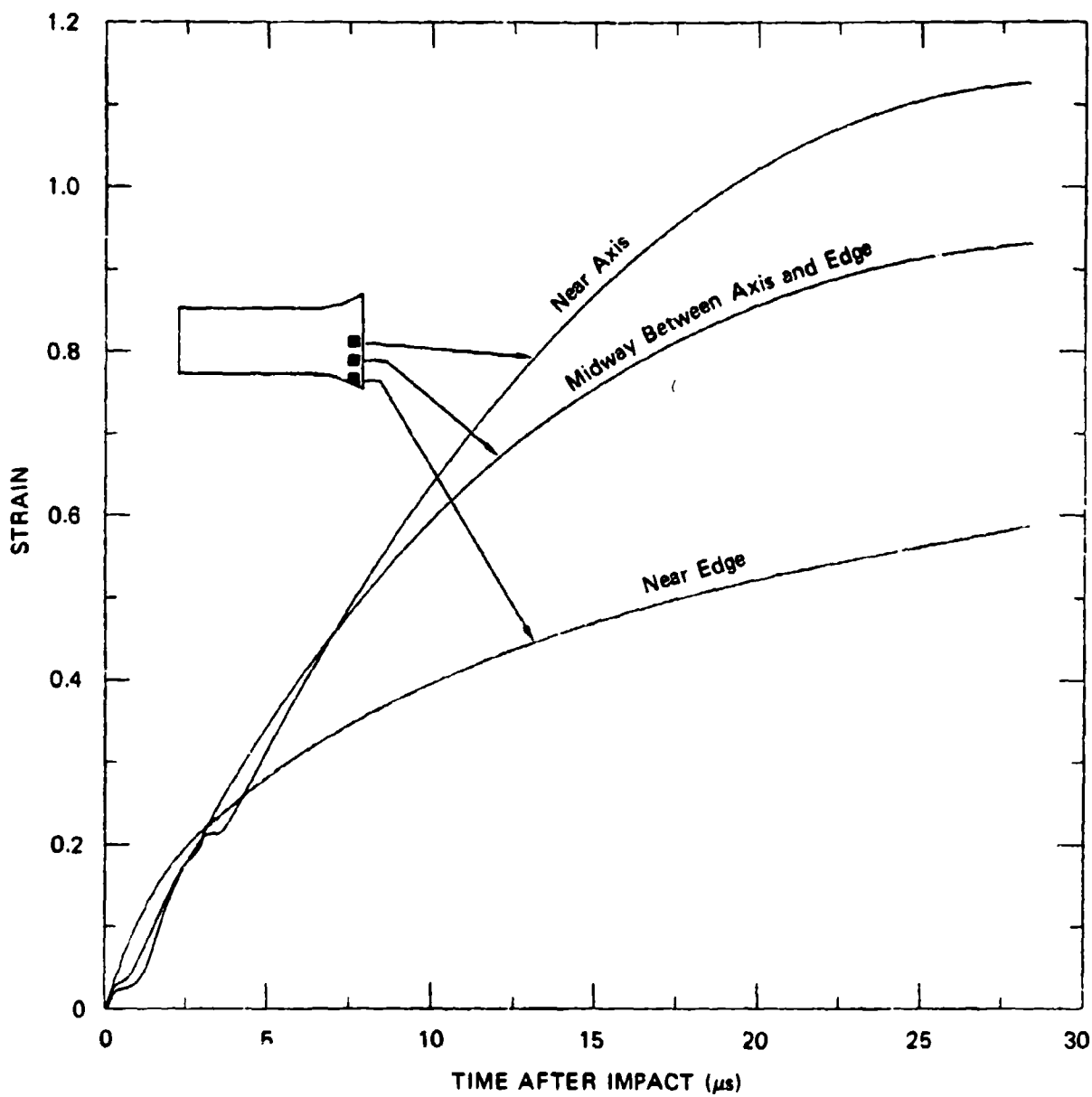
(a) Stress Space



(b) Strain Space

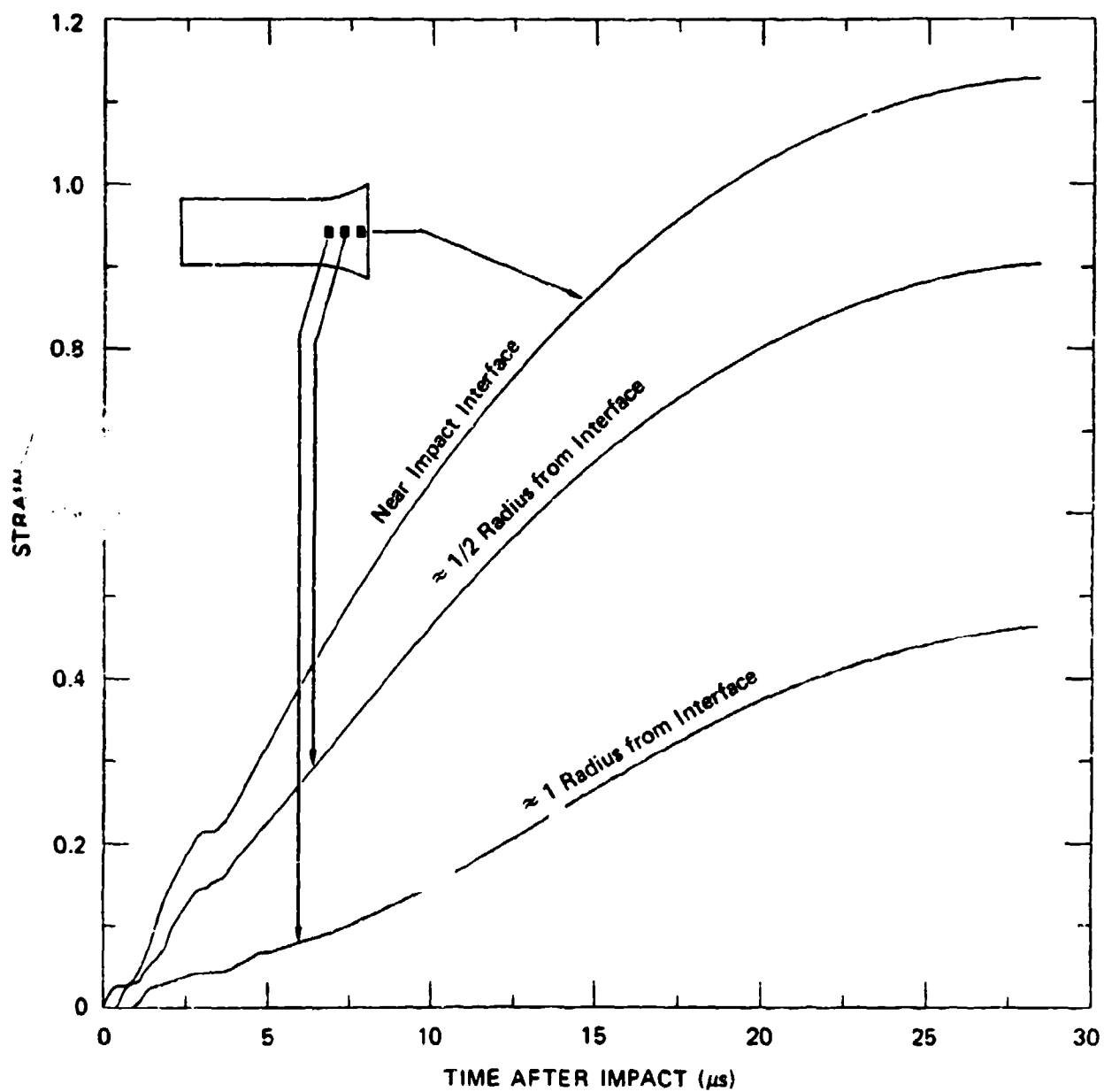
JA-314632-52

FIGURE IV.13 VECTORIAL REPRESENTATIONS OF PRINCIPAL STRESSES AND STRAINS DURING AN INTERVAL OF PLASTIC FLOW WITH WORK-HARDENING



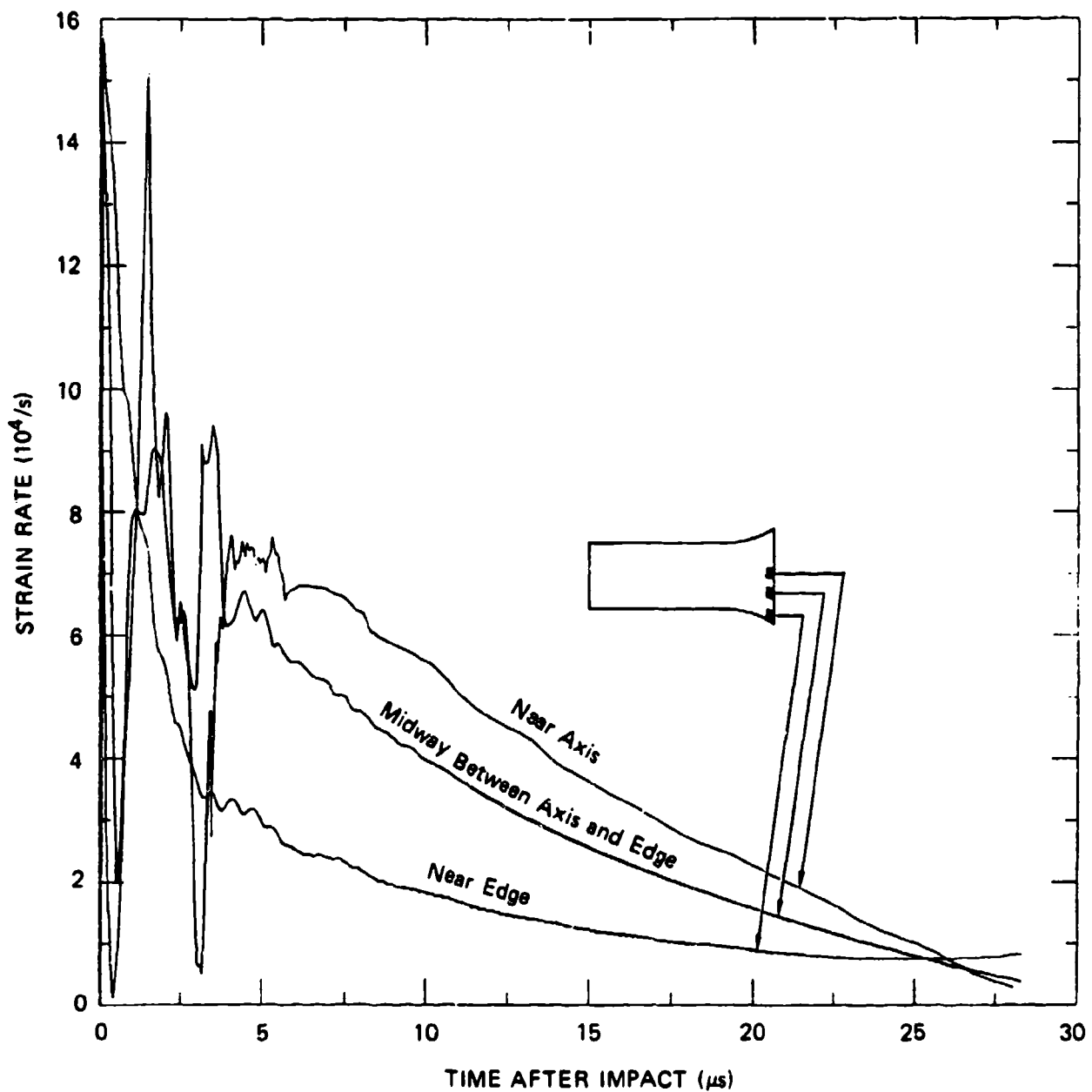
JA-3722-67

FIGURE IV.14 EQUIVALENT PLASTIC STRAIN HISTORIES AT IMPACT INTERFACE



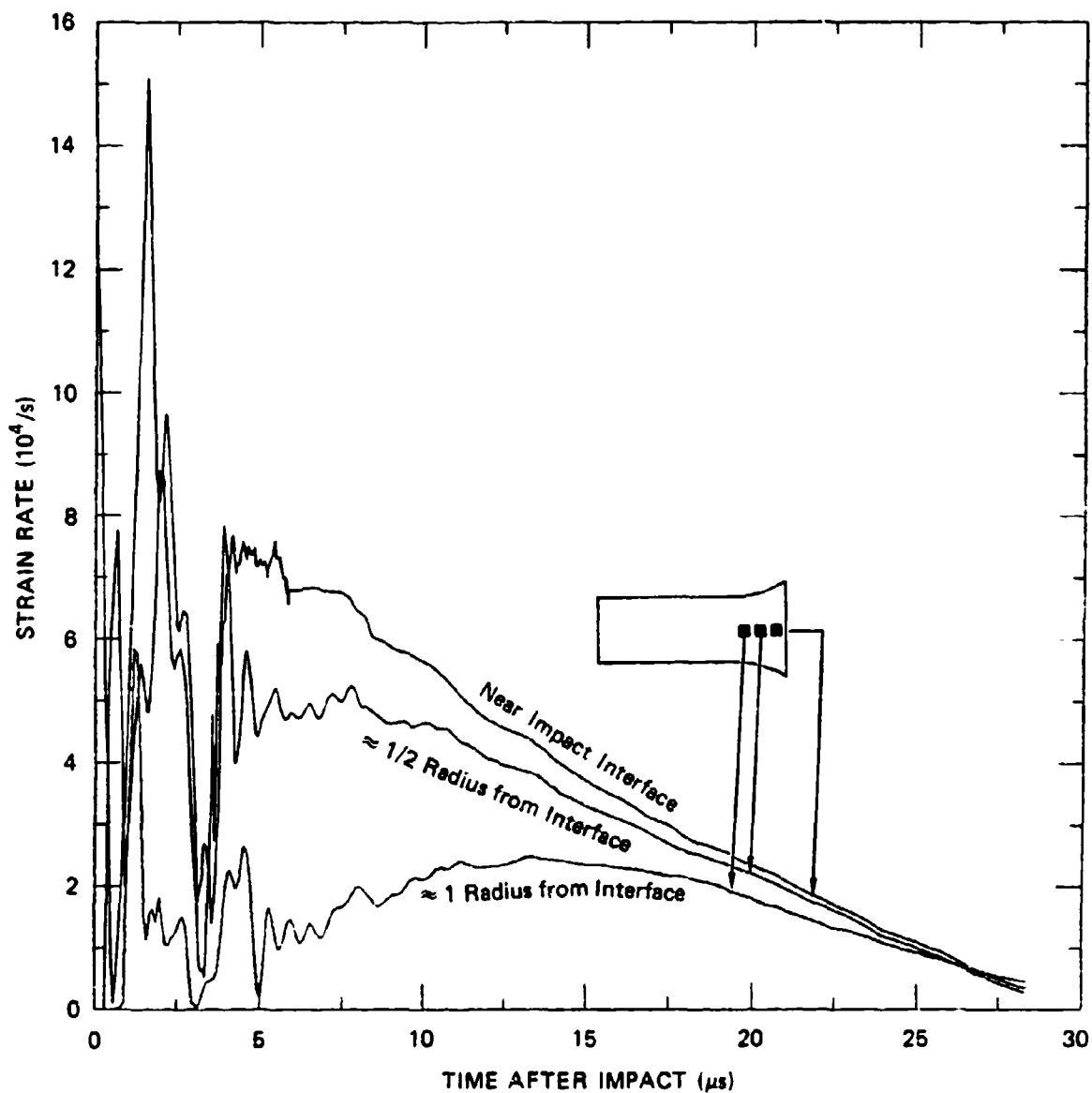
JA-3722-69

FIGURE IV.15 EQUIVALENT PLASTIC STRAIN HISTORIES ALONG ROD AXIS



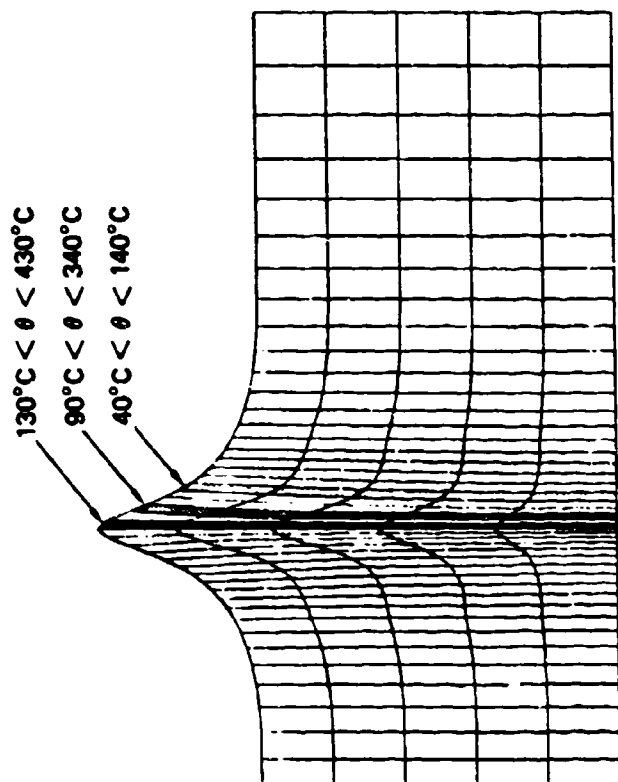
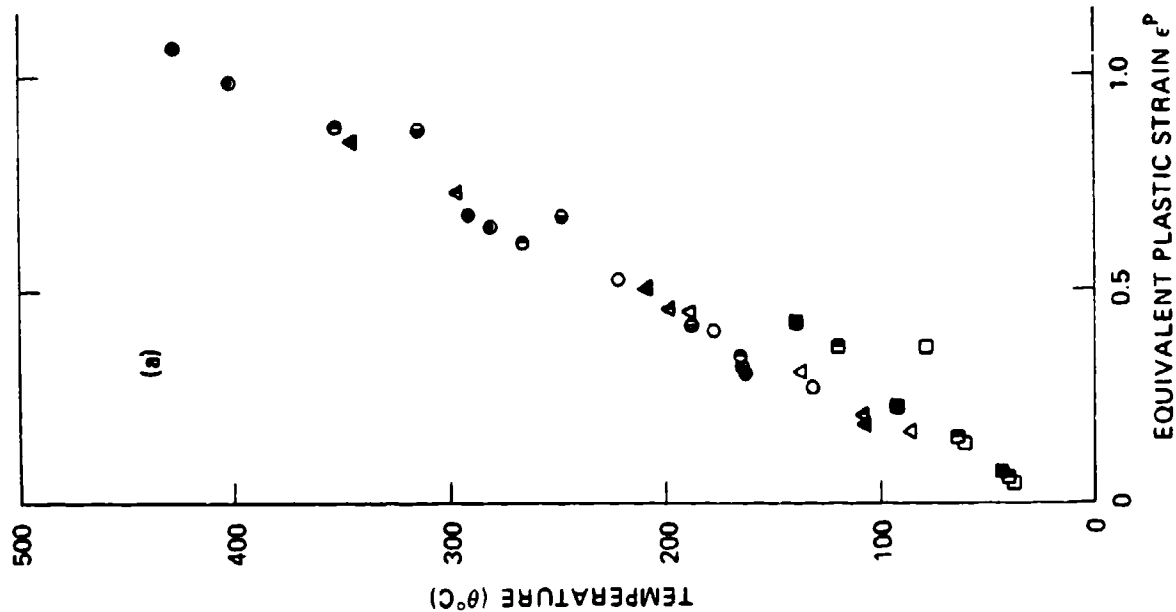
JA-3722-68

FIGURE IV.16 EQUIVALENT PLASTIC STRAIN RATE HISTORIES AT IMPACT INTERFACE



JA-3722-70

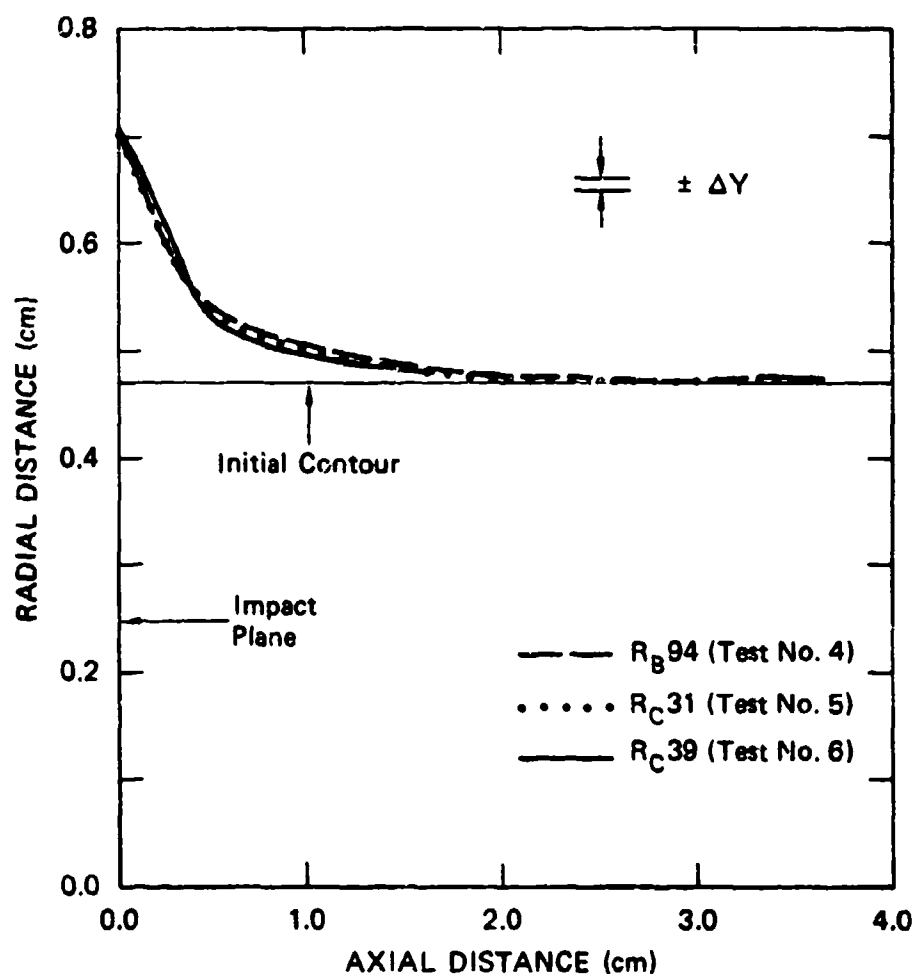
FIGURE IV.17 EQUIVALENT PLASTIC STRAIN RATE HISTORIES ALONG ROD AXIS



JA-314532-71A

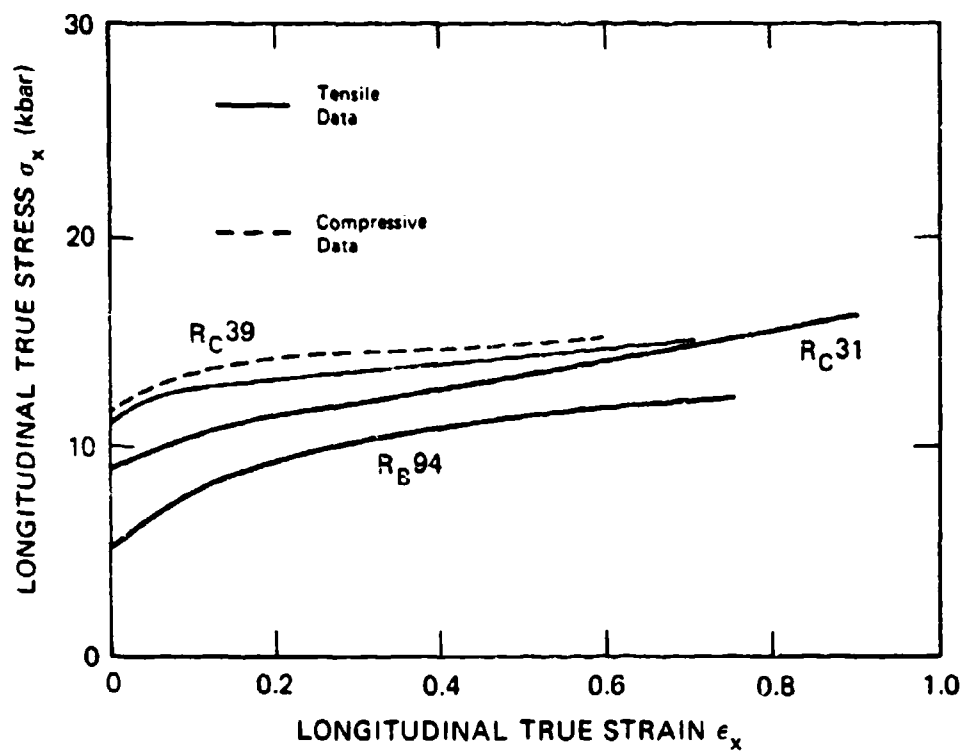
(b) Ranges of Deformation-Induced Temperatures,
20 μ s After Impact

FIGURE IV.18 TEMPERATURE CALCULATED FROM C-HEMP SRI SIMULATION OF TEST NO. 4
(a) AS A FUNCTION OF EQUIVALENT PLASTIC STRAIN AND (b) AT VARIOUS
POSITIONS WITHIN THE ROD



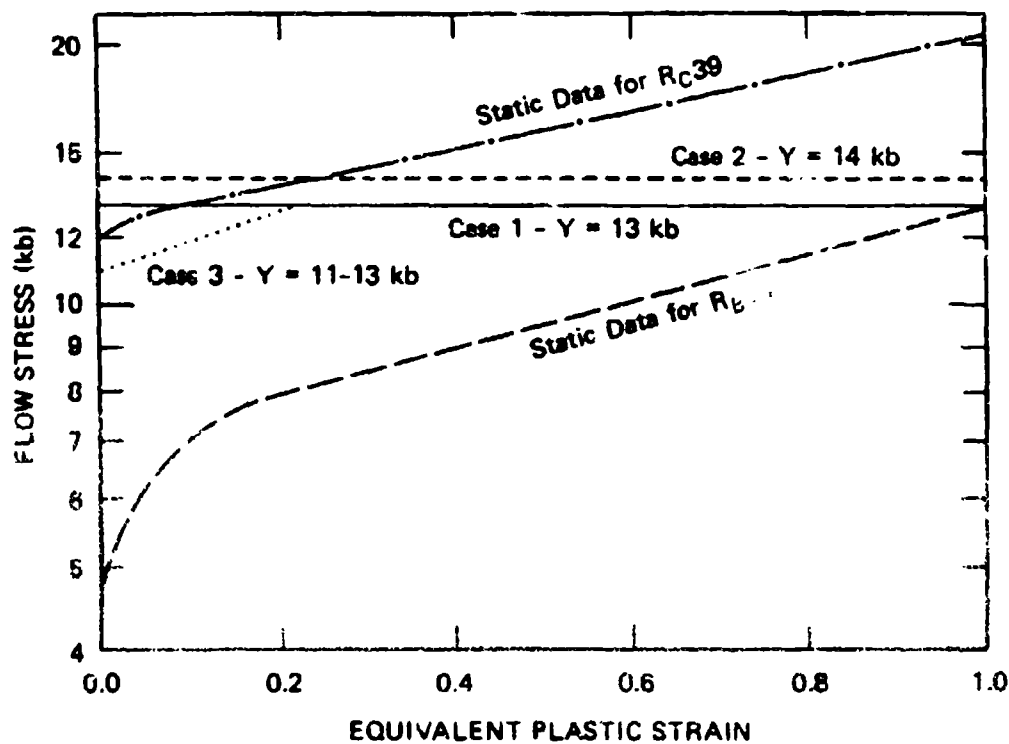
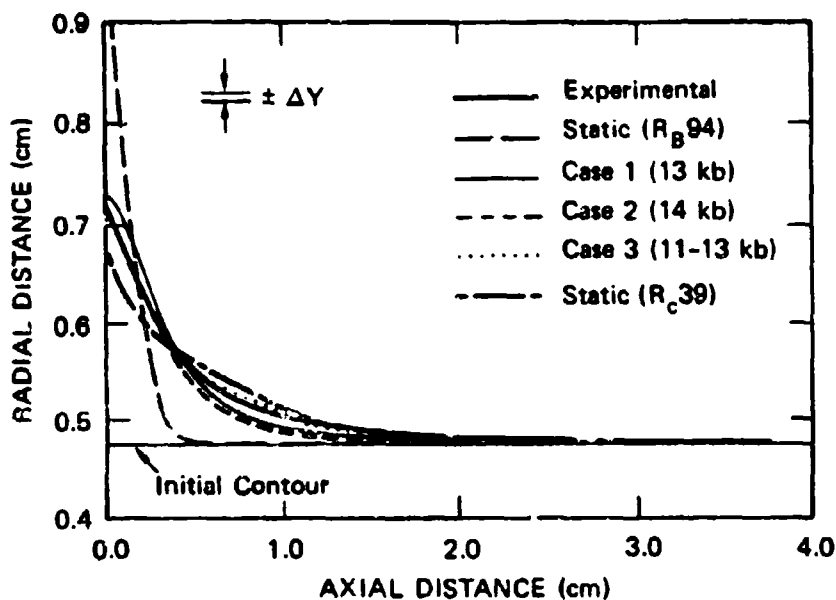
JA-3722-228

FIGURE IV.19 DEFORMATION CONTOURS 28 μ s AFTER 4340 STEEL SYMMETRIC ROD IMPACTS AT 457 m/s



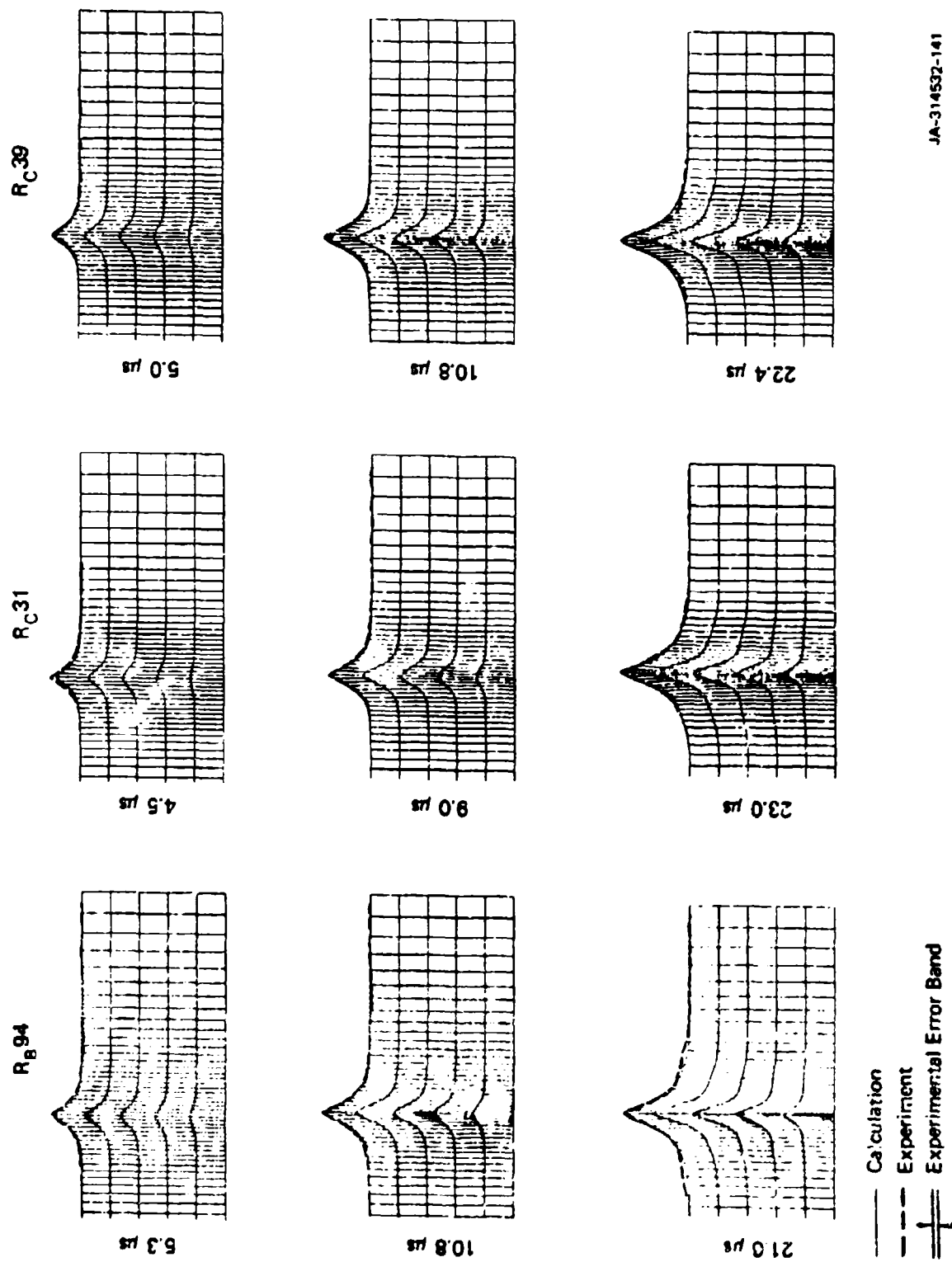
JA-314632-68A

FIGURE IV.20 STATIC TENSILE AND COMPRESSIVE DATA FOR 4340 STEEL, AMBIENT TEMPERATURE, FOR THREE HARDNESSES



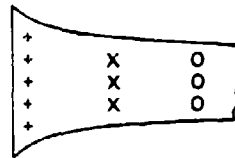
JA-3722-518

FIGURE IV.2: COMPARISON OF EXPERIMENTAL PROFILES OF 20 μ s AFTER SYMMETRIC IMPACT OF 430 STEEL RODS, WITH COMPUTED PROFILES, USING DIFFERENT FLOW CURVES



JA-314532-141

FIGURE IV.22 CALCULATED AND EXPERIMENTAL PROFILES AT INTERMEDIATE TIMES AFTER IMPACT AT 457 m/s

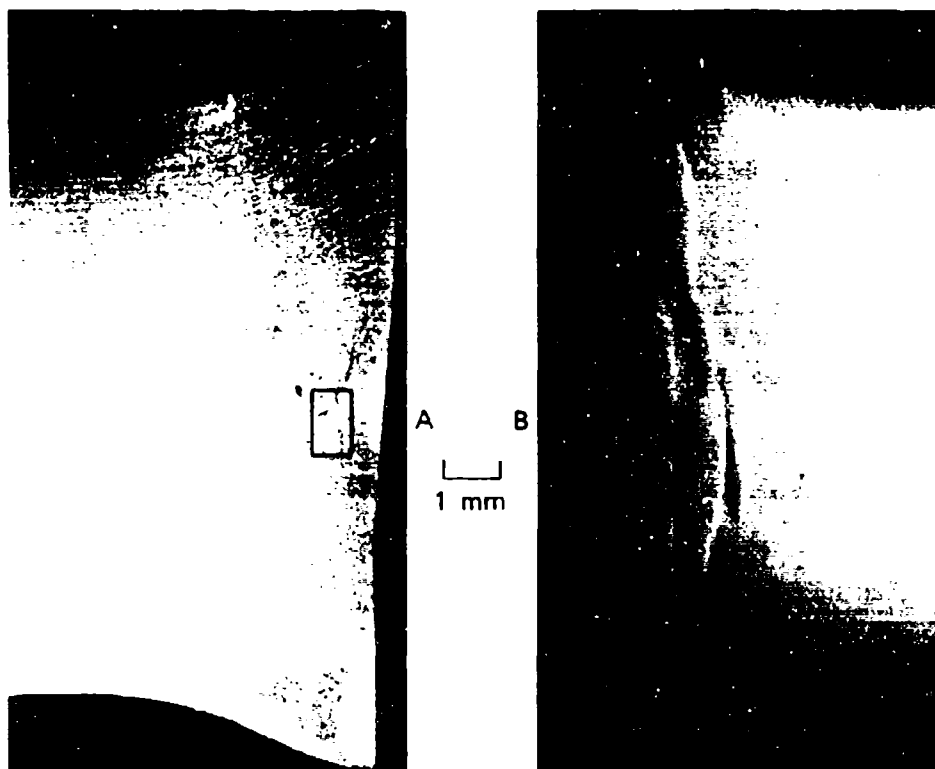


FINAL AVERAGE HARDNESS

Initial Hardness	+ + + + + + Along Impact Edge ($\epsilon \approx 80-100\%$)	X X X X ≈ One Diameter Distant ($\epsilon \approx 15-20\%$)	O O O O ≈ Two Diameters Distant ($\epsilon < 5\%$)
R _B 94	R _C 38-39	R _C 36-37	R _C 30-31
R _C 31	R _C 38-39	R _C 37	R _C 32-33
R _C 39	R _C 42-43	R _C 41-42	R _C 40-41

JA-3722-37

FIGURE IV.23 MEASURED HARDNESS VALUES IN DEFORMED REGIONS OF 4340 STEEL RODS RECOVERED FROM SYMMETRIC IMPACT AT 457 m/s



Magnified detail from above



Magnified detail from above

JP-3/22-28

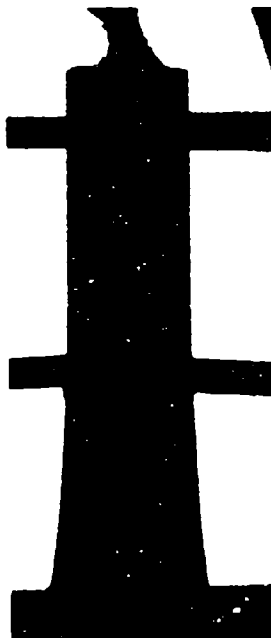
FIGURE IV.24 SLICE THROUGH IMPACT REGION OF 4340 STEEL RODS ($R_B 94$)
RECOVERED FROM SYMMETRIC IMPACT AT 457 m/s, AND
ENLARGED VIEWS OF THE DAMAGED REGION



(a) 9.5 μ s



(b) 19.3 μ s



(c) 43.7 μ s



(d) 63.2 μ s

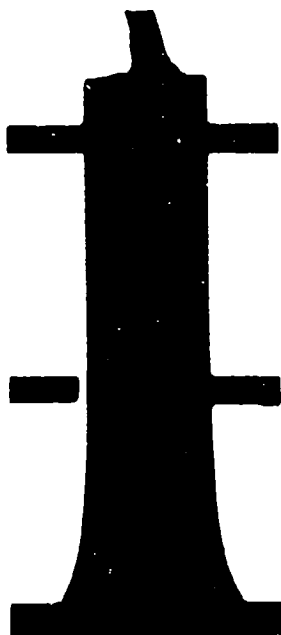
JA-3722-91

FIGURE IV.25 SILHOUETTES OF 4340 STEEL ROD AT 721°C FOLLOWING ASYMMETRIC IMPACT AT 178 m/s (TEST NO. 12)

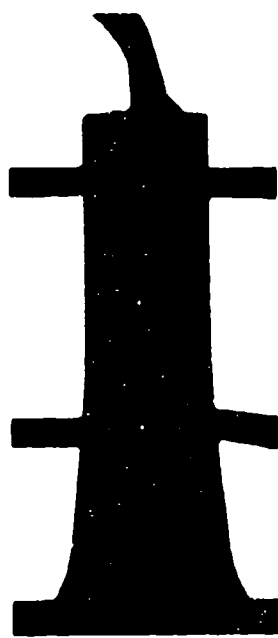
Times shown are from impact. Original rod dimensions are 4.45 by 0.95 cm.



(a) 8.6 μ s



(b) 27.8 μ s



(c) 47.0 μ s

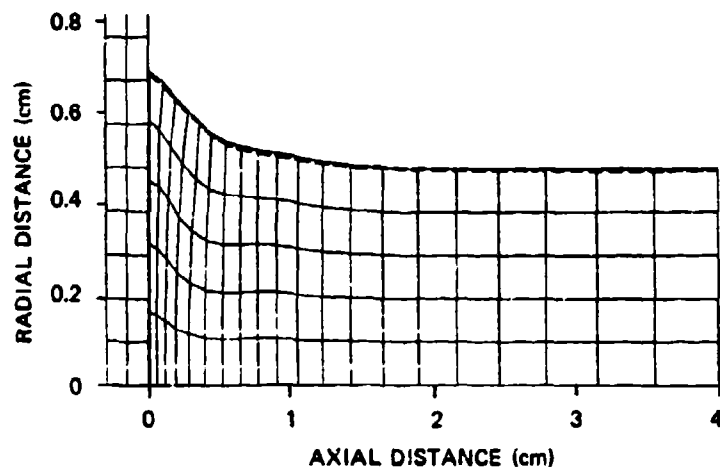


(d) 66.2 μ s

JA-3722-92

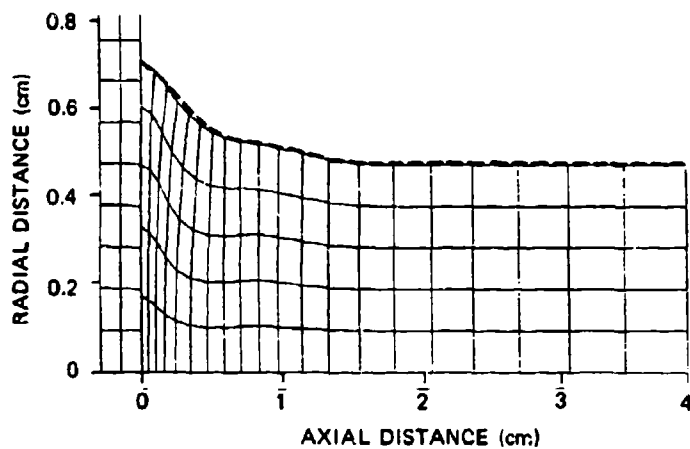
FIGURE IV.26 SILHOUETTES OF 4340 STEEL ROD AT 947° C FOLLOWING ASYMMETRIC IMPACT AT 181 m/s (TEST NO. 13)

Times shown are from impact. Original rod dimensions are 4.45 by 0.95 cm.



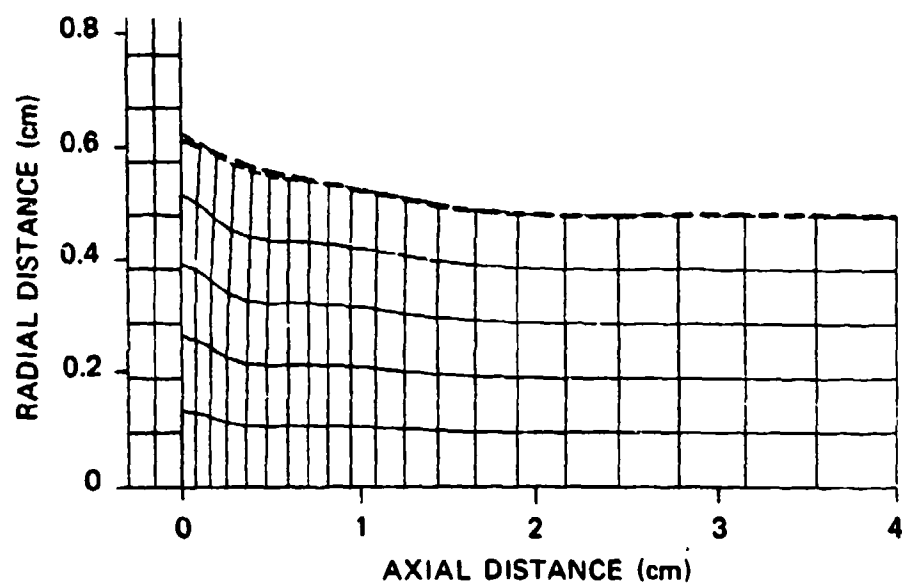
JA-314832-143

FIGURE IV.27 COMPARISON OF FINAL EXPERIMENTAL ROD PROFILE (DOTTED LINE) AND COMPUTATIONAL PROFILE 50 μ s AFTER SIMULATED IMPACT FOR ASRI TEST NO. 9 (4340 STEEL AT 340°C)



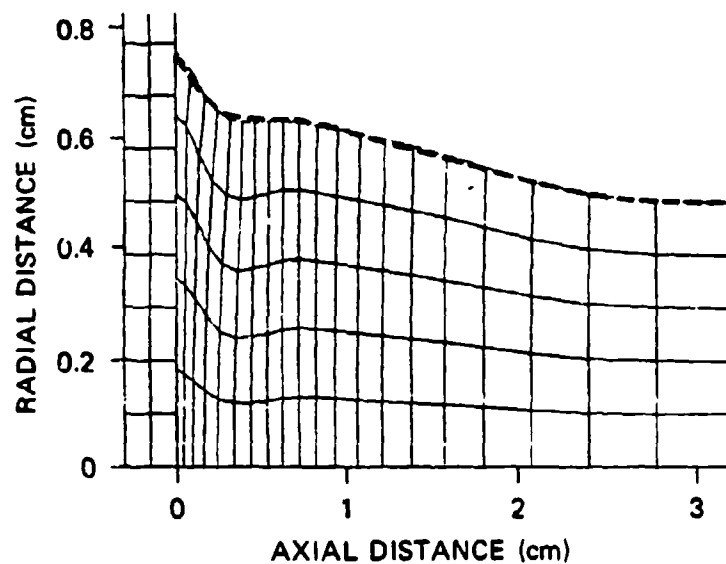
JA-314832-144

FIGURE IV.28 COMPARISON OF FINAL EXPERIMENTAL ROD PROFILE (DOTTED LINE) AND COMPUTATIONAL PROFILE 50 μ s AFTER SIMULATED IMPACT FOR ASRI TEST NO. 10 (4340 STEEL AT 403°C)



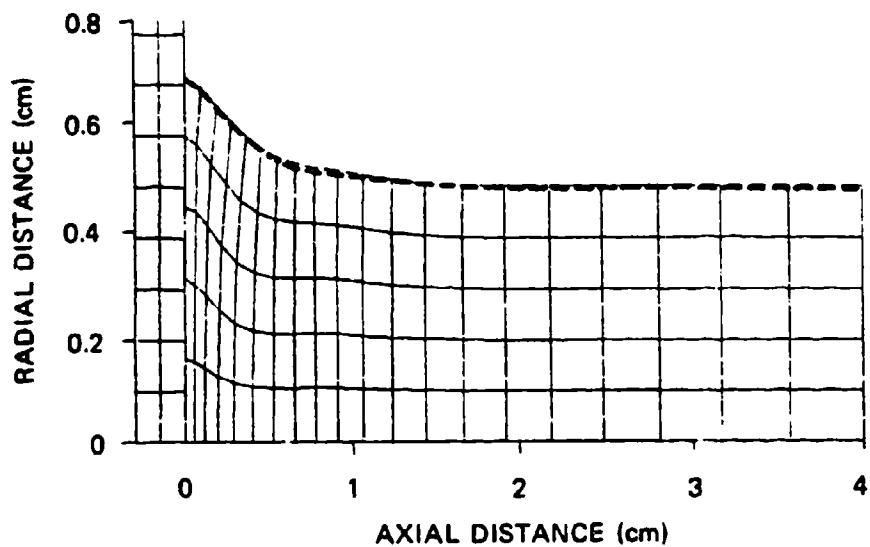
JA-314532-145

FIGURE IV.29 COMPARISON OF FINAL EXPERIMENTAL ROD PROFILE (DOTTED LINE) AND COMPUTATIONAL PROFILE 50 μ s AFTER SIMULATED IMPACT FOR ASRI TEST NO. 12 (4340 STEEL AT 721°C)



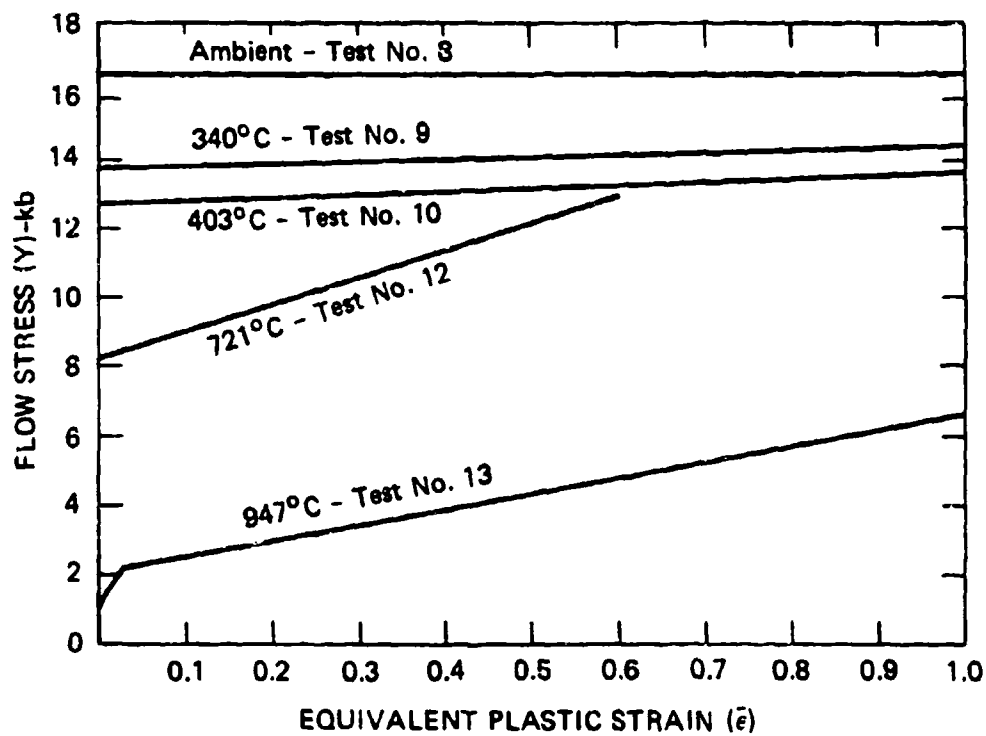
JA-314532-146

FIGURE IV.30 COMPARISON OF FINAL EXPERIMENTAL ROD PROFILE (DOTTED LINE) AND COMPUTATIONAL PROFILE 100 μ s AFTER SIMULATED IMPACT FOR ASRI TEST NO. 13 (4340 STEEL AT 947°C)



JA-314832-147

FIGURE IV.31 COMPARISON OF FINAL EXPERIMENTAL ROD PROFILE (DOTTED LINE) AND COMPUTATIONAL PROFILE 40 μ s AFTER SIMULATED IMPACT FOR ASRI TEST NO. 8 (4340 STEEL AT AMBIENT TEMPERATURE)



JA-314632-148

FIGURE IV.32 INPUT FLOW CURVES USED IN C-HEMP SIMULATIONS OF 4340 ASRI TESTS

CONTENTS

V DERIVATION OF THE ADIABATIC SHEAR BAND NUCLEATION AND GROWTH RATE FUNCTIONS USED IN SHEAR4

A.	Introduction.....	V-1
B.	Nucleation Rate.....	V-2
C.	Growth Rate.....	V-8
D.	Size of Jog, B.....	V-9
E.	Discussion.....	V-10
F.	References.....	V-10

V DERIVATION OF THE ADIABATIC SHEAR BAND NUCLEATION AND GROWTH RATE FUNCTIONS USED IN SHEAR4

A. Introduction

As described in Section VI, the SHEAR4 subroutine for describing adiabatic shear band kinetics assigns all plastic slip to a discrete number of planes (up to nine) in a given material element. The material element (computational cell) represents a material point in continuum mechanics. SHEAR4 also generates shear bands on each material plane in the material element. Rather than attempt to describe each individual shear band, SHEAR4 assigns to each plane a distribution of shear bands of various sizes, and updates the distribution as new bands are nucleated and old bands grow (extend). The evolving shear band distribution functions serve as the link between the microscopic and continuum levels, and also have the desirable feature of making the evolving shear band damage independent of computational cell size.

A complete specification of the shear banding in SHEAR4 thus requires a nucleation rate function that specifies, on each plane, threshold criteria for nucleation, and the rate at which the number of bands per unit volume increases after the threshold criteria are met. The nucleation rate function must also specify the band sizes (extent) on nucleation.

In addition to the nucleation rate function, we must also specify the rate at which the bands grow (extend) after nucleation. Finally, we must specify the band "jog", B (i.e., the slip accommodated by each band). B is the macroscopic equivalent of the Burgers vector for atomic dislocations.

The nucleation and growth rate functions form the "damage evolution" relation that is required for any internal state variable description of

damage. In the following subsections we derive the nucleation and growth rate relations that are currently used in SHEAR4.

B. Nucleation Rate

The conditions for localization of a planar flow perturbation of infinite extent have been studied, both numerically¹ and analytically² (also, T. W. Wright and R. C. Batra, personal communication). However, the adiabatic shear bands observed in our experiments are not infinite, but appear to nucleate at points and grow radially outward like macroscopic dislocations with edge and screw components.

To better understand the nucleation process for such bands, we performed the numerical calculation illustrated in Figure V.1. SHEAR4 was used in its plasticity mode only (no shear bands were created) to computationally simulate a situation in which a planar crack was loaded remotely in pure shear across the crack face. Plane strain conditions were assumed.

We see from Figure V.1 that strain concentrations occur at the crack tips and extend about one crack half-length, R , from the tips. There is a strain-free "dead zone" extending about $R/2$ from each crack face. For the 4340 HRC 40 steel properties used in the calculation, when the remotely applied strain in the crack plane was 0.13, the strain magnification at the crack tips was about 2.

Because there is no characteristic size governed by material properties in the calculation, the size of the region of magnified strain at the crack tip, r , is a given fraction of the crack half-length, R , for a given remotely applied strain. This result will hold as long as material rate effects and inertia are negligible.

If the deformation occurs rapidly enough to maintain adiabatic conditions around the crack, the threshold condition for nucleation is that the strain at the crack tips is sufficient to cause the stress to drop. In short, we assume that the nucleation threshold condition for a

planar imperfection is identical to the growth (extension) threshold condition.

Figure V.2 shows static adiabatic yield curves for three hardnesses of 4340 steel. Under these conditions, most of the material strength has been lost for strains exceeding 1.0 to 1.4, and the stress begins to drop at strains of 0.2 to 0.3. The nucleation threshold condition is thus that the local strain at the crack tip reaches 0.2 to 0.3.

Our criterion for adiabaticity is that significant heat cannot flow a distance R (out of the dead zone) during the loading time of interest. That is, the imperfection must remain thermally autonomous.

To make this requirement precise, refer to Figure V.1. The remotely applied strain in the crack plane is approximately given by

$$\Delta \epsilon_R \approx B/R \quad (V.1)$$

Furthermore, the remote strain rate is given by

$$\dot{\epsilon}_R = \Delta U/R, \quad (V.2)$$

where ΔU is the difference in particle velocity measured from R/2 above the crack to R/2 below it.

We now state our criterion for adiabaticity:

$$\Delta U > v_H, \quad (V.3)$$

where v_H is a pseudovelocity of heat flow. That is, if particles on either side of the crack are moving past one another faster than heat can flow between them, adiabaticity will be approximately maintained.

The value of v_H was derived from analysis of heat flow away from a hot slab, maintained at constant temperature, suddenly placed in contact with a cold material. The well-known heat diffusion equation can be examined to determine the pseudovelocity of propagation of a given

temperature. If the temperature chosen is one-fourth that of the hot slab temperature, one finds that

$$v_H \approx \frac{10k}{d} \quad , \quad (V.4)$$

where k is the thermal diffusivity and d is the distance the heat has flowed, i.e., the distance into the originally cold material.

If we now replace d with R in Eq. (V.4), and combine with Eqs. (V.2) and (V.3), we obtain for the adiabaticity criterion:

$$R > \sqrt{\frac{10k}{\dot{\epsilon}_R}} \quad (V.5)$$

Inequality (V.5) provides information regarding the minimum size of crack-like imperfections that can be nucleated. That is, for the CFC experiments discussed in Section VI and Ref. 1, the strain rates during nucleation were about 10^4 s^{-1} . For steels, $k \approx 0.1 \text{ cm}^2/\text{s}$, so (V.5) tells us that cracks smaller than about 0.1 mm will not be nucleated in such experiments. This analysis agrees with observations that the smallest bands seen were about 0.1 mm in extent, and no obvious microscopic nucleation sites were seen, although void patches about 0.1 mm in size were seen in the Hopkinson bar experiments (see Section III), and void nucleation in tensile tests was observed at prior austenitic grain boundaries, which also have a characteristic size of 0.1 mm (see Section VII).

We next discuss the size distributions of the nucleated imperfections. In our experimental observations of shear band size distributions, we found that they usually approximated the form

$$N_g = N_0 \exp(-R/R_1) \quad , \quad (V.6)$$

where N_g is the number of bands per unit volume in a given material plane with sizes greater than R , N_0 is the total number of bands per unit

volume in the plane, and R_1 is the characteristic size of the distribution.

If a material had an initial distribution of crack-like imperfections given by Eq. (V.6), Eq. (V.5) tells us that only those imperfections large enough to satisfy the inequality will be nucleated. However, it is inconvenient to have a lower size cutoff during nucleation in SHEAR4, and as we shall see later, the smallest bands will grow very slowly. Therefore, we simply let R_1 be the "adiabatic limit size" from (V.5):

$$R_1 = \sqrt{\frac{10k}{\dot{\epsilon}_R}}, \quad (V.7)$$

and we nucleate the bands with the distribution given by Eq. (V.6).

Another problem with Eq. (V.6) is that it produces a few very large bands upon nucleation. Such large bands are not observed experimentally unless correspondingly large imperfections are initially present. Therefore, SHEAR4 contains an upper cutoff for the imperfection size, R_{\max} . For values of $R > R_{\max}$, N_g is set to zero. R_{\max} must be determined experimentally.

We now are in a position to derive the nucleation rate function. We begin by writing

$$\begin{aligned} \dot{N} &= \frac{\text{Number of available nucleation sites}}{\text{Incubation time}} \\ &= \frac{N_0 f - N}{\tau}, \end{aligned} \quad (V.8)$$

where

\dot{N} = number of bands nucleated per unit volume per unit time

N_0 = density of nucleating imperfections

f = fraction of N_0 that can become nucleation sites

τ = incubation time.

Thus,

$N_0 f - N$ = current density of nucleation sites.

If the nucleating imperfections are widely spaced so no interaction between them is possible, then $f = 1$. However, if there is a high density of nucleating imperfections, band autonomy requires that the bands be spaced at least one heat flow spacing apart; i.e., the closest possible band spacing is given by the minimum from inequality (V.5):

$$\text{Minimum spacing} = \sqrt{\frac{10k}{\dot{\epsilon}_R}}$$

If the bands are spaced with the above minimum spacing, the volume per band is on the order of $(10k/\dot{\epsilon}_R)^{3/2}$. Thus, the density of bands with minimum spacing is on the order of $(\dot{\epsilon}_R/10k)^{3/2}$.

To cover both widely spaced and closely spaced nucleating imperfections, we take

$$f = \text{Min} \left[(\dot{\epsilon}_R/10k)^{3/2}/N_0, 1 \right] \quad (\text{V.9})$$

We next estimate the incubation time, τ . Referring again to Figure V.1, we see that the local strain rate at the crack tip can be written

$$\dot{\epsilon}_L = M \dot{\epsilon}_R, \quad (\text{V.10})$$

where M was about equal to 2 in the example calculation. We estimate the incubation time to be the time required to bring the crack tip strain to

the completely softened value, ϵ_m (1-1.4 for 4340 steel), from the nucleation value, ϵ_{cr} . Thus

$$\tau \approx \frac{(\epsilon_m - \epsilon_{cr})}{M \dot{\epsilon}_R} \quad , \quad (V.11)$$

where ϵ_{cr} is the adiabatic strain at which the stress begins to drop.

Values of $\epsilon_m - \epsilon_{cr}$ can often be obtained from thermal softening data in handbooks. However, a rough estimate can be obtained from the formula

$$\sigma_y (\epsilon_m - \epsilon_{cr}) \approx \rho E_m \quad , \quad (V.12)$$

where σ_y is the yield strength at the onset of nucleation, ρ is the density, and E_m is the specific melt energy. Since ρ and E_m are easily available material properties and since Eq. (V.11) is only approximate in any case, we replace (V.11) with

$$\tau = \frac{\rho E_m}{\sigma_y M \dot{\epsilon}_R} \quad (V.13)$$

We now combine Eqs. (V.8), (V.9), and (V.13) to obtain the nucleation rate function:

$$\dot{N} = \left(\frac{\sigma_y}{\rho E_m} \right) M \dot{\epsilon}_R \left[(\dot{\epsilon}_R / 10k)^{3/2} - N \right] H \left(\epsilon_R - \frac{\epsilon_{cr}}{M} \right) \quad (V.14)$$

for closely spaced nucleation sites, i.e., $(\dot{\epsilon}_R / 10k)^{3/2} / N_0 < 1$,

and

$$\dot{N} = \frac{\sigma_y}{\rho E_m} M \dot{\epsilon}_R [N_0 - N] H(\epsilon_R - \frac{\epsilon_{cr}}{M}) \quad (V.15)$$

for widely spaced nucleation sites, i.e., $(\dot{\epsilon}_R/10k)^{3/2}/N_0 \gg 1$, where $H(\epsilon_R - \frac{\epsilon_{cr}}{M})$ is a Heaviside function.

C. Growth Rate

To derive the adiabatic shear band growth rate used in SHEAR4, we refer again to Figure V.1. We now interpret the crack-like imperfection in the figure as a nucleated shear band. The criteria for band growth (extension) are that adiabaticity be maintained and that the strain at the band tip attains ϵ_m . The time to reach ϵ_m is the incubation time from Eq. (V.11). The growth rate is thus

$$\dot{R} = \frac{r M}{(\epsilon_m - \epsilon_{cr})} \dot{\epsilon}_R \quad (V.16)$$

where r is the size of the magnified strain region at the band tip. As discussed earlier, in the absence of material rate effects or inertial effects, r is proportional to R :

$$r = \beta R \quad (V.17)$$

Thus, (V.16) becomes

$$\dot{R}/R = \frac{\beta M}{(\epsilon_m - \epsilon_{cr})} \dot{\epsilon}_R \quad (V.18)$$

The values of β , M , ϵ_m , and ϵ_{cr} are material properties and must come from analyses or numerical simulations like that of Figure V.1. From that calculation, we estimate

$$\beta \cong 1$$

$$M \cong 2.$$

As discussed earlier, $\epsilon_{cr} \cong 0.2$, $\epsilon_m \cong 1$.

Thus, for 4340 steel, Eq. (V.18) becomes

$$\dot{R}/R \approx 2.5 \dot{\epsilon}_R \quad (V.19)$$

This expression is expected to hold until inertial effects become important. At that point, SHEAR4 limits the band velocity to the shear wave velocity. Recent work by Wu, Toullos, and Freund⁴ also suggests a wave velocity limit.

D. Size of Jog, B

From Figure V.1 we obtained Eq. (V.1):

$$\Delta\epsilon_R \approx B/R$$

We can also rewrite Eq. (V.10) as

$$\Delta\epsilon_L = M \Delta\epsilon_R \quad ,$$

where $\Delta\epsilon_L$ is the local strain at the band tip. The threshold condition for band nucleation and growth is

$$\Delta\epsilon_L = \epsilon_{cr} \quad . \quad (V.20)$$

Thus,

$$\Delta\epsilon_R = \frac{B}{R} = \frac{\epsilon_{cr}}{M} \quad ,$$

$$\text{or } B \approx (\epsilon_{cr}/M)R \quad . \quad (V.21)$$

This linear dependence of the jog, B, on band length, R, was observed in the experiments discussed in Section VI and Ref. 1.

E. Discussion

The derived nucleation and growth relations are approximate and can only serve as starting points for iterative computations with SHEAR4 to simulate experimental results. Nevertheless, comparisons with experimental data show reasonable agreement not only for the form of the equations, but also for the numerical values. Table V.1 compares the derived and experimentally determined SHEAR4 parameters from Hopkinson torsion bar and controlled fragmenting cylinder experiments described in Sections III and VI, and Ref. 1.

F. References

1. L. Seaman, D. R. Curran, D. C. Erlich, T. Cooper, and O. Dullum, Proceedings of DYMAT conference, Paris, Sept. 2-5, 1985
2. A. M. Merzer, J. Mech. Phys. Solids 30, 323 (1982).
3. T. G. Shawki, R. J. Clifton, and G. Majda, Technical Report No. 3, U.S. Army Research Office Grant DAAG29-81-K-0121 (1983).
4. F. H. Wu, M. Toullos, and L. B. Freund, Brown University NSF Material Research Laboratory Report No. MRL E-151 (1984).

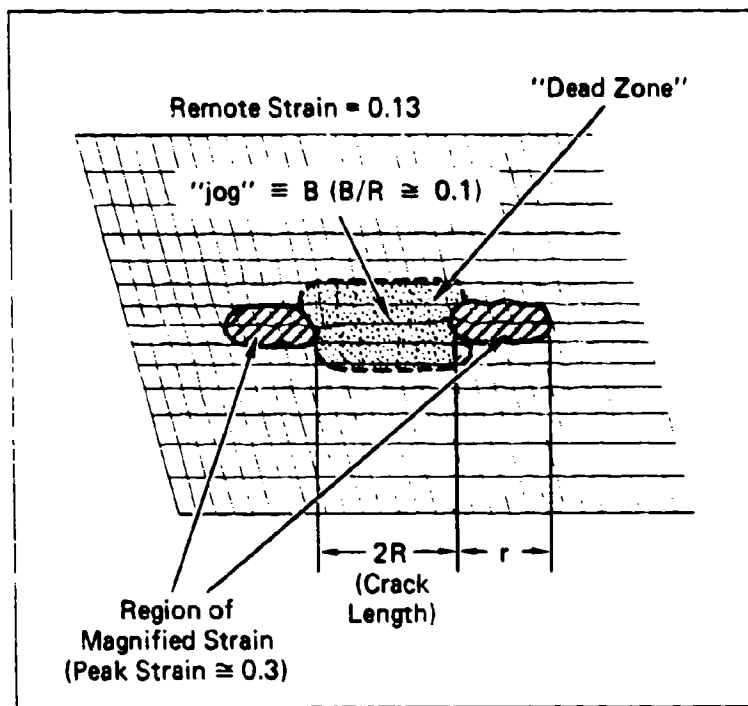
Table V.1

COMPARISON OF DERIVED AND EXPERIMENTALLY DETERMINED SHEAR⁴ NUCLEATION
AND GROWTH PARAMETERS FOR 4340 STEEL EXPANDING CYLINDER AND
HOPKINSON TORSION BAR EXPERIMENTS

Variable	Value Experimentally Determined	Value Derived
R_1 (nucleation size parameter)	0.01 cm ^(b)	0.01 cm ($\dot{\epsilon} = 10^4 \text{ s}^{-1}$)
ϵ_R (nucleation threshold)	0.1 ^(a) to 0.24 ^(b)	$\frac{\epsilon_{cr}}{M} \approx \frac{0.2}{2} = 0.1$
B/R (ratio of jog to band length)	0.07 ^(b)	0.1
$\frac{\beta M}{\epsilon_m - \epsilon_{cr}}$ (growth coefficient)	60 ^(b)	2.5
$\tau = \frac{\epsilon_m - \epsilon_{cr}}{M \dot{\epsilon}_R}$ (incubation time)	$\sim 45 \mu\text{s}$ ^{(a)*}	$\frac{(1 - 0.2)}{(2)(5900 \text{ s}^{-1})} = 60 \mu\text{s}.$

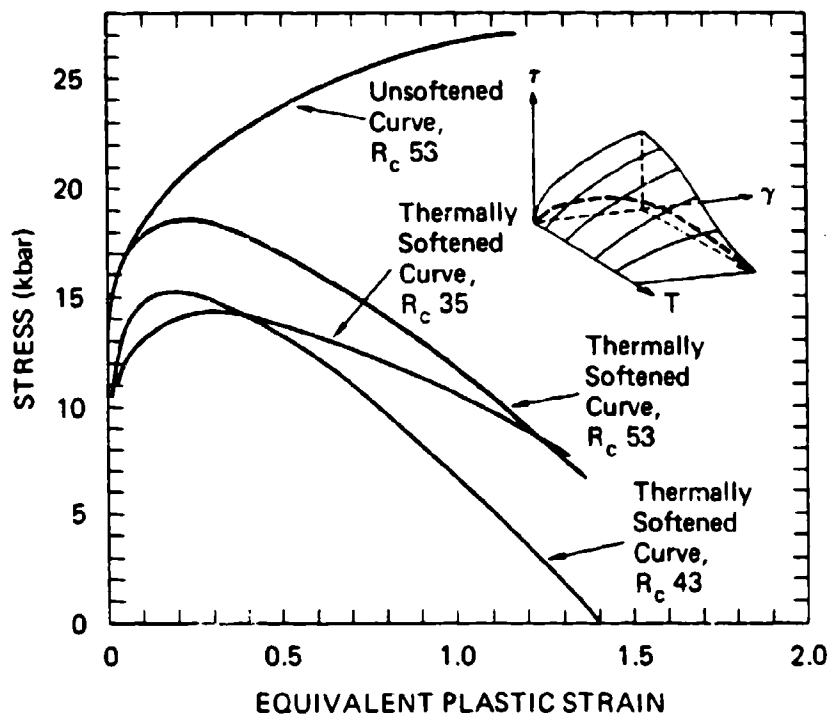
(a) = Hopkinson torsion bar, (b) = Expanding cylinder

*Test NT9 (see Figure III.32), strain rate = 5900 s⁻¹.



JA-314522-81

FIGURE V.1 COMPUTATIONAL SIMULATION OF PLANE STRAIN CRACK LOADED IN PURE SHEAR



MA-7893-19B

FIGURE V.2 STATIC ADIABATIC YIELD CURVES FOR 4340 STEEL

CONTENTS

VI THE SHEAR BAND MODEL (SHEAR4)

A.	INTRODUCTION	VI-1
1.	Nature of the Model	VI-1
2.	Background	VI-3
3.	Scope	VI-4
B.	ORIENTATIONS AND SIZE DISTRIBUTIONS	VI-5
1.	Orientation	VI-5
2.	Size Distributions	VI-7
C.	MICROPROCESSES FOR THE SHEAR BANDS	VI-8
1.	Nucleation	VI-8
2.	Growth	VI-10
3.	Coalescence	VI-12
4.	Tensile Opening of Cracks in Elastic-Plastic Material	VI-12
a.	Background on Crack Opening	VI-13
b.	Tensile Opening for Distributions of Cracks	VI-17
c.	Unloading and Reloading Processes in Tensile Opening	VI-18
D.	STRESS-STRAIN RELATIONS FOR SHEAR4	VI-19
1.	Elastic-Plastic Relations for Intact Material	VI-19
2.	Shear Stress Calculations on Each Plane	VI-21
3.	Solution Procedure for the Stress State	VI-25
E.	FITTING THE SHEAR BAND MODEL TO DATA	VI-28
F.	SAMPLE RESULTS WITH THE SHEAR BAND MODEL	VI-34
G.	CONCLUDING REMARKS	VI-37
H.	REFERENCES	VI-38

VI THE SHEAR BAND MODEL (SHEAR4)

A. Introduction

1. Nature of the Model

The (SHEAR4) shear banding model is based on a previous model (SHEAR3)¹⁻³ that represents the observed processes of nucleation, growth, and coalescence of shear bands. In addition to these processes, standard continuum mechanics relations are used to develop the stress-strain relations for material undergoing damage.

The previous shear banding model was guided by observations and data from experiments on fragmenting cylinders. For the fragmenting cylinder experiment, a thick-walled cylinder of the test material is filled with a high explosive. Immediately after detonation of the internal explosive, the cylinder begins to expand, and the plastic strain is taken homogeneously. With increasing strain, bands begin to form, especially along the inner radius of the cylinder. With continued straining, the bands increase in number and size until they coalesce and form fragments. Figure VI.1 is a photo of a cylinder just as it is separating into fragments.⁴ A sample view of the inside of a partially fragmented cylinder is shown in Figure VI.2. Bands are shown in a range of sizes, and all are lying in planes along the axis of the cylinder. By counting the bands appearing on the inner surface, we obtain quantities on the order of 100 per cm². These bands occur mainly in two orientations, both with normals at 45 degrees between the radial and circumferential directions.

Cross sections of fragments such as the one in Figure VI.2 have revealed that the shear bands are usually semicircular with their diameter lying along the inner radius of the cylinder, or penny-shaped and lying entirely within the cylinder wall. These planar features were termed "bands" by earlier investigators probably because when the shear

surfaces are seen in cross section, they appear as strips or bands of intense shearing. Actually, in three dimensions they are disk-shaped surfaces of intense shear strain. They have the geometry of a macrodislocation with edge and screw components. Only after considerable growth do these half-penny or penny-shaped surfaces link to form a jagged plane of separation as seen in Figure VI.2a.

The SHEAR4 model is intended to represent all the processes of nucleation, growth, and coalescence of bands in many orientations, as noted in the preceding paragraphs. The bands are not treated individually in the model, but as statistical distributions of bands of various sizes and orientations. A discrete set of orientations was selected for the shear bands. On each orientation the bands occur in a range of sizes. These distributions are internal state variables giving the density (intensity in number per unit volume) of bands and the size of those bands at a point in the material. This band density is homogeneously distributed in the vicinity of any point of interest and fulfills the normal requirements of continuum mechanics for smoothly varying quantities.

The discrete number of selected orientations are a major feature of the new SHEAR4 model. In the stress-strain relations for the model, all plastic flow is restricted to these orientations. Yield processes on each plane are associated with the plastic strain and normal stress on that plane. As the material deforms during a simulation, the shear band orientations rotate independently with the material. Thus, highly anisotropic behavior under large deformations can be followed by the model.

The stress-strain relations for shear-banded material account for the reduced strength and moduli associated with the bands. However, these stresses and strains are the average or macroscopic quantities normally dealt with in engineering. Hence, the model joins the macroscopic world of engineering to the microscopic world of materials science.

The SHEAR4 model differs in two distinct ways from micromodels that are now being constructed by other researchers:

- (1) The included processes are actually observed, not merely hypothesized.
- (2) The model retains the microproperties (number and sizes of shear bands) throughout the calculation.

Because of these characteristics, the calculated microfeatures have a specific experimental meaning. At the end of the calculation, these computed features can be compared directly to the corresponding experimentally observed features.

This model is intended to be used with a detailed experimental program. In such a program, a small set of carefully controlled properties tests are made to determine the shear banding parameters and also the usual stress-strain relations (at high strain rate). Then the model is fitted to the results of these tests. Finally, predictive calculations may be undertaken of high rate experiments with similar strain histories, but different geometries, using the derived material properties.

2. Background

A multiple-plane slip model, as we are using the term here, provides a number of specific planes or orientations on which yielding can occur. Such models have often been used for single crystal studies in which the planes of interest were known initially. Other models have treated polycrystalline materials. In these, a large number of planes were provided to represent approximately the continuum of possible orientations for slip. In either case (single or multiple crystals), calculations allowed slip only on the specific planes.

An early model of the multiple-plane type was given by Batdorf and Budiansky⁵ for use in metals. They were successful in simulating yielding in a polycrystalline material. Como, Grimaldi, and D'Agostino^{6,7} developed a multiple-plane model and simulated the work-hardening, anisotropic yielding, and Bauschinger effect observed in

experiments of Naghdi et al.⁸ Bazant has recently begun formulation of a multiple-plane model⁹ to represent anisotropic plastic flow and fracture in concrete. For this model, he has initially dealt with the accuracies to be expected for different numbers and orientations of planes. Peirce et al.²³ used a two-plane model to analyze yielding in single crystals with two slip planes. These workers provided for rate-dependent slip processes on the planes and for rotation of the planes, and discovered that rate-dependent slip was needed to permit a unique motion solution under all imposed deformations.

We have also used multiple-plane models previously to represent high-rate brittle fracture¹⁰ and shear banding.^{11,12} The model for brittle fracture (BFRAC_T) uses one or more planes to represent crack orientations. These discrete planes provide for the strong anisotropy that develops during brittle fracture. Our latest shear band model (SHEAR₄) provides for seven discrete planes on which plastic flow, shear banding or shear cracking, and tensile fracture can occur. As with BFRAC_T, the shearing model permits a very strong anisotropy to develop as damage occurs on the planes. This anisotropy allows fracture to take place in one direction, but maintains full strength in orthogonal directions. Both these models are micromechanical because they provide explicitly for the nucleation and growth of microfractures and for the effect of these microprocesses on the macro stress-strain relations.

3. Scope

The SHEAR₄ model is a multiple-plane plasticity model onto which the shear band microprocesses have been added. Therefore, this section begins with a description of the planes or orientations on which all plastic strain and shear banding is permitted to occur. These specific orientations represent a numerical discretization of all possible orientations for the bands. Next, we consider the representation of the range of band sizes on each orientation. Then the empirical processes of shear band nucleation, growth, and coalescence are introduced. For treating tensile states, we also present a method for allowing the bands

to open under a normal tensile load. With the damage fully defined, stress-strain relations are presented that account for the presence of the shear band damage in the material. Finally, a solution procedure is given for determining the stress tensor under imposed strain increments.

This section concludes with sample calculations and results, plus our method for fitting the model to experimental data to obtain the shear band parameters.

B. Orientations and Size Distributions

Observed shear bands appear in a range of sizes and with many orientations. This variety of appearances is simplified somewhat for representation in the SHEAR4 model. In the model, the shear bands (taken as circular) are treated as groups, not as individual bands. In this treatment each point in the material may have a size and orientation distribution of bands assigned to it. This distribution is like a stress, density, internal energy, or other quantity represented as a cell-centered property in finite-difference calculations. The distribution provides the number per unit volume of bands of a certain size and orientation. The band sizes are represented by a continuous analytical function over all radii, but the orientation variation is treated by a set of discrete directions.

1. Orientations

The selected orientations are central to the model formulation because all plastic strain as well as shear banding occur on these orientations.

Some of the possible sets of orientations that could be used in the model are listed in Table VI.1. Each of these sets of orientations is complete and isotropic: It does not favor any quadrant around a point.

To guide our selection of orientation sets, we examined our experimental results. In the fragmenting cylinder, the most active band plane is YZ, but XY planes are active near the free ends (X is along the

Table VI.1

ORIENTATION OPTIONS FOR SHEAR BAND MODELING^a

No. of Planes		Coordinate Axes	45° Planes ^b	Equiangular Planes ^d
2-D	3-D			
3	3	X, Y, Z	None	None
5	7	X, Y, Z	None	(X,Y,Z), (-X,Y,Z) [(X,-Y,Z), (-X,-Y,Z)] ^c
7	9	X, Y, Z	XY, YZ, XZ, (-X,Y), [(-Y,Z), (-X,Z)] ^c	None
9	13	X, Y, Z	XY, YZ, XZ, (-X,Y), [(-Y,Z), (-X,Z)] ^c	(X,Y,Z), (-X,Y,Z), [(X,-Y,Z), (-X,-Y,Z)] ^c

^aThe 2-D state is taken as either plane strain or axisymmetry. Here there are no shears in the YZ and XZ directions. This symmetry makes certain that the 3-D planes are all identical: for example, YZ and (-Y,Z). Therefore, for 2-D problems, these two planes can be treated as a single plane. Orientations are designated by the directions of the normals to the damage planes.

^bNormals to these band planes are at 45 degrees between the coordinate directions. For example, -X,Y means the normal is at 45 degrees between the -X and Y axes.

^cOrientations listed in brackets are needed only for 3-D symmetry.

^dNormals to the equiangular planes are directed along lines that have equal angles to each of the listed coordinate axes.

cylinder axis, Y is radial, and Z is circumferential). In a target being penetrated by a cylindrical projectile traveling along the X axis, X and Y (radial) planes are active. In the projectile, the XY and XZ planes develop bands. Hence, to handle the problems of primary interest, we need to provide bands in the X, Y, XY, XZ, and YZ orientations. The third set in Table VI.1 is therefore essentially the required set. In two-dimensional problems, there is no shear on the Z plane. Therefore, we are providing seven planes, but only six are active. The set of orientations are shown in their initial positions in Figure VI.3. Here the additional two planes required for a three-dimensional model are also shown. A second representation of six of the planes is shown in Figure VI.4.

For a calculation, the planes are given initial orientations in the external coordinate directions. However, during the calculation, each of the orientations is allowed to rotate with the deformation of the material. When nucleation occurs on a plane, that plane is provided with a size distribution of bands. Further nucleation of bands occurs by adding more bands to each of the currently available band sizes. Growth occurs by the increase of these band sizes. These nucleation and growth processes are further outlined in Section V.

2. Size Distributions

In the model the damage is represented by size distributions in each orientation. The shape of the size distribution was derived from the counted bands obtained from the fragmented cylinders. A typical set of counts at several axial positions in a shear-banded cylinder is shown in Figure VI.5. The numbers of bands are given by an areal density (number per unit area of internal surface of the cylinder). Because of the much larger number of small bands, it is convenient to display these numbers on a logarithmic scale. For the model calculations the size distribution for each orientation was chosen as a series of linear intervals in a semilogarithmic plot such as that in Figure VI.6, because this has a similar appearance to the experimental distributions. The data for such

a distribution is a table of number and size (N, R) values for the coordinate points at the nodes of the broken line. Between the nodes, the distribution is given by the exponential expression

$$N = N_m \exp (A_m R) \quad (VI.1)$$

where N_m and A_m are parameters that can be derived from the given tabular values.

C. Microprocesses for the Shear Bands

During the experiments of interest, the shear bands nucleate, grow, coalesce, and open under tensile loading. We intend that the SHEAR4 model represent all these microprocesses in some detail. In this subsection analytical formulations are presented for each of these processes, and the methods for incorporating them into the model are outlined.

1. Nucleation

New bands are formed in the model as a function of plastic strain and strain rate. This formation corresponds to the rate at which bands reach a size at which they have been observed experimentally--a few micrometers in length. This appearance rate is termed "nucleation" for the model calculations. Nucleation in the model includes two features:

- Formation of several new bands, ΔN_i , in the i_{th} orientation
- Distribution of those bands over a range of sizes.

The size distribution follows the exponential law

$$N = N_0 \exp (-R/R_n) \quad (VI.2)$$

where N_0 is the total number (here, the total number of new bands), N is the number greater than R , and R_n is the nucleation size parameter. These new bands are added onto the existing size distribution. Note that

nucleation with a range of sizes implies that some bands initiate at a large size (several millimeters long): such initiation could occur if the band were formed from a large inclusion or other heterogeneity. Thus nucleation at a range of sizes is required to allow the model to reproduce observed band size distributions.

The nucleation rate function has been developed from considerations of material behavior in the vicinity of a nucleation site, such as a microcrack, inclusion, or other feature. The applied shear strain is amplified near the crack, leading to heating from plastic work. As the tip material approaches melting, material separation occurs and the shear band begins to extend. The heat generated at the tip gradually flows away from the tip, so the rate at which strain is applied affects the rate of nucleation. Large bands may shadow adjacent small potential bands and retard their nucleation. These factors are all included in the nucleation rate function derived in Section V.

The rate function given there is

$$N = \frac{\sigma_y M \dot{\epsilon}_p}{\rho E_m} \left\{ \min \left[(\dot{\epsilon}_p / 10h)^{3/2}, N_0 \right] - N \right\} H(\epsilon_p - \epsilon_{cr}/M) \quad (VI.3)$$

where σ_y is the yield strength, σ is density, E_m is the melt energy, and h is the thermal diffusivity. N_0 is the total number of potential nucleation sites. M is the strain amplification factor at the tip of the growing band (approximately 2 in one case studied). H is a heaviside step function and ϵ_{cr} is the threshold strain for nucleation (about 20% for 4340 steel at HRC 40).

A limit on the rate of nucleation is provided by requiring that the total distortion represented by the new bands not exceed the total imposed plastic shear strain. For this calculation we need to define the amount of distortion of each band and then relate that distortion to the overall strain absorbed. From our experimental observations (Figure VI.7),⁵ we found that the amount of shear offset B of bands was a constant fraction b of the band radius R ; that is, $b = B/R$. We assumed

that the offset was distributed parabolically over the band area and equal to bR at its center. By integrating the area under the parabolic distribution, we find that the average relative offset over the area is $b/2$. Then the deformation of a new band is

$$\delta_1^P = 3\pi b \Delta N_1 R_n^3 \quad (\text{VI.4})$$

By requiring that the deformation δ_1^P not exceed the deformation imposed on the i th plane, Equation (VI.4) then provides an upper bound on the number ΔN_1 nucleated in any time interval.

2. Growth

The bands grow in accordance with a law in which the growth rate is proportional to the imposed strain rate. The basic law, as derived in Section V, is as follows:

$$\frac{dR_j}{dt} = T_1 \frac{d\epsilon_1^{ps}}{dt} R_j \quad (\text{VI.5})$$

where R_j is the j th band size in the distribution on the i th plane, T_1 is a dimensionless material constant, and ϵ_1^{ps} is the plastic shear strain on the i th shear band plane. This growth law is similar to the equation for expansion of a spherical bubble in a viscous liquid. T_1 is then the inverse of the coefficient of viscosity. This growth law allows a size distribution of bands to retain an exponential form during growth, and our observations indicate that the distributions are approximately exponential at all stages of growth.

When this growth process is applied to a size distribution, the entire distribution increases in size. The resulting distribution has the same quasi-exponential form, the number of bands are unaffected, and the changes in the radii are obtained through the use of Equation (VI.7).

Two constraints are applied to the growth law to limit the maximum growth velocity to the sound speed and to require that the total distortion represented by the growth does not exceed the total imposed

plastic shear strain. The velocity limit dictates that the radius R_2 at the end of a time interval Δt is

$$R_2 < R_1 + V_m \Delta t \quad (\text{VI.6})$$

where V_m is the shear wave velocity. The distortion limit on growth is derived in the same manner as in equation (VI.4). The increase in plastic strain $\Delta \epsilon_1^G$ associated with the band growth on the i th plane is

$$\Delta \epsilon_1^G = \frac{\pi b}{2} \left[\int_0^{R_{2\max}} R_2^3 dN - \int_0^{R_{1\max}} R_1^3 dN \right] \quad (\text{VI.7})$$

where R_2 and R_1 here denote radii on the size distribution (such as in Figure VI.6) after and before the time interval. The first integral in equation (VI.7) is evaluated by computing the R values at each node using the growth law, integrating from node to node, and summing the values obtained between all nodes. If $\Delta \epsilon_1^G$ exceeds the imposed shear strain $\Delta \epsilon_1^{ps}$, the R values are all reduced proportionately to make $\Delta \epsilon_1^G$ equal to $\Delta \epsilon_1^{ps}$.

The integral of equation (VI.5) for a constant strain rate over some time interval is

$$R_2 = R_1 \exp(T_1 \Delta \epsilon^{ps}) \quad (\text{VI.8})$$

where $\Delta \epsilon^{ps}$ is the increment in plastic shear strain. Although equation (VI.5) appears as a rate equation, the growth is actually independent of strain rate unless the shear velocity V_m or the strain limit equation (VI.7), is reached.

The model provides for a strong interaction between the nucleation and the growth processes. When plastic shear strain is applied, that strain can be absorbed by homogeneous plastic strain, by growth of existing bands, and by nucleation of new bands. We have assumed that strain would be taken in that mode in which the least energy would be

required to accommodate the strain. The amount of strain that can be taken in growth is limited by the growth law above. If growth does not absorb all the applied strain, then nucleation can occur. Because we allow nucleation of bands of finite sizes, the nucleation also absorbs some strain. If some applied strain still remains, this residual strain is taken homogeneously.

3. Coalescence

In the model it is assumed that the bands are initially isolated, and that their nucleation and growth can be treated as if they were each a single band in an infinite medium. However, at some time the bands begin to interact, coalesce, and finally to form fragments. Hence, we are assuming that the most energy is consumed in homogeneous plastic strain, less energy in nucleation, and still less in growth for a unit of applied strain. The condition for full fragmentation is written by considering the fragmented state. Each fragment has some small number of faces, each formed by bands. The sizes of the fragment faces are related to the band sizes. With these considerations, we have derived a criterion D for fragmentation:

$$D = \pi \gamma \Sigma N_i R_i^3 \quad (VI.9)$$

The factor γ allows for the spacing of bands normal to their plane. The parameter D describes the degree of fragmentation. When D reaches 1.0, full fragmentation is declared. The factor D is used to reduce the yield strength while the normal stress on a plane is tensile.

4. Tensile Opening of Cracks in Elastic-Plastic Material

A procedure for treating tensile opening is provided for the shear-banding routine SHEAR4. The shear bands, which are crack-like features, are allowed to open and the tensile stress normal to the plane of the cracks is thereby reduced.

In this subsection, we first review the available theories for tensile opening of cracks. Then these are compared and one is selected for use in SHEAR4. Finally, this selected tensile opening relation is extended to the case of a size distribution of cracks, instead of a single crack, and to unloading and reloading.

For these calculations, we consider elastic behavior and also plastic response with work-hardening. The shear bands or cracks are assumed to be penny-shaped. Each crack is assumed to be in an infinite medium and not to interact with its neighbors. Thus, the crack opening occurs without reference to other cracks in the distribution nor to cracks in other orientations; hence, the opening for the distribution can be computed by simply summing the openings for each crack in the distribution. Because the field is assumed to be infinite, there is no crack size effect nor propagation of yield lines to the boundaries. However, we do assume that the stresses are large enough that general yielding can occur throughout the field. The analysis is developed for arbitrary three-dimensional stress states that include tension and compression normal to the crack plane.

a. Background on Crack Opening

The fracture literature has been examined for theoretical and numerical analyses of the opening of a single crack in either plane strain or in axisymmetric loading. First, the elastic treatment is given, then perfect plasticity, and then plasticity with work-hardening.

Sneddon and Lowengrub¹³ have given the following formulas for crack opening for the plane strain and axisymmetric cases:

$$\delta = \frac{2(1 - \nu^2)\sigma a}{E} \quad \text{plane strain} \quad (\text{VI.10})$$

$$\delta = \frac{4(1 - \nu^2)\sigma a}{\pi E} \quad \text{axisymmetric} \quad (\text{VI.11})$$

Here δ is half the crack opening in the center of the crack, ν is Poisson's ratio, a is the crack radius, σ is the stress normal to the

crack plane, and E is Young's modulus. The ratio of the opening of the axisymmetric crack to the opening of the plane strain crack is $2/\pi$.

To treat the crack opening in a field where there is some plastic deformation, Rice¹⁴ used the Dugdale-Barenblatt model for yielding along a strip ahead of the crack tip. The resulting crack tip opening for the plane strain and axisymmetric cases is

$$\delta_t = \frac{8(1 - \nu^2)\sigma_o a}{\pi E} \ln \sec \left(\frac{\pi \sigma_\infty}{2\sigma_o} \right) \quad \text{plane strain} \quad (\text{VI.12})$$

$$\delta_t = \frac{8(1 - \nu^2)\sigma_o a}{\pi E} \left\{ 1 - \left[1 - \left(\frac{\sigma_\infty}{\sigma_o} \right)^2 \right]^{1/2} \right\} \quad \text{axisymmetric} \quad (\text{VI.13})$$

where σ_o is the yield stress, and σ_∞ is the stress normal to the crack plane and at a great distance from the crack. These crack tip openings are not strictly comparable to the elastic openings above because they represent the total opening rather than half opening, and also because they are the opening at the tip in the yielding zone. Thus, the actual total opening might be better given as the sum of those from eqs. (VI.10) and (VI.12) or from (VI.11) and (VI.13). Then, for the penny-shaped crack,

$$\delta = \frac{4(1 - \nu^2)a}{\pi E} \left\{ \sigma + \sigma_o \left[1 - \left(1 - \frac{\sigma_\infty^2}{\sigma_o^2} \right)^{1/2} \right] \right\} \quad \text{axisymmetric} \quad (\text{VI.14})$$

This equation for opening is displayed in Figure VI.5 along with the elastic solution. Equation (VI.14) shows a gradual variation from the strictly elastic case. Note that when the applied stress approaches the yield stress, the opening increases without limit. Because the formulation is only appropriate for very limited amounts of yielding near the crack tip, this opening behavior near general yielding is to be expected.

For general yielding in power-law hardening material, Wells¹⁵ proposed the following solution for the half-opening of a circular crack in plane strain:

$$\delta = \pi a \epsilon \quad (VI.15)$$

where ϵ is the tensile strain normal to the crack plane. The power-law hardening material has the stress-strain relation:

$$\epsilon = \alpha \left(\frac{\sigma}{\sigma_0} \right)^n \quad (VI.16)$$

where n is the work-hardening exponent. It may be noted that the expression for crack opening (VI.15) does not contain the value of n , nor does it agree with the elastic solution for $n = 1$. This equation is also shown in Figures VI.8 and VI.9 with the previous solutions. The stress-strain relations used in the three opening expressions are shown in Figure VI.10; to make the openings comparable, all three curves are forced to pass through the yield point at σ_0 . In Figure VI.8, Eq. (VI.15) shows much less opening at small stresses than the elastic case; however, this is understandable because the modulus is very large at small stresses. The opening does not increase without limit when the yield stress is approached, but there is a rapid increase in the vicinity of yield. In Figure VI.9, it is apparent that the opening according to eq. (VI.15) is linear with strain and has a modulus about half that of the elastic opening.

In an attempt to treat a combined elastic and plastic crack opening, Tsai¹⁶ suggested using a combination of the Dugdale-Barenblatt solution and the Wells solution. He considered only the crack-tip opening in eq. (VI.12), not the combination with the elastic solution in eq. (VI.14) above. Then he separated the applied strain into elastic and plastic portions, with the latter being given by the power law, eq. (VI.16). The resulting expression for crack opening is

$$\begin{aligned} \delta &= \delta_{el} + \delta_{pl} \\ \delta &= \pi a \left\{ \epsilon - \left[\epsilon_{el} - \frac{4}{\pi} \left(\frac{\bar{\sigma}}{\sigma_0} \right) \ln \sec \left(\frac{\pi \sigma_0 \epsilon_{el}}{2 \bar{\sigma} \epsilon_0} \right) \right] \right\} \end{aligned} \quad (VI.17)$$

where $\epsilon_{01} = \sigma/E$, $\bar{\sigma}$ is the flow stress, σ_0 is initial yield strength, and ϵ_0 is the strain at yield. Because this equation does not include the linear elastic solution, it gives unphysical results at low stresses.

He and Hutchinson¹⁷ have recently made a thorough numerical and analytical study of the problems of a crack in an infinite medium of power-law hardening material in either plane strain or axisymmetric conditions. For the axisymmetric case, their analytical solution for the crack volume is

$$V_c = \frac{8 \epsilon a^3}{\sqrt{1 + 3/n}} \left(\frac{\sigma}{\bar{\sigma}} \right) \quad (\text{VI.18})$$

where n is the power-law hardening exponent, σ is the stress normal to the crack plane, and $\bar{\sigma}$ is the equivalent or Mises stress. If the crack is assumed to be an ellipsoid (it is only approximately ellipsoidal), then the half-opening can be calculated from eq. (VI.18)

$$\delta = \frac{6 \epsilon a \sigma}{\pi \bar{\sigma} \sqrt{1 + 3/n}} \quad (\text{VI.19})$$

Equation (VI.19) can now be compared with the earlier results for crack volume. For $n = 1$ and Poisson's ratio of 0.5 (no volume change), the opening from eq. (VI.19) is equal to the elastic opening. For $n = \infty$, the opening is similar to that from Well's expression, eq. (VI.15), when it is modified by $2/\pi$ to account for the change from plane strain to axisymmetry. This opening formula is also displayed in Figures VI.8 and VI.9 for comparison. He and Hutchinson describe eq. (VI.18) as the first term in a series in $\sigma/\bar{\sigma}$. This analytical result matches the numerical results for $\sigma/\bar{\sigma}$ from 0 to 2 quite well but is not very accurate for larger values.

From the foregoing assessment, it appears that the He-Hutchinson formula is probably the best result for large stresses and strains. However, for small strains it is reasonable to expect that the elastic result is correct and that with increasing stress or strain, there would be a gradual change from the elastic slope toward the power-law formula

for opening. Therefore, probably some combination of the elastic opening and the power-law opening should be used.

b. Tensile Opening for Distribution of Cracks

The model for crack opening to be used with SHEAR4 must provide for the processes of loading, unloading, and reloading in tension. There should be provision for elastic behavior under small loads and plastic response under larger loads. Thus, there may be some residual opening of the cracks after the tensile stress is removed. The background articles mainly concentrate on the maximum crack opening, but for the analysis of SHEAR4, the total crack volume is the factor of interest. In the subroutine there is a distribution of crack (shear band) sizes and this must be used in determining the total crack volume. Finally, the loading is applied in increments, with possible sign reversal in between increments, so the equations must be recast in incremental form. These factors are all considered in the following discussion.

The crack opening equations are transformed to crack volume expressions based on the assumption that the crack is an ellipsoid with semiaxes a , a , and δ . Then the elastic crack volume is obtained in eq. (VI.11).

$$v_c = \frac{16(1 - \nu^2)a^3\epsilon}{3} \quad (\text{VI.20})$$

The crack volume for power-law hardening material according to Hutchinson is given in eq. (VI.18).

In the shear band subroutine, the bands in each orientation are given by a size distribution. This distribution is initially specified such that the number of cracks larger than any given radius is an exponential function of the radius. After some growth and further nucleation, the distribution is no longer simply an exponential, but is given by a series of points on a graph of $\log N$ versus a . The total volume of all the cracks in a distribution is given for the elastic case by the integral

$$\begin{aligned}
V_v &= \int_0^{\infty} v_c \, dN \\
&= \frac{16(1 - \nu^2)\epsilon}{3} \int_0^{\infty} a^3 \, dN
\end{aligned}
\tag{VI.21}$$

where v_c is the volume of a single crack of radius a , and dN is the number of cracks with that radius. The integral is evaluated numerically from the size distribution and is termed τ_z ; it is used elsewhere in the subroutine as a measure of the total damage.

$$\tau_z = \pi \int a^3 \, dN \tag{VI.22}$$

With the use of τ_z , the total void volume of the distribution can be put into the following forms for the elastic and plastic cases.

$$V_v = \frac{16(1 - \nu^2)\epsilon \tau_z}{3\pi} \quad (\text{elastic}) \tag{VI.23}$$

$$V_v = \frac{8 \sigma \epsilon \tau_z}{\pi \bar{\sigma} \sqrt{1 + 3/n}} \quad (\text{power-law}) \tag{VI.24}$$

c. Unloading and Reloading Processes in Tensile Opening

Next, we need a mechanism for using these void volumes to treat a sequence of loadings and unloadings. Such a possible sequence is shown in the strain-volume plot of Figure VI.11. This figure represents an assumption about elastic-plastic crack behavior and has not been verified by any experiments or analyses. Initially, the response is elastic up to some critical strain level, ϵ_{cr} . Above that strain, yielding occurs and the void volume increases according to eq. (VI.24) in incremental form. If unloading occurs (application of strain in the compressive direction), then the cracks close elastically, following eq. (VI.23) in incremental form. Reloading also occurs elastically until the earlier yield point is reached and then the volume change follows the plastic path. If unloading continues into the compressive strain range, plastic volume change can occur if the compressive strain becomes less than $-\epsilon_{cr}$. For strains less than $-\epsilon_{cr}$, the volume change is always plastic.

The foregoing hypothesis is probably physically reasonable and qualitatively correct; it should therefore give reasonable results in SHEAR4. At this point in the development of SHEAR4, the main requirement is a process that will not be unstable or otherwise adversely affect calculations that are intended to be primarily in the compressive range.

D. Stress-Strain Relations for SHEAR4

The stress-strain relations are developed here for the response of the material to mechanical loading. The presence of shear banding damage affects the shear strength, and therefore the stress-strain relations.

The intact solid material is represented by a standard elastic-plastic model with work-hardening and strain-rate dependence. The material is isotropic; hence, its stress tensor can be separated into pressure and deviatoric components. Whereas the solid material is isotropic, the presence of shear band damage can lead to highly anisotropic behavior. The following stress-strain relations have been constructed to reflect this anisotropy and to provide for continuity between the undamaged and damaged states. The stress calculations are made using Cauchy stresses in the current configuration.

1. Elastic-Plastic Relations for Intact Material

The intact material is assumed to be isotropic. Therefore, we can separate the stress tensor into a pressure and a stress deviator tensor. The pressure is the average stress $P = \sigma_{11}/3$, where σ_{1j} is a component of the stress tensor and repeated subscripts mean summation. The stress deviator elements are

$$\sigma'_{1j} = \sigma_{1j} - P \delta_{1j} \quad (\text{VI.25})$$

where δ_{1j} is the Kronecker Δ . The pressure is then given by the Mie-Gruneisen relation:

$$P = C\mu + D\mu^2 + S\mu^3 + \Gamma\rho_s(E - E_h) \quad (\text{VI.26})$$

where $\mu = \rho_s / \rho_0 - 1$
 ρ_s, ρ_0 are current and initial solid density,
 $C, D,$ and S are coefficients with the units of moduli
 (this series defines the Hugoniot for the material),
 Γ is the Gruneisen ratio (dimensionless),
 E is the internal energy (energy per unit mass), and
 E_h is the energy at the same density on the Hugoniot.

With this formulation, the pressure responds to thermal and mechanical effects, while the deviator stress is normally a function of the mechanical changes. It is noted here that ρ is the solid density and not the gross density of the material at the point. Hence, if shear bands occur and open under tensile loading, this reduction in density will affect the gross density but not the solid density. Therefore, the preceding equation will be appropriate for damaged as well as for intact material.

The deviator stress is computed from the standard elastic relation:

$$\sigma'_{ij} = \sigma'_{ijo} + 2G\Delta\epsilon'_{ij}^E \quad (\text{VI.27})$$

where G is the shear modulus,

$\Delta\epsilon'_{ij}^E$ is the incremental change in elastic deviator strain. As usual, the total deviator strain increment is separated into elastic and plastic components:

$$\Delta\epsilon'_{ij} = \Delta\epsilon'_{ij}^E + \Delta\epsilon'_{ij}^P \quad (\text{VI.28})$$

The next step for computing the deviator stresses is to determine the plastic strain increments. These plastic strains are computed on the individual planes in the SHEAR4 model. Therefore, we consider next the formulation of the shear strength and shear stress-shear strain relations on these planes.

2. Shear Stress Calculations on Each Plane

To begin the shear stress calculations for each plane, we first prescribe the shear strength. The strength is composed of the initial strength plus work-hardening based on the plastic strain generated on that plane. This strength is then reduced by the area of the shear bands that have been formed. If the elastically computed shear stress exceeds the shear strength, the stress is reduced according to a stress-relaxation process.

The shear stress calculation begins with an elastic calculation of the total deviator stress tensor σ'_{ij} . Then the stress vector acting on the k^{th} plane is resolved into a normal stress σ_{nk} and a shear stress σ_{sk} . Then the yield criterion is applied. If the shear stress exceeds the yield strength, the stress is relaxed and a plastic strain $\Delta\epsilon_k^P$ is computed. All the $\Delta\epsilon_k^P$ from all the planes are assembled into a tensor $\Delta\epsilon_{ij}^P$. With the plastic strain known, eqs. (VI.27) and (VI.28) are used to compute the deviatoric stress tensor σ'_{ij} . The following paragraphs outline somewhat further the prescription of the shear strength and the procedure for determining the plastic strain on each plane.

The shear strength on each plane is given by a work-hardening Coulomb friction model. This strength, τ_{ky} on the k^{th} plane, is a sum of two functions--a cohesion that varies with shear strain, and a normal stress effect that acts in the Coulomb fashion, as shown below.

$$\tau_{ky} = (1 - D_k) Y_s (\epsilon_k^P) + D_k S_{kn} \tan \phi_k \quad (\text{VI.29})$$

Here Y_s is the usual shear yield strength and work-hardening function, except that it pertains only to the k^{th} plane, and work-hardening is a function only of the plastic strain on that plane. D_k is the damage on the k^{th} plane. S_{kn} is the normal stress on the k^{th} plane. ϕ_k is the angle of friction, which may be a function of the plastic strain and of the shearing and fracture damage. The derivation of the damage quantity is derived from the following physical picture of the way that shear bands develop and intersect or coalesce to form fragments. D_k is

intended to be zero for no damage and to grow to one as full separation or fragmentation is reached. For this coalescence process, we imagine a small volume around each shear band. In the plane of the band, its area is the same as the band's area (πR^2), but in the third dimension, its distance is some fraction of R , say γR . Then the volume of the affected region is

$$V_b = \pi \gamma R^3 \quad (\text{VI.30})$$

If we then consider the coalescence volume for all the bands in the distribution, we obtain a damage quantity. This damage is defined in terms of the number N and radius R of the shear bands on each plane:

$$D_k = T_8 \int R_i^3 dN_i \quad (\text{VI.31})$$

where T_8 is an input coefficient representing the combination $\pi \gamma$ and equals about 1. The integral over i represents the sum of areas from all the bands in the size distribution. Because N is the number of bands per unit volume, D_k is dimensionless. We have also defined D_k to range from zero to one. Thus D_k makes a good measure of damage.

Now we can see that eq. (VI.29) contains two terms. The first is the usual yield strength for an intact, work-hardening material, but it is reduced by the factor $(1 - D_k)$ so that only the intact portion of the material on the plane is considered. The damaged portion of the plane is considered to have no intrinsic shear strength, but to have a Coulomb shearing resistance in proportion to the normal stress across the bands.

With a prescription of the shear strength on each plane, we can now account for plastic flow and rate-dependence in computing the shear stress. These features are combined into a rate-dependent model of the linear type proposed by Malvern.¹⁸

$$\frac{d\sigma'_k}{dt} = 2G \frac{d\epsilon'_k}{dt} - \frac{\sigma_k - \tau_{ky}}{T} \quad (\text{VI.32})$$

where σ'_k is the vector sum of the shear stress on the k^{th} orientation plane, G is the shear modulus, $\dot{\epsilon}'_k$ is the tensor shear strain acting along the k^{th} plane, T is the time constant, and τ_{ky} is the current shear yield strength on the k^{th} plane. This one-dimensional expression for shear stress will be solved initially and then later we will account for the two-dimensional nature of the shear stress on the plane. The yield strength varies in a general manner with the plastic strain on the plane. However, for any strain interval the strength is assumed to work-harden linearly during the time step, Δt , as follows:

$$\tau_{ky} = \tau_{ky0} + \frac{\Delta \tau}{\Delta t} t \quad (\text{VI.33})$$

where τ_{ky0} is the shear yield strength at the beginning of the time interval, $\Delta \tau$ is the incremental increase in yield strength, and t is time running from 0 to Δt during the time interval. To perform the integration of eq. (VI.32) to obtain the shear stress at the end of the interval, multiply each term by $\exp(t/T)$. The solution is

$$\sigma'_k = \sigma'_{k0} X + (2GT\dot{\epsilon}'_k + \tau_{ky0})(1 - X) + \Delta \tau_{ky} \left[1 - \frac{T}{\Delta t} (1 - X) \right] \quad (\text{VI.34})$$

where $\dot{\epsilon}'_k$ is the applied deviator strain rate, and $X = \exp(\Delta t/T)$.

Having the stress from eq. (VI.34), we can now determine the plastic strain that occurs in the time interval. For this calculation, we separate the applied strain into elastic and plastic components:

$$\Delta \epsilon' = \Delta \epsilon'^E + \Delta \epsilon'^P \quad (\text{VI.35})$$

and use the elastic stress-strain relation:

$$\sigma'_k = \sigma'_{k0} + 2G\Delta \epsilon'^E_k \quad (\text{VI.36})$$

By subtracting the two equations for σ'_k , (VI.34) and (VI.36), and using the expression for the plastic strain implied in eq. (VI.38), we can obtain

$$\begin{aligned}
& (\sigma'_{ko} - 2G\dot{\epsilon}'_k - \tau_{kyo})(1 - X) - \Delta\tau_{ky}\left[1 - \frac{T}{\Delta t}(1 - X)\right] \\
& + 2G(\Delta\epsilon'_k - \Delta\epsilon_k^P) = 0
\end{aligned} \tag{VI.37}$$

Then we can solve for the plastic strain:

$$\Delta\epsilon_k^P = \frac{(\sigma'_{ko} - \tau_{kyo})(1 - X) + 2G\dot{\epsilon}'_k[\Delta t - T(1 - X)]}{2G + M_w\left[1 - \frac{T}{\Delta t}(1 - X)\right]} \tag{VI.38}$$

where $M_w = \Delta\tau/\Delta\epsilon_k^P$ is a work-hardening modulus. Thus, the plastic strain absorbed on each plane can be computed.

Now that we have completed the one-dimensional calculation, we can explore the actual two-dimensional shear stress state on the k^{th} plane. Figure VI.12 is a sketch of the plane with two shear stresses in orthogonal coordinates. The stress σ'_{ko} existed at the beginning of the time interval and the stress σ_k^E was computed elastically for the end of the interval. Some portion of the difference between these two stresses represents an elastic change and another portion represents a plastic change. Only the plastic change will be affected by the plasticity and rate-dependent processes. (Note that on the k^{th} plane, we are considering a normality or radial return rule for the plastic flow.) Hence, we wish to perform our stress-relaxation calculation along the direction of the radial vector to σ_k^E . Thus, we can use eq. (VI.32) and its solution, eq. (VI.38), once we correctly interpret its terms in the two-dimensional context. The first term in eq. (VI.38) on the right-hand side is replaced by

$$2G \frac{d\epsilon'_k}{dt} = \frac{\sigma_k^E - \sigma'_{ko}}{\Delta t} \tag{VI.39}$$

Now we can interpret the plastic strain computed in eq. (VI.38) as the resultant plastic change in the direction of σ_k^E . The individual components of plastic strain can be computed because the direction and magnitude of the resultant are now known.

3. Solution Procedure for the Stress State

In the foregoing derivation a one-dimensional solution was developed for computing the shear stress and plastic strain on each plane. Now it is necessary to account for all the active planes (those with stresses above the yield strength) simultaneously to determine the stress and plastic strain tensors.

The stress solution procedure must fit into a standard finite difference or finite element computer program. Therefore, the stress will be computed at each cell or element at many time intervals. For each time interval, our solution procedure must take the preceding stress tensor and the strain increment tensor, and compute a new stress tensor appropriate to the current time. For this solution procedure we have in mind the following sequence of operations:

- (1) Compute the new stress tensor from the imposed strain increment tensor, treating the strains as entirely elastic. Include here the pressure computed from the Mie-Grüneisen relation.
- (2) Transform the stresses to determine the normal stress and two components of shear stress acting on each of the designated planes.
- (3) Compute the plastic shear strains on each of the planes. This step follows the procedure outlined in the previous section.
- (4) Transform the plastic shear strains from each plane to the tensor orientation and sum to form the terms of the tensor.
- (5) Recompute the stress tensor, using for the elastic strain increment tensor the imposed strain minus the plastic strain tensor.

In this sequence, steps (1), (2), (4), and (5) are standard operations; step (3) is more complex, and hence is the topic of this section.

Before presenting a method for obtaining the stress solution on each plane, we will describe some other attempts to solve this problem and some of our requirements for an acceptable scheme. We do not believe that an exact solution method is available in general, although there are

methods that can handle special cases. Taylor²² showed that five planes are needed in general to absorb an arbitrary strain. For fewer planes, no solution is available; for more planes, there may in some case be no unique solution.²² Peirce et al.²³ have solved a special case for two slip planes in a two-dimensional geometry. We are attempting to determine the stress state with a large (and indefinite) number of planes without a fixed orientational relation between the planes and with different strengths on each plane. We are aiming for an engineering solution--that is, not an exact solution--but a physically realistic approximation.

To clarify the purpose for the solution procedure, let us explore several multiple plane cases and try to estimate what the physically correct result should be in each case. Our solution procedure must be able to handle all of these with reasonable accuracy. Consider the case in which there are two orthogonal planes with equal shear stresses and yield strengths on each plane. Then if one plane were allowed to yield in the one-dimensional fashion of the equations in the preceding section, that plane would absorb all the plastic strain and reduce the shear stresses on both planes to the yield level. Probably a more reasonable solution would be obtained if each plane received just one-half of the plastic strain.

Now consider a second case with two planes, but here one plane has an elastically computed shear stress twice as high as the shear on the other plane. Under a gradually applied (quasi-static) loading, the first plane might absorb all the plastic strain. This plastic strain would relax both shear stresses, and probably the shear stress on the second plane would actually never reach yield. If the material is rate-dependent and the loading were applied rapidly enough, the shear on the second plane would also exceed yield and so some plastic strain should also accumulate on that plane. Thus, we would expect that the plastic strain should be more uniformly distributed over the planes for higher rate loadings.

A relaxation solution procedure is proposed for determining the shear stresses on all planes simultaneously. Here we treat the case of rate-independent plastic flow; therefore, we are using the apparent rate-dependence in eq. (VI.32) only as a numerical device for gaining the solution. Our solution procedure is completed when no shear stresses exceed the yield strength. The relaxation process begins after step (2) above, in which the elastically computed stresses have been determined on each plane. Then we move from plane to plane and use eq. (VI.38) (or its rate-independent equivalent) to determine the plastic strain that would allow complete relaxation on each plane (the plastic strain requested by each plane). This requested plastic strain is then multiplied by a factor f . The value of f is usually in the range of $1/2$ to 1 , depending on the number of active planes and on the precision we are intending. With these fractions of the plastic strain, the calculation proceeds on through steps (4) and (5), and then back to step (2). Now at step (3) again, the shear stresses on all planes are compared with the yield strength on that plane. If yield has not been exceeded on any plane, the solution is complete. However, if the shear stress exceeds yield on one or more planes, the preceding steps are repeated until all the excess shear stress has been relaxed.

The precision of the preceding relaxation solution is controlled by three factors:

- (1) The imposed strain increment size. If the strains from the calling program are too large, these strains can be divided into subincrements and imposed in a series of subcycles. The acceptable strain size can be related to the acceptable precision on the shear stress.
- (2) The fraction f of the requested plastic strain absorbed on each cycle. Large values near 1.0 will produce more rapid convergence, but also more overrelaxation (excessive plastic strain). We have used $f = 1/\sqrt{n}$, where n is the number of active planes.
- (3) The convergence criterion, based either on the shear stress above yield, or the increment of plastic strain generated during the current iteration.

These three factors should be coordinated to represent about the same level of precision for an efficient calculation.

The foregoing solution procedure is fairly lengthy and requires considerable computing time in some cases. The accuracy obtained as well as the computing time strongly depends on the settings of the precision factors. Because the number of subcycles and the number of active planes at any time naturally adjust to handle the imposed strain, the computing time is dependent on the amount of strain. For practical problems there are usually only a few cells or elements that are undergoing large strains. For such a case the increase in the computing time over that for a simpler plastic procedure is not very important.

The relaxation solution procedure has a number of beneficial features. Although no mathematical proof has been attempted, the solution obtained is expected to converge to a unique stress state for decreasing strain increment sizes. The accuracy of the method can be adjusted simply by modifying the strain increment size and the other precision factors. Any number of active planes can be accommodated in the method, and the planes can be at any orientation with respect to each other. Thus, an initially orthogonal system need not remain orthogonal to be solvable. Additional, and highly nonlinear processes, can be added without requiring modifications in the solution method. Such processes are thermal softening, tensile or spall opening, and cross-hardening (work hardening of one plane caused by shearing strain on another plane).

E. Fitting the Shear Band Model to Data

Based on the analysis of the 4340 fragmenting cylinder data, the following tentative procedure has been developed for determining shear band model parameters from the data. Determination of parameters requires a well-planned series of contained fragmenting cylinder experiments in which the damage level is varied uniformly from low damage to nearly full fragmentation. Multiple simulations of the cylinder tests are made, first to determine plastic strains, and then to compute shear band damage for direct comparison with the data.

The contained fragmenting cylinder data should represent a range of damage levels and strain rates. The cylinders are sectioned, and then shear bands are counted at several positions along the cylinders and assembled to cumulative size distributions as in Figure VI.13. These surface counts (Figure VI.13b) are then transformed to volume counts (Figure VI.13c) using a standard metallurgical transformation process such as that of Scheil^{19,20} or of Seaman et al.²¹ The volume size distributions are each fitted to the exponential function

$$N_g = N_0 \exp (-R/R_1) \quad (VI.40)$$

where N_g is the number/cm³ with radii greater than R , and N_0 and R_1 are parameters of the distribution. The N_0 and R_1 parameters are then plotted versus their position along the cylinder.

To obtain estimates of the strains in the cylinder, one makes a computer simulation (without damage) of each cylinder test using a two-dimensional wave propagation code and the SHEAR4 model. The final radii and elongation of the simulated cylinder should be compared with the experimental values to verify that the explosion process and material properties are correctly represented in the simulation. The values of c_k^P , plastic shear strain on the k_{th} shear band plane, are derived from these simulations for the locations along the cylinders where the counts were made. Such computer-generated strain histories are shown in Figure VI.14. Then the experimental parameters N_0 and R_1 are plotted versus the computed shear strains to obtain estimates of the nucleation and growth rate parameters for the shear band model, as shown in Figures VI.15 and VI.16. The large scatter in Figures VI.15 and VI.16 may indicate some errors in data gathering and interpretation, or that additional parameters (peak pressure, for example) must be accounted for. Alternatively we may assume that the scatter is largely caused by the simplicity of the initial simulation (with no damage). The no-damage calculation suppresses many features important to shear banding. Therefore, we have simply drawn trend lines through the data and derived an initial set of shear banding parameters. Then we can begin the

simulations accounting for damage, expecting some improvement in the match between experimental and computed shear band statistics.

With these initial estimates of the shear band parameters, the cylinder tests are simulated again using SHEAR4 to obtain computed values of N_0 and R_1 as functions of axial location. These computed values of N_0 and R_1 are compared with the measured values at each axial location for each cylinder. This comparison may suggest revisions in the growth or nucleation parameters. If so, the parameters are changed, the simulations are repeated, and the results are again compared. Alternatively, the computed and observed surface distribution parameters n_0 and r_1 may be compared to determine how to modify the nucleation and growth parameters.

From the nucleation and growth equations, it might appear that there would be no need for repeated simulations of the experiments to obtain the shear band parameters. However, the model is written with an interaction between nucleation, growth, and stress-relaxation that causes some nonlinearity. As mentioned in Section VI.C.1 (under Nucleation) the plastic strain is first taken in growth. The remaining strain causes nucleation of new bands. If some strain has not been absorbed in growth and nucleation, that remainder is taken homogeneously. The developing damage causes stress relaxation that may alter adjacent damage growth. Therefore, multiple simulations of the experiments are required to obtain a reasonable match to the experimental shear band data.

The total set of parameters characterizing a material for shear banding include the nucleation and growth parameters mentioned above, plus some coalescence parameters, bulk and shear moduli, and a work-hardening yield curve. These parameters are listed in Table VI.2 with some notes on the methods for obtaining each one. Table VI.3 contains values for 4340 steel at a hardness of HRC 40 and rolled homogeneous armor steel with HRC 23.

Table VI.2
INPUT DATA FOR SHEAR4^a

Variables	Nominal ^b Values	Definition
BFR(1,M)	60	T_1 , growth coefficient in $dR/dt = T_1 R d\epsilon/dt$. Derive from slope of growth data in plot such as Figure VI.12.
BFR(2,M)	1 per cm^3	Nucleation coefficient.
BFR(3,M)	0.01 cm	R_n , nucleation size parameter. Derive from the intercept of the trend line of R_1 values at the threshold strain line level, as in Figure VI.12.
BFR(4,M)	0.146 per s	Thermal diffusivity = thermal conductivity/(density times specific heat at constant pressure).
BFR(5,M)	0.24	ϵ_n , nucleation threshold strain.
BFR(6,M)	0.07	b, relative maximum shear distortion associated with a band. Determine from sectioning and measuring the shear offset across a band.
BFR(7,M)	0.04 cm	R_B , maximum band size at nucleation. Determine from measured band sizes for small amounts of growth.
BFR(8,M)	1.0	Relative volume of fragments. This leads to a fragment volume of $R_f^3 V_{FR}$.
BFR(9,M)	0.577	$\tan \phi$, where ϕ is the internal friction angle used in computing shear resistance on the band areas.

Table VI.2 (Concluded)

Variables	Nominal ^b Values	Definition
BFR(10,M)	2	Indicator for storage of plastic strains, ϵ_i : 0 no storage 1 store strains for $FNUC_i \neq 0$ 2 store all strains.
BFR(11,M)	1	Designator for TAU, a damage indicator for triggering slide lines. For $i = BFR(M,32)$, $TAU = \tau_z(i)$. Select as appropriate of the problem being treated.
BFR(12,M)	0.	Unused.
BFR(13,M)	8	Number of radii used for each size distribution.
FNUC(1,M) (6 values)	1.0	Indicator array and weighting factor for orientations to be used. Use 1.0 for any active orientation. Use 0. for inactive orientations.
YS(1,M)	1.E10, 1.1E10 1.3 E10 dyn/cm ²	Yield strength values at chosen along the work-hardening curve.
EST(1,M)	0., 0.02, 1.0	Plastic strain values at chosen points along the work-hardening curve.

^aIn the free field input form, these data could be entered as follows:
SHEAR4 BFR = 60., 1., 0.01, 0.146, 0.24, 0.07, 1., 0.577, 2., 1., 0.,
8.; YS = 1.E10, 1.1E10, 1.30E10; ES = 0., 0.02, 1.; FNUC = 1., 1.,
1., 1., 1., 1.: END

^bNondimensional unless otherwise specified.

Table VI.3

SHEAR BANDING AND YIELD PARAMETERS FOR 4340 AND RHA STEELS

Model	Parameter		4340 Steel	RHA Steel
	Type		HRC 40	HRC 23
SHEAR4	Shear banding kinetics parameters:	B ₁	60.0	20.0
		B ₂	1.0	2.0
		B ₃	0.01	0.01
		B ₄	0.146	0.146
		B ₅	0.24	0.35
		B ₆	0.07	0.07
		B ₇	0.04	0.04
		B ₈	1.0	1.0
		B ₉	0.577	0.577
		B ₁₀	2.0	2.0
		B ₁₁	2.0	2.0
		B ₁₂	0.0	0.0
		B ₁₃	8.0	8.0
	Yield curve parameters	(Y, ϵ)	10.3, 0.0	6.8, 0.0
			10.7, 0.03	7.7, 0.02
			13.7, 1.0	8.7, 0.07
				9.5, 0.12
				10.4, 0.17
				11.1, 0.27
				12.4, 0.47
				14.0, 1.3

F. Sample Results with the Shear Band Model

The SHEAR4 model has been tested under a variety of conditions, including simulations of fragmenting cylinders, projectile penetrations, and Taylor tests. The model has also been used as an anisotropic plasticity model in a number of problems where shear banding does not occur. Thus, SHEAR4 can be used as a plasticity model when detailed information is required about the orientations of the plastic flow that occurs in the test.

We present three cases to give an indication of the problems to which SHEAR4 has been applied. The first is a fragmenting round of the type used for the initial determination of the shear banding parameters. The second is a projectile penetration into a hard steel target, and the third is the impact of a blunt projectile onto a hard target (Taylor test).

The first simulation is of a contained fragmenting cylinder of 4340 steel with a hardness of HRC 40. The cylinder was 15.24 cm long, with a 6.85 cm outer diameter and 1.145 cm wall thickness. A low density PETN explosive ($\rho_c = 1.35 \text{ g/cm}^3$) was used to produce a Chapman-Jouguet pressure of 16.3 GPa. The cylinder was surrounded by a PMMA tube of 1.15 cm thickness and a steel mandrel of 5.145 cm thickness. The results of the simulation are illustrated in Figure VI.17. The contours of plastic strain on the cross section show only the strains for the mode 1 orientation. (The plane of each band contains lines that lie along the axis and at 45 degrees to a radius.)

The fragmenting cylinder simulation provides information that can be compared with many aspects of the measurements. For example, the final distorted shape of the cylinder is directly comparable. The number and sizes of bands can be compared for several stations along the axis of the cylinder.

The projectile impact case is one in which we fired a 4340 steel projectile (HRC 40) at a rolled homogeneous armor steel target. Several shots were fired at a range of velocities to establish a ballistic limit

at about 750 m/s. The rod was 6.35 mm in diameter and 12.7 mm long. The round target was 6.35 mm thick and had a diameter of 76.2 mm. In our simulation we used a velocity of 750 m/s. The shear banding parameters had already been determined for both the projectile and target materials, so this was a purely predictive calculation (although performed after the experiment).

The cross sections taken from the calculation at 9.85 and 12.3 μ s after impact are shown in Figure VI.18. (The simulation was halted at this point because of excessive cell distortion.) The dark shaded regions in this figure represent cells that have been completely damaged by shear banding and thus no longer retain any shear or tensile strength. The lighter shaded regions represent cells that have undergone partial shear banding damage. The damaged region occupies the impact end of the projectile. In the target, there is a small amount of shear banding damage along the upper surface of the target, plus a line of damage extending through the target plate. The line of damage appears as a macro shear band defining a central plug that would probably be pushed out of the plate during the next few microseconds. At this time the projectile is about halfway through the target, yet retains 38% of its original kinetic energy.

Hence the predicted damage to the target shows that a largely intact plug is forced out with a diameter approximating that of the projectile. Some distortion is present at the impact plane in both the residual target and the plug. These results agree well with our experimental data at this velocity.

Many models have been able to predict a known limiting velocity. However, usually they also show penetration for a great range of impact velocities. Hence, we tried a similar impact at 500 m/s. A dent was made in the plate, but no cells in the target were fragmented; this result also agrees with our observations.

Next we attempted to simulate an impact at 1550 m/s, more than twice the limiting velocity for this configuration. Figure VI.19 shows a large zone of damage ahead of the rod and no defined shear band that will

release a plug. Again, this behavior is like that observed in highly overmatched cases: the rod is eroded, but passes through, accompanied by a shower of fragments from both the rod and the plate.

Thus it appears that, with parameters determined from CFC tests, SHEAR4 is able to predict the limiting velocity for penetration, extent of collateral damage, and the changing trend in the damage distribution in the plate. Hence many of the phenomena in the model must be accurate.

The Taylor test, the impact of a blunt rod onto a hard anvil, is very similar to the penetrating impact discussed above, so we expected to make satisfactory simulations with the SHEAR4 model. Here, however, the emphasis is on the rod instead of on the plate. Figure VI.20 shows views of a rod after impacting a quartz plate. The rod has been shear banded into a separate cone in the center, an outer ring, plus the remainder of the rod, which is now sharpened. We should expect to find these results in simulations of the Taylor test.

Figure VI.21 shows the results of simulations of a Taylor test of 4340 steel at HRC 40 launched at 457 m/s. The contours show the plastic strains in the orientation that can lead to a cone at the front of the rod. The contour lines show that the most important shear strain levels are in the center at the impact plane, rather than in the regions that actually shear band in the tests.

Next, we considered the hypothesis that the stress-strain relations should include thermal softening and that the threshold criterion for shear banding should be adjusted. Figure VI.22 shows a schematic yield curve for the material, indicating an initial work-hardening region, followed by a peak of the curve where thermal softening becomes important. However, we now assume that although this peak is important for softening effects, it is not sufficient for shear banding. Shear banding is assumed to occur at a strain somewhat farther along. Clifton and co-workers²⁴ recently found analytically that the peak point of the curve may not cause instability, but some continuing strain is required.

With this expanded criterion for shear banding and an approximate thermal softening process, we simulated the Taylor test again, this time with a thermal softening process, but no shear banding. Some results are shown in Fig. VI.23. Note that the computational grid is now severely distorted. Here we see the development of a region of intense shear that is forming a cone adjacent to the impact plane. Now the largest strains are along the cone-forming plane and not along the axis or in the other shear band orientations (not shown) as before. The current Taylor test results should be considered exploratory and not definitive because the yield curve used was selected arbitrarily and not for accuracy in representing 4340 steel.

From these comparisons, we conclude that some thermal softening process must be reflected in the yield curve to obtain the correct plastic strain distributions in the rod. The adjustments needed to handle phenomena in impacting rods suggest that the stress-strain relations are more important for rods. In the contained fragmenting cylinder experiment, the shear banding processes are greatly overdriven by the explosive, so the stress-strain relations have less influence. In the target ahead of the rod, the stress-strain relations are important in representing the anisotropy necessary to correctly orient the plane of separation; however, the material is well confined by the surrounding target. In the rod, however, there are free surfaces nearby, permitting large amounts of slip to occur. These differences in the three types of tests appear to be fruitful areas for pursuing our understanding of the shear banding processes.

G. Concluding Remarks

This section outlined a shear banding model (SHEAR4) containing many features of the shear banding kinetics. All these features have been suggested by the experimental observations we have made, and all seem necessary to represent qualitatively some aspects of shear banding phenomena.

Within the model are the macroscopic stress-strain relations with their strongly anisotropic character. The micro processes include nucleation, growth, and coalescence of size distributions of shear bands.

The multiple-plane, micromechanical shear banding model can represent contained fragmenting cylinder experiments in considerable detail, including the final deformed shape of the cylinder, numbers and sizes of shear bands, and the distribution of the bands throughout the length of the cylinder.

With the model based on CFC data, surprisingly accurate predictions can be made for rod impacts onto hard steel plates. The predictions include the limiting velocity for penetration, collateral damage in the plate, and the nature of the damage in the plate. At the present level of development, the model is not accurate for the damage in the rod. Preliminary calculations indicate that inclusion of thermal softening and a modification in the nucleation threshold would improve the accuracy of the simulations of the rod.

We further conclude that shear banding is the dominant failure mechanism in all three types of experiments, although the current results suggest that the shear banding process in the rod may be more dependent on the details of thermal softening.

H. References

1. L. Seaman et al., "Development of a Shear Band Model for Fragmentation in Exploding Cylinders," SRI International Final Report No. N00178-74-C-0450 for Naval Surface Weapons Center, Dahlgren, VA (August 1974).
2. D. C. Erlich et al., "Development and Application of a Computational Shear Band Model," SRI International Final Report on Contract DAAD05-76-C-0762 for U.S. Army Ballistic Research Laboratory, Aberdeen, MD (May 1977).
3. D. C. Erlich, D. R. Curran, and L. Seaman, "Further Development of a Computational Shear Band Model," SRI International Final Report No. DAAG46-77-C-0043 for U.S. Army Materials and Mechanics Research Center, Watertown, MA (May 1979).

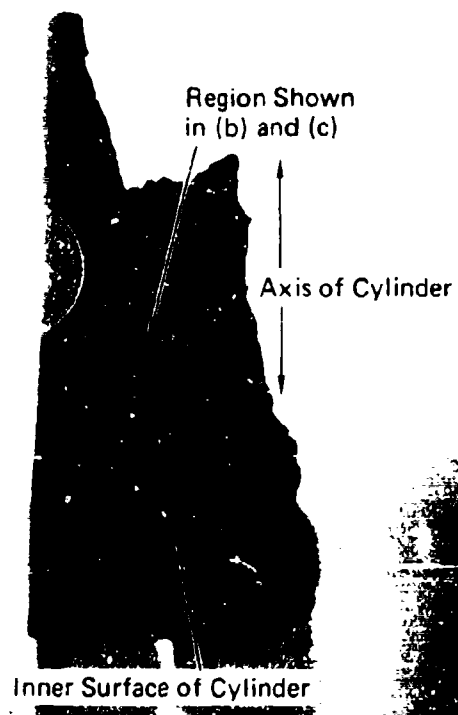
4. C. R. Crowe, W. Mock, and D. Brunson, "A Review of the Mechanisms of Fragmentation," private communication, Naval Surface Weapons Center, Dahlgren, VA.
5. S. B. Batdorf and B. Budiansky, "A Mathematical Theory of Plasticity Based on the Concept of Slip," National Advisory Committee for Aeronautics Technical Note No. 1871 (Washington, April 1949).
6. M. Como and S. D'Agostino, "Strain Hardening Plasticity with Bauschinger Effect," *Meccanica* 4 (2) 146-158 (1969).
7. M. Como and G. A. Grimaldi, "Analytical Formulation of the Theoretical Subsequent Yield Surfaces of Metals with Strain-Hardening and Bauschinger Effect in an Ideal Tension-Torsion Test," *Meccanica* 4 (4) 286-297 (1969).
8. P. M. Naghdi, F. Essenburg, and W. Koff, "An Experimental Study of Initial and Subsequent Yield Surface in Plasticity," *J. Appl. Mech.* 25 201-209 (1958).
9. Z. P. Bazant and B. H. Oh, "Microplane Model for Fracture Analysis of Concrete Structures," Proceedings of the Symposium on the Interaction of Non-Nuclear Munitions with Structures (U.S. Air Force Academy, Colorado, May 10-13, 1983).
10. L. Seaman, D. R. Curran, and W. J. Murri, "A Continuum Model for Dynamic Tensile Microfracture and Fragmentation," *J. Appl. Mech. ASME*, to appear.
11. L. Seaman, D. R. Curran, and D. A. Shockey, "Scaling of Shear Band Fracture Processes," Proc. of the 29th Sagamore Conference on Material Behavior Under High Stress and Ultrahigh Loading Rates, J. Mescall and V. Weiss, Eds. (Plenum Press, New York, 1983).
12. L. Seaman and J. L. Dein, "Representing Shear Band Damage at High Strain Rates," IUTAM Symposium on Nonlinear Deformation Waves (Tallinn, Estonia, August 22-28, 1982).
13. I. N. Sneddon and M. Lowengrub, Crack Problems in the Classical Theory of Elasticity, (John Wiley and Sons, Inc., New York, 1969).
14. J. R. Rice, "Mathematical Analysis in the Mechanics of Fracture," Chapter 3 of Vol. II of Fracture, H. Liebowitz, Ed. (Academic Press, New York and London, 1968).
15. A. A. Wells, *British Welding Journal*, 10, 563 (1963).
16. C. K. Tsai, H. W. Shen, X. X. Chen, L. G. Luo, and M. Z. Zheng, "High Strain Fracture Analysis," Vol. 4 of Advances in Fracture Research, D. Francois, ed., 5th International Conference on Fracture, Cannes, France, 1447 (1981).

17. M. Y. He and J. W. Hutchinson, "The Penny-Shaped Crack and the Plane Strain Crack in an Infinite Body of Power-Law Material," J. Appl. Mech., 48, 830 (December 1981).
18. L. E. Malvern, "The Propagation of Longitudinal Waves of Plastic Deformation in a Bar of Materials Exhibiting a Strain-Rate Effect," J. Appl. Mech. 18, 203-208 (1951).
19. E. Scheil, Die Berechnung der Anzahl und Grossenverteilung Kugelformiger Kristalle in undurchsichtigen Korpern mit Hilfe durch einen ebenen Schnitt erhaltenen Schnittkreise, Z. Anorg Allgem. Chem., 201, 259 (1943).
20. E. Scheil, Statistische Gefügeuntersuchungen I, Z. Metallk., 27, 199 (1935).
21. L. Seaman, D. R. Curran, and R. C. Crewdson, "Transformation of Observed Crack Traces on a Section to True Crack Density for Fracture Calculations," J. Appl. Phys. 49(10), 5221-5229 (October 1978).
22. G. I. Taylor, "Plastic Strain in Metals," J. Inst. Metals 62, 307 (1938).
23. D. Peirce, R. J. Asaro, and A. Needleman, "Material Rate Dependence and Localized Deformation in Crystalline Solids," Acta. Metall. 31, 1951-1976 (1983).
24. R. J. Clifton, J. Duffy, K. A. Hartley, and T. G. Shawki, "On Critical Conditions for Shear Band Formation at High Strain Rates," Scripta Met. 18, 443 (1984).



MP-3503-20

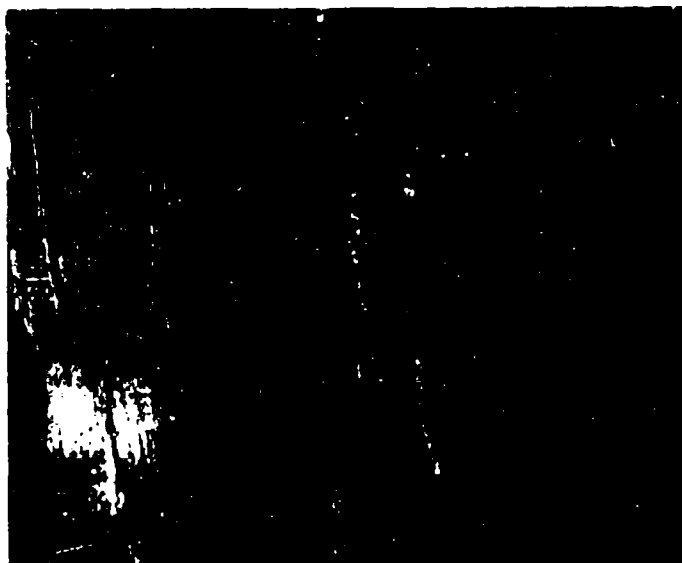
FIGURE VI.1 FRAMING CAMERA PHOTOGRAPH OF ARMCO IRON FRAGMENTING-ROUND
CYLINDER 4.5-IN. O.D. x 15 IN. x 0.75 IN. WALL THICKNESS 56 μ sec
AFTER DETONATION



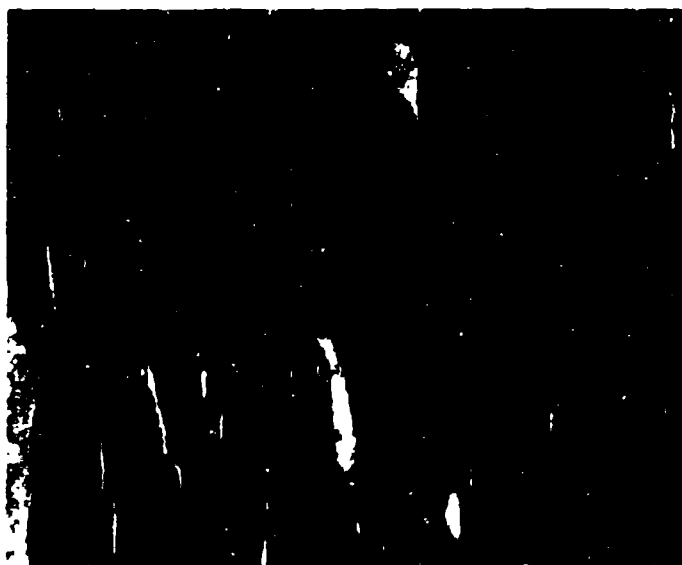
(a) Fragment of 4340 Steel

MP-6408-14A

FIGURE VI.2 FRAGMENT (a) OF 4340 STEEL OF R_C 40 AND PHOTOMICROGRAPHS (b and c) OF A PORTION PHOTOGRAPHED WITH THE LIGHT FROM DIFFERENT DIRECTIONS TO CONTRAST THE DIRECTIONS OF SLIP ON THE BANDS



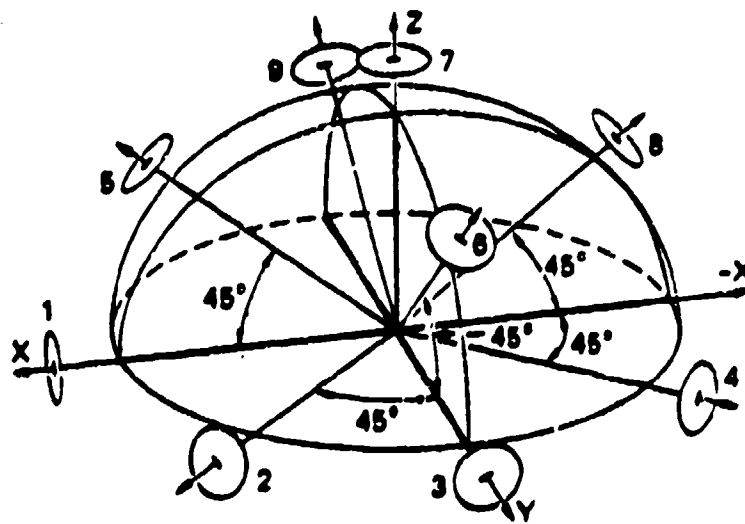
(b) Detail of Fragment with Illumination
from the Right



(c) Detail of Fragment with Illumination
from the Left

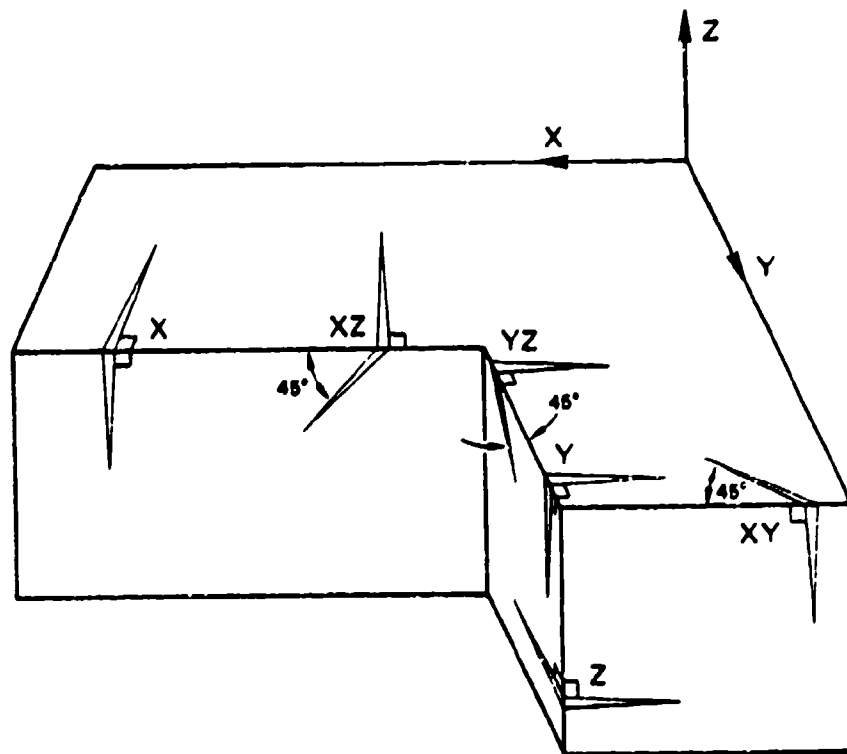
MP-8408-14B

FIGURE VI.2 (Concluded)



MA-7893-3A

FIGURE VI.3 RELATIVE LOCATIONS OF THE COORDINATE DIRECTIONS AND INITIAL ORIENTATION OF THE SHEARING PLANES



MA-7893-171

FIGURE VI.4 SIX SHEAR BAND ORIENTATIONS PROVIDED IN THE SHEAR 4 MODEL

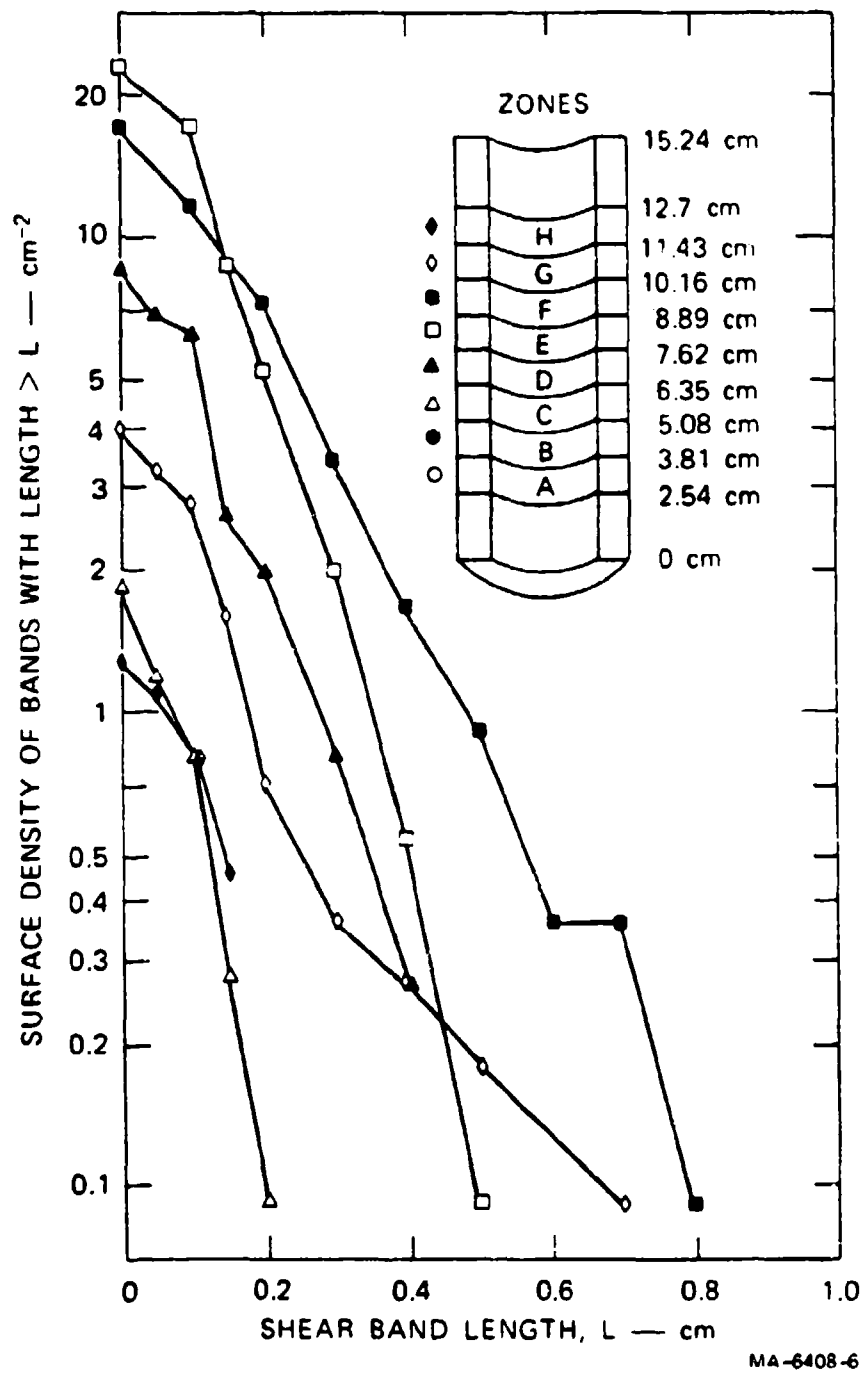
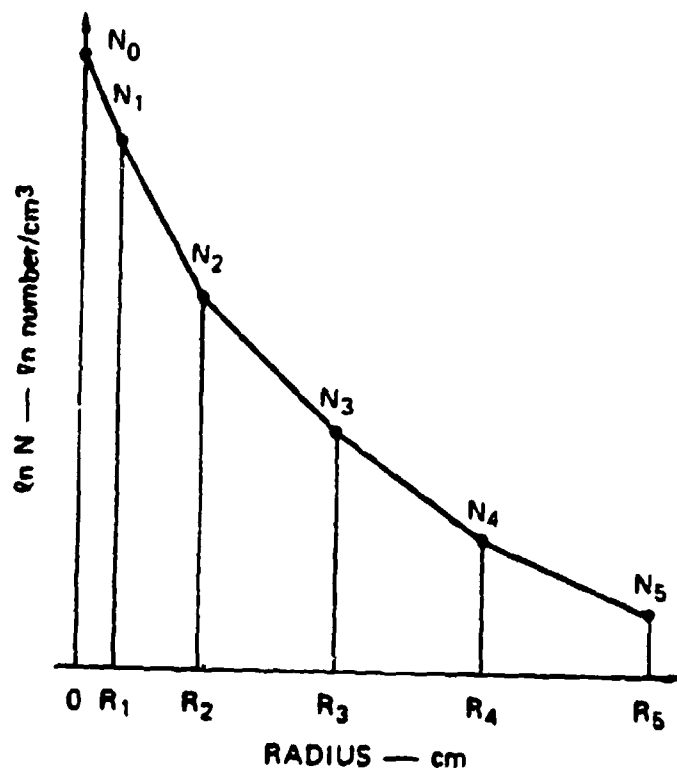
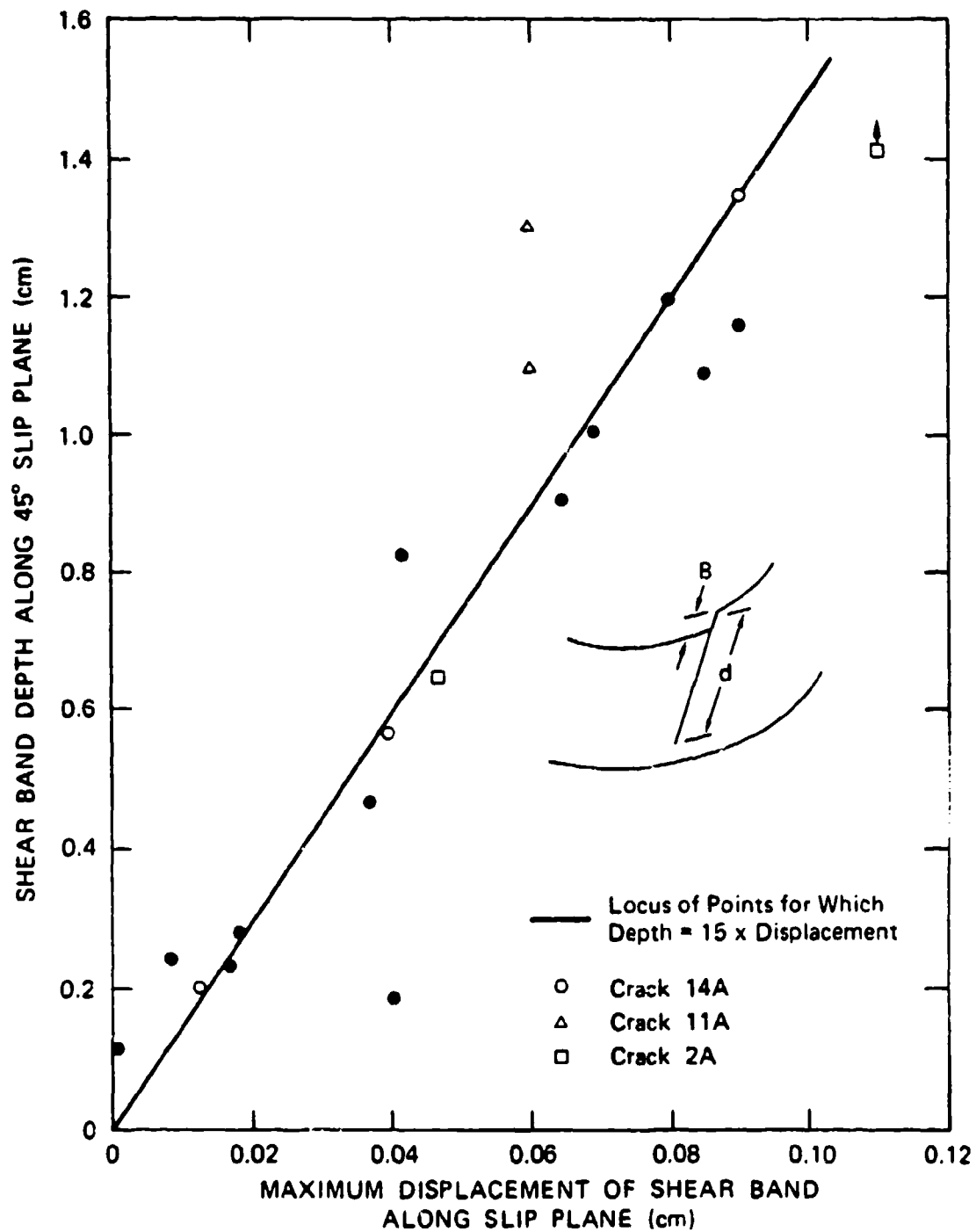


FIGURE VI.5 SHEAR BAND DISTRIBUTION FOR EXPERIMENT 2
IN 4340 STEEL, HRC 40



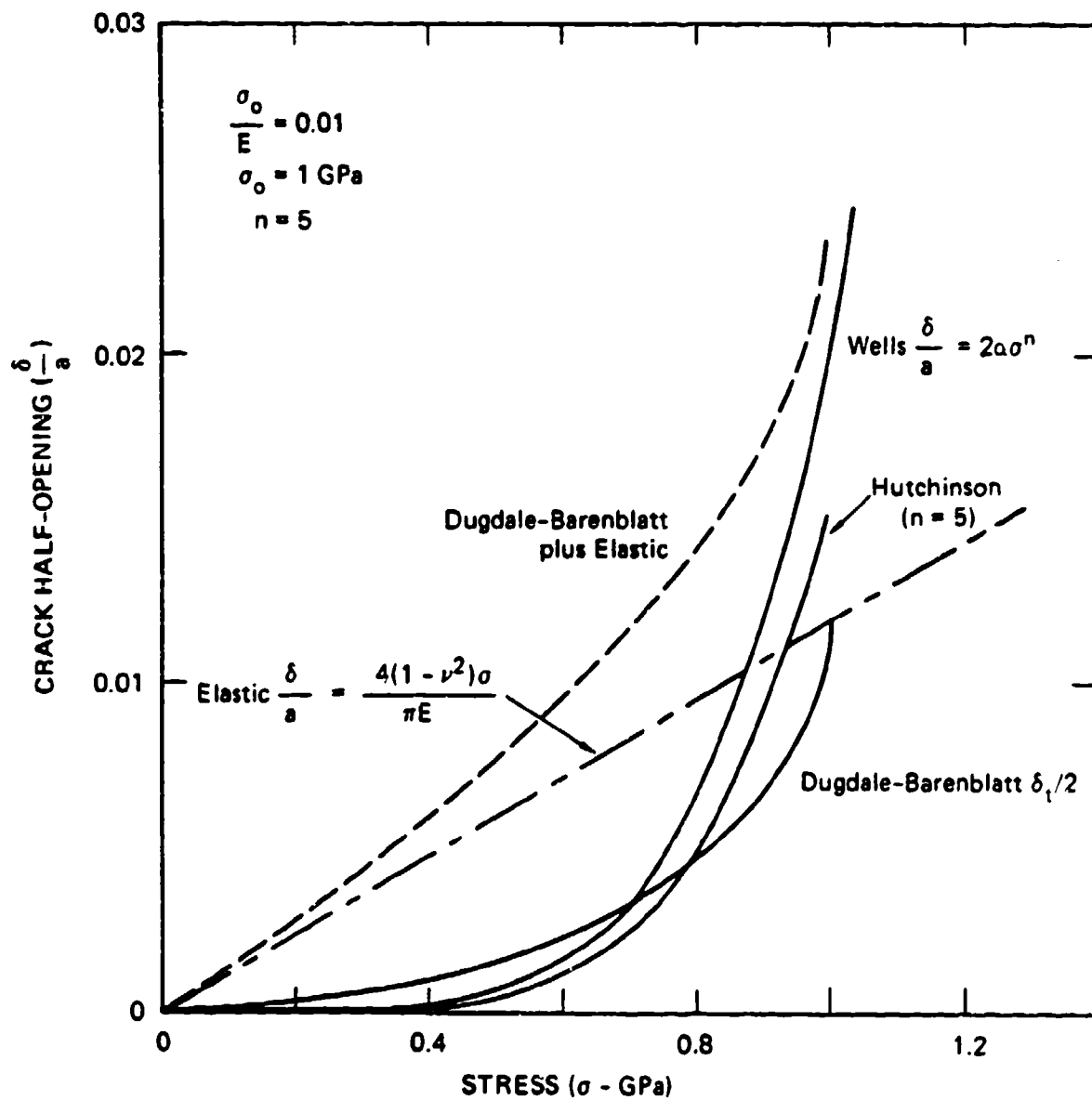
MA-7893-101A

FIGURE VI.6 SHEAR BAND SIZE DISTRIBUTION
REPRESENTED BY A SERIES OF
POINTS AND EXPONENTIAL LINE
SEGMENTS



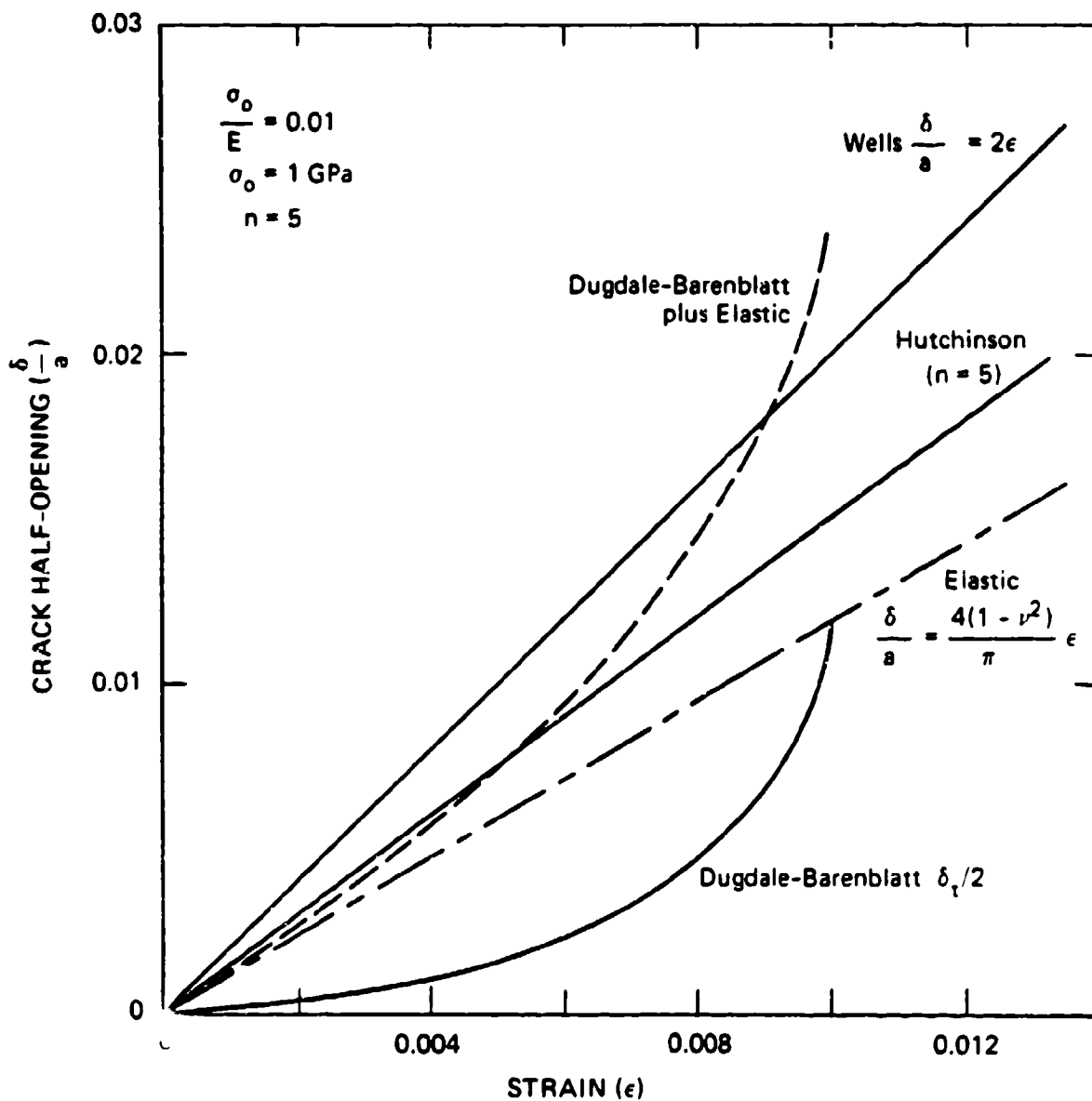
MA-5084-10

FIGURE VI.7 SHEAR BAND DEPTH d VERSUS DISPLACEMENT B DATA



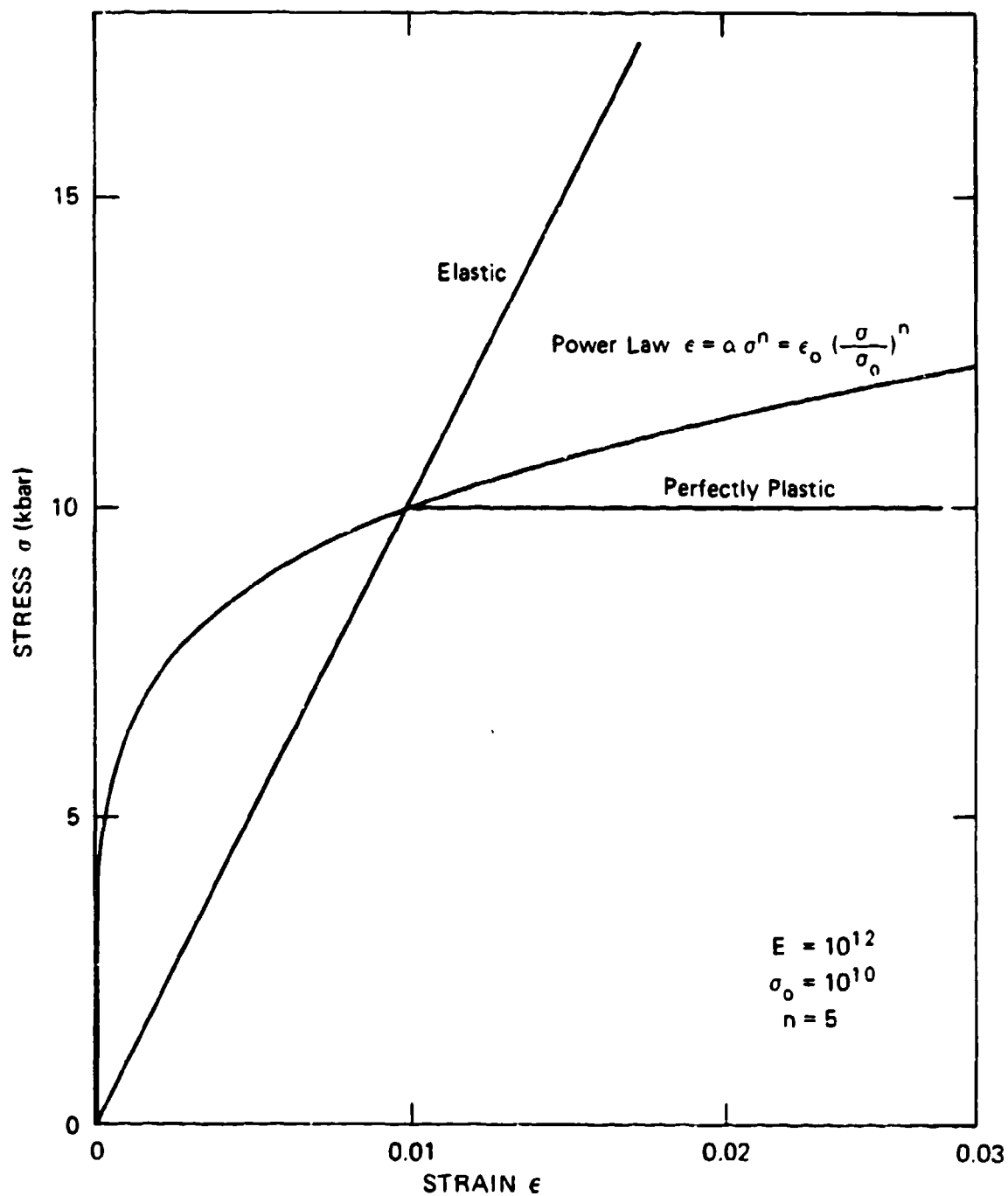
JA-314525-82

FIGURE VI.8 COMPARISON OF CRACK OPENING AS A FUNCTION OF STRESS FROM SEVERAL THEORIES



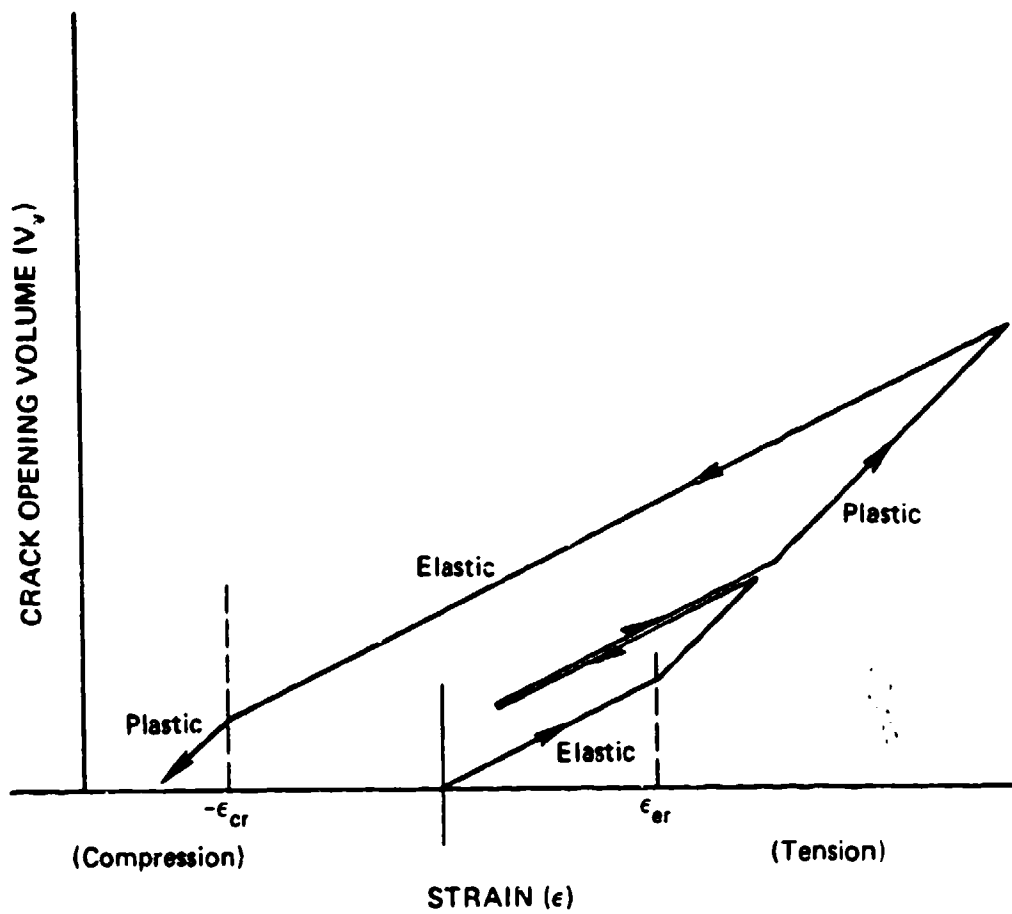
JA-314525-63

FIGURE VI.9 COMPARISON OF CRACK OPENING AS A FUNCTION OF STRAIN FROM SEVERAL THEORIES



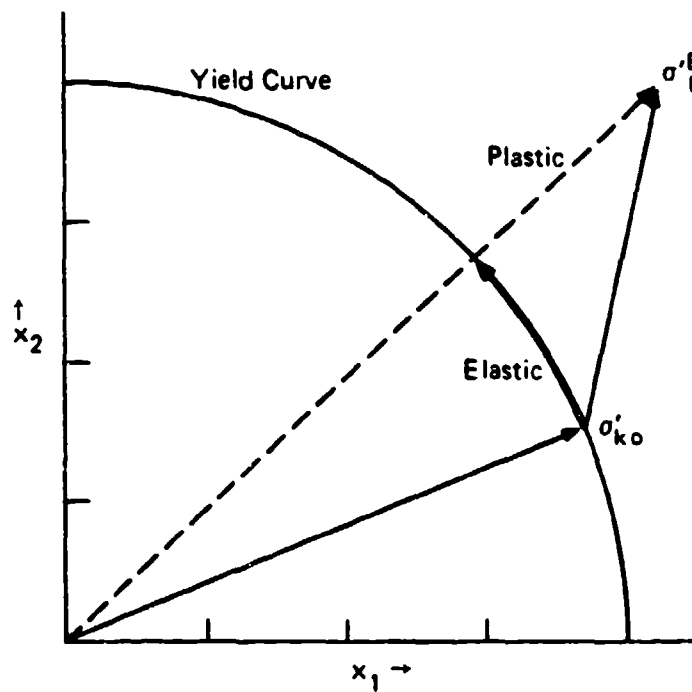
JA-314525-84

FIGURE VI.10 STRESS-STRAIN RELATIONS ASSUMED IN THE THEORETICAL MODELS FOR CRACK OPENING



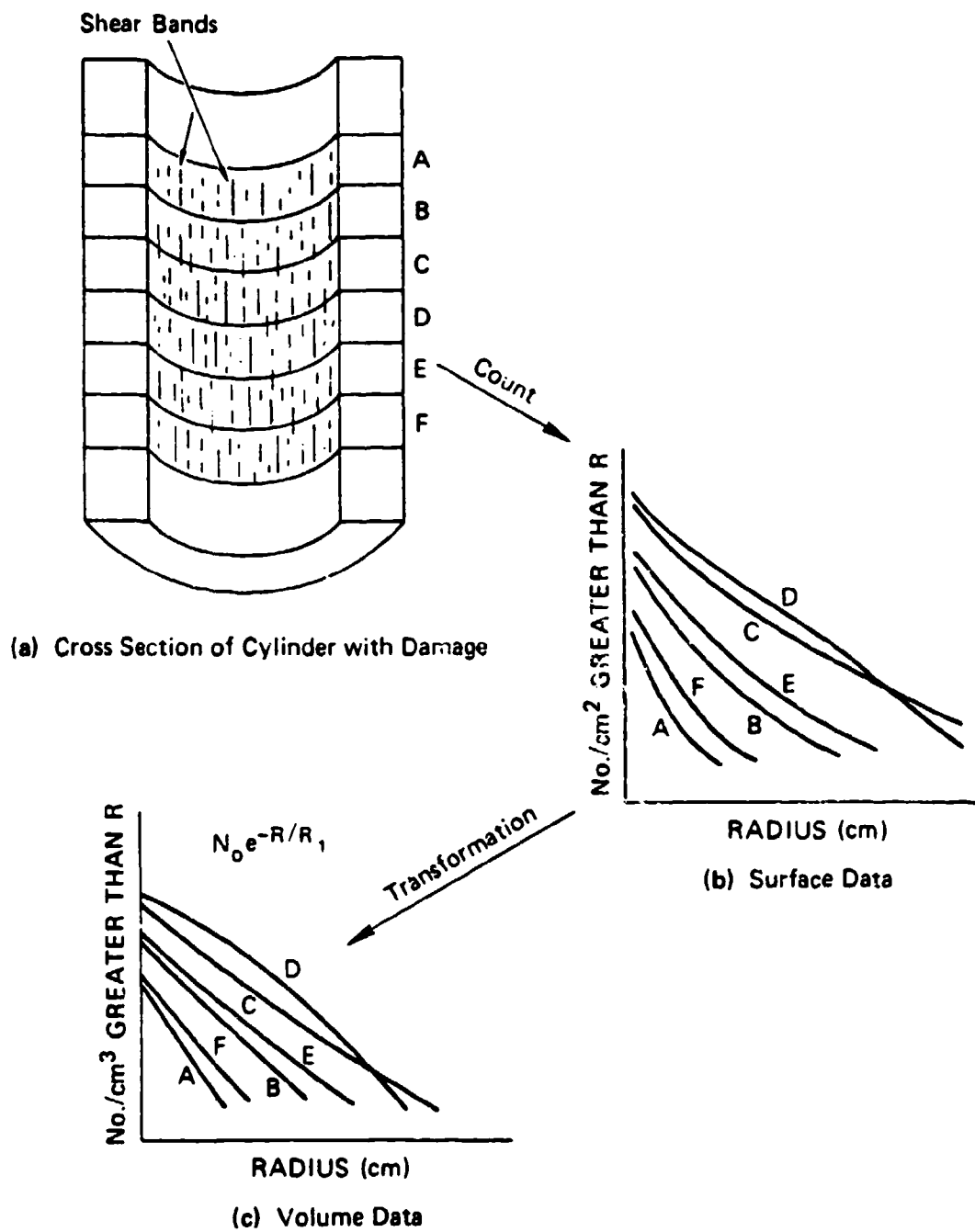
JA-314525-85

FIGURE VI.11 ASSUMED CRACK OPENING VOLUME CHANGES DURING LOADING, UNLOADING, AND RELOADING



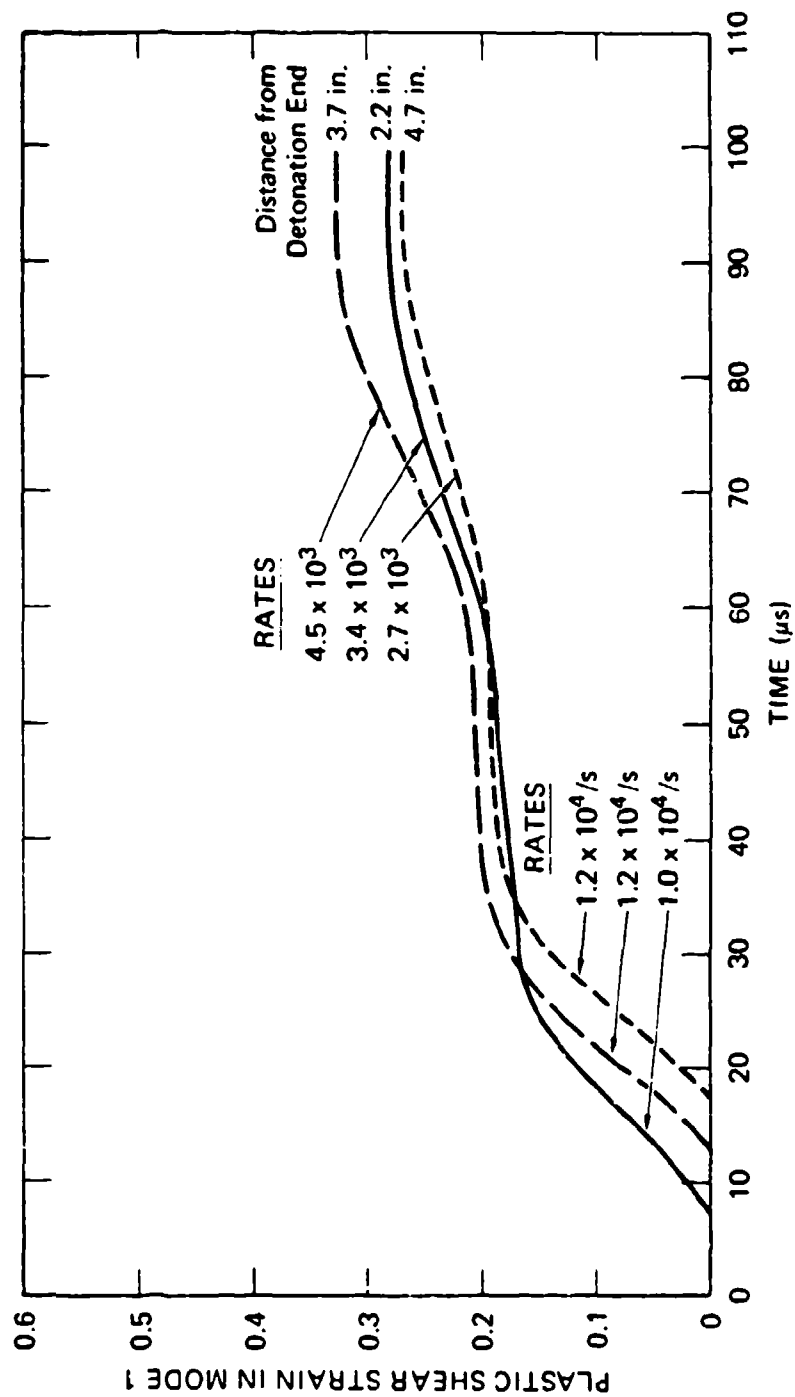
JA-314583-36A

FIGURE VI.12 ONE OF THE ORIENTATION PLANES SHOWING LOADING FROM AN INITIAL STATE σ'_{ko} TO A FINAL STATE σ'^E_k BY A COMBINATION OF ELASTIC AND PLASTIC STRAINS



MA-7893-98

FIGURE VI.13 STEPS IN OBTAINING CUMULATIVE SHEAR BAND DISTRIBUTIONS FROM CONTAINED FRAGMENTING CYLINDER DATA



MA-7893-84

FIGURE VI.14 COMPUTED PLASTIC SHEAR STRAIN IN THE MODE 1 DIRECTION AT THREE AXIAL POSITIONS IN 4340 STEEL CYLINDER 2

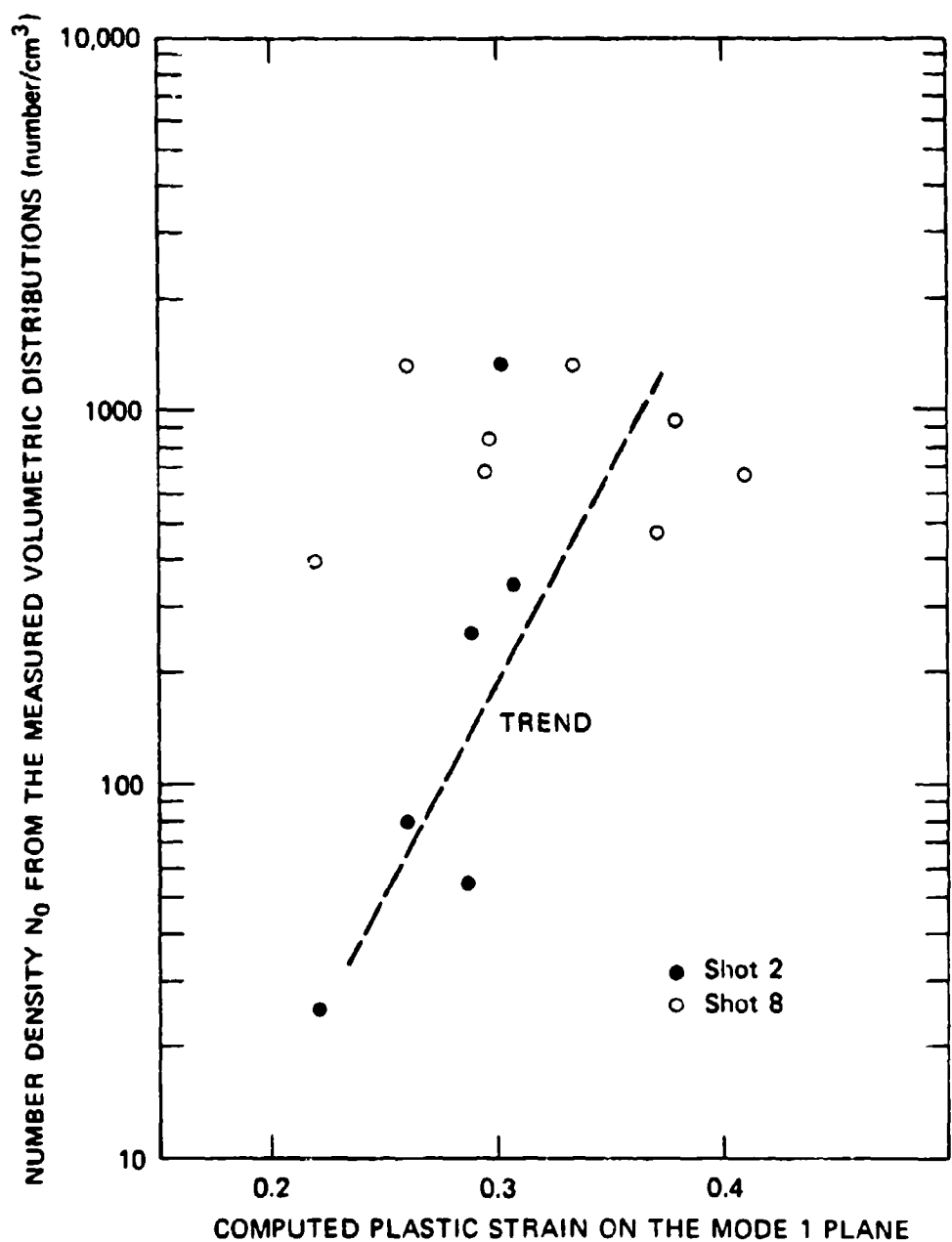


FIGURE VI-56 MEASURED NUMBER OF SHEAR BANDS VERSUS COMPUTED PLASTIC STRAIN FOR DETERMINING AN INITIAL ESTIMATE OF THE NUCLEATION RATE PARAMETER

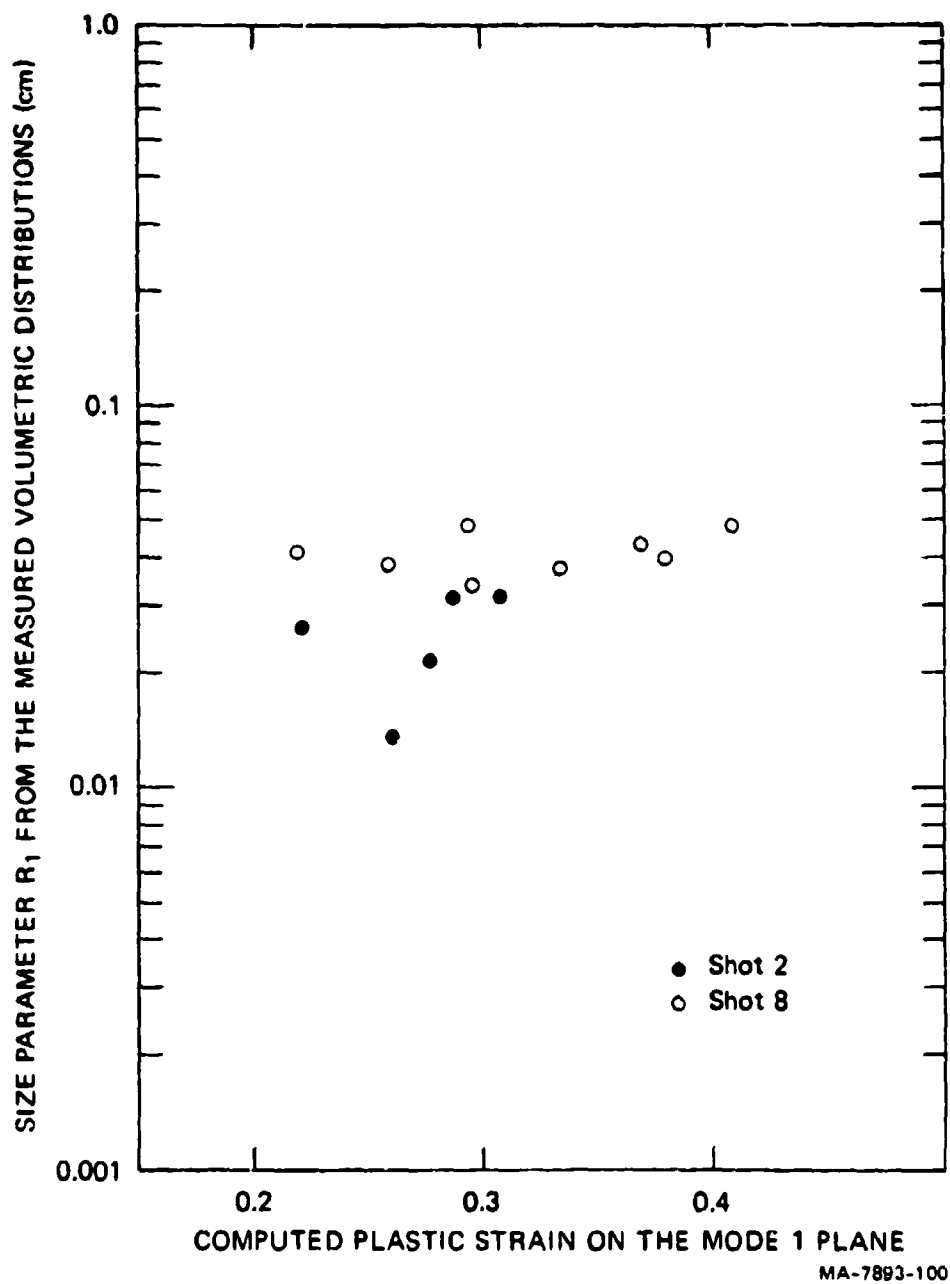
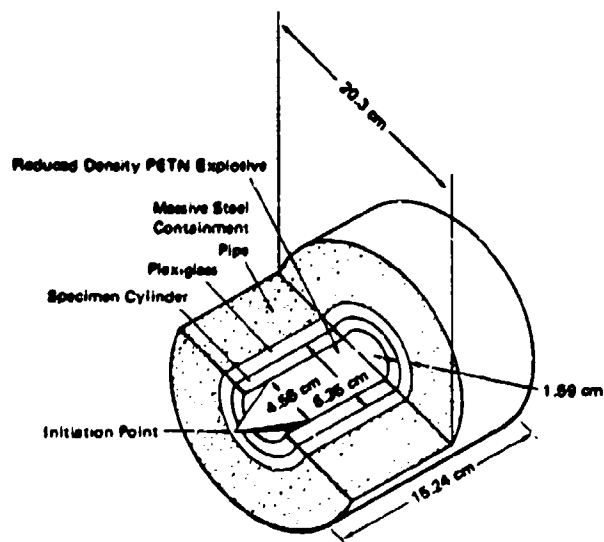
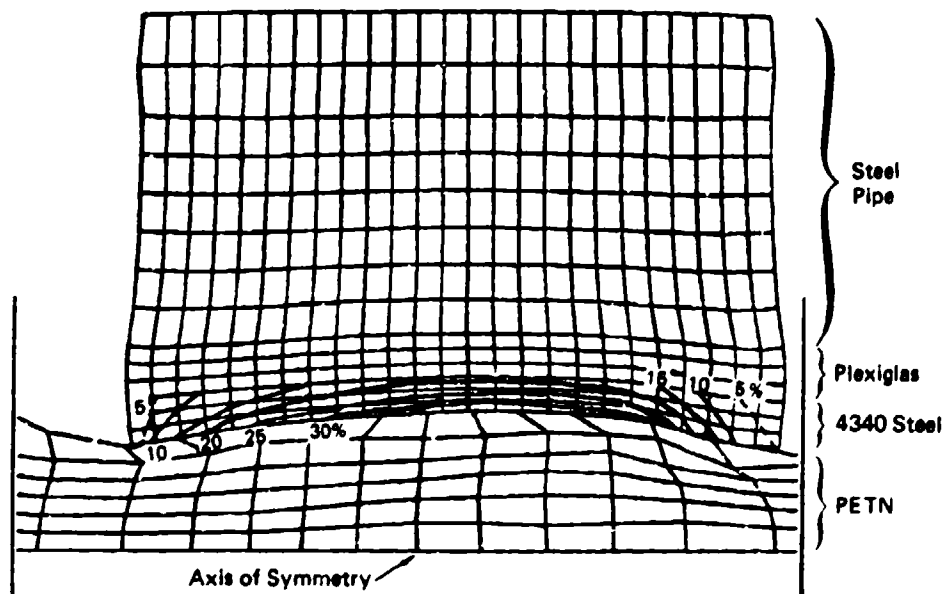


FIGURE VI.18 MEASURED SIZE PARAMETER FOR SHEAR BANDS VERSUS COMPUTED PLASTIC STRAIN FOR DETERMINING AN INITIAL ESTIMATE OF THE GROWTH RATE PARAMETER

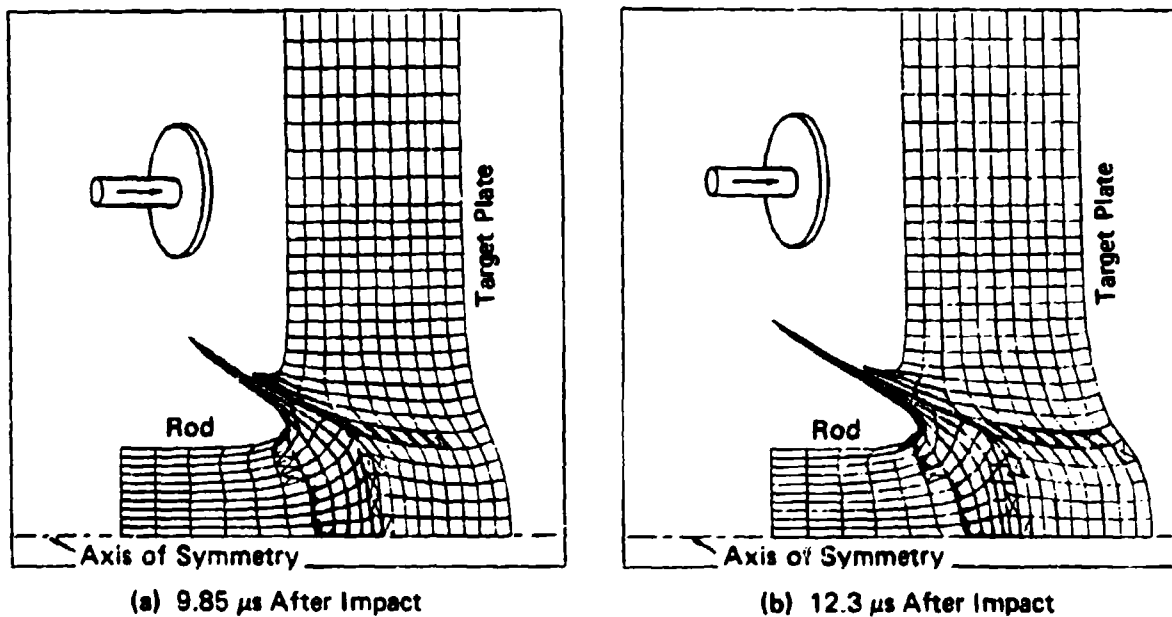


**SCHEMATIC OF CPC EXPERIMENTS FOR
STUDYING SHEAR BAND KINETICS**



JA-314525-86

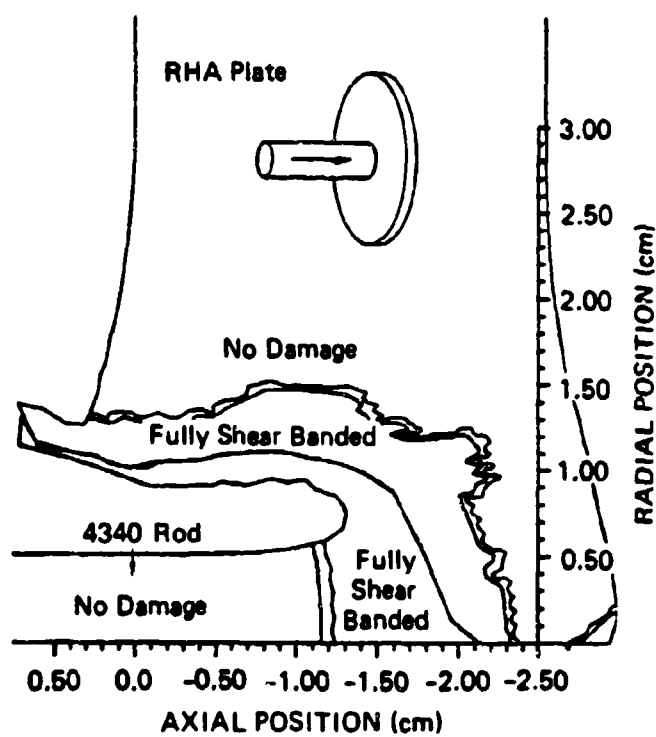
**FIGURE VI.17 PLASTIC STRAIN CONTOURS IN 4340 STEEL FRAGMENTING
CYLINDER IN THE MODE 1 ORIENTATION AT 100 μ s AFTER
DETONATION: SHEAR4 SIMULATION**



JA-314532-99A

FIGURE VI-18 SIMULATION OF A BLUNT 4340 STEEL ROD PENETRATING A RHA PLATE AT THE BALLISTIC LIMIT (750 m/s)

Shaded cells were fully shear-banded in at least one orientation; cells with a cross contain some bands.



JA-314632-102A

FIGURE VI-19 SIMULATION OF A BLUNT 4340 STEEL ROD PENETRATING A RHA PLATE AT 1560 m/s (AT 28 μ s).



(a)



(b)



(c)

MP-3206-5

FIGURE VI-20 THREE VIEWS OF A STEEL CYLINDER AFTER IMPACTING A QUARTZITE TARGET AT 140 m/s

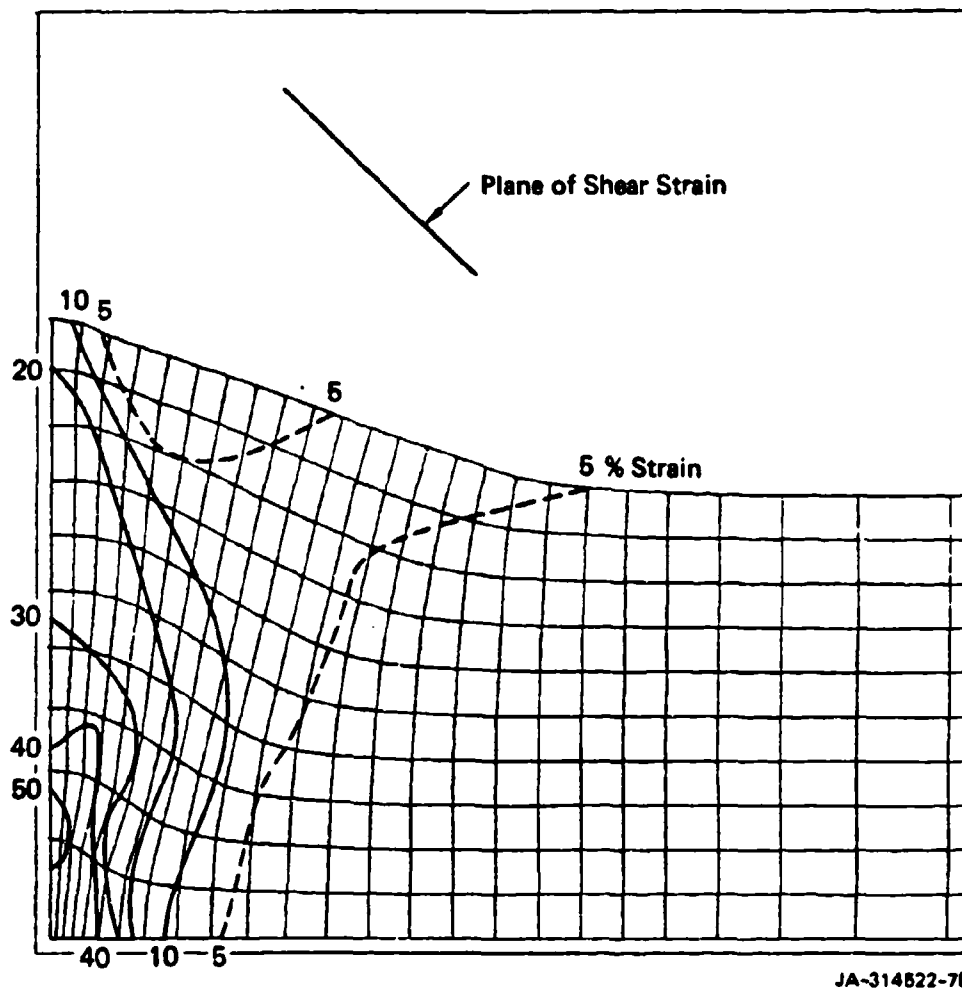
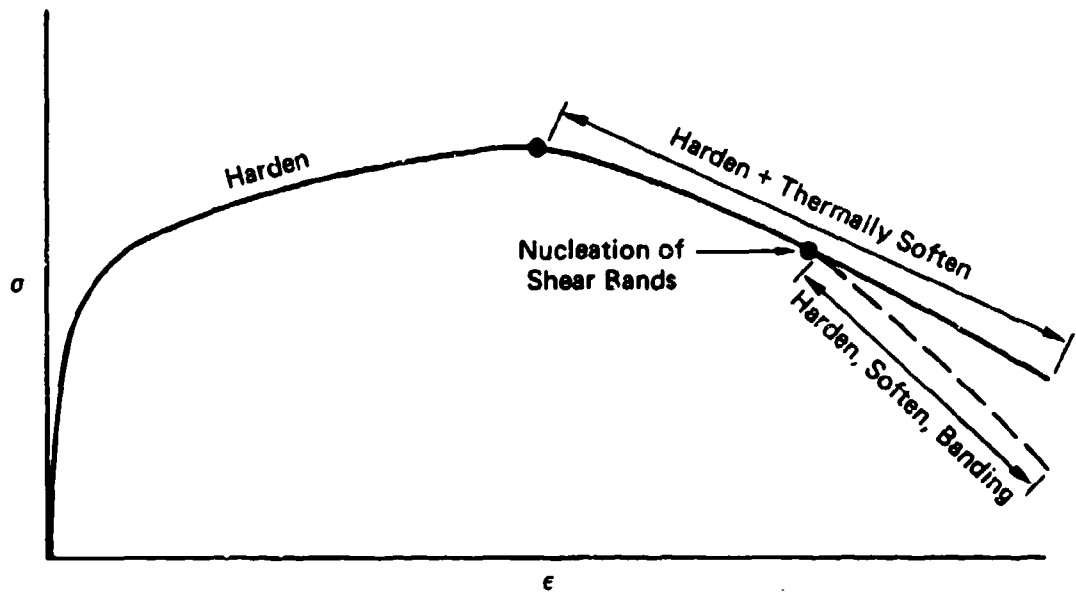
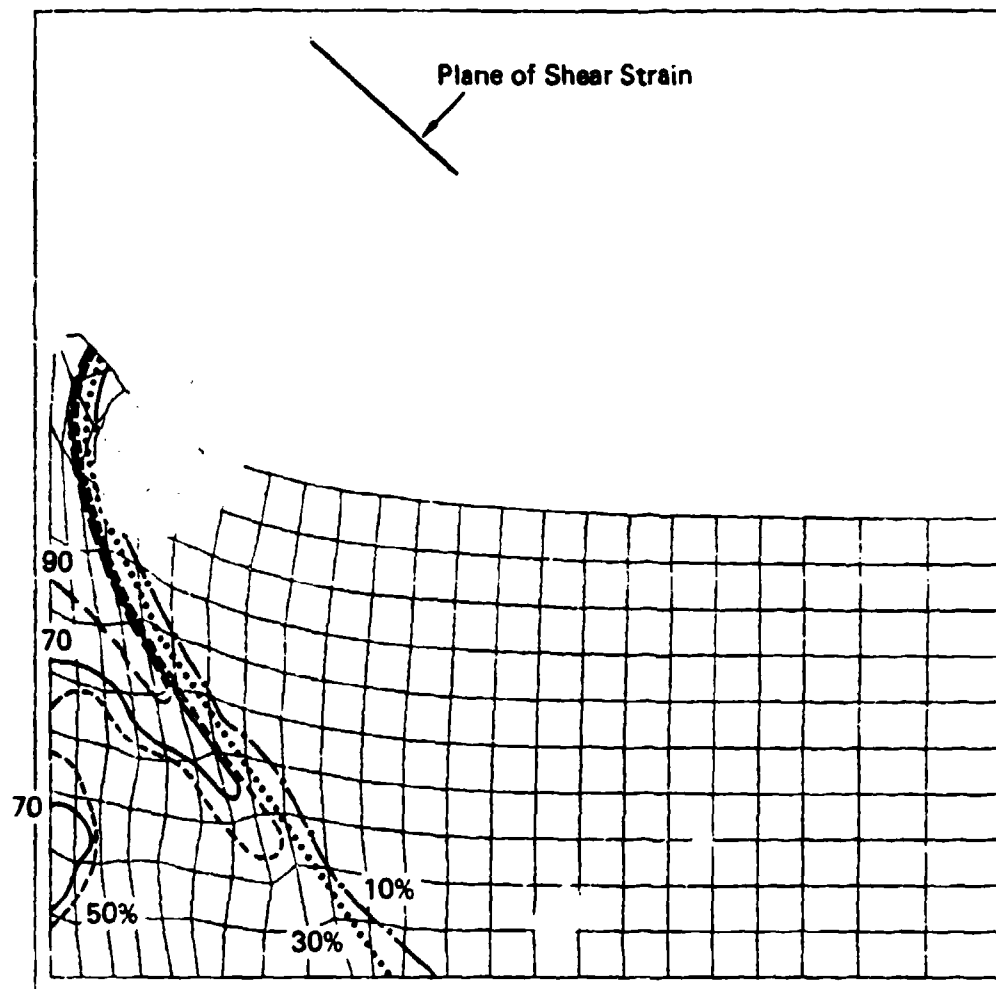


FIGURE VI-21 CONTOURS OF PLASTIC STRAIN IN THE DIRECTION
TO FORM A CONE AT THE HEAD OF THE PROJECTILE:
SHEAR4 SIMULATION OF A TAYLOR TEST WITH 4340
STEEL



JA-314822-79

FIGURE VI-22 PROPOSED STRESS-STRAIN PATH SHOWING THERMAL SOFTENING AND THE NUCLEATION THRESHOLD FOR SHEAR BANDING



JA-314522-80

FIGURE VI-23 RESULTS OF A SHEAR4 SIMULATION OF A TAYLOR TEST, USING THERMAL SOFTENING: CONTOUR LINES ARE FOR THE CONE-FORMING ORIENTATION OF SHEAR BANDS

CONTENTS

VII MECHANISM OF DUCTILE TENSILE FRACTURE IN VAR 4340 STEEL

A. Introduction.....	VII- 1
B. Previous Work.....	VII- 2
C. Topographic Analysis of Fracture Surfaces: The Concept..	VII- 3
D. Experimental Procedures.....	VII- 4
E. Reconstruction of the Fracture Process.....	VII- 5
F. Influence of Microstructure on Microfailure Processes.....	VII- 8
G. Discussion.....	VII- 10
H. References.....	VII- 11

VII MECHANISM OF DUCTILE TENSILE FRACTURE IN VAR 4340 STEEL

A. Introduction

Although the penetration of metallic armor and the disintegration of rod-like metallic projectiles occurs in many cases predominantly by shear, tensile fracture frequently accompanies the shear failure and in many cases importantly influences the result of the penetrator/armor impact. For example, the ejection of fragments from the rear surface of impacted armor plate is promoted by ductile tensile fracture produced by reflected stress waves. Such tensile fractures may also be expected to reduce the residual strength and hence reduce the load-carrying ability of structural armor, and adversely affect the capability of the armor to survive subsequent projectile attack.

Further, the rod-on-plate impact experiments discussed in Section IV imply that ductile tensile fracture enhances failure by shear banding by providing initiation sites for shear localization. The occurrence of tensile fracture thus likely reduces the level of strain and strain rate necessary for shear band nucleation. Moreover, examination of shear band failures in specimens tested with the split Hopkinson torsion bar showed that once shear bands had formed, they often coalesced with one another and failed by ductile tensile fracture.

The observations described above suggest that material failure models for simulating penetrator/armor encounters must include the tensile fracture mode to be useful. Thus a goal in the present program was to improve an existing computational model for ductile fracture, namely DFRAC¹, and modify it as necessary to apply to the program baseline material.

To be reliable, the model must be based on the physical mechanism of the ductile fracture process, and the values of the model parameters must be obtained from data from tensile fracture experiments on the baseline

material. To establish the mechanism and obtain the necessary fracture data, we first reviewed the literature on the subject and then supplemented the literature results by performing experiments on the baseline material.

This section reports pertinent literature data on ductile fracture behavior of 4340 steel, describes the experimental work performed on the baseline material, and discusses the implications for computational modeling.

B. Previous Work

The mechanism of ductile tensile fracture has been the subject of many investigations over the years. The work of Puttick², Rogers³, Cox and Low⁴ and others has clearly shown that ductile fracture in a wide variety of metals and alloys occurs by a three-stage process. This process includes the nucleation of holes at inclusions or second phase particles, the plastic expansion of the holes under combined shear and dilatational stresses, and coalescence of the holes by plastic impingement or void sheet formation.

Particularly relevant to the present program is the work of Cox and Low⁴, who performed detailed mechanistic and metallographic investigations on commercial purity and high purity 4340 steel specimens that were given a heat treatment similar to the standard heat treatment of the baseline material in the present work. Tensile specimens were loaded to various predetermined levels of strain, unloaded, and sectioned longitudinally. The sectioned surfaces were then polished and etched for metallographic examination. Void nucleation occurred by fracture of the interface between manganese sulfide inclusions and the matrix. Nucleation occurred at lower strains at the larger inclusions and void growth proceeded more rapidly from the larger inclusions. Tensile stress triaxiality had little effect on nucleation, but it substantially affected void growth rates.

Coalescence of neighboring voids occurred by the localization of plastic flow in the ligaments between the voids on surfaces oriented

approximately 45 degrees from the tensile axis. The high strains on these surfaces caused much smaller voids to nucleate and grow from tiny cementite precipitates in the quenched and tempered lath interfaces. The resulting void sheets precluded coalescence by impingement of neighboring voids, such as occurs in 18 Ni 200 grade maraging steel. This difference in coalescence mechanism is cited as the reason that the 4340 steels are less tough than 18 Ni maraging steels at the same strength level.

Although the data generated by Cox and Low are subject to errors (e.g., from material inhomogeneity, anisotropy, and the conversion of surface observations to volume data), they are useful in modeling the void nucleation and growth processes. By plotting the percentage of inclusions having voids as a function of true strain, these workers obtained a nucleation function. Similarly, by plotting the radius of the largest void on a cross section for many specimens, they essentially defined a growth function. An analogous function for coalescence, the third stage of the fracture process, was not attained. Nevertheless, the work of Cox and Low provides a major part of the data necessary to generate a computational model.

To obtain the needed data for a void coalescence function and to acquire void nucleation and growth data for the baseline material of the present program, a fracture surface analysis technique being developed at SRI was applied to a round bar tensile specimen of VAR 4340 fractured under quasi-static load. This technique allows the fracture process to be reconstructed in an approximate way by computer matching of conjugate fracture surface topographs.^{5,6} The technique is especially appropriate for investigating the void coalescence stage.

C. Topographic Analysis of Fracture Surfaces: The Concept

The principle underlying the method used for fracture process reconstruction is as follows. Consider a material under tension that is beginning to fail by developing microcracks. As each microcrack forms, the stress on the new crack faces falls to zero and material adjacent to the crack faces relaxes and undergoes no further deformation. The

applied load shifts to nearby unbroken material, which continues to deform plastically until fracture. Thus, the process of deformation and fracture is experienced by each tiny volume of material in the fracture path at some time in the fracture process, and the sequencing of the process for each material volume in the overall fracture event is reflected in the fracture surface. Hence, by determining the amount of plastic deformation normal to the fracture surface, we can determine the sequence of the microfracture activity, and thereby reconstruct the macrofracture event.

We implement this principle by quantitatively assessing the fracture surface topography and then superimposing and incrementally displacing conjugate areas of the topographs via computer.

D. Experimental Procedures

We chose for analysis a round bar tensile specimen of the baseline HRC 40 VAR 4340 steel pulled to fracture at a strain rate of about $4 \times 10^{-5} \text{ s}^{-1}$ at room temperature. Scanning electron microscope (SEM) photographs of the two conjugate fracture surfaces are shown in Figure VII.1. Stereophotographs of each fracture surface were made with the SEM at several magnifications by first aligning the axis of the round bar tensile specimen with the axis of the electron beam, then rotating the specimen stage 4 degrees to the right and to the left of the axis and photographing the surface in each orientation. Stereopairs of the two conjugate fracture surfaces at 1000 x magnification are shown in Figures VII.2 and VII.3.

These stereopairs were then sent to an aerial surveying company who used semiautomated cartographic equipment to digitize the elevation information from the photos and to produce topographic contour maps. The elevation data were obtained by placing the negatives of a stereopair in a cartographic viewer and carefully aligning the two images; an operator then measured the elevation of a point above a selected baseline level by adjusting a micrometer setting until a floating dot superimposed upon a reference dot. Approximately eight hours of operator time were required

to evaluate the stereopairs shown in Figures VII.2 and VII.3. Topographic maps for the conjugate stereopairs are shown in Figure VII.4. (Note that the map A is inverted.)

E. Reconstruction of the Fracture Process

An indication of how the fracture surfaces formed was obtained by comparing conjugate areas of the surfaces. This was done quantitatively by using the topographic data generated by the cartographic company. The procedure was as follows.

The topographic data obtained from the conjugate stereopairs (Figures VII.2 and VII.3) and displayed graphically in Figure VII.4 were used in the analysis. One map was inverted (e.g., the map shown in Figure VI.4) and superimposed over the conjugate map, translated, and rotated until identifiable corresponding points were aligned. Then the spacing between the two conjugate topographic maps was reduced to negative values everywhere so that there were no void regions between the two surfaces. (Physically this procedure would be unrealistic because material on one surface is forced to overlap material on the other surface.) The computational reconstruction of the fracture process was begun by incrementally displacing the two topographic fracture surfaces. After each increment of displacement, the map interf. was scanned to see if and where gaps developed. The appearance of a gap signifies a separation of the material--that is, the formation of a microvoid or microcrack. The size, shape, and location of the gap was recorded in the computer. Changes in gap profiles with increasing map displacements indicate the growth history of the microfailure; these changes were also recorded. As the surfaces are displaced further, other gaps form, previous gaps get larger, and neighboring gaps join together. These observations are interpreted as caused by the nucleation, growth, and coalescence of microvoids in the material.

Gap (microvoid) development is best illustrated in a computer-made motion picture; several movies were made using these results, and presented at the program review meetings. The results can also be

displayed in fractured area projection plots, cross-section fracture plots, and three-dimensional gap profile plots.

Figure VII.5 shows the projection of the gapped area for several map displacements. Taken together, this series of computer figures illustrates the development of fracture. The number in the upper right-hand corner of each plot indicates the relative displacement of the conjugate maps measured in micrometers from an arbitrary reference plane. In the initial plot (zero relative displacement), the appearance of the first gap is detected (to the right of center). Displacing the maps an additional 8 μm (the next plot) causes the gap to grow moderately, and reveals additional gaps in the same general area. In the third plot, representing a 16- μm displacement, further growth of the initial gap and the gap in plot 2 are indicated, additional gaps appear, and several gaps have merged. These basic features of gap nucleation, growth, and coalescence continue to occur in the nine subsequent fractured area projection plots, which provide a detailed picture of the fracture process.

We see that microfractures nucleate at a number of sites in the tensile bar and at different times in the tensile bar's strain history. The latter observation suggests that microfractures nucleate continuously as a function of strain. A measure of the overall strain is given by the map displacement shown in the upper right-hand corner of each plot. Somewhat later in this section we identify the microstructural features associated with individual gaps by matching the gaps in the FAP plots with the SEM micrographs of Figures VII.2 and VII.3.

The increases in size of individual gaps from plot to plot indicate the growth behavior of microfractures. In general, the gaps expand rather symmetrically, although instances of directional growth producing elongated shapes are occasionally seen. Estimates of growth rates as a function of specimen displacement or strain are obtainable by measuring the increase in characteristic gap dimension from plot-to-plot and dividing by the displacement or strain increment. Microfailure growth velocities can be inferred in a similar way by converting displacements

to time through the cross-head speed of the tensile machine. Information on the paths taken by the growing microfractures and the three-dimensional shapes of the microfractures can be obtained from cross-sectional plots of the topographic data and by correlation with the photomicrographs, as will be shown later.

Microfracture coalescence behavior is also graphically illustrated in the plots. Linking of neighboring growing microfractures occurs in such a way as to produce a relatively symmetric fracture area. Unbroken ligaments of material engulfed by the fracture area are a common feature. These ligaments are apparently more ductile than the surrounding material, perhaps because of local differences in chemical composition or microstructure, or because of a favorable orientation with respect to the tensile axis.

Coalescence rates, or rates of expansion of the fractured area can be obtained, as discussed for microfracture growth, by measuring some characteristic size of the fractured area in successive plots and dividing by the increment of displacement, strain, or time.

Cross-sectional views of the fractured area projection plots are shown in Figure VII.6. These cross-section profiles were taken along the line A-A indicated in the first plot in Figure VII.5, and successive cross-sectional plots show the fracture behavior at 10- μ m increments. The first plot at zero relative displacement shows total overlap of the conjugate surface before any gap appeared. In the second plot a gap occurs near the center of the plot and begins to expand in plot 3 on a plane whose trace is about 45 degrees from the tensile axis. This observation suggests that microfracture is occurring by a shear process. In plot 4 the original gap has widened and is beginning to look more like a void. In addition, another gap has appeared nearby, but on a different plane. It, too, begins its growth in a 45-degree shear mode, then widens and becomes more equiaxed (plot 5). The coalescence behavior of the two growing microfractures is graphically shown in plots 6 and 7. Link up occurs in a shear mode as the two microfractures grow toward each other on a 45-degree plane. The coalesced microfractures widen

considerably in plots 8-10 as the material at the microfracture tips deforms and stretches. New microfractures appear to the right of the coalesced fractures in plots 8 and 9 and form a ligament, plot 10, before coalescing in plot 11.

It is to be remembered that the appearance of a gap in the cross-sectional plots does not necessarily imply microfracture nucleation, as it did in the fracture area projection plots of Figure VII.5. Rather, gap appearance in Figure VII.6 could be caused by growth of an already nucleated microfracture that penetrates the cross-sectional plane being examined. This ambiguity can be resolved, and a three-dimensional picture can be obtained, by considering the FAP plots and cross-sectional plots simultaneously.

F. Influence of Microstructure on Microfailure Processes

Microstructural features that serve as microfracture nucleation sites, determine fracture propagation paths, and produce ligaments can be identified by comparing those locations indicated on the fractured area projection (FAP) plots and cross-sectional (CS) plots in Figures VII.5 and VII.6 with the corresponding areas on the fracture surfaces, Figures VII.2 and VII.3.

Figure VII.7 shows how this correlation is accomplished. By superimposing the FAP plots (Figures VII.7c and 7d) onto the photomicrographs (7a) and fracture surface topograph (7b), we can pinpoint the sites of microfracture nucleation on the fracture surface. Metallographic examination of these sites suggests that a key microstructural feature responsible for microfracture nucleation is the prior austenite grain structure (discussed later). The topographic maps show that the initiation sites are situated primarily at the bottoms of valleys or the tops of peaks. Microfractures thus grow on surfaces inclined at roughly 45 degrees to the tensile axis. Information on why the indicated sites are nucleation sites should be sought by examining them in greater detail with the SEM at high magnification, and by using x-rays to establish local compositions and composition gradients. A

further technique is to section the specimen through the site, then polish and etch the surface to reveal the structure. Similar analyses should be performed to pinpoint and examine the unbroken ligaments. Goals would be to determine the failure mechanism, the degree of stretching, and the microstructural characteristics of these patches of apparent high ductility material.

The topographic data show a substantial periodicity in the fracture surface roughness. This is recognizable from the cross-section profile, as, for example, in Figure VII.6. The wavelength of the undulation (i.e., the approximate average distance between peaks or valleys) is about 20 μm . To establish whether this observed wavelength corresponded to a microstructure characteristic, we sectioned one-half of the broken tensile bar parallel to and about 5 mm below the fracture surface, then polished and etched this surface in preparation for metallographic examination. Figure VII.8a shows the tempered martensite structure of this surface as revealed by a 2% nital etch (approximately 20 seconds), and Figure VII.8b shows the prior austenite structure brought out by a different etching procedure.*

The average size of the prior austenite grains, as shown in Figure VII.8b, agrees well with the average wavelength of the fracture surface roughness, suggesting that the prior austenite grain structure importantly influences the fracture process.

One can speculate from these topographic and metallographic observations that microfailure nucleates preferentially at prior austenite grain boundaries that are oriented normal to the direction of the maximum tensile stress (the tensile axis). These microfailures propagate along the boundaries, producing failure surfaces lying at large

*Etchant consisted of 0.5 g picric acid, 2.0 g cupric chloride, in 30 ml of distilled water. The surfaces were etched by immersing the specimen in the heated etchant (65 to 70°C) for 30 to 40 seconds, swabbing the surfaces with NH_4OH to remove the brown stain, and polishing lightly with Al_2O_3 .

angles to the tensile axis, and eventually join with one another. At the magnification used here, the angled surfaces were featureless and flat. To investigate the role of inclusions, the topographic analysis should be performed at higher magnification.

G. Discussion

The results of the topographic fracture surface analysis are in accord with the results obtained by Cox and Low from examination of sectional surfaces through interrupted tensile tests. Void nucleation, growth, and coalescence occur continuously with increasing strain. The rates at which these processes proceed with strain are quantifiable from the data, and should be pursued in future work.

The topographic work reported here complements the microstructural effort of Cox and Low. Whereas the Cox and Low investigations were performed at the 1 to 10 μm level, our work was performed at the 10-100 μm level. Thus the main microstructural features studied by Cox and Low were the MnS inclusions and the cementite particles, whereas the prior austenite grains were the prominent feature at the 10-100 μm level. It would be interesting to perform the topographic work at higher magnification to examine the effects of inclusions and cementite particles.

For example, qualitative observations with the SEM at higher magnification showed that the mountains and valleys characterized by the present analysis are covered by minute dimples 1 to 2 μm in diameter. These dimples are probably the halves of voids that nucleated at tiny inclusions, grew by plastic flow (maintaining a roughly spherical shape), and coalesced by impinging with neighboring expanding voids. Details of this process can be obtained by applying the topographic analysis procedure at a magnification of about 5000x.

The resolution of the cartographic equipment used to evaluate the stereopairs in Figures VII.2 and VII.3 is about 10 μm on the photographic plate. Thus, the elevation resolution for our stereopairs, which were produced with an included angle of 8 degrees, is about 7 μm . Higher

resolution can be obtained from photographs taken at higher magnification. For example, 0.07 μm of elevation resolution can be obtained from 100x photographs.

The topographic analysis concepts described in this section and applied to quasi-static fracture in a round bar tensile specimen promise to provide other insights into micro- and macro-fracture behavior. For example, crack opening displacements are indicated in cross-sectional plots and provide a local measure of material toughness and toughness variation.

Furthermore, the technique offers a number of advantages over the straining, interrupting and sectioning technique used by Cox and Low; for example less material and fewer tests are required, better statistics are attained, the development of individual voids can be tracked, and void coalescence phenomena are more readily studied.

H. References

1. D. A. Shockey, K. C. Dao, L. Seaman, R. Burbach, and D. R. Curran, "Computational Modeling of Microstructural Fracture Processes in A533B Pressure Vessel Steel," SRI International Final Report for EPRI, Project 1023-1 (May 1980).
2. K. E. Puttick, "Ductile Fracture in Metals," Phil. Mag 4, 964-969 (1959).
3. H. C. Rogers, "The Tensile Fracture of Ductile Metals" AIME Trans. 218, 498 (1960).
4. T. B. Cox and J. R. Low, Jr., "An Investigation of the Plastic Fracture of AISI 4340 and 18 Nickel-200 Grade Maraging Steels," Met. Trans. 5, 1457-1470 (1974).
5. T. Kobayashi, G. R. Irwin, and X. J. Zhang, "Topographic Examination of Fracture Surfaces in Fibrous-Cleavage Transition Behavior," in Fractography of Ceramic and Metal Failures, ASTM STP 827, J. J. Mecholsky, Jr., and S. R. Powell, Jr., Eds., American Society for Testing Materials, pp. 234-251 (1984).
6. T. Kobayashi, and D. A. Shockey, "Environmentally Accelerated Cyclic Crack Growth Mechanisms in Reactor Steel Determined from Fracture Surface Topography," in FRACTURE: Interactions of Microstructure Mechanisms and Mechanics, J. M. Wells and J. D. Landes, Eds., The Metallurgical Society of AIME, New York, pp. 447-463 (1984).



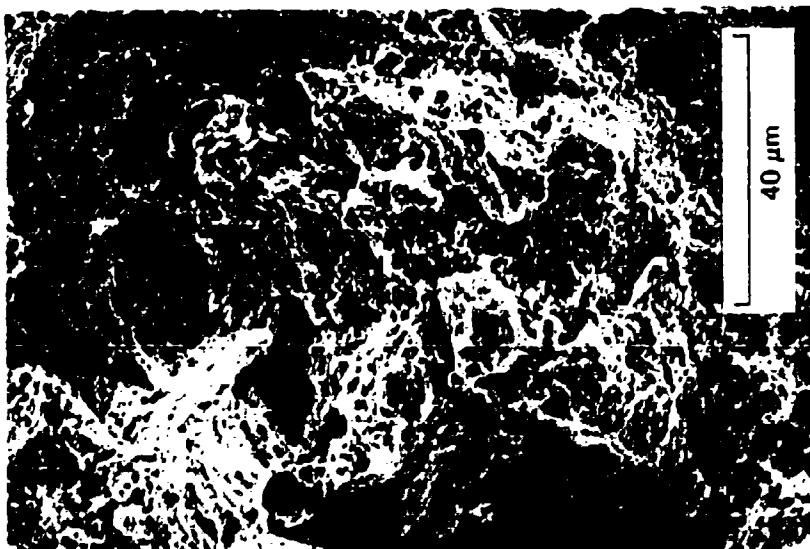
Surface B



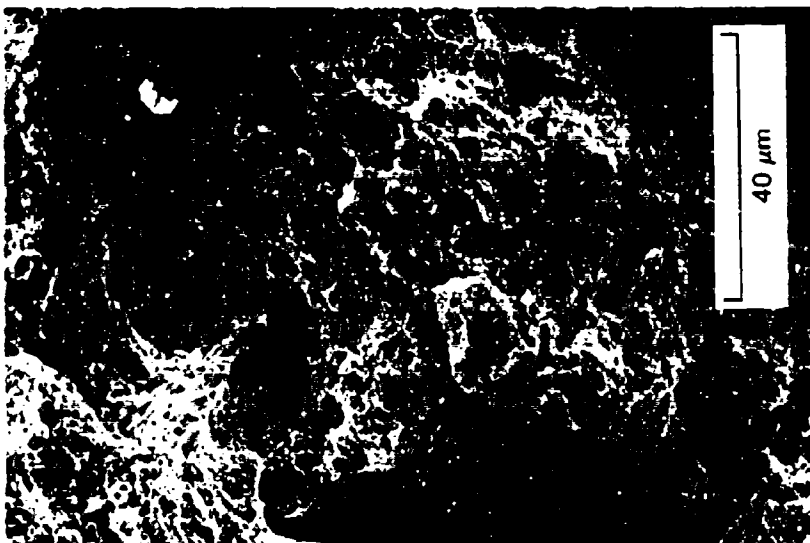
Surface A

FIGURE VII.1 SEM PHOTOGRAPHS OF CONJUGATE FRACTURE SURFACES IN HRC 40
VAR 4340 TENSILE BAR

JP-3722-148



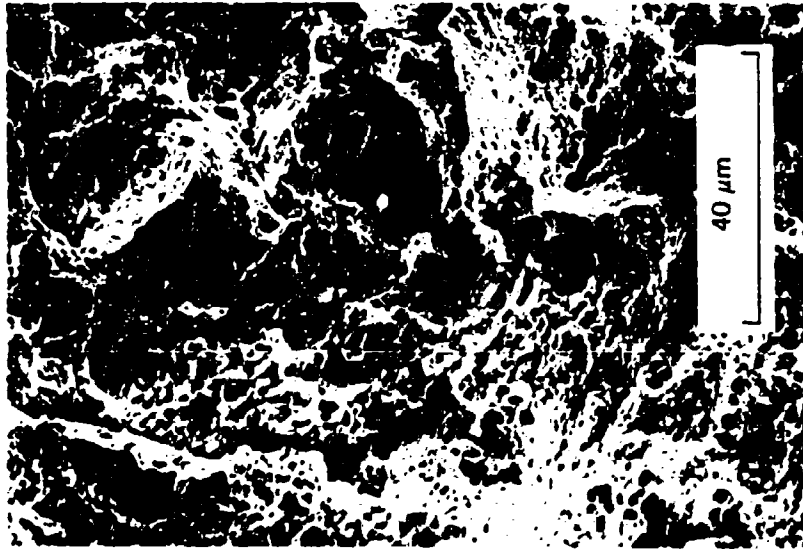
Left 4 Degrees



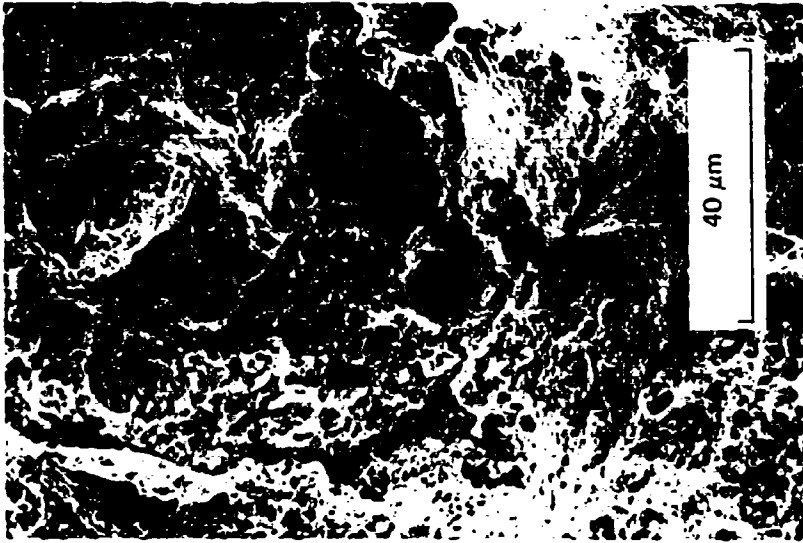
Right 4 Degrees

JP-318583-47

FIGURE VII.2 STEREOPAIR OF SEM PHOTOGRAPHS OF FRACTURE SURFACE A
(IN FIGURE VII.1) AT 1000 X MAGNIFICATION



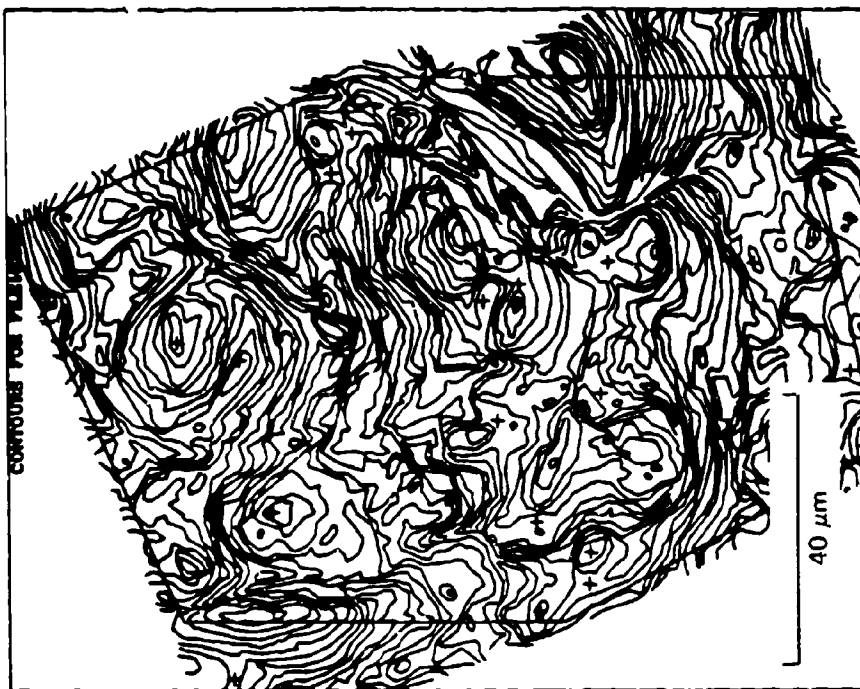
Left 4 Degrees



Right 4 Degrees

JP-318583-48

FIGURE VII.3 STEREOPAIR OF SEM PHOTOGRAPHS OF FRACTURE SURFACE B
(IN FIGURE VII.1) AT 1000 X MAGNIFICATION



Surface B

JP-318583-49



Surface A

FIGURE VII.4 CONJUGATE TOPOGRAPHIC MAPS FOR STEREOPAIRS IN FIGURES VII.2 AND VII.3

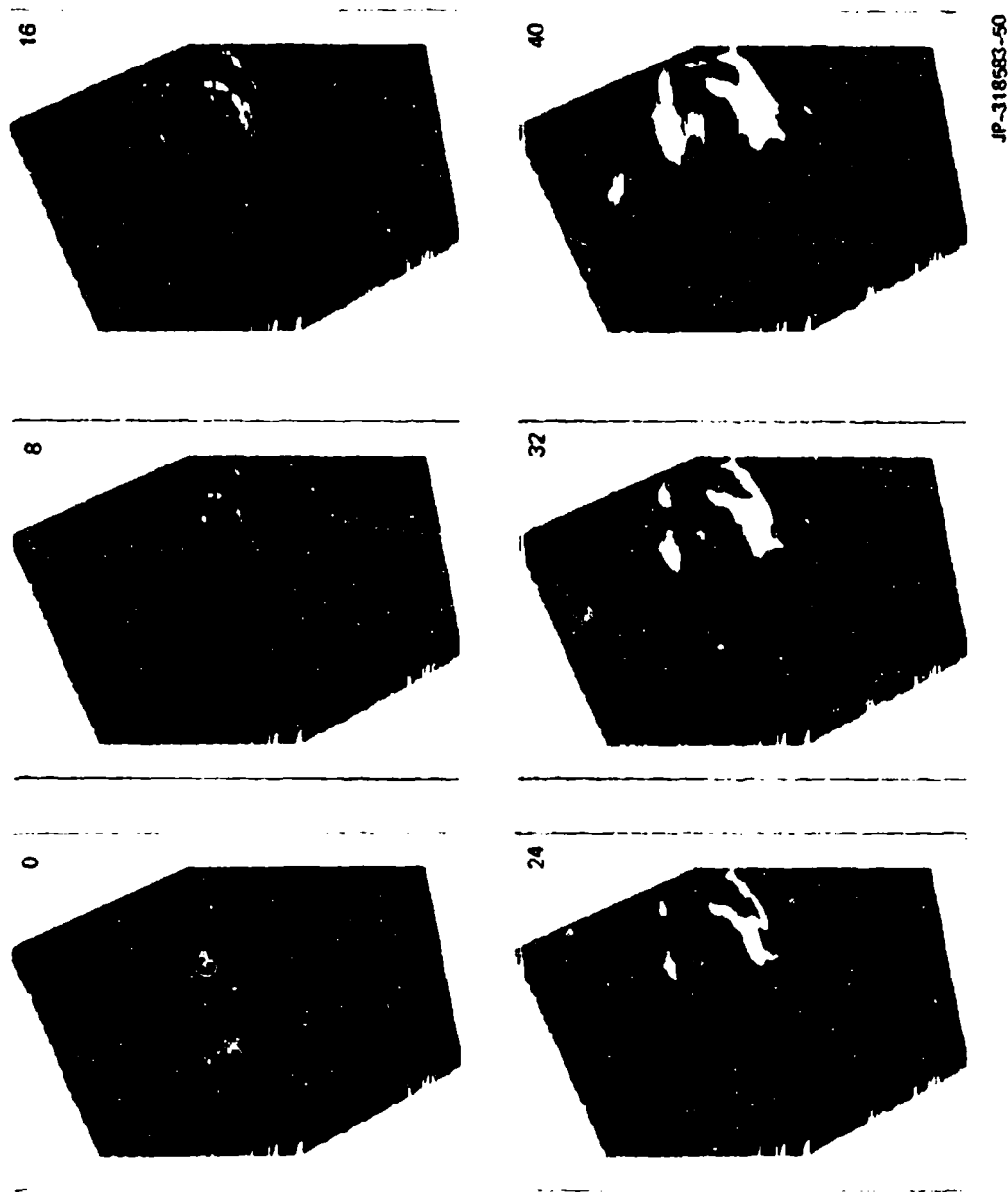
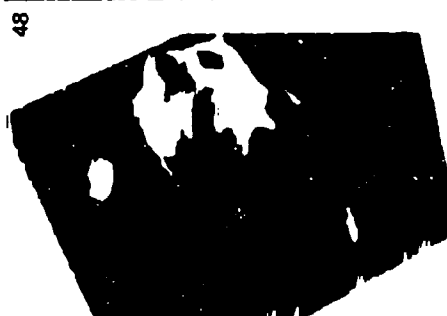
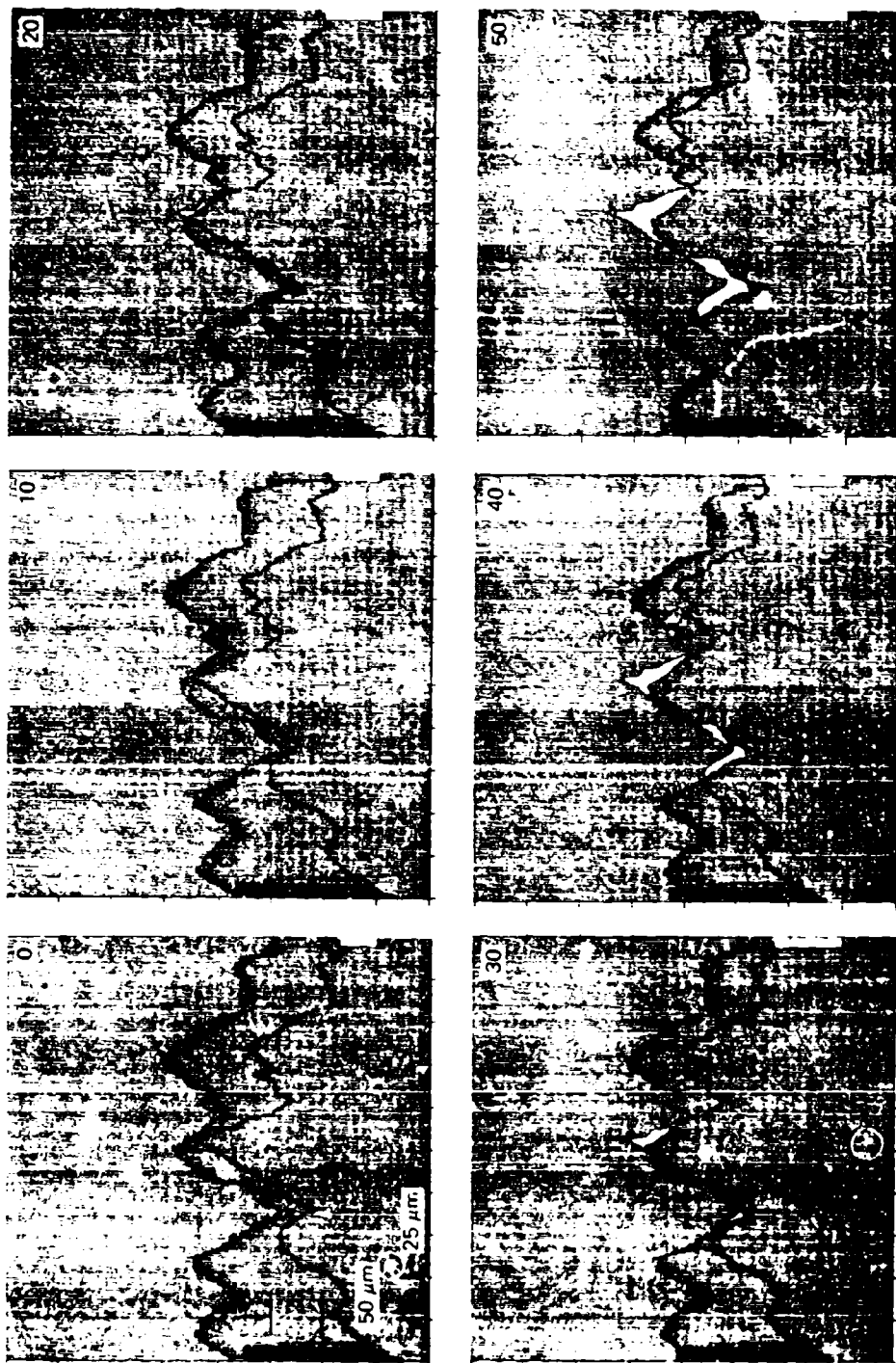


FIGURE VII.5 FRACTURED AREA PROJECTION PLOTS
(Fracture surface displacement indicated in micrometers
in upper right-hand corners).



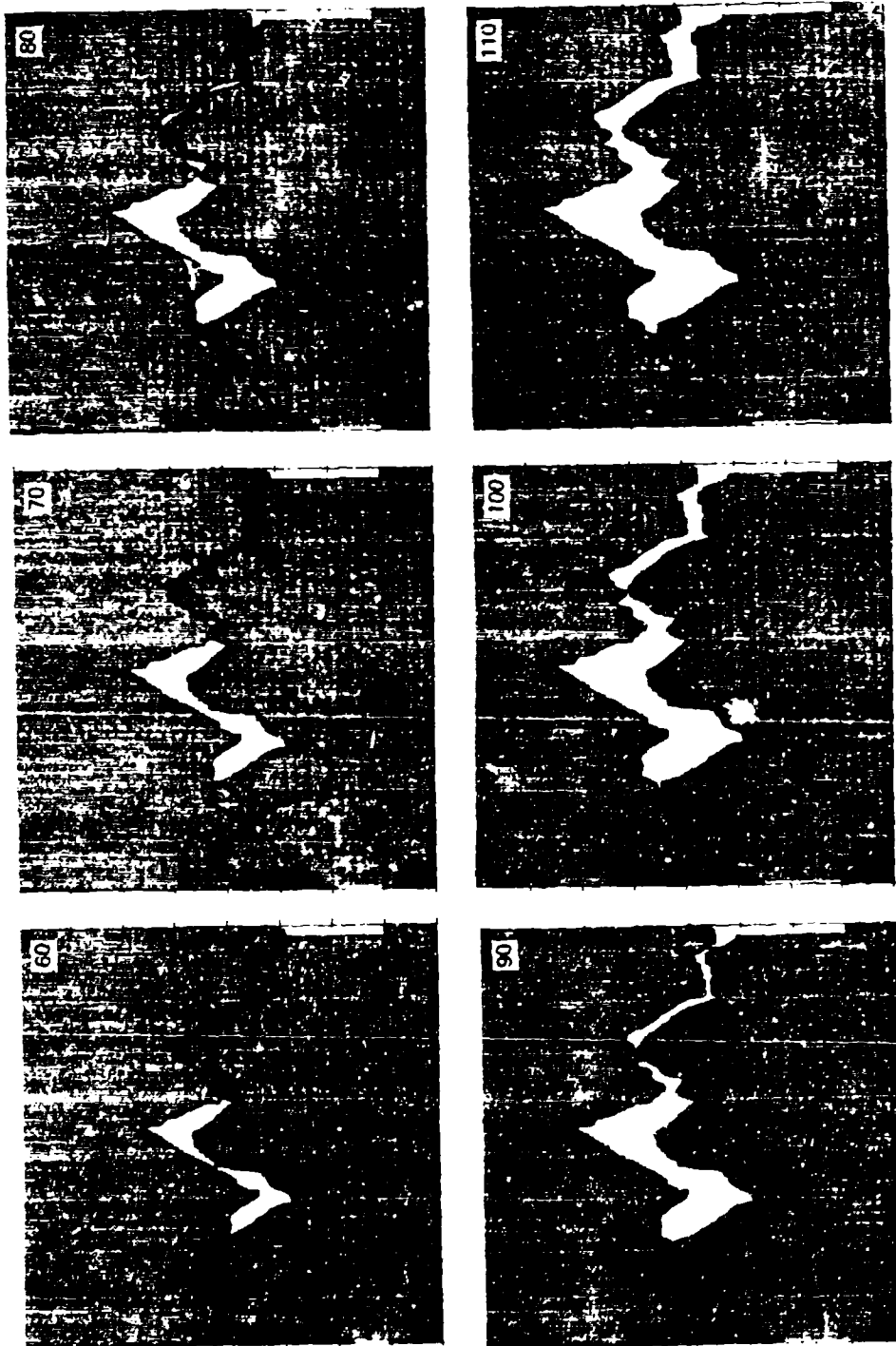
JP-318583-51

FIGURE VII.5 FRACTURED AREA PROJECTION PLOTS (Concluded)



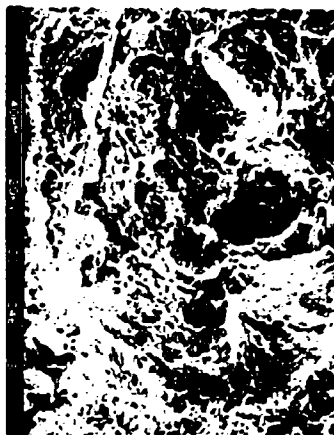
JP-318583-52

FIGURE VII.6 CROSS-SECTIONAL VIEWS OF FAP PLOTS



JP-318583-52

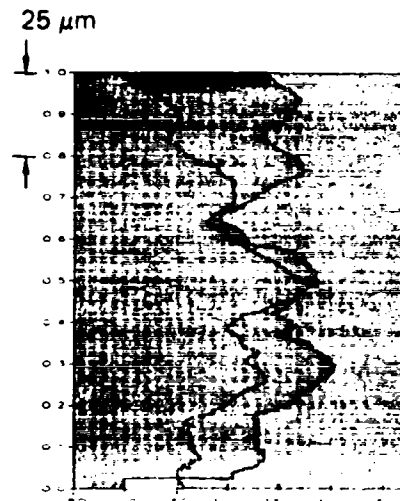
FIGURE VII.6 CROSS-SECTIONAL VIEWS OF FAP PLOTS (Concluded)



(a) SEM Photograph of Fracture Surface (4340 Steel, R_C 40)



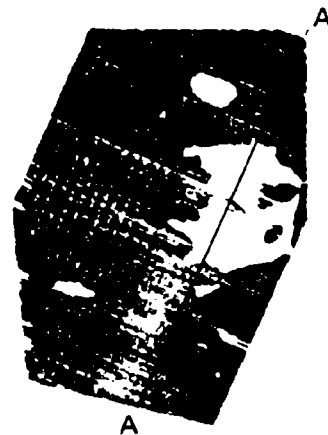
(c) Fractured Area Map by Conjugate Contour Matching (Separation $18\ \mu\text{m}$)



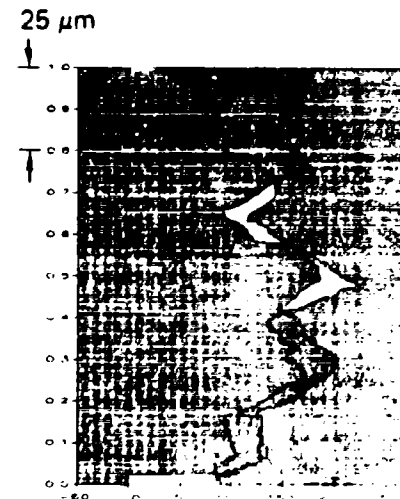
(e) Cross-Sectional View Along Line A-A



(b) Topographic Contour Map



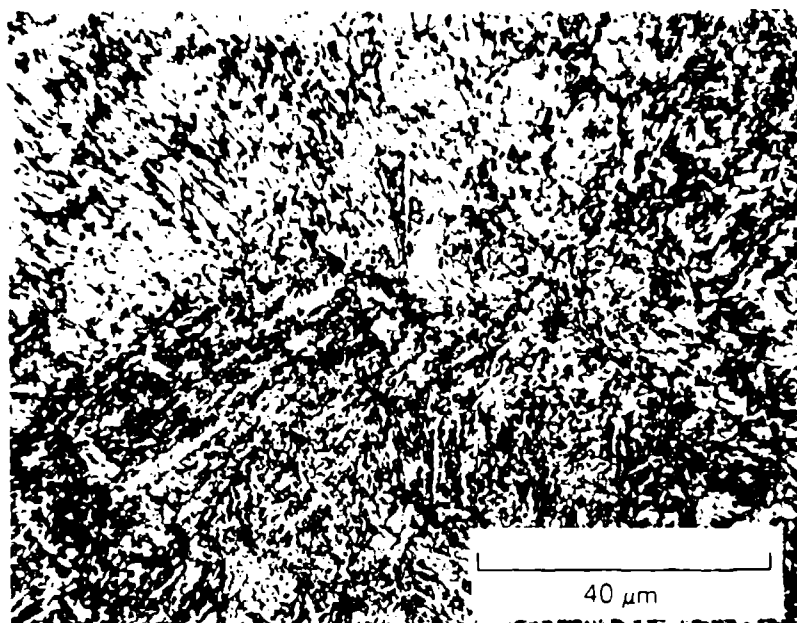
(d) Fractured Area Map by Conjugate Contour Matching (Separation $54\ \mu\text{m}$)



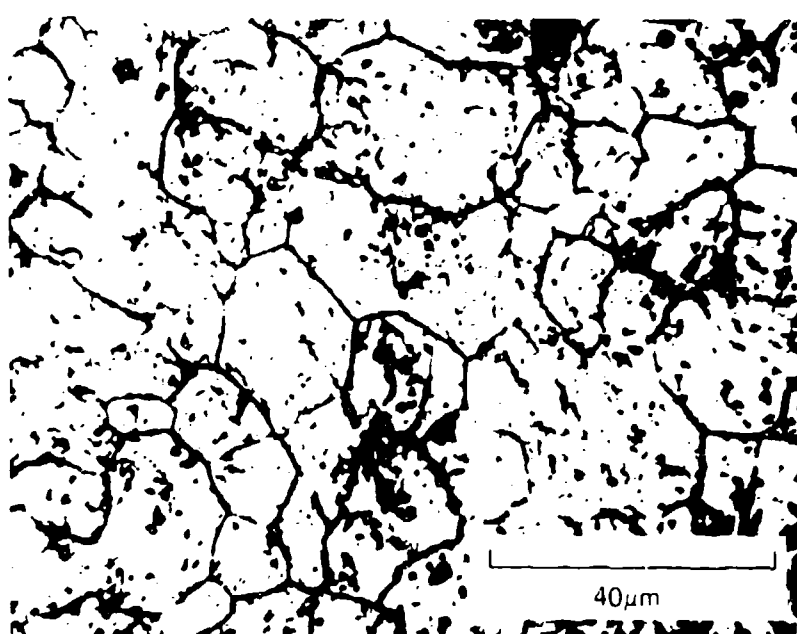
(f) Cross-Sectional View Along Line A-A

JA-318583-45

FIGURE VII.7 CORRELATION OF FAP TOPOGRAPHIC DATA WITH MICROSTRUCTURAL FEATURES ON THE FRACTURE SURFACE



(a) Tempered Martensite Structure



(b) Prior Austenite Grains

JP-314532-149

FIGURE VII.8 MICROSTRUCTURES OF VAR 4340 STEEL ON PLANES BENEATH THE FRACTURE SURFACE, AS REVEALED BY DIFFERENT ETCHANTS

CONTENTS

VIII A MICROSTATISTICAL MODEL (DFRACT2) FOR DUCTILE FRACTURE UNDER LOADINGS RANGING FROM QUASI-STATIC TO IMPACTS

A. INTRODUCTION.....	VIII-1
B. PREVIOUS WORK.....	VIII-1
1. Quasi-Static, Hydrostatic Loading.....	VIII-2
2. Quasi-Static, General Loading.....	VIII-3
3. Dynamic Loading.....	VIII-10
4. Summary of Past Work.....	VIII-10
C. FEATURES OF THE MODEL.....	VIII-11
1. Introduction.....	VIII-11
2. Nucleation Process.....	VIII-11
3. Growth Process.....	VIII-13
4. Size Distribution.....	VIII-14
5. Stress-Strain Relations for Material with Damage....	VIII-15
6. Solution Procedure for Stress and Damage.....	VIII-21
D. TESTS OF THE MODEL	VIII-25
E. EXPLORATIONS WITH THE DFRACT2 MODEL.....	VIII-27
F. SUMMARY.....	VIII-29
G. REFERENCES.....	VIII-29

VIII A MICROSTATISTICAL MODEL (DFRACT2) FOR DUCTILE FRACTURE UNDER LOADINGS RANGING FROM QUASI-STATIC TO IMPACTS

A. Introduction

Ductile microscopic fracture processes in applications often occur at intermediate loading rates, but precise laboratory measurements have usually been performed at the extremes of impact or quasi-static loading. A microstatistical model (called DFRACT2) was constructed to represent ductile fracture over the complete range of loading rates to facilitate computational simulations for applications. Nucleation of voids in the model occurs by processes derived from both impact and quasi-static data. Void growth in the model follows a viscous growth law for stress states outside the Gurson¹ yield curve developed for quasi-static fracture.

The three main developments in this section are

- (1) Specification of a growth law for loading rates from quasi-static to impact.
- (2) A solution procedure for economically treating quasi-static, intermediate, and impact loading rates.
- (3) An examination of rate effects and scaling effects in ductile fracture processes.

Because the model relies heavily on previous work, a review is given of the relevant literature, including introduction of the appropriate equations.

B. Previous Work

Voids grow by microscopic plastic flow around their surfaces when the mean stress on the material is tensile. Several theories have been developed during the last 35 years to describe this growth process. In outlining these theories, we will begin with quasi-static, hydrostatic

loading, and then consider quasi-static loading with combinations of mean tension and shear stresses. Finally we introduce some work on dynamic loading.

1. Quasi-Static, Hydrostatic Loading

The growth of voids under a spherically symmetric tensile field has been studied by several investigators, and now a fairly comprehensive treatment is possible. Chadwick² and Hopkins³ provided early results in this field, but we also cite the works of Carroll and Holt^{4,5} because their study encompasses static and dynamic, compressive and tensile, elastic-plastic and rigid-plastic cases. In addition, works of other researchers will be cited to show comparisons with experimental data and some recent theoretical results.

Carroll and Holt⁴ treated a single void contained in a sphere of elastic-plastic material in their basic analysis. Under a uniform tensile stress, P , applied to the external surface of the sphere, the material first yields at the inner surface, adjacent to the void. With continued loading, the elastic-plastic boundary at $r = r_p$ gradually moves from $r_p = a$ (the void radius) to $r_p = b$ (the external radius of the sphere of material). Eventually the entire sphere of material is at yield.

The elastic-plastic relations for a spherical void in a sphere of material were integrated numerically using a method based on Hill's⁶ analysis (p. 98) to illustrate the load deformation process. A series of tensile stress-deformation paths are shown in Figure VIII.1 for several initial relative void volumes. The ratio of yield strength Y to bulk modulus is 0.015, and Poisson's ratio is 1/3. Deformation is plotted as total volume, V , divided by the initial volume of the solid material. In each case the loading is initially linearly elastic to a point marked "initial yield," when the stresses at the void reach yielding. At that point the external tension is $P = P_c$:

$$P_c = \frac{2Y}{3} (1 - v_v) \quad (\text{VIII.1})$$

where Y is the yield strength and v_v is the relative void volume. Above this point the plastic zone enlarges around the void, but the deformation is still very small because of the elastic confinement. With continued radial motion of the outer boundary, the plastic zone reaches the outer boundary. Thereafter, the stress reduces and the deformations become large.

All of these postyielding, unloading curves shown in Fig. VIII.1 appear to coalesce into a single path. This path is given approximately by the result of Carroll and Holt, derived for a special elastic-plastic material that is incompressible:

$$P_c = -\frac{2}{3} Y \ln v_v \quad . \quad (\text{VIII.2})$$

Carroll and Holt made an approximate correction to this equation to account for compressibility, and obtained the following implicit relation for P_c :

$$V_{s0}/V = -P_c/K + 1 - \exp (\pm 3P_c/2Y_0) \quad (\text{VIII.3})$$

The plus-or-minus sign is interpreted as plus for compression and minus for tension, and P_c is positive in tension for eq. VIII.3. Points from both eqs. VIII.2 and VIII.3 in Fig. VIII.1 indicate that eq. VIII.2 is a good approximation, but eq. VIII.3 is essentially an exact representation of the composite postyield curve.

Hence a complete analysis is available for an elastic-plastic material containing spherical voids and loaded under spherically symmetric tension.

2. Quasi-Static, General Loading

The growth of spherical and ellipsoidal voids in a plastically deforming matrix under quasi-static loads has been intensively studied, both experimentally and analytically. Landmark analytical papers on the

subject include those by Berg,⁷ McClintock,⁸ Rice and Tracey,⁹ and Gurson¹. Here we consider loadings that are some combination of pressure and shear stress. The material may be an infinite medium with a single void, or a finite region with a void in it. The latter case makes it possible to describe the effects of the void volume on the stresses, and also to indicate some of the effect of voids on their neighbors.

Void growth usually occurs under conditions of combined tensile and shear stresses. Here the analytical models are not as complete as those for uniform tension alone. Mechanisms for both void enlargement and shape change are considered, although growth (enlargement) is of primary importance.

Berg performed an analysis of the expansion and shape change of an elliptic hole in a plate under principal tensile stresses σ_1 and σ_2 . The plate is made of a viscous, incompressible fluid. The average radius, R , and elliptic ratio, m , are defined as

$$R = \frac{a + b}{2} \quad (\text{VIII.4})$$

$$m = \frac{a - b}{a + b}$$

where a and b are the major and minor semiaxes of the ellipse.

Under a constant tensile loading in plane strain, the growth of the radius follows a viscous-type law:

$$R = R_0 \exp \left[\frac{\sigma_1 + \sigma_2}{4\eta} t \right] \quad (\text{VIII.5})$$

The exponential argument here contains $(\sigma_1 + \sigma_2)/4\eta$ instead of $P/4\eta$ as it does for the spherical case. This difference of about a factor of 2 probably arises from the difference in dimensionality. The factor m for the special case where the principal stress directions and semiaxes of the ellipse coincide is

$$m = \frac{\sigma_1 - \sigma_2}{\sigma_1 + \sigma_2} + \left(m_0 - \frac{\sigma_1 - \sigma_2}{\sigma_1 + \sigma_2} \right) \exp \left[- \frac{(\sigma_1 + \sigma_2)}{2\eta} t \right] . \quad (\text{VIII.6})$$

From eq. VIII.6 it appears that the elliptic ratio gradually transforms from the initial ratio m_0 to one matching the stress configuration. Comparing the definition of m in eq. VIII.4 with eq. VIII.6, we see that the ratio of semiaxes becomes

$$\frac{a}{b} = \frac{\sigma_1}{\sigma_2} \quad (\text{VIII.7})$$

for a sustained loading.

The viscous fluid results of Berg were used by McClintock⁸ to derive a growth law for voids in a plastically deforming sheet of incompressible material. In transforming from a viscous to a plastic solution, he uses the relations

$$\begin{aligned} \epsilon &= \dot{\epsilon} t \\ G &= \eta / t \end{aligned} \quad (\text{VIII.8})$$

where ϵ is strain, G is shear modulus, η is coefficient of viscosity, and t is a representative time. The growth law is then

$$\ln \frac{R}{R_0} = \frac{3\bar{\epsilon}(\sigma_1 + \sigma_2)}{4\bar{\sigma}} + \frac{\epsilon_1 + \epsilon_2}{2} \quad (\text{VIII.9})$$

where ϵ_1 and ϵ_2 are strains in the principal directions (and along the semiaxes of the ellipse), and $\bar{\sigma}$ and $\bar{\epsilon}$ are equivalent stress and strain, defined as follows using the Einstein summation convention:

$$\bar{\sigma}^2 = 3/2 (\sigma'_{ij} \sigma'_{ij}) \quad (\text{VIII.10})$$

$$\bar{\epsilon}^2 = 2/3 (\epsilon'_{ij} \epsilon'_{ij}) \quad (\text{VIII.11})$$

and

$$\bar{\sigma} = 3G \bar{\epsilon} \quad . \quad (\text{VIII.12})$$

McClintock amplified eq. VIII.9 to account for a work-hardening exponent n in the plastic stress-strain relation

$$\bar{\sigma} = \sigma_R \bar{\epsilon}^n \quad . \quad (\text{VIII.13})$$

The result is

$$\ln \frac{R}{R_0} = \frac{\bar{\epsilon} \sqrt{3}}{2(1-n)} \sinh \frac{\sqrt{3}(1-n)}{2} \frac{(\sigma_1 + \sigma_2)}{\bar{\sigma}} + \frac{\epsilon_1 + \epsilon_2}{2} \quad . \quad (\text{VIII.14})$$

The final term, which is the volume strain, is normally omitted on the assumption that the material is incompressible. Then the growth is proportional jointly to the equivalent strain (= plastic shear strain for incompressible material) and to the ratio of mean stress $(\sigma_1 + \sigma_2)$ to yield stress $\bar{\sigma}$. For small values of $(\sigma_1 + \sigma_2)/\bar{\sigma}$, the hyperbolic sine is approximately equal to its argument, so the hardening coefficient has no significant effect. eq. VIII.14 is a step toward a complete growth process, accounting for accumulation of plastic strain for work-hardening, and for the stress state.

The growth of voids in a rigid-plastic, infinite, three-dimensional medium was treated analytically by Rice and Tracey.⁹ Only one void is considered so that neither void interaction nor necking may occur. The growth law determined was

$$\frac{1}{R} \frac{dR}{dt} = \left[0.558 \sinh \left(\frac{3P}{2y} \right) + 0.008\nu \cosh \left(\frac{3P}{2y} \right) \right] d\bar{\epsilon} \quad (\text{VIII.15})$$

where ν is a Lode variable, $\nu = -3\epsilon_2/(\epsilon_1 - \epsilon_3)$ and the principal strains at infinity ($\epsilon_1, \epsilon_2, \epsilon_3$) are listed in order of decreasing size. When

the small hyperbolic cosine term is neglected in eq. VIII.15, this equation differs from McClintock's equation (eq. VIII.14) only by a small factor.

Recently, Shockey et al.¹⁰ reported that when inertial and viscous effects can be neglected, under conditions with significant plastic strain, the initial void growth in A533B steel is well described by a simplified form of the Rice-Tracey formula:

$$v/v_0 = \exp [1.67 \Delta \bar{\epsilon}^P \sinh (3\sigma_m/2\sigma_y)] \quad (\text{VIII.16})$$

where v and v_0 are the relative void volumes at the end and beginning of the strain increment, respectively. The initial value of v_0 is that at nucleation; that is, v_0 is usually taken as the relative volume of the inclusions or other heterogeneities that form the nucleation sites.

The most complete treatment heretofore of void growth under combined loading is that of Gurson¹. Gurson treated a sphere of rigid-plastic material containing a spherical void. As the tensile stress state was increased, regions of plastic deformation formed around the void. The void growth threshold was reached when the plastic zones had extended to the point that void expansion could occur without resistance by the remaining rigid materials. Stress states from pure shear to uniform tension (hydrostatic) were examined. The threshold stress function was written as a yield curve ϕ , where

$$\phi = \frac{\bar{\sigma}^2}{Y^2} + 2f \cosh \left(\frac{3P}{2Y} \right) - 1 - f^2 = 0 \quad (\text{VIII.17})$$

where $\bar{\sigma}^2 = \frac{3}{2} \sigma'_{ij} \sigma'_{ij}$

Y = yield strength,

f = void volume fraction

$P = \frac{1}{3} \sigma_{ii} = \frac{1}{3} (\sigma_{xx} + \sigma_{yy} + \sigma_{zz})$ = average stress.

Gurson also showed that a normality flow rule describes the stress-strain relations for the material in the yielding range. The normality rule is a condition between the stresses, σ_{ij} (average values over the boundary of the sphere of material), on the yield curve and the average strains, ϵ_{ij}^P , throughout the sphere.

$$\sum d\sigma_{ij} d\epsilon_{ij}^P = 0 \quad (\text{VIII.18})$$

This normality flow rule is commonly used in some form in most plasticity treatments to determine the plastic strains.

To illustrate the meaning of normality on the Gurson yield curve, consider that the current stress state is at point A inside or on the yield curve shown in Fig. VIII.2. Now a strain increment is applied and we compute the stress that would be obtained if no yielding or void growth occurred: The resulting stress state is at some point B outside the yield curve. However, because the material cannot support the stress state B, we must bring the stress state back to the yield curve. Following Gurson¹ we find the point C that is on the yield curve and positioned such that the plastic strain tensor associated with BC is normal to the yield surface at C (thus satisfying eq. VIII.18). As usual, we can associate the decrease in $\bar{\sigma}$ from B to C with an increase in the plastic strain $\bar{\epsilon}^P$. In the Gurson model we can similarly associate the decrease in pressure from B to C with an increase in the relative void volume v_v .

Gurson's yield curve (eq. VIII.17) has been used by other investigators to follow the growth of a void through a general loading process. For example, the initial relative void volume may be v_0 when the yield curve is reached. Under the imposed loads there is a void volume increase to v_1 according to the Gurson model calculations. Subsequently, the void volume v_1 is again increased using the Gurson model and the current stress state.

However, this may not be an appropriate application of Gurson's model. Gurson derived the curve by starting with an initial void volume

v_0 , and applying external loads that were taken first elastically and then partially plastically as plastic enclaves formed around the void. The curve was obtained by considering void growth at the moment when the plastic region surrounding the void extended to the boundaries of the finite volume; then the void expansion was no longer confined elastically. Hence, the step in going from v_0 to v_1 by other investigators follows the path used in Gurson's derivation, but the subsequent growth from v_1 does not. The subsequent growth starts from the unconfined plastic state and with a void that should no longer be spherical (according to the results of McClintock). Thus we should be cautious in using the Gurson model to follow void growth over an extended loading.

In a recent study Carroll¹¹ has been able to compute the Gurson yield curve using loading paths tangent to the curve. Hence, when the void is constrained to be spherical, it appears that the curve is unique, independent of the loading path to reach the curve.

Tvergaard¹² has examined the appropriateness of the Gurson model through two-dimensional simulations of material with voids. He found that the Gurson model is somewhat too stiff, and has recommended the use of amplification factors for the second, third, and fourth terms in the expression for ϕ (eq. VIII.17). This modification provides a somewhat stronger strength reduction with void growth.

In a recent study of ductile fracture in tensile specimens, Needleman¹³ also used a modified Gurson model. He used an amplification factor for some terms in the Gurson curve (eq. VIII.17) such that the strength went to zero for a void volume of a few percent. His tensile test simulations showed very realistic behavior of the fracture process.

We now have an indication from the results of Berg and McClintock^{7,8} of the way in which cylindrical voids grow and deform under non-spherical loading, and Gurson has shown how a spherical void in a finite volume begins to grow.

3. Dynamic Loading

At very high loading rates where inertial and viscous effects dominate, Seaman et al.¹⁴ and Stevens et al.¹⁵ show that the void growth rate is given by

$$\dot{R}/R = \frac{\sigma_m - \sigma_{go}}{4\eta} \quad (\text{VIII.19})$$

or

$$\dot{v}/v = \frac{3(\sigma_m - \sigma_{go})}{4\eta}$$

where σ_m is the mean tensile stress, σ_{go} is a growth threshold related to the static yield stress, and η is a constant with the dimensions of viscosity (GPa-sec, for example). In the original DFRAC model¹⁴ the threshold σ_{go} was a constant. However, in later versions¹⁶ of the model, we used the quasi-static pressure-volume relation of Carroll and Holt (eq. VIII.2) as the threshold. This Carroll-Holt threshold is more realistic because it allows for the decrease in strength with increasing void volume.

4. Summary of Previous Work

The theoretical background we have reviewed is concerned mainly with spherical voids, although there has been some study of elliptic and ellipsoidal voids also. The emphasis has been on growth, but some work is also available on nucleation processes.

For high rate loading, nucleation appears to occur throughout loading and to be a strong function of the mean stress. At normal tensile testing rates the nucleation seems to happen suddenly, at a particular strain level and usually near the strain associated with the peak of the engineering stress-strain curve.

Growth under static conditions occurs in proportion to the plastic strain, with the mean stress acting as an amplification factor. Under high rates, the growth rate is proportional to the mean stress above some

threshold stress. In either case, the growth rate is proportional to the current void size.

These nucleation and growth features are incorporated into the model described in the following subsections.

C. Features of the Model

1. Introduction

The DFRACT2 model was constructed to represent quasi-static and dynamic ductile fracture by void nucleation and growth under general stress states. The voids occur in statistical size distributions within the model and are represented by internal-state variables. The model is a continuum model because all properties vary smoothly within the material; it is microstatistical because of the size distribution of the voids.

The fracture model represents the micro process of the voids and the stress-strain relations of the solid material.

For low stresses, the model represents an elastic or elastic-plastic material. When the stresses or plastic strains exceed threshold values, size distributions of voids begin to nucleate and grow. These void processes follow physically based laws derived from theoretical analyses and experimental data. The void volume affects the threshold values and the stress-strain relations, providing an interaction between stress and damage.

In the following sections the nucleation and growth processes and stress-strain relations are outlined and the solution procedure is developed.

2. Nucleation Process

Nucleation in the DFRACT2 model occurs by a combination of the processes associated with static and dynamic loading.

Under quasi-static loading^{10,17} nucleation was associated with the development of plastic strain in the sample. The idealized nucleation function we derived from tension tests in A533B steel is shown in Figure VIII.3. Because data describing void nucleation in VAR 4340 steel were not yet available from the topographic analyses of Section VII, we used a function that described nucleation in a steel that failed by a similar mechanism in order to avoid delays in the model development. This quasi-static nucleation process was incorporated into the DFRAC2 model in the following form:

$$\begin{aligned} \frac{dN_q}{dt} &= \frac{T_9 d\bar{\epsilon}^P}{dt} & T_8 < \bar{\epsilon}^P < T_{10} \\ & & & \\ &= T_{11} \frac{d\bar{\epsilon}^P}{dt} & T_{10} < \bar{\epsilon}^P \end{aligned} \quad \text{(VIII.20)}$$

where N_q is the number of voids that form under quasi-static loads, T_9 , T_{11} are material constants with the units of number/cm³, and T_8 , T_{10} are material constants with the units of strain. T_8 and T_{10} probably differ by only 1% strain and represent the plastic strain at which the majority of the large inclusions debond from the matrix material. The total number of voids ΔN_0 nucleated in this strain interval is

$$\Delta N_0 = T_9(T_{10} - T_8) \quad \text{(VIII.21)}$$

From this equation and an experimental value for ΔN_0 , T_9 can be calculated. The constant T_{11} can be set to permit a small continuing level of nucleation. The values of these constants will be set by the results obtained from further analysis of the topographic data of Section VII.

Since plate impact tests on VAR 4340 steel were beyond the scope of the program, we used other data and observations to describe the nucleation function at high loading rates. Impact tests in aluminum and

copper disks^{18,19,14} led to the following mean-stress-dependent nucleation rate

$$\frac{dN_1}{dt} = T_4 [\exp((P - T_5)/T_6) - 1] \quad P > T_5 \quad (\text{VIII.22})$$

where N_1 is the number of voids that form under impact loads, and T_4 , T_5 , and T_6 are material constants. T_5 is a threshold mean stress; according to Carroll and Holt's analysis⁴ and our experimental results,

$T_5 = 4Y$, where Y is the yield strength. T_4 is the nucleation rate constant with units of number/cm³/s. This constant has been derived directly from impact experimental data^{14,19,20} and from a theoretical analysis of diffusion in creep processes^{21,22}. T_6 is a stress sensitivity factor with the units of stress. It has also been derived both from impact data and from creep studies.

In the DFRAC2 model the nucleation process is assumed to be a combination of the quasi-static and impact nucleation processes:

$$\frac{dN}{dt} = \frac{dN_q}{dt} + \frac{dN_1}{dt} \quad (\text{VIII.23})$$

This combination is logical from a computational viewpoint, because it produces a model that can match data at both extremes of strain. At high rates, the stresses are high but the strains are low, so only the dN_1/dt term contributes. For quasi-static tests the mean stress rarely exceeds Y at any point in the specimen (and certainly not $4Y$), so only dN_q/dt contributes.

3. Growth Process

Growth of voids in the DFRAC2 model has been developed as a natural combination of the processes for high rate void growth and for quasi-static void growth. For quasi-static tension we use the analysis of Gurson¹ where growth and yielding combine to produce a yield curve in $P - \bar{\sigma}$ space like that shown in Fig. VIII.2. For high rate tensile

loading, we use the viscosity-dominated growth law when the tensile stress exceeds a threshold.

These two growth processes are readily combined in a consistent way by making the quasi-static curve of Gurson become the threshold curve for the high rate case. That is, σ_{go} in eq. VIII.19 is provided by Gurson's curve. We can then use normality to determine the point on the Gurson curve that will be used as the threshold point. In this way we should have behavior that agrees with that in the high rate model under rapid loading conditions. For slow loading problems, the calculations will show that the stress point followed a path that went outside the yield curve briefly, but returned soon to the point designated as normal on the curve. Thus the DFRAC2 model behavior should also match that of the low rate model for quasi-static cases.

4. Size Distribution

Throughout the damage process, the voids are presumed to appear with a range of sizes. Our observations have indicated that the voids have a size distribution with approximately the following exponential form:

$$N_g = N_0 \exp(-R/R_1) \quad (\text{VIII.24})$$

where N_g is the number per cubic centimeter with a radius greater than R , N_0 is the total number of voids per unit volume, and R_1 is the size parameter. At nucleation, the size distribution is presumed to have the form of eq. VIII.24, with $R_1 = R_n$, the nucleation size parameter.

The total volume of voids V_t contained within the size distribution is obtained by summing the individual void volumes.

$$V_t = \int \frac{4\pi R^3}{3} dN \quad (\text{VIII.25})$$

Differentiating eq. VIII.24 with respect to radius, we can replace dN in eq. VIII.25 with $-N_0/R_1 \exp(-R/R_1) dR$. Then the integral becomes:

$$V_t = \frac{4\pi N_0}{3R_1} \int_0^{\infty} R^3 \exp(-R/R_1) dR \quad (\text{VIII.26})$$

$$= 8\pi N_0 R_1^3$$

This is the total volume of the void distribution at any time.

5. Stress-Strain Relations for Material with Damage

The stress-strain relations in the DFRAC2 model account separately for the behavior of the solid and void components. The voids are treated as a new property distributed uniformly within the fracturing material. The behavior of the voids is handled by the nucleation and growth laws of the previous sections. The solid material is treated as isotropic, with separate expressions for the pressure and deviatoric stresses. Some of the stress-strain relations for the damaged material are developed from considerations of the mixture of void and solid. The void content is a scalar property, so the mixture is also isotropic.

The behavior of the mixture is illustrated in Figure VIII.2, showing a Gurson yield curve with coordinates $\bar{\sigma}$ and P , the stress state of the mixture. Elastic loading for a stress state within the yield curve follows the usual elastic relations for material with voids. When loading moves the stress point outside the curve, dynamic stress relaxation, void growth, and plastic flow occur.

We proceed with the stress calculation by first calculating a stress state B , assuming all strain is taken elastically. Then a point on the yield curve is computed representing a normality solution. The coordinates of this normal point are then the threshold stresses for relaxing the pressure and deviatoric stress. These two stress invariants follow their own relaxation equations, so the deviators reduce more rapidly than the pressures. These two stress calculations are derived from standard mechanics laws for solid material, including thermal expansion. The pressure relaxation process accompanies void growth and the deviatoric relaxation is associated with plastic flow.

The following paragraphs describe the strain consistency relations (basis for combining the void and solid behaviors), deviatoric stress relations, the pressure expression, and the determination of the normal points. Then a procedure is constructed for simultaneously solving the full set of equations.

a. Strain Consistency

A consistent strain formulation is used to partition the strain between the solid and void components. The strain rate tensor can be partitioned as follows:

$$\frac{d\epsilon_{ij}}{dt} = \frac{d\epsilon_{ijs}}{dt} + \frac{d\epsilon_{ijv}}{dt} \quad (\text{VIII.27})$$

where ϵ_{ijs} and ϵ_{ijv} refer to the strains in the solid and void. All these strains are defined as averages over the composite material, not over the component. That is, $d\epsilon_{ijv}$ is not a change in the void dimension with respect to the void size, but a change in the void dimension with respect to the dimension of the composite material. For our present application we have simplified the consistency requirements as follows to volumetric and deviatoric requirements:

$$\frac{dV}{dt} = \frac{dV_s}{dt} + \frac{dV_v}{dt} \quad (\text{VIII.28})$$

and

$$\frac{d\epsilon'_{ij}}{dt} = \frac{d\epsilon'_{ijs}}{dt} \quad (\text{VIII.29})$$

where V , V_s , and V_v are specific volumes (with respect to the mass of the composite material) of the composite, solid, and void elements.

ϵ'_{ij} and ϵ'_{ijs} are deviatoric strains of the composite and solid materials. By using eq. VIII.29 we are assuming that the solid material takes all the deviatoric strain, and also recognizing that the spherical voids can absorb no shear strains.

b. Deviatoric Stresses

For the solid material the stress tensor is separated into a pressure and a deviatoric stress tensor. The expression for the deviatoric stress is derived from the standard relaxing solid formulation.

$$\begin{aligned} \frac{d\tau}{dt} &= G \frac{d\gamma}{dt} & \tau < Y_s & \quad (VIII.30) \\ &= G \frac{d\gamma}{dt} - G \frac{\tau - Y_s}{\eta} & \tau > Y_s & \end{aligned}$$

where τ is the shear stress, γ is the engineering shear strain, G is the shear modulus, η is the coefficient of viscosity, and Y_s is the yield strength in shear. For steady loading over some period of time, the solution to eq. VIII.30 approaches

$$\tau = Y_s + \eta \frac{d\gamma}{dt} \quad (VIII.31)$$

as required for the definition of viscosity. Using the definitions of $\bar{\sigma}_s$ and $\bar{\epsilon}$ in eqs. VIII.10 and VIII.11, we can rewrite eqs. VIII.30 as*

$$\begin{aligned} \frac{d\bar{\sigma}_s}{dt} &= 3G \frac{d\bar{\epsilon}}{dt} & \bar{\sigma}_s < \sigma_{th} & \quad (VIII.32) \\ &= 3G \frac{d\bar{\epsilon}}{dt} - G \frac{(\bar{\sigma}_s - \sigma_{th})}{\eta} & \bar{\sigma}_s > \sigma_{th} & \end{aligned}$$

where σ_{th} is the threshold stress for yielding. For material without voids σ_{th} is the yield strength, but for material with a void volume σ_{th}

*This expressions is appropriate only for proportional strain loading problems. Later in this section it is transformed for general loadings.

is identical to σ_c , the stress at the normal point on the Gurson curve. Note here that we are using $\bar{\sigma}_s$, the equivalent stress in the solid, rather than $\bar{\sigma}$, the equivalent stress on the mixture of solid and void. The two stress quantities are related by the Carroll-Holt relation

$$\bar{\sigma} = \bar{\sigma}_s (1 - v) \quad (\text{VIII.33})$$

where v is the relative void volume, V_v/V . For a constant strain rate loading over a time interval Δt , eq. VIII.32 can be integrated to obtain:

$$\bar{\sigma}_2 = \bar{\sigma}_1 \exp(-G\Delta t/\eta) + \left(3\eta \frac{d\bar{\epsilon}}{dt} + \sigma_y \right) [1 - \exp(-G\Delta t/\eta)] \quad (\text{VIII.34})$$

The time constant for the exponential stress relaxation is η/G .

To apply this one-dimensional (or proportional loading) relation (eq. VIII.32) to our general loading case, we will interpret the equivalent strain rate term as the equivalent stress reached in elastic loading, and then obtain the following form for eq. VIII.32

$$\frac{d\bar{\sigma}_s}{dt} = \frac{d(\bar{\sigma}_s^B - \bar{\sigma}_{s0})}{dt} - \frac{G_s(\bar{\sigma}_s - \sigma_y)}{\eta} \quad (\text{VIII.35})$$

where $\bar{\sigma}_s^B$ is the equivalent stress that would be reached if the strain increment were taken elastically, and $\bar{\sigma}_{s0}$ is the equivalent stress at the beginning of the increment. The individual deviatoric stress components are obtained in the usual way:

$$\sigma_{ij} = \sigma_{ijs}^B \frac{\bar{\sigma}_s}{\bar{\sigma}_s^B} (1 - v) \quad (\text{VIII.36})$$

where σ_{ij}^B represents the elastically computed stress components.

c. Pressure-Volume Relation

The pressure-volume relation is also written in a differential form:

$$\frac{dP_s}{dt} = \frac{K}{V} \frac{dV_s}{dt} + \rho_o \Gamma \frac{dE}{dt} \quad (\text{VIII.37})$$

where P_s is the pressure in the solid material,
 K is the bulk modulus of the solid,
 V_s is the specific volume of the solid material,
 ρ_o is the initial density,
 Γ is the Grueneisen ratio, and
 E is the internal energy.

Now we use eq. VIII.28 to replace the solid specific volume by the total volume and the void volume. Further, we separate the rate of change of void volume into growth and nucleation contributions, using eqs. VIII.19 and VIII.26. For use here, eq. VIII.26 is divided by V to form a volume strain and N_o is replaced by the nucleation rate dN/dt . The resulting relation for pressure is:

$$\frac{dP_s}{dt} = \frac{K}{V} \frac{dV}{dt} - K \frac{3(P_s - P_{th})v}{4\eta} - \frac{K}{V} 8\pi R_n^3 \frac{dN}{dt} + \rho_o \Gamma \frac{dE}{dt} \quad (\text{VIII.38})$$

Here the threshold pressure P_{th} replaces the constant σ_{go} in eq. VIII.19. The derivative on the left-hand side plus the first two terms on the right-hand side (these three dominate the response) constitute an equation with a stress-relaxing nature very similar to that of eq. VIII.32 for $\bar{\sigma}$. The major difference between eqs. VIII.32 and VIII.38 is that the effective time constant in eq. VIII.32 is

$$T_s = \eta/G \quad (\text{VIII.39})$$

while in eq. VIII.38 it is

$$T_p = 4 \eta / 3 K v \quad . \quad (VIII.40)$$

Because of the presence of v in (VIII.40), the apparent time constant for the pressure relaxation varies as a function of the current relative void volume. The ratio of the time constants is

$$T_s/T_p = 3 K v / (4 G) \quad (VIII.41)$$

Because v cannot exceed about 0.5 and K is not more than twice G , the pressure time constant is always considerably longer than the time constant for deviatoric stress. Consequences of this fact will be considered further in Section C.6, Solution Procedure.

d. Normality and Yielding

The solution for yielding and the normal point follows closely the discussion of the Gurson curve in the Background section (VIII.B). To aid in visualizing the Gurson curve, the intercepts in the $\bar{\sigma}$, P plane are given by

$$\bar{\sigma} \text{ axis} \quad Y(1 - v) \quad (VIII.42)$$

$$P \text{ axis} \quad \frac{2Y}{3} \ln v$$

Both intercepts depend on the void volume and current yield strength. A series of Gurson curves for several void volumes are shown in Figure VIII.4. Note that for large void volumes the curve is approximately an ellipse, but for decreasing void volumes it approaches a rectangle.

To test for yielding, ϕ in eq. VIII.17 is evaluated: positive values of ϕ mean the stress point is outside the yield curve.

The normal point C (Fig. VIII.2) on the yield curve is determined by requiring that the plastic strain increment tensor be normal to the yield curve, that is,

$$d\epsilon_{ij} = \frac{\partial \phi}{\partial \sigma_{ij}} d\lambda \quad (\text{VIII.43})$$

In strain-invariant space the normality requirement can be replaced by relations between stress invariants and slopes at the normal point C.

$$\frac{d\bar{\sigma}^P}{dP^P} = \frac{3G}{K_g} \frac{\partial \phi / \partial \bar{\sigma}}{\partial \phi / \partial P} \quad (\text{VIII.44})$$

Here $d\bar{\sigma}^P$ and dP^P are pseudo stress changes representing the plastic strains:

$$d\bar{\sigma}^P = 3G d\epsilon^P \quad (\text{VIII.45})$$

$$dP^P = K d\epsilon_{ij}^P$$

The slope $d\bar{\sigma}^P/dP$ is represented by $(\bar{\sigma}_C - \bar{\sigma}_B)/(P_C - P_B)$ in Figure VIII.2. We notice that the ratio of derivatives on the right-hand side of eq. VIII.44 provides the usual normal to the curve in invariant space. Thus the normal direction in the plasticity sense and the usual normal to the curve differ by the factor $3G/K$.

The coordinates of point C are found by requiring that these coordinates satisfy the normality relation (eq. VIII.44) and lie on the yield curve (eq. VIII.17). $\bar{\sigma}_C$ can be easily eliminated between these two expressions, producing a single equation in P_C . P_C is then found by an iterative technique using the Newton-Raphson method.

6. Solution Procedure for Stress and Damage

The series of void processes and stress-strain relations are assembled here and a procedure is developed for determining stress states and damage simultaneously. Because this model is planned for use in finite element or finite difference calculations, the solution procedure is only developed for treating constant strain rates over a short interval of time. A series of such time increments can approximate any loading history.

The solution has the following four components: elastic stress calculation; test for yielding and determination of the normal point on the yield curve; relaxation of the stresses toward the normal point; and determination of the individual stress components.

The basic four equations for stress and damage are:

Nucleation --

$$\begin{aligned} \frac{dN}{dt} &= \frac{dN_q}{dt} + \frac{dN_i}{dt} \\ &= T_9 \frac{d\bar{\epsilon}}{dt} + T_4 \left[\exp \left(\frac{P_s - P_{th}}{T_6} \right) - 1 \right] \end{aligned} \quad (\text{VIII.46})$$

Growth --

$$\frac{dv}{dt} = 3 \left(\frac{P_s - P_{th}}{4\eta} \right) v \quad (\text{VIII.47})$$

Pressure --

$$\frac{dP_s}{dt} = - \frac{KdV}{Vdt} + K_v 3 \frac{(P_s - P_{th})}{4} + \frac{K8\pi R_n^3 dN}{V \frac{dN}{dt}} + \rho_o \Gamma \frac{dE}{dt} \quad (\text{VIII.48})$$

Deviatoric Stress --

$$\frac{d\bar{\sigma}_s}{dt} = \frac{3Gd\bar{\epsilon}}{dt} - \frac{G(\bar{\sigma}_s - \sigma_{th})}{\eta} \quad (\text{VIII.49})$$

This coupled set of differential equations can be solved by many standard methods. We chose two methods. The first is a fourth order Runge-Kutta method that is suitable for the high rate loadings. For lower rate loadings and large void volumes, we derived an analytical approximation to the set of equations.

The direct procedure for using a Runge-Kutta method would require that all four equations (VIII.46 to VIII.49) be treated equally.

However, in our attempts this procedure led to small disagreements between P_g , V_g , and V_v . That is, eq. VIII.28 and VIII.37 could not be simultaneously satisfied. Therefore, equations for N , V_v , and $\bar{\sigma}_g$ were integrated by the standard numerical method, and pressure was evaluated from eq. VIII.37.

An appropriate time step for the Runge-Kutta integration can be obtained from the stability requirements of eqs. VIII.47 and VIII.48. The maximum stable time increments are

$$\Delta t_g = \frac{4\eta}{3(P_g - P_{th})} \text{ in the growth equation} \quad (\text{VIII.50})$$

$$\Delta t_p = \frac{4\eta}{3Kv} \text{ in the pressure equation} \quad (\text{VIII.51})$$

Usually Δt_p is less than Δt_g and will therefore govern.

Typical results for a loading of constant tensile strain rate are shown in Figure VIII.5. The tensile mean stress reaches a peak and decreases thereafter. During the decreasing portion of the stress history, the stress approaches the threshold level P_{th} . In the Runge-Kutta method, the usual result oscillates about the threshold. Also in the region, the stable time step (governed by Δt_p) becomes quite small, so the calculation becomes both inaccurate and time-consuming.

An approximate analysis was developed for the decreasing part of the stress history in which the mean stress is approximately equal to the threshold stress and the void volume is large. For this analysis we consider primarily eqs. VIII.48 and VIII.49. The nucleation rate in (VIII.48) is replaced by the two terms in eq. VIII.46. The first term, dN_0/dt , is taken as a constant during any time interval. The term dN_1/dt is approximated as follows by expanding the exponential in a series and then truncating it.

$$\frac{dN_1}{dt} = T_4 \left[\exp\left(\frac{P_g - P_{th}}{P_6}\right) - 1 \right] \approx \frac{T_4 (P_g - P_{th})}{P_6} \quad (\text{VIII.52})$$

With this approximation, eq. VIII.48 becomes

$$\begin{aligned} \frac{dP_s}{dt} = & -\frac{K}{V_o} \frac{dv}{dt} + \frac{3(P_s - P_{th})Kv}{4\eta} + 8\pi R_n^3 K T_4 \frac{(P_s - P_{th})}{P_6} \\ & + 8\pi R_n^3 K \frac{dN}{dt} + \rho_o \Gamma \frac{dE}{dt} \end{aligned} \quad (VIII.53)$$

During a time increment we assume that the first, fourth, and fifth terms on the right-hand side are constant. Then we write eq. VIII.53 as

$$\frac{dP_s}{dt} + A P_s = D \quad (VIII.54)$$

$$\text{where } A = -K \frac{3v}{4\eta} = \frac{8\pi R_n^3 T_4}{P_6}, \text{ and}$$

$$D = -\frac{Kdv}{V_o dt} + AP_{th} + 8\pi R_n^3 K \frac{dN}{dt} + \rho_o \Gamma \frac{dE}{dt}$$

Because v , the relative void volume, varies during the time interval, we must consider eq. VIII.54 an approximation that can be used only over small strain intervals. Integration of VIII.54 leads to

$$P_s = P_{s0} \exp(-A\Delta t) + \frac{D}{A} [1 - \exp(-A\Delta t)] \quad (VIII.55)$$

where P_{s0} is the tensile pressure at the beginning of the time increment.

With the aid of eq. VIII.55 the pressure is determined by a series of iterations. First, all the constants in VIII.53 are computed, and v is equated to its initial value in the time interval. P_s is computed from VIII.55. Then v_s and v_1 are computed from VIII.37 and VIII.28, respectively. Another estimate is made of v and the calculation is repeated until there is a satisfactory correspondence between the estimate of v and the computed value v_1 . The estimates are controlled by a modified regula falsi method.

Results of the analytical approximation were compared with the integrations using the Runge-Kutta method. These comparisons showed that accurate results could be obtained in the decreasing portion of the pressure-volume curve.

For routine calculations we decided to optimize the computing time by using the Runge-Kutta method only in the early portion of the pressure-volume curve, and then transfer to the analytical method. The transfer was made at that point in the calculation where Δt_p from eq. VIII.51 is equal to the time step. At this point the two calculations are approximately equally lengthy.

Following determination of the mean stress P , the equation for deviators, VIII.49, is integrated. Actually, we use the more general form in eq. VIII.35 (for general loading paths). For constant loading rate over a short time interval, and assuming that the threshold stress and yield strength are constant, we obtain

$$\bar{\sigma}_s = \bar{\sigma}_{s0} \exp(-G\Delta t/\eta) + \left[\frac{(\bar{\sigma}_s^B - \bar{\sigma}_{s0})}{G\Delta t} + \bar{\sigma}_{sth} \right] \left[1 - \exp(-G\Delta t/\eta) \right] \quad (\text{VIII.56})$$

Thus the deviator stresses also relax exponentially. Individual deviator stresses are computed by eq. VIII.36.

D. Tests of the Model

After the model was developed, it was incorporated into a computer subroutine. The subroutine was used to simulate experimental fracture data obtained from impacts on 1145 aluminum^{5,9} and quasi-static tensile tests on A533B nuclear reactor steel^{7,8}. In these previous studies two fracture models (DFRACT and DFRAC8) were developed and used to simulate the respective experiments. In the current study, we used the same parameters (Table VIII.1) to simulate the earlier tests. Simulations using parameters for VAR 4340 will be performed when the values of the fracture parameters are determined.

For the impact simulations the models DFRACT and DFRACT2 are alike except that the current model has a threshold stress, $\sigma_{go} = P_{th}$, that is initially high and gradually reduces with void volume, whereas the earlier model had a constant σ_{go} . Also, the current model has a marked

Table VIII.1
FRACTURE PROPERTIES

Fracture Parameters	Values
1145 Aluminum (impact)	
\dot{N}_4	$3 \times 10^9 \text{ (cm}^{-3} \text{ s}^{-1}\text{)}$
P_5, P_6	0.3, 0.04 GPa
η	7.5 Pa-s (75 poise)
R_n	10^{-4} cm
A533B Steel (quasi-static)	
$\epsilon_8, \epsilon_{10}$	0.11, 0.13
N_9, N_{11}	$5 \times 10^6, 10^5/\text{cm}^3$
R_n	10^{-3} cm

reduction of the deviator stresses with damage. When we simulated a one-dimensional impact experiment with the DFRAC2 model, we computed about half the void volume that we obtained both in the earlier calculation and in the experimental data. Also we computed twice as many voids. These differences in the number and volume of voids is expected because of the higher growth threshold throughout most of the calculation. Thus, we expect that some changes will be required in the fracture parameters to make a satisfactory match to the 1145 aluminum impact data with the DFRAC2 model.

The quasi-static tensile fracture data in A533B steel was matched satisfactorily in the earlier study using a growth law that approximated that of Rice and Tracey,⁹ and no reduction of the yield strength. The present model was tested in one-cell simulations of uniaxial stress

states and stress states similar to those in the center of the tensile specimen. The results also showed no decrease in the apparent yield strength and void growth consistent with the Rice-Tracey law. Thus, the DFRACT2 model does appear to appropriately represent the ductile fracture processes in these two materials at both impact and quasi-static loading rates.

E. Explorations with the DFRACT2 Model

With DFRACT2 we explored strain rate effects, details of the model processes, meaning and effects of normality, and sources for instabilities. In these studies we made one-cell simulations, proceeding through several stress states and at various strain rates.

Uniaxial strain calculations were performed at strain rates from 10 to 10^6 to aid in understanding the impact experiment. The stress (in the loading direction) versus the imposed strain is shown in Figure VIII.6 for these strain rates. The void volumes at each point are also shown to aid in understanding the damage process. The results at a strain rate of 10^6 are shown in Figure VIII.6, which also includes the pressure, $\bar{\sigma}$, and the thresholds for both the pressure and $\bar{\sigma}$. This figure indicates that the pressure rises above the pressure threshold only after there is some significant void volume. Near the peak of the stress history, the deviator stress and threshold (apparent shear strength) both drop suddenly. If an experiment were conducted in which there was an opportunity for shearing motion, we could expect a strong shear instability to follow this sharp drop in shearing resistance. Note that during much of the void growth history the stress state is nearly hydrostatic because of the greatly diminished shear strength. In such a stress state we expect the voids to grow into nearly spherical shapes. Indeed, this calculation may show why spherical voids have usually been observed in impact fractures^{14,18}. Throughout the calculation the shear stress stays just above the threshold by the amount $3\eta\dot{\epsilon}$ as expected.

In Figure VIII.7 we see the paths taken by the pressure and $\bar{\sigma}$ throughout the uniaxial strain tests at rates of 10 and 10^6 . For

the high rate case, the path first moves along the horizontal portion of the undamaged yield curve, and then down the steeper portion near the pressure-intercept of the curve. Although the stress point is on the horizontal portion, most of the void volume increase is from nucleation because the pressure and pressure threshold almost coincide. However, when the stress point reaches the right end of the yield curve, growth becomes rapid. This is also the region where the deviator stresses decrease suddenly. During each time step so far, the deviator stresses have relaxed almost to their threshold, but the pressures have reduced only slightly because their time constant is so long. In the later portion of the path while the pressure is increasing, the pressure and the deviators are both relaxing significantly. During the later stages of loading the stress gradually moves toward a point at which the elastically computed stress vector is normal to the current yield curve.

The variation of peak stress with strain rate in the uniaxial strain calculations may be deduced from the curves in Figure VIII.8. There is a linear increase in stress with log of strain rate for strain rates above 10^3 . Note that this strain rate effect is associated only with the void nucleation and growth processes and the stress relaxation processes; the yield strength is treated as rate-independent in the model.

In the discussion of the figures above we have reached some strong conclusions on the nature of ductile fracture. We emphasize that these conclusions depend strongly on the use of normality with the Gurson curve, on the use of the curve for continuous yielding rather than just the curve for initial yield, and on the stress relaxation processes used.

Two kinds of uniaxial stress loading were used in the simulations shown in Figure VIII.9. For a zero lateral stress, the stress state is required to lie on a particular stress vector passing through the origin, as shown in Figure VIII.4. During the experiment (and in the calculation) the strain increments are arranged so that the stress state always lies on the vector. Under such conditions, the normality condition and the rate effects are unimportant. Thus, the stress-strain curves shown in Figure VIII.9 for $\sigma_2 = 0$ show very little effect of

rate. As Yamamoto³² observed in his use of the Gurson model, there is no sudden drop in the stress-strain curve as we might expect for fracture. In the center of a tensile specimen the mean stress increases during neck formation. A second series of computations were conducted to represent this state in which the mean stress increases. Figure VIII.9 shows that the computed results are rate independent and that the results of these calculations are identical for all rates up to 10^5 .

Scaling effects are usually closely associated with strain rate effects. Therefore, for uniaxial stress states and similar states in which the mean stress does not exceed the yield strength, the DFRACT2 model will predict no scaling effects. However, for stress states such as those found in the uniaxial strain test, there will be noticeable scaling effects, especially for strain rates above about 10^3 .

F. Summary

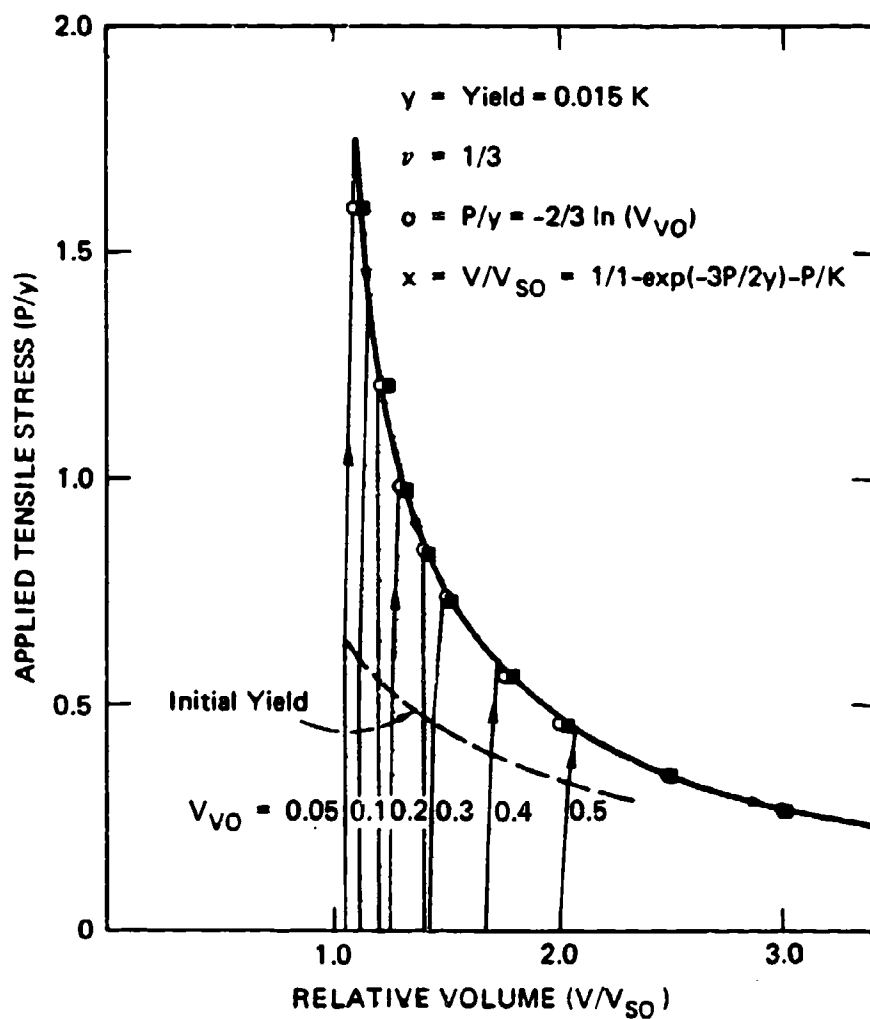
A continuum model with microstatistical features has been developed to describe ductile fracture in metals. A new growth law was outlined that is consistent with both dynamic and quasi-static data. Time-dependent stress-strain relations were derived for material containing voids. The governing differential equations were solved by methods that are economical enough for use in wave propagation and structural calculations. Some of the effects of scaling, strain rate, and normality were explored. The model stands ready for application to VAR 4340 steel. The fracture surface analysis described in Section VII showed that DFRACT2 models the correct physical mechanism of ductile fracture; it remains to determine the model parameters for VAR 4340 by further reduction of the topographic data.

G. References

1. A. L. Gurson, "Continuum Theory of Ductile Rupture by Void Nucleation and Growth: Part I - Yield Criteria and Flow Rules for Porous Ductile Media," J. Engin. Materials and Tech., Trans. of ASME, Jan. 1977, pp. 2-15.

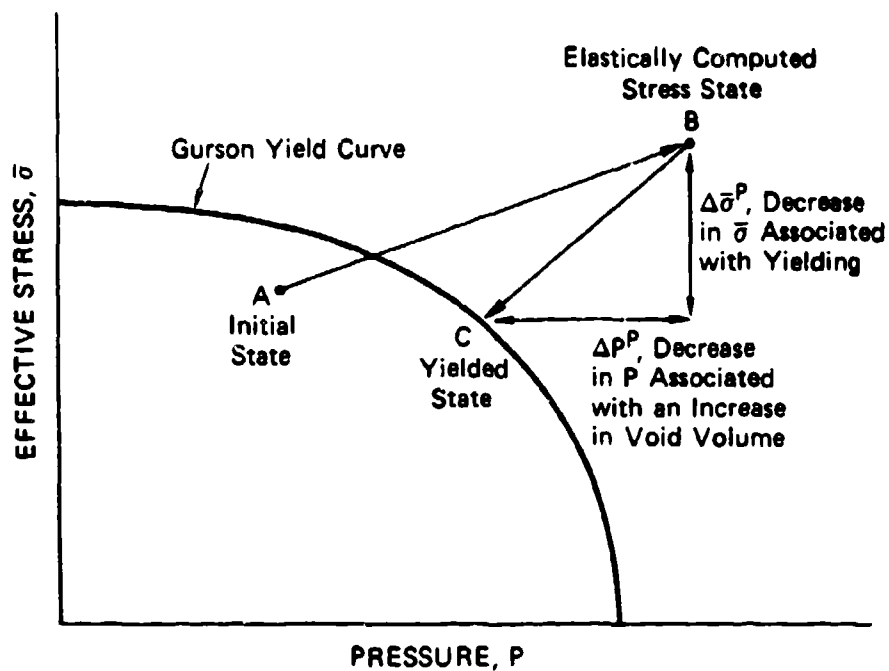
2. P. Chadwick, The Quasi-Static Expansion of Spherical Cavity in Metals and Ideal Soils, Quarterly J. Mech. and Appl. Math., 12, 52-71 (1959).
3. H. G. Hopkins, "Dynamic Expansion of Spherical Cavities in Metals," Chap. III of Progress in Solid Mechanics, Vol. I, I. N. Sneddon and R. Hill, Eds. (Interscience Publishers, Inc., New York, 1960).
4. M. M. Carroll and A. C. Holt, "Static and Dynamic Pore-Collapse Relations for Ductile Porous Materials," J. Appl. Phys., 43(4), 1626-1636 (April 1972).
5. M. M. Carroll and A. C. Holt, Suggested Modification of the P- α Model for Porous Materials, J. Appl. Phys., 42, 759 (February 1972).
6. R. Hill, The Mathematical Theory of Plasticity, (Clarendon Press, Oxford, 1959).
7. C. A. Berg, "The Motion of Cracks in Plane Viscous Deformation," Proc. Fourth U.S. National Congress of Appl. Mech., Vol. 2, p. 885 (1962).
8. F. A. McClintock, "A Criterion for Ductile Fracture by the Growth of Holes," J. Appl. Mech., Trans. of the ASME, 35, 363-371 (June 1968).
9. J. R. Rice and D. M. Tracey, "On the Ductile Enlargement of Voids in Triaxial Stress Fields," J. Mech. Phys. of Solids, 17, 201-217 (1969).
10. D. A. Shockey, K. C. Dao, L. Seaman, R. Burback, and D. R. Curran, "Computational Modelling of Microstructural Fracture Processes in A533B Pressure Vessel Steel," Final Report by SRI for Electric Power Research Institute, Palo Alto, CA, 94304, EPRI RP 1023-1 (September 1979).
11. M. M. Carroll, private communication, Nov. 1984
12. V. Tvergaard, "Influences of Voids on Shear Band Instabilities Under Plane Strain Conditions," Danish Center for Appl. Math. and Mech., Report 159 (1979).
13. A. Needleman, "Finite Element Analysis of Flow Localization and Failure," presented at Workshop on Inelastic Deformation and Failure Modes, Nov. 18-21, 1984, Northwestern University, Evanston, Illinois.
14. L. Seaman, D. R. Curran, and D. A. Shockey, "Computational Models for Ductile and Brittle Fracture," J. Appl. Phys., 47(11) 4814 (November 1976).

15. A. L. Stevens, L. Davison, and W. E. Warren, "Void Growth During Spall Fracture of Aluminum Monocrystals," In Dynamic Crack Propagation, G. C. Sih, Ed. (Noordhoff International Publishing, The Netherlands, 1973), p. 37.
16. L. Seaman, R. E. Tokheim, and D. R. Curran, "Computational Representation of Constitutive Relations for Porous Material," Final Report by SRI for Defense Nuclear Agency, Report DNA 3412P (May 1974).
17. D. A. Shockey, L. Seaman, K. C. Dao, and D. R. Curran, "A Computational Model for Fracture of Pressure Vessel Steel Derived from Experimental Data," Paper No. 78-PVP-92, presented at the Joint ASME/CSME Pressure Vessels and Piping Conference, Montreal, Canada, June 25-30, 1978.
18. T. W. Barbee, Jr., L. Seaman, R. Crewdson, and D. R. Curran, "Dynamic Fracture Criteria for Ductile and Brittle Metals," J. Materials, JMLSA, 7(3), 393-401 (September 1972).
19. L. Seaman, T. W. Barbee, Jr., and D. R. Curran, "Dynamic Fracture Criteria for Homogeneous Materials," Final Report by SPI for Air Force Weapons Laboratory, Kirtland Air Force Base, Albuquerque, New Mexico 87117, Tech. Rep. No. AFWL-TR-71-156 (December 1971).
20. T. W. Barbee, Jr., L. Seaman, and R. C. Crewdson, "Dynamic Fracture Criteria of Homogeneous Materials," Final Report by SRI for Air Force Weapons Laboratory, Kirtland Air Force Base, Albuquerque, New Mexico 87117, Tech. Rep. No. AFWL-TR-70-99 (November 1970).
21. D. R. Curran, L. Seaman, and D. A. Shockey, "Linking Dynamic Fracture to Microstructural Processes," in Shock Waves and High-Strain-Rate Phenomena in Metal, Marc Meyers and Lawrence Murr, Eds. (Plenum Press, New York, 1981), p. 249.
22. R. Raj and M. F. Ashby, "Intergranular Fracture at Elevated Temperature," Acta Metallurgica, 23, 653-666 (June 1975).
23. H. Yamamoto, "Conditions for Shear Localization in the Ductile Fracture of Void-Containing Materials," Int. J. Fracture, 14, 4 (1978).



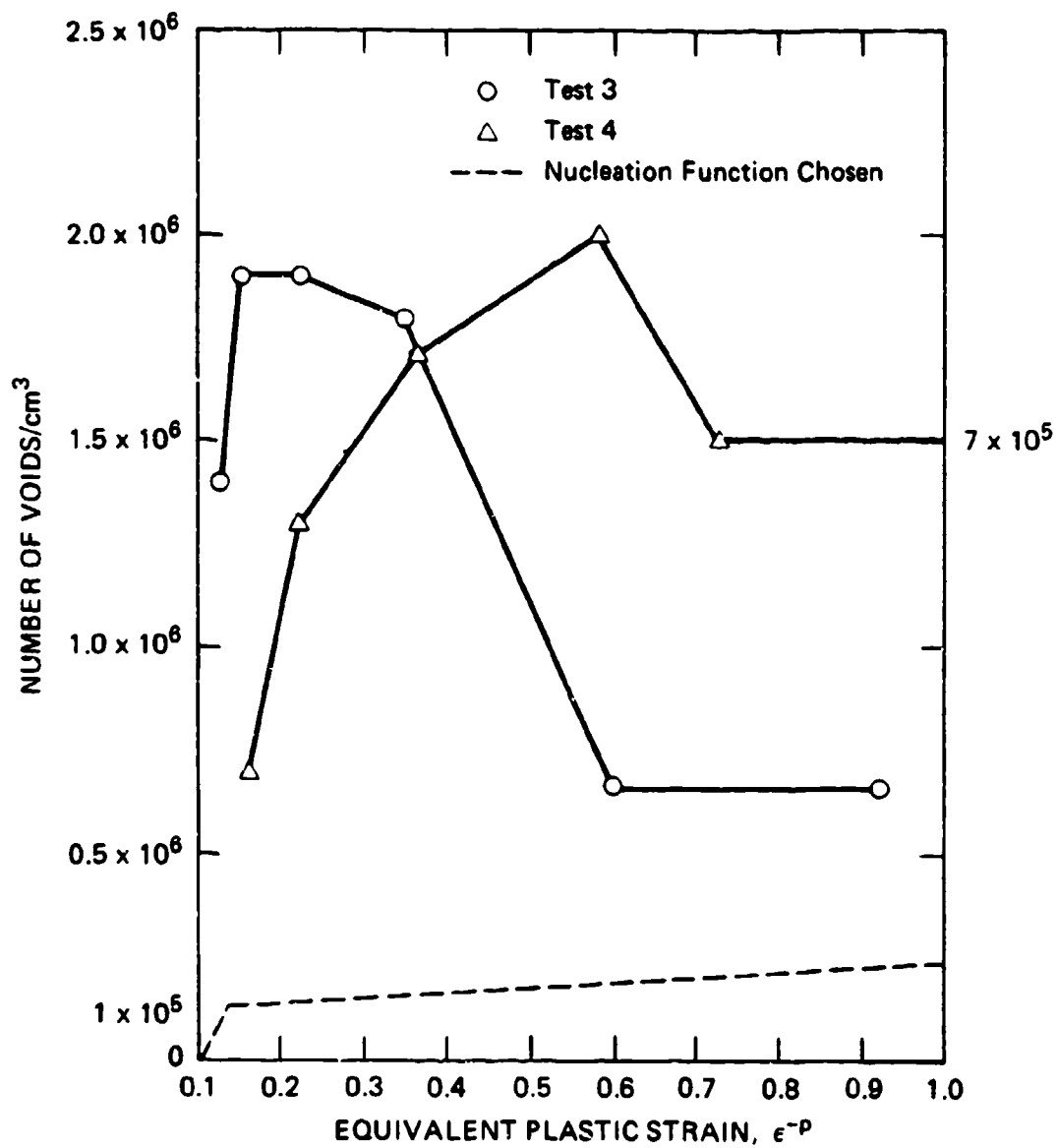
JA-314522-86

FIGURE VIII.1 VOID EXPANSION UNDER EXTERNAL TENSION FOR SEVERAL INITIAL RELATIVE VOID VOLUMES



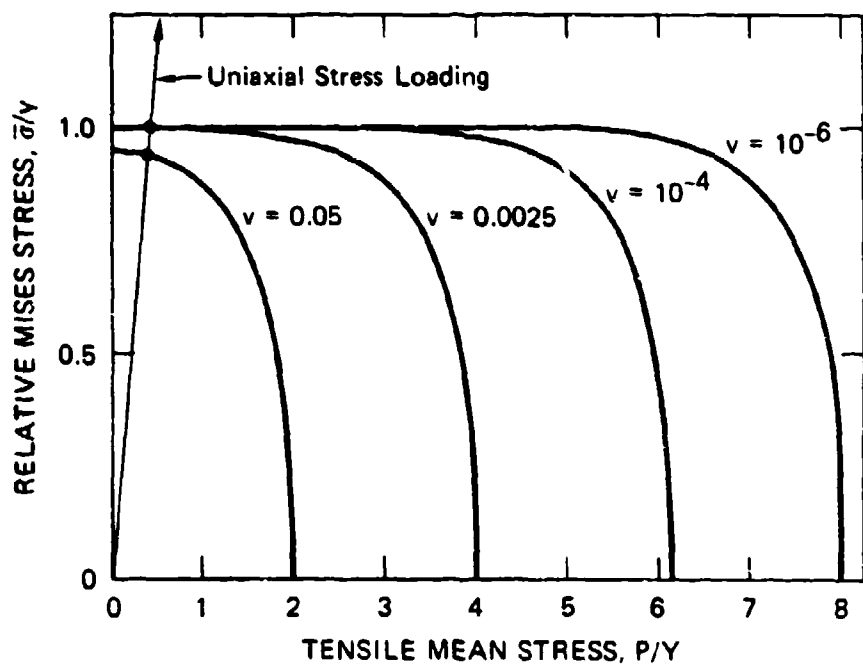
JA-314622-67

FIGURE VIII.2 RELATIONS BETWEEN THE ELASTICALLY COMPUTED STRESS STATE, THE YIELDED STATE, AND THE GURSON YIELD CURVE FOR A NORMALITY CONDITION



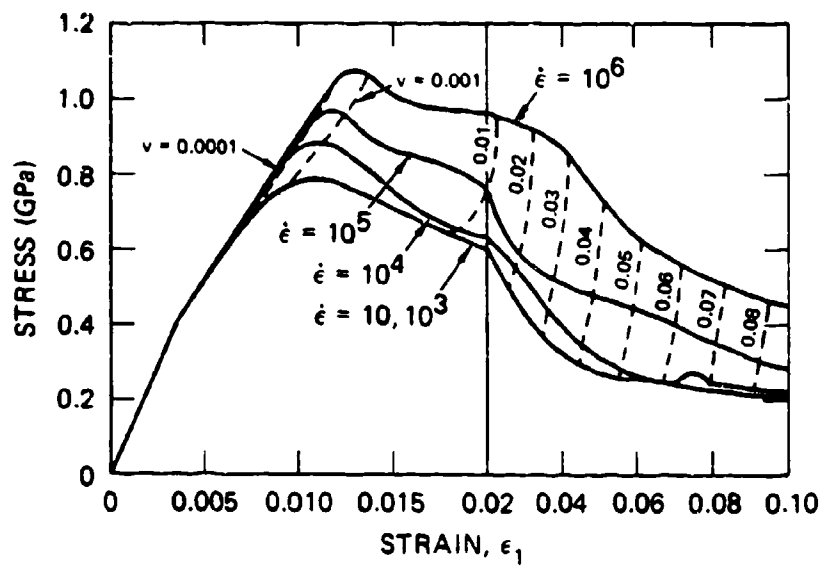
MA-6110-64B

FIGURE VIII.3 NUCLEATION OF VOIDS IN THE SMOOTH ROUND BAR TENSION TEST



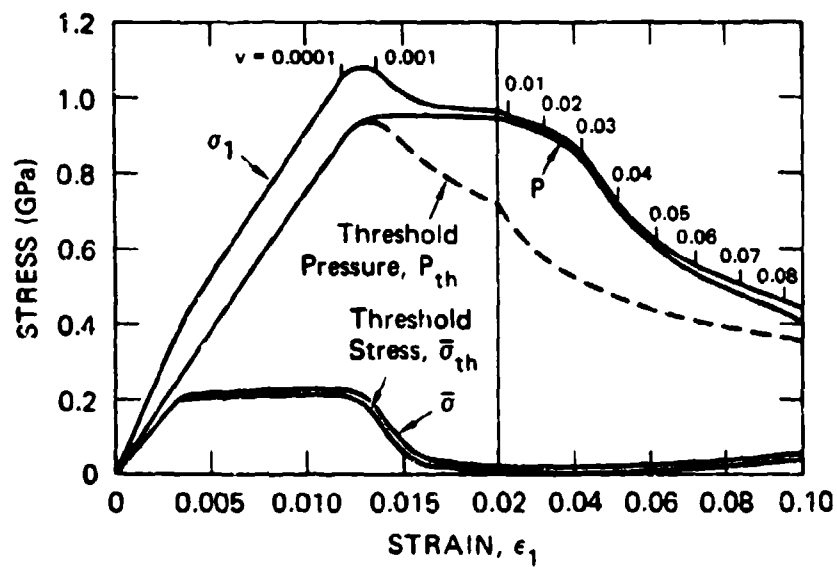
JA-314522-68

FIGURE VIII.4 A FAMILY OF GURSON YIELD (THRESHOLD) CURVES
FOR SEVERAL RELATIVE VOID VOLUMES



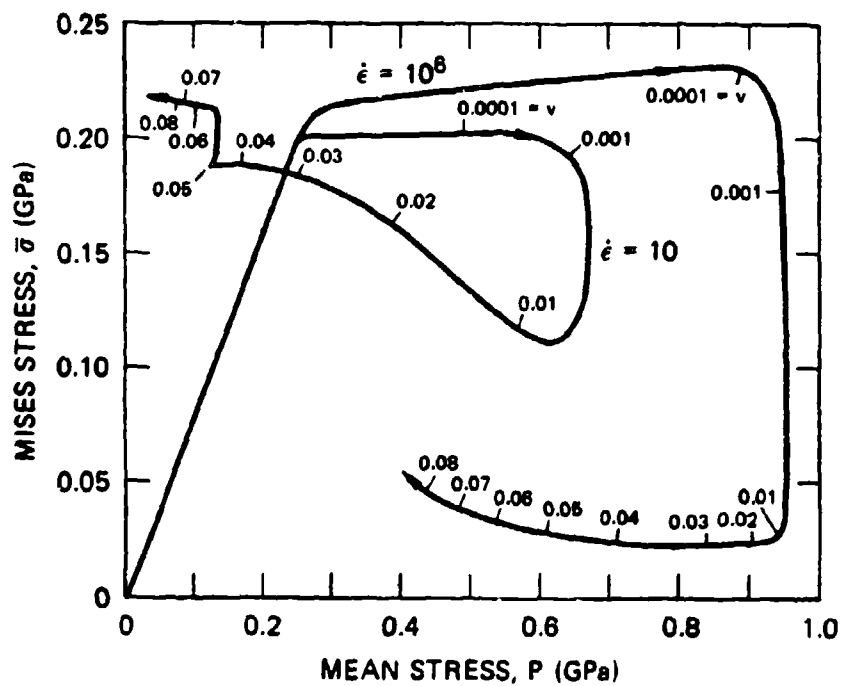
JA-314522-71

FIGURE VIII.5 STRESS-STRAIN PATHS FOR UNIAXIAL STRAIN
SIMULATION OF SEVERAL STRAIN RATES (1145
Al WITH YIELD = 0.2 GPa)



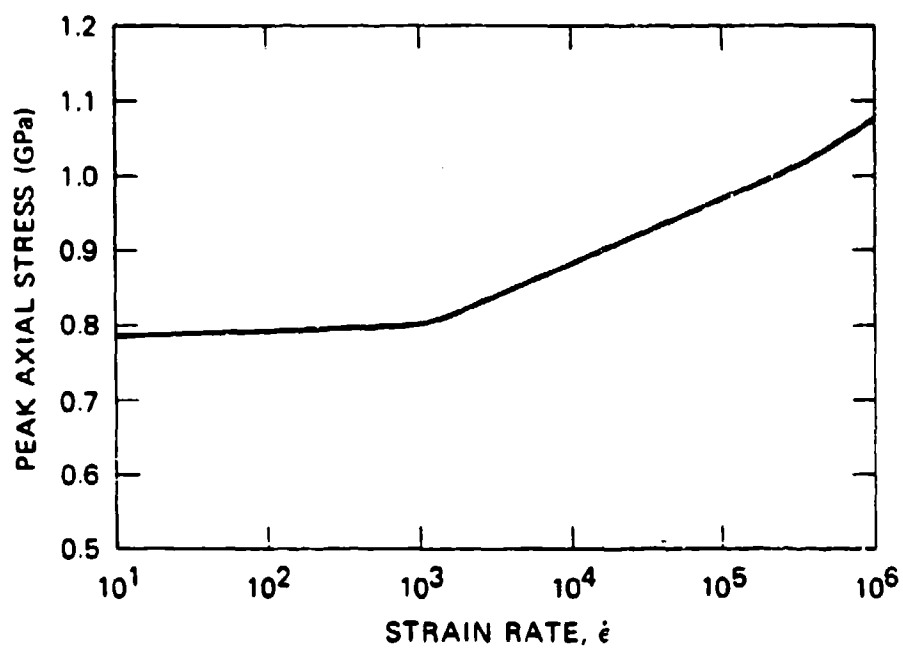
JA-314522-72

FIGURE VIII.6 COMPUTED HISTORIES OF AXIAL STRESS (σ_1), MEAN STRESS (P), MISES STRESS (σ), THRESHOLD PRESSURE (P_{th}), AND THRESHOLD YIELD STRESS (σ_{th}) FOR UNIAXIAL STRAIN TEST AT A STRAIN RATE OF 10^8



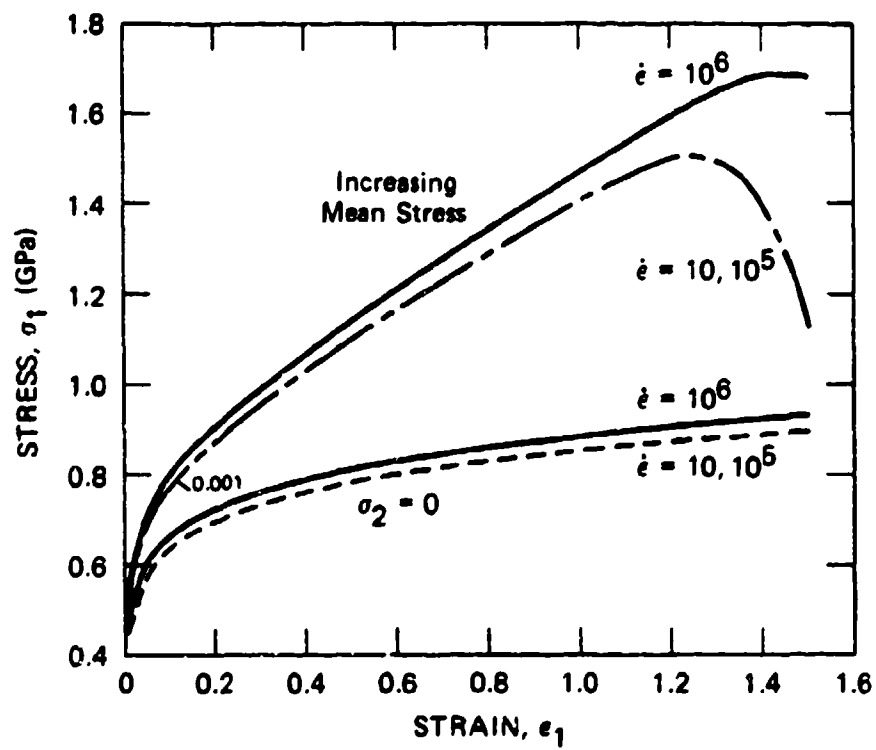
JA-314522-75

FIGURE VIII.7 PRESSURE-SHEAR STRESS PATHS FOLLOWED BY FRACTURING ALUMINUM AT TWO STRAIN RATES IN UNIAXIAL STRAIN



JA-314522-74

FIGURE VIII.8 PEAK AXIAL STRESS AS A FUNCTION OF STRAIN RATE
FOR UNIAXIAL STRAIN EXPERIMENTS



JA-314822-76

FIGURE VIII.9 UNIAXIAL STRESS LOADING AT SEVERAL STRAIN RATES

IX RECOMMENDATIONS FOR FUTURE WORK

This research program has brought the evolving SHEAR4 and DFRACT2 models to the point where they can be evaluated and refined by simulation both of simple, well-controlled experiments and of ordnance events. As described in the Introduction, the iterative computational/experimental procedure is effective in pointing up deficiencies in the model and in material property values, and in indicating appropriate modifications. Thus we recommend that the models now be applied to simulate various dynamic failure scenarios. We first describe simulations for evaluating and refining the SHEAR4 model, and features that should be added to extend the capabilities of the model. We next discuss split Hopkinson torsion bar experiments and topographic analyses of ductile tensile fracture experiments needed to support development of the SHEAR4 and DFRACT2 models, respectively. Then, we recommend simulations be performed to evaluate and improve DFRACT2. Finally, we recommend SHEAR4 and DFRACT2 be combined to allow computation of mixed mode failure.

Simulations of SHTB Experiments and Modifications to SHEAR4

A particularly simple, well-controlled and easily conducted shear band experiment is the split Hopkinson torsion bar (SHTB) experiment described in Section III. Simulation of SHTB experiments, and comparison of the computed and measured results will help establish the dependence of shear band nucleation and growth on macroscopic stress and strain, and will allow a stress-strain relation to be inferred for material being permeated by shear bands. Simulations and experiments should be performed at various strain rates to study distributions of plastic strains in the specimen, the rotations of the damage and the planes of plastic flow, and possible initiation criteria. Comparison of measured torsional forces with computed forces would allow evaluation of the damage-caused strength reduction mechanism now in the SHEAR4 model.

Simulation of dynamic torsion specimens containing a crack would be useful in determining shear band growth behavior and how growth depends on the stress-strain relation when many bands are present.

Since the SHTB specimens are thin walled in the gage section, the stress state of the shear banding material is one of plane stress. Therefore, to simulate the SHTB experiments, it is necessary to include in SHEAR4 a provision for plane stress conditions. This provision will alter the present solution procedure somewhat, but because the present solution method allows a gradual approach to the correct answer, it appears possible to incorporate the provision for plane stress without a total change in method. We recognize, however, that this requirement poses a mixed boundary problem.

The tensile opening process developed in the current program has caused difficulties in obtaining a solution for some of the simulations discussed in Section VI. In particular, the plasticity results appear to be sensitive to the tensile opening process; hence we recommend that the solution procedure be examined for accuracy and appropriateness to the multiplane problem.

For studying the solution procedure, we recommend beginning with the plasticity problem alone (i.e., in the absence of shear bands), and comparing SHEAR4 results with standard analytical results for Mises and Tresca models. Because of the finite number of planes in SHEAR4, the correspondence will not be exact, but should be within a few percent. These studies will indicate appropriate accuracy criteria to be used with SHEAR4 and will also serve to indicate changes needed in the basic solution procedure.

The multiplane plasticity feature of SHEAR4 should be applied to single-crystal plasticity in the manner of Peirce, Asaro, and Needleman. Many existing problems in plasticity theory could be examined profitably in this way, including the role played by latent hardening and the conditions for formation of isothermal microscopic shear bands.

SHTB Experiments to Support SHEAR4 Development

Classical Hopkinson bar methods that use the reflected and transmitted torsional waves measured by strain gages to determine the stress strain relations of a material yield only information averaged over the whole specimen width; only limited information about strain localization is obtained. However, localization information is necessary for shear band model development.

During the current program a unique capability was developed for investigating localization behavior, namely the high performance split Hopkinson torsion bar coupled with high-speed photography of a fine grid on the specimen. We recommend that this capability be used to measure the strain profile across the specimen gage width as a function of time. Specific objectives would be to:

- (1) Determine precisely at what point along the stress-average strain curve localization starts to occur.
- (2) Measure the time evolution of the strain profile across the zone of localized deformation after the onset of instability.
- (3) Establish the conditions of strain and strain rate for strain localization by performing measurements at several strain rates and compare these conditions with the conditions derived from average strain measurements.
- (4) Investigate how the load carrying capacity of the specimen is affected by the shear localization process.
- (5) Attempt to measure shear band growth velocity.

These experimental results would be most useful in testing and in improving the nucleation conditions in the current shear banding model. The nucleation function should be further tested by simulating experiments of different geometries and loading conditions, or experiments in which artificial perturbations of known size, spatial, and severity distributions have been introduced.

By relating the true strain in the shear band rather than the average specimen strain to the stress carried by the specimen, the strength reduction due to shear banding can be more accurately

assessed. This experimental information will be useful in evaluating and improving the algorithm in SHEAR4 for softening planes that have acquired shear bands.

To investigate shear band growth behavior, we recommend introducing a slot or crack-like defect in the gage section of a SHTB specimen to trigger a shear band at a specified location, and then observing the progress of the band that emerges with the high-speed photographic capability.

Because in most practical instances, shear bands form under stress states consisting of compression and shear, we recommend that the effect of compressive stress on shear band behavior be investigated. This could be accomplished with a SHTB apparatus in which a static axial compressive preload is applied to the bar. An objective of the compressive/shear experiments should be to determine the effect of increasing compressive stress on the threshold conditions for nucleation.

The detailed examination of failure surfaces of SHTB specimens (Section III) showed that failure occurred by a combination of shear bands and highly sheared ductile voids, and provided valuable insight into the mechanisms, sequence, characteristic sizes and spacing, and kinetics of shear microfailure processes. Additional examinations should be performed to quantify these aspects of the microfailure process and to investigate the interaction of voids and shear bands. The topographic fracture surface analysis technique described in Section VII should be applied to study dimples and shearing features observed on failed Hopkinson torsion bar specimens. These failure features should be correlated with metallographic features to obtain a understanding of how microstructure influences microfailure behavior.

Furthermore, the tensile specimens tested at elevated temperatures in this program should be subjected to topographic examination to look for effects of temperature. Similar fracture surfaces produced at temperatures up to 1200°C should be analyzed in light of the shear band temperature measurements reported in Section III and the dimpled nature of shear failure surfaces also discussed in Section III.

Ductile Fracture Model Development

For continued development of the ductile fracture model DFRACT2, the following specific tasks should be accomplished:

- The topographic analysis data extractable from the work in Section VII should be reduced to determine how strain relates quantitatively to void nucleation, void growth, and void coalescence.
- Supplemental topographic analyses should be performed at a higher magnification to examine the role of inclusions and carbide particles on the microfailure process. The results should be correlated with the results obtained by Cox and Low in their sectioning studies of interrupted tensile tests.
- Fracture surfaces of plate impact or other dynamically loaded tensile specimens should be examined by the topographic technique to establish the importance of rate effects on tensile microfracture behavior.
- Additional correlation of metallographic features with topographic fracture surface features should be done to more firmly establish effects of microstructure on microfailure processes.

The reliability of the DFRACT2 model for ductile tensile fracture should be evaluated by using it to simulate the tensile fracture experiments analyzed in Section VII. Plate impact experiments should be performed on the VAR 4340 HRC 40 baseline material to provide a comparable high-strain rate evaluation of the model. The model should be applied to compute fracture experiments of different geometry and loading conditions to check its versatility.

Finally, DFRACT2 should be combined with SHEAR4 to allow predictions of failure behavior in mixed mode. Simulations of the combined void/shear failure observed in the Hopkinson torsion bar experiments should be useful in consolidating the two failure models; simulations of armor penetration experiments would provide a useful and practical test of reliability.

X PARTICIPATING SCIENTIFIC PERSONNEL

R. D. Caligiuri	
P. F. Chartagnac	(International Fellow)
D. R. Curran	(Principal Investigator)
J. L. Dien	
O. Dullum	(International Fellow)
D. C. Erlich	
J. H. Giovanola	
J. Hancock	(Visiting Scientist)
J. A. Kempf	
T. Kobayashi	
L. Seaman	(Principal Investigator)
D. A. Shockey	(Principal Investigator)
M. Stelly	(International Fellow)

XI PUBLICATIONS AND PRESENTATIONS

The following manuscripts were presented and either published or submitted for publication under complete or partial support from ARO during this program.

Publications

1. D. A. Shockey, L. Seaman, and D. R. Curran, "Application of Microstatistical Fracture Mechanics to Dynamic Fracture Problems," in Material Behavior Under High Stress and Ultrahigh Loading Rates, Vol. 29, J. Mescall and V. Weiss, Eds., Sagamore Army Materials Research Conference Proceedings (Plenum Press, New York, 1983), pp. 273-293.
2. L. Seaman, D. R. Curran, and D. A. Shockey, "Scaling of Shear Band Fracture Processes," in Material Behavior Under High Stress and Ultrahigh Loading Rates, Vol. 29, J. Mescall and V. Weiss, Eds., Sagamore Army Materials Research Conference Proceedings (Plenum Press, New York, 1983), pp. 295-307.
3. D. C. Erlich, D. A. Shockey, and L. Seaman, "Dynamic Flow Curve for 4340 Steel," in Shock Waves in Condensed Matter, J. R. Asay, R. A. Graham, G. K. Straub, Eds., Elsevier Science Publishers, B. V., 1984, pp. 129-132.
4. D. A. Shockey, L. Seaman, and D. R. Curran, "Microstatistical Approach to Dynamic Fracture," invited contribution to Special 20th Anniversary Issue of International Journal of Fracture to be published in December 1984.
5. L. Seaman and J. L. Dein, "Representing Shear Band Damage at High Strain Rates," in Nonlinear Deformation Waves, U. Nigul and J. Engelbrecht, eds., IUTAM Symposium, Tallin, Estonia, (Springer-Verlag, Berlin Heidelberg New York, 1983) pp. 229-234.
6. T. Kobayashi and D. A. Shockey, "A Fracture Surface Topographic Study of Ductile Tensile Failure Processes in VAR 4340 Steel," to be submitted to the Journal of Materials.
7. P. F. Chartagnac, "Analysis of the SRI Symmetric Taylor Test Data on 4340 Steel," to be submitted.

8. L. Seaman and D. R. Curran, "A Microstatistical Model for Ductile Fracture Under Loadings Ranging from Quasistatic to Impacts," in High Energy Rate Fabrication, I. Berman and J. W. Schroeder, Eds. (ASME New York, 1984), pp. 99-106.
9. D. C. Erlich, "Determination of the Dynamic Flow Curve of Metals at Ambient and Elevated Temperatures by Rod Impact Techniques," submitted to the International Conference on Mechanical and Physical Behavior of Materials Under Dynamic Loading (DYMAT, 85) to be held in Paris, September 1985.
10. D. C. Erlich, "Rod Impact (Taylor) Test," section in chapter entitled "High Rate Compression Testing" in "High Strain Rate Mechanical Testing" section of the Metals Handbook (Vol. 8) to be published in 1985 by American Society for Metals.
11. D. R. Curran and L. Seaman, "Computational Models for Nucleation, Growth, and Coalescence of Adiabatic Shear Bands," submitted to the International Conference on Mechanical and Physical Behavior of Materials Under Dynamic Loading (DYMAT, 85) to be held in Paris, September 1985.
12. L. Seaman, D. R. Curran, D. C. Erlich, T. Cooper, and O. Dullum, "Shear Band Observations and Derivation of Requirements for a Shear Band Model," submitted to the International Conference on Mechanical and Physical Behavior of Materials Under Dynamic Loading (DYMAT, 85) to be held in Paris, September 1985.
13. L. Seaman, J. Gran, and D. R. Curran, "A Multiplane CAP Model to Represent the Strong Anisotropy of Damage in Concrete," presented and published in the proceedings of the NATO Advanced Research Workshop on Applications of Fracture Mechanics to Cementitious Composites (S. P. Shah, Ed.) held at Northwestern University, September 4-7, 1984, sponsored by the NATO Scientific Affairs Division (Craig Sinclair) and the U.S. Army Research Office (George Mayer, John Bailey).
14. D. A. Shockey, L. Seaman, and D. R. Curran, "Development of a Computational Shear Band Model for Armor Design," presented at and to be published in the proceedings of the 1984 Army Symposium on Solid Mechanics, Advances in Solid Mechanics for Design and Analysis, 1-3 October 1984, The Viking Hotel, Newport, R.I.

Presentations

1. D. A. Shockey, D. C. Erlich, and L. Seaman, "Measurement of Dynamic Constitutive Relations of Metals," Innovations in Mechanical Testing, Golden Gate Metals and Welding Conference, Sheraton Palace Hotel, San Francisco, CA, February 9-11, 1983.

2. D. A. Shockey, D. C. Erlich, and L. Seaman, "Measurements of Dynamic Constitutive Relations at High Temperatures," 1983 Gordon Conference on Physical Metallurgy, Holderness School, Plymouth, NH, June 20-24, 1983.
3. D. C. Erlich, D. A. Shockey, and L. Seaman, "Dynamic Flow Curve for 4340 Steel," Third Topical Conference of the American Physical Society on Shock Waves in Condensed Matter, Santa Fe, NM, July 18-21, 1983.
4. T. Kobayashi, "Topographic Analysis of Fracture Surfaces: An Important New Failure Analysis Technique," invited seminar presented at the Army Materials and Mechanics Research Center, Watertown, MA, Army Research and Development Command, Dover, NJ, and Benet Weapons Laboratory, Watervliet, NY, April 1984.